2015

Aerosol formation in the Antarctic sea-ice region

Ruhi Humphries
University of Wollongong

Aerosol Formation in the Antarctic Sea-Ice Region

Ruhi Humphries

Supervisors:
Associate Professor Stephen Wilson & Dr Melita Keywood
Co-supervisor:
Dr Clare Murphy (Paton-Walsh)

This thesis is presented as required for the conferral of the degree:

Doctor of Philosophy

The University of Wollongong
School of Chemistry

May 2015

Declaration

I, Ruhi Humphries, declare that this thesis submitted in fulfilment of the requirements for the conferral of the degree Doctor of Philosophy, from the University of Wollongong, is wholly my own work unless otherwise referenced or acknowledged. This document has not been submitted for qualifications at any other academic institution.

Ruhi Humphries
November 10, 2015

Abstract

Particles in the atmosphere, or aerosols, are vital components of many chemical and physical processes including the Earth's radiative balance. The mechanisms of aerosol formation, along with their interactions with clouds and subsequent effect on the radiative balance, are among the largest uncertainties present in our understanding of the climate system. Recent modelling studies have shown that the greatest gains in reducing these uncertainties will be achieved through the study of pristine, natural aerosol processes.

There are very few observations in the Antarctic and Southern Ocean regions. Those that have been made have been primarily limited to boundary layer air-masses at spatially sparse coastal and continental research stations, or to ship-based measurements in the Southern Ocean. The dynamic Antarctic sea ice region, when at its maximum spatial extent, covers more area than the continent itself, however aerosol measurements within this region have only been performed once before.

This thesis describes results from atmospheric measurements made on-board Australia's flagship ice-breaker, *Aurora Australis*, during a marine science voyage to the sea ice region off the East Antarctic coast during the spring of 2012. Measurements of aerosols and various trace gases were made continually throughout the voyage, resulting in significant advances in the scientific understanding of the region which this research has shown to be atmospherically distinct from adjacent areas. The collected aerosol dataset has two main features. Firstly, background aerosol concentrations were higher than any other previously recorded in the Antarctic and Southern Ocean region. Secondly, a single new particle formation event was observed during the 32 day aerosol record which could not be explained by known nucleation chemistry.

As the voyage moved south in the sea ice, background aerosol number concentrations were observed to exhibit a 10-fold increase moving across the atmospheric Polar Front, resulting in Polar Cell concentrations of particles larger than 3 nm (CN_3), averaging 1130 cm^{-3} - higher than any other observed in the Antarctic region. These populations were found not to be growing, and air-mass trajectory calculations using the HYSPLIT model suggested populations had come recently from the Antarctic free-troposphere, a commonly identified source in the region. Simula-

tions using global chemical and transport models suggested that these aerosols were not the result of dimethyl sulfide (DMS) oxidation - the precursor typically identified in the region - although measurements and modelling limitations prevented further identification of the source. Additional trajectory calculations suggested sea ice boundary layer air-masses travel equator-ward, transporting young aerosol nuclei and nucleation precursors to the Southern Ocean, where they grow by condensation and cloud processing to climate relevant sizes. This previously unrecognised aerosol load could yield cloud condensation nuclei (CCN) currently missing in the Southern Ocean in climate models.

The new particle formation event, which occurred within a spatially extended air-mass, was characterised by CN_3 number concentrations rising from background levels of 370 cm^{-3} up to almost 7700 cm^{-3}. The rate of increase resulted in formation rates ranging from $0.2 - 1.13 \pm 0.1\ cm^{-3}.s^{-1}$, similar to those observed at other Antarctic locations. A 75 minute delayed increase in the larger aerosol size bin was observed, reflecting growth rates of $5.6 \pm 0.9\ nm.hr^{-1}$. The event occurred on the only day during the measurement period that experienced extended periods of solar radiation above 600 $W.m^{-2}$, suggesting photochemically driven nucleation. Negligible measured concentrations of halogen and organic compounds ruled out the possibility of their involvement in nucleation. Further investigations into the chemistry of nucleation using a chemical box model found that known sulfur chemistry could not reproduce aerosol activity unless seed particles with diameters less than 3 nm were present onto which sulfur species could condense. These results suggest that currently known nucleation chemistry is not responsible for the earliest stages of genesis. Surprising correlations with Total Gaseous Mercury (TGM) were found that, together with other data, suggested a mercury catalysed photochemical nucleation mechanism. This previously unrecognised chemistry could be occurring throughout the atmosphere where sufficient solar irradiance and TGM concentrations exist, and could represent a non-negligible fraction of nucleating species.

These aerosol measurements represent the first in the East Antarctic sea ice and are among the few that have occurred in any Antarctic sea ice. This study has revealed that the sea ice region is atmospherically distinct from surrounding areas, particularly during spring-time, highlighting the need for further study. The identification of new nucleation chemistry could have implications for aerosol formation throughout the atmosphere, particularly in particle-free air-masses with high mercury concentrations, such as those found in power plant plumes. The results described in this thesis represent significant advances in the scientific understanding of aerosol nucleation in both the Antarctic region and the global atmosphere and highlight the need for further work to more fully understand these processes.

Acknowledgments

The work presented in this thesis is based on measurements from a large campaign which required significant input and collaboration from many people. I would like to thank all those involved in the SIPEX-II project, from the crew who kept the ship going while we worked and slept, the staff in the galley that cooked amazing meals to keep us fed and warm, to the scientists all working on and sharing their own work. In particular, the Australian Antarctic Division (AAD) port staff who helped setup the ship were incredible - no job was too big or small and they did it with professionalism, laughter and astonishing efficiency. I would also like to thank the hard-working individuals who were involved in the arduous work of logistics and planning for a big project like this.

In particular, I would like to thank a number of AAD individuals who went above and beyond the call of duty to make SIPEX-II and Project 4032 a success. These people include Lloyd Symons, Kim Briggs, Miles Jordan, Matt Longmire, Ian McLean, Jono Reeve and Klaus Meiners.

The voyage to Antarctica took two months to undertake. This would have been arduous if it weren't for the many wonderful people on board that provided much laughter and fun during the cruise. In particular, I would like to thank a few who will remain close friends for a long time to come: Maria Zatko, Molly Jia, Julie Jansen and Olivier Lecomte.

The atmospheric component of the voyage, Project 4032, was itself a large collaborative effort and each aspect of the project provided valuably to the final results. Robyn Schofield (University of Melbourne) valiantly lead the project. Ian Galbally and Suzie Molloy (CSIRO Marine and Atmospheric Research) provided and installed ozone instrumentation. Paul Johnston, Karin Kreher and Alan Thomas (NIWA) provided the MAX-DOAS instrumentation and support for the GC-ECD supplies by Andrew Robinson and Neil Harris (Cambridge University). Melita Keywood and Jason Ward (CSIRO Marine and Atmospheric Research) provided the aerosol instrumentation. Caitlin Gionfriddo and John Moreau (University of Melbourne) worked on mercury data, from instruments supplied by Michael Tate and David Krabbenhoft (USGS).

During analysis, Andrew Klekociuk was instrumental in running HYSPLIT tra-

jectory models and led the way in thinking differently about how to represent trajectory data. This change in thinking revealed significant information about circulation patterns that otherwise may not have been discovered. His work in analysing and interpreting ozone data was also valuable.

The support and encouragement of Paul Johnston and Karin Kreher during difficulties in managing the MAX-DOAS instrument were greatly appreciated and helped keep moving through frustrating periods of the voyage. Paul's humility during day-to-day analysis was also an inspiring characteristic that I hope to possess throughout my career.

Matthew Woodhouse was very flexible and accommodating and this collaboration was greatly appreciated. His comments on my work provided opportunities to look at science in a new light and his dedication to hard work and problem solving allowed a timely completion of my thesis.

Jason Ward is one of the most helpful individuals I've worked with. Although very busy, he always put aside time to teach me about his instruments, and taught me a lot about experimental design and field work. His humour and genuine nature meant he was a pleasure to work with and I look forward to doing so into the future.

I would also like to thank my annual review committee at UoW, who included Steven Blanksby and Glennys O'Brien, who gave some important and very useful advice in directing my thesis very early on. Additionally, Glennys has been a wonderful support and example for the development of my tertiary teaching skills and experience. It has been wonderful working with such a committed and caring individual in raising up the next generation.

I wish to acknowledge the various funding that has made my PhD possible and the incredible international experience it has been. The Australian Postgraduate Award from the Australian Government; the CSIRO OCE Postgraduate Top-Up scholarship; and travel allowances in the form of the UOW Travel Scholarship and the Larry and Marylin Hick Award.

Although Robyn Schofield wasn't an official supervisor, she very much assumed that role throughout my candidature. She provided humble guidance and direction and combined this will honest consultation and collaboration as well as constant encouragement and support. I was lucky to have her involved in my thesis project and will treasure her continued friendship into the future.

Melita Keywood was my associate supervisor based at CSIRO and was huge asset to the project and key to its success. Her scientific and professional guidance, as well as her support, both academically, but also personally, was invaluable. I was very lucky to have such a kind, patient and selfless individual serving as my supervisor throughout my PhD. I look forward to working with her in the future and her continued friendship.

Clare Paton-Walsh (Murphy), my co-supervisor at UOW, was a source of guidance, laughter, and of course, one of the key hosts of the many CAC parties. Clare provided an invaluable perspective to my research, and asked important questions to expand my thinking and drastically improve the quality of the final results. Her humility has helped me, and many of the other students in CAC, feel welcome and comfortable at UOW and provided a treasured friend.

Steve Wilson, my primary supervisor. Where do I start. I started my PhD with Steve after having worked with him successfully for some time prior, but also at the same time as he was promoted to Head of the School of Chemistry. During this time in particular, I saw many inspiring qualities. He continually exhibited selflessness and dedication to the professional and emotional health and happiness of his colleagues, all the while shielding them significantly from many of the changes occurring within the university during the time. While managing the whole school, he still found time to counsel individuals with difficulties they may have been having in their personal lives, going out of his way to check up them. During these busy times, he managed to find time, every week, to sit down and spend time with me - both just for a chat, but also to assist me in my project, and help develop my research ability and critical thinking skills (not to mention my statistics!). I hope that these weekly meetings were as enjoyable and fruitful for him as they were for me. Steve's dedication to research excellence, as well as emotional stability and work-life balance in his staff and students was a refreshing contrast to the experience of many other PhD students. Throughout the years, Steve has become a cherished friend, a mentor, and a valued guide and example to which to aspire.

I would also like to thank the rest of the staff in the Centre for Atmospheric Chemistry. David Griffith for being a valuable sound-board throughout my time here; Graham Kettlewell for his friendship, technical and IT support, and wisdom in all things astronomical and philosophical; Martin Riggenbach for his crazy humour, friendship and technical prowess; Travis Naylor for his frequent laughter, dad jokes, support and throwing things at me across the room; Elise-Andrée Guérette for her patience, scientific curiousity and joy; Rebecca Buchholz (RiRi), my ERCA buddy, for her treasured friendship, her humble conversations about teaching, her frequent "ooo's and aahhh's" at pretty graphs as she walked past the computer, and of course, her timeless age of 27; my other PhD buddies Chris Caldow and Xue Shi, and the rest of the team, Frances Phillips, Nick Jones, Jenny Fisher, Nick Deutscher, Ron Macatangay, Dagmar Kubistin, Voltaire Velazco, Max Desservettaz, Jesse Greensdale, Joel Wilson, Doreena Dominick and Kaitlyn Lieschke, for your friendship and support in all the various ways you have helped me throughout my candidature, of which there are too many to name.

Of course, my PhD couldn't have been completed without the continuous sup-

port of my loving family and friends. My numerous visits to Melbourne, for 'work' and to visit my then girlfriend, now wife, were supported by the Solopotias and Roberts family, time which I think fondly of. To my immediate family, my parents and many siblings and their families for being such a unified rock throughout my life. In particular, my parents, who have brought all of us kids up with such wisdom, responding to the needs of each of us differently. My mum for her constant encouragement and inspiring selfless example. My dad for his love of science, knowledge and the desire to better the world, which invariably is why I am here in the first place. I know he gave up his dreams of a scientific career for his children and I hope in some small way he can live it vicariously through my career.

My old housemates and best buds, Baz, Luke and Ves, have provided me treasured friendship, and emotional, physical and intellectual support throughout my PhD. We had some amazing and inspiring conversations and experiences together and they have helped me in ways they probably aren't aware. I would also like to thank the rest of my friends around the world, of which there are too many to name, but have all made their own special contributions to my life and enhanced it in their own way. My new family, the Kouhbor's, have also been an invaluable support for me, providing me with a roof over my head while we were preparing to get married and I was between houses, and for all the love and laughter that has already, and will assuredly come in the future.

And finally, to my dear, beloved wife Gilda. You have enhanced my life in every aspect. Your humour, selflessness, understanding and patience, are a drop in the ocean of the qualities that make you the woman I am lucky enough to spend the rest of my life with.

Ruhi

Contents

Chapter 1

Introduction

1.1 The Earth's Changing Climate

The Earth's climate is an interactive system consisting of five major components: the atmosphere, the hydrosphere, the cryosphere, the land surface and the biosphere. Both natural and anthropogenic factors influence the climate system in various ways. Recent anthropogenic activities, primarily in the atmosphere but also in the biosphere and land surface, have significantly influenced all spheres of the climate system (IPCC, 2007). To mitigate the deleterious effects of climate change, a thorough understanding of the different components of the climate system, as well as their mutual interactions, must be sought.

The Earth's climate is driven primarily by solar radiation and its interaction with the surface and atmosphere. A summary of the Earth's energy balance is given in Figure 1.1. Since the Sun approximates to a blackbody radiator at ~5800 K, the majority of the Sun's radiation incident on the Earth's surface (mean annual radiation of 342 $W.m^{-2}$ at the top of the atmosphere) falls between the Ultra-Violet (UV) and Infra-Red (IR) wavelength regions. A large fraction (31%) of incident solar radiation is reflected back into space by clouds, particles and gases in the atmosphere, as well as the Earth's surface, with the remaining 69% being absorbed by the various remaining climate components. The Earth itself also acts as a blackbody radiator, with an effective emission temperature of 254 K, resulting in peak radiation in the thermal infrared. These wavelengths are effectively absorbed by greenhouse gases (GHGs) in the atmosphere resulting in its warming. The short-term (several years) imbalance of net incoming and outgoing radiation, caused primarily by changing atmospheric composition, followed by the system's re-establishment of equilibrium, is the fundamental cause of climate change. (IPCC, 2007; IPCC, 2013)[a]

[a]Throughout this thesis, where a whole paragraph of background information is sourced from the one or two documents, the citation will be placed at the end of that paragraph, outside the final sentence.

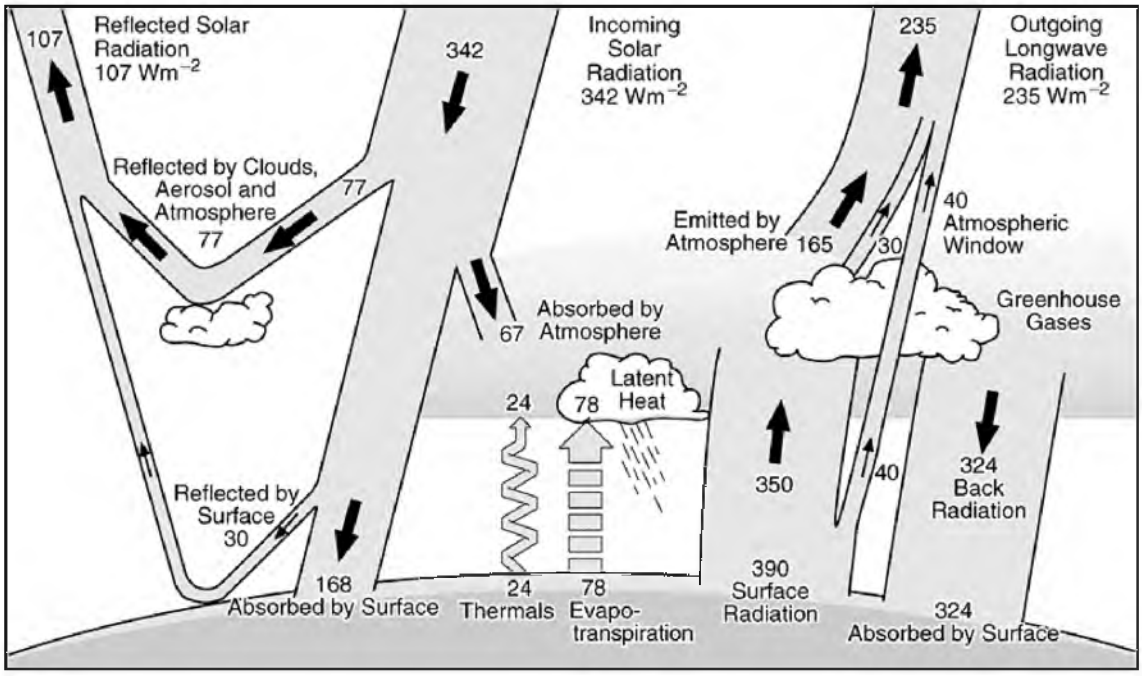

Figure 1.1: The Earth's annual and global mean energy balance. All values given have units of $W.m^{-2}$. Figure courtesy IPCC (2001).

The major components of the atmosphere which affect the Earth's energy balance include water vapour, GHGs, aerosols, clouds and the albedo of the surface. The various agents and mechanisms which affect the radiative balance are summarised in Figure 1.2 along with their respective level of confidence (IPCC, 2013). Long-lived GHGs can be seen to be dominating the net radiative forcing. Aerosols, including their direct interactions with radiation and those associated with clouds (described in detail in Section 1.4 below) are the second largest factor influencing global radiative forcing but have the largest uncertainties in their estimated impact. This high uncertainty feeds into future projections of the global climate that are used for economic and humanitarian policy. As such, since the Fourth Assessment Report by the Intergovernmental Panel on Climate Change (IPCC) in 2007, research activity in aerosol science has significantly intensified.

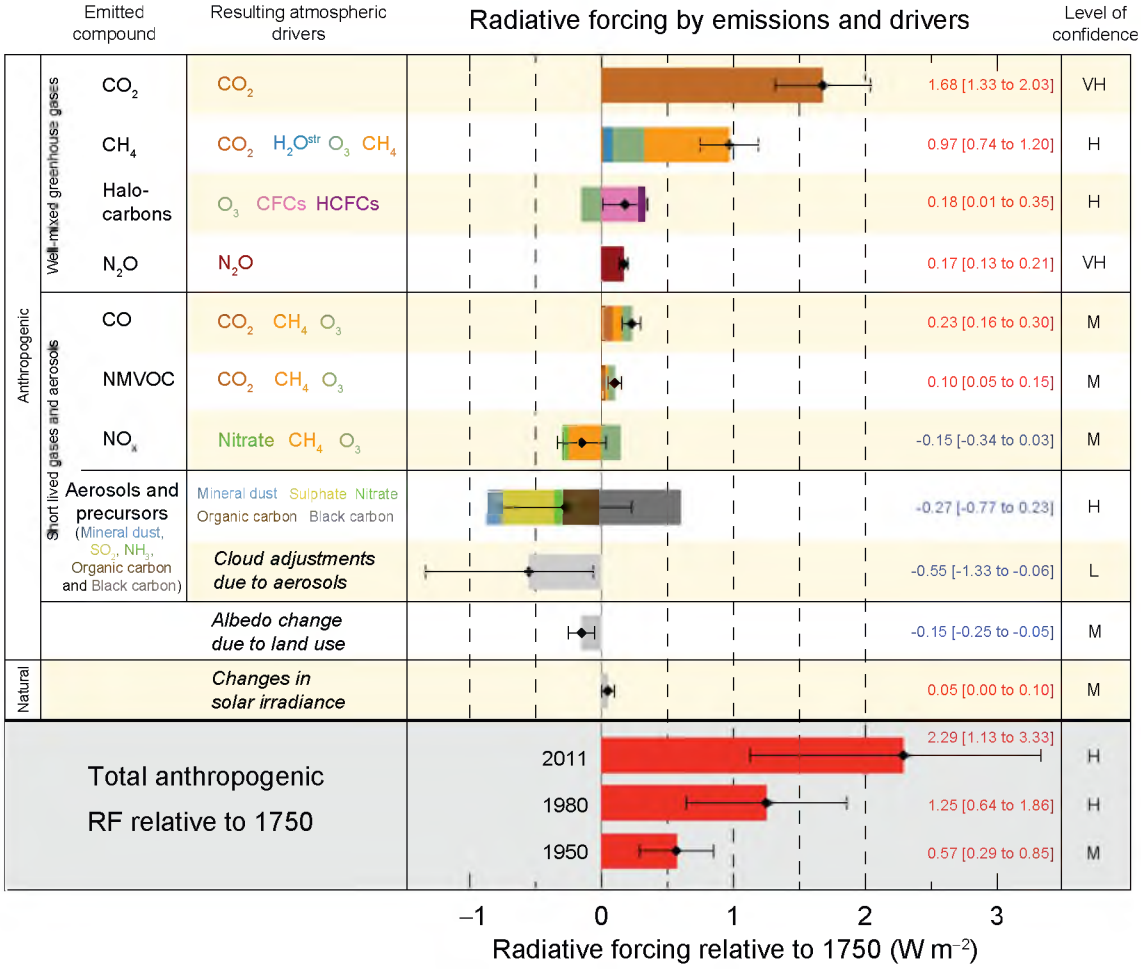

Figure 1.2: Summary of globally averaged radiative forcing estimates in 2011 relative to 1750 with aggregated uncertainties for the main drivers of climate change. Best estimates of net radiative forcing are shown as black diamonds with corresponding uncertainty intervals; numerical values are shown to the right, along with qualitative confidence levels (VH - very high, H - high, M - medium, L - low, VL - very low). Taken from Figure SPM.5 of IPCC (2013).

1.1.1 Albedo

The Earth's albedo is an important factor in any consideration of the radiative balance. Albedo is a measure of the reflectivity of the Earth's surface and is described as a fraction of shortwave solar energy[b] reflected from the Earth back into space, zero for no reflection and one for a perfect white reflector. Different parts of the Earth system have different albedos. The global annual mean surface albedo is shown in Figure 1.3 for all available data as well as the subset that represents only cloud-free conditions. A number of important features are observed in this figure. Firstly, when cloud is not present, most of the Earth's surface, in particular oceans,

[b]Shortwave solar energy refers to the radiation with wavelengths ranging from the near UV to the near-infrared, including the visible spectrum. These wavelength regions are not formally defined, however instruments used to measure albedo commonly cover the wavelength region 350 - 2500 nm.

have a very low albedo. In contrast, ice and snow covered regions, such as the polar ice sheets and sea ice areas, have albedos close to 1. Land surfaces exhibit large heterogeneity in terms of albedo, with desert areas, such as those found in northern Africa and the Middle East, having a higher albedo compared to largely vegetated areas such as the Amazon basin. What is most striking, is the magnitude of the effect of clouds on the surface albedo - a feature explored later in this chapter.

Being an important component of the radiative balance, albedo significantly influences the temperature of the planet. For example, with the current albedo distribution, the Earth's average temperature is around 15°C. If the Earth was completely covered by water, a so-called aquaplanet, the albedo would decrease significantly, despite the increased cloud, and the global average temperature would rise to 27°C (Smith, Dubois, and Marotzke, 2010). Conversely, if a snowball Earth situation was present, where the surface was completely covered in ice[c], a global average temperature of -12°C would prevail (Warren, 2002).

Albedo primarily acts upon incoming short-wave radiation. Since GHGs don't absorb appreciably at these wavelengths, almost all the radiation reflected by the surface escapes back to space within minimal radiative interaction with the atmosphere. Of course, it isn't this simple, since some components of the atmosphere (clouds and aerosols) reflect a portion of the surface reflected radiation back to the surface again, providing additional chances for absorption and incorporation into the system to occur, however this effect is small.

Overall, consideration of albedo is vital for an accurate description of the Earth's climate system and the spatial distribution of warming and cooling effects. Additionally, the surface albedo is important to understand when determining the magnitude of any changes in the albedo of atmospheric components. For example, additional high albedo clouds or aerosols over high albedo ice surfaces would have minimal affect on the radiative balance compared to the same changes over the lower albedo oceans. This idea will be important in the interpretation of results described in Chapter 3.

[c]In this situation, the albedo arising from clouds is taken into account through an average of clear and cloudy skies through a transmittance variable in the model.

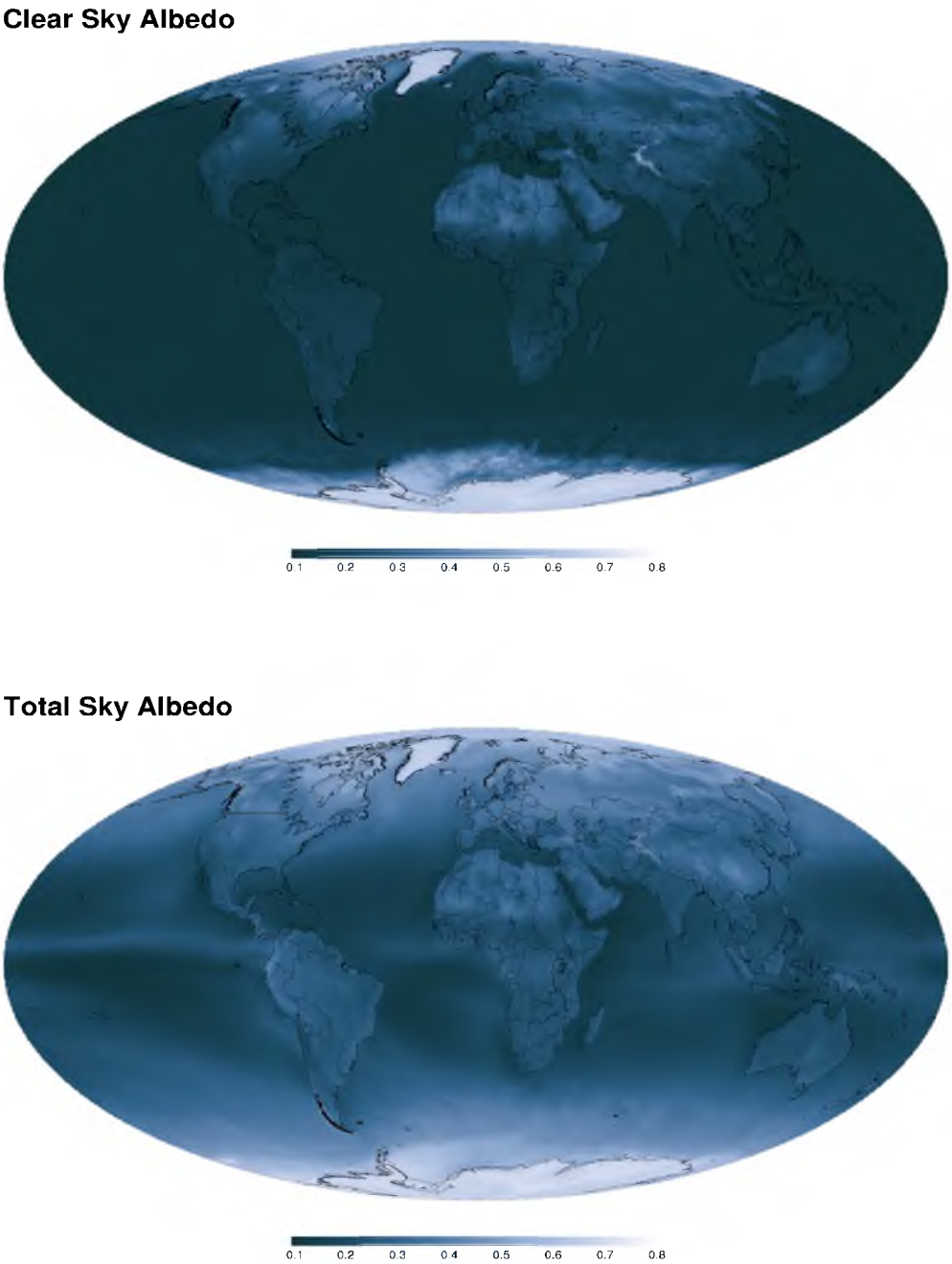

Figure 1.3: CERES-Aqua 2003-2004 mean annual clear sky and total sky albedo. Clear sky albedo is calculated using only cloud-free days while total sky albedo includes all data. Image: http://en.wikipedia.org/wiki/Albedo uploaded by user Giorgiogp2, data source: http://daac.gsfc.nasa.gov/giovanni/.

1.2 Atmospheric Circulation

The effect of atmospheric constituents on the radiative balance and the climate is also affected by their spatial and temporal distribution - properties determined by source distributions and *in-situ* chemistry, but also largely by regional and global transport mechanisms. Although globally the total energy received is approximately equal to that being released back to space, this is not true at the more local scale, with the tropics receiving more than they emit and the opposite case at the poles. This differential solar heating drives global atmospheric transport which, combined with a phenomenon known as the Coriolis effect, results in the Earth's major circulation patterns. In contrast, regional scale atmospheric circulation patterns are driven more prominently by the surface topography and land mass distribution.

Antarctica's circulation patterns are primarily driven by global scale transport systems. This is a result of two main factors. First, the minimal surface topography of the Antarctic continent, a result of a relatively homogeneous ice-sheet covered surface, results in only one type of topographically driven wind patterns. The primary topographic winds in Antarctica are the katabatic winds[d] however these are primarily limited to only a few hundred metres above the surface. Secondly, the location of the continent on the Earth's rotational axis, together with it being surrounded by a contiguous Southern Ocean, allows large weather systems and ocean currents to develop that minimise influence from other areas. The resulting factors that influence this area and its circulation are primarily the result of relatively large scale transport mechanisms.

1.2.1 Solar Heating

The annual average solar irradiance incident on a surface at the top of the Earth's atmosphere perpendicular to the Sun, known as the solar constant and measured by satellite, is around $1360.8 \pm 0.5\ W.m^{-2}$ (Kopp and Lean, 2011). Of this, approximately 30% is reflected back to space by the Earth's surface (resulting in its albedo), while around 20% is absorbed by the atmosphere, with the remainder taken in by the oceans and land surfaces (IPCC, 2013).

As depicted in Figure 1.4, the energy per square metre received at the surface is significantly larger at the equator than at the poles, a result of the high sphericity of the Earth[e]. This equator-pole differential heating results in a latitudinal temperature gradient that provides the atmosphere with a convective current leading to

[d]Surface cooling causes an increase in air density resulting in downslope density-driven air flows.

[e]It is interesting to note that the Earth is not a true sphere, but rather an oblate spheroid, a sphere that has been flattened to bulge around the equator. However, this fact has minimal effect in most atmospheric applications.

the major circulation cells that influence global weather patterns. It is by this atmospheric circulation mechanism that the Earth is able to redistribute around 60% of its incident energy from areas with excess energy to those with an energy deficit. Although driven by energy redistribution, these circulation systems also transport atmospheric constituents (e.g. gases, aerosols and clouds) around the globe resulting in the heterogeneity present in the atmosphere.(Seinfeld and Pandis, 2006)

If we approximate the fluid of the atmosphere as a closed tank of air, we can simulate, to a first approximation, the circulation of the Earth's atmosphere by heating one end of the tank (the tropics) and cooling the (the poles). Heated air rises due to its decreased density, while cooling air becomes more dense and falls. The buoyant rise results in low pressure at the heated surface, while the descent leads to a high surface pressure at the cooled end. This pressure difference results in a surface flow from high to low pressure. Mass conservation requires the rising air to travel along the top of the tank to the cooled end, resulting in a single large circulation. This circulation, proposed by amateur meteorologist George Hadley (1685-1768) and consequently known as the Hadley cell, provided some useful explanations of the north-south motion of the atmosphere, however it missed out on some vital concepts that explain the east-west motion, namely the effect of the rotation of the Earth on the atmosphere known as the Coriolis effect. (Seinfeld and Pandis, 2006)

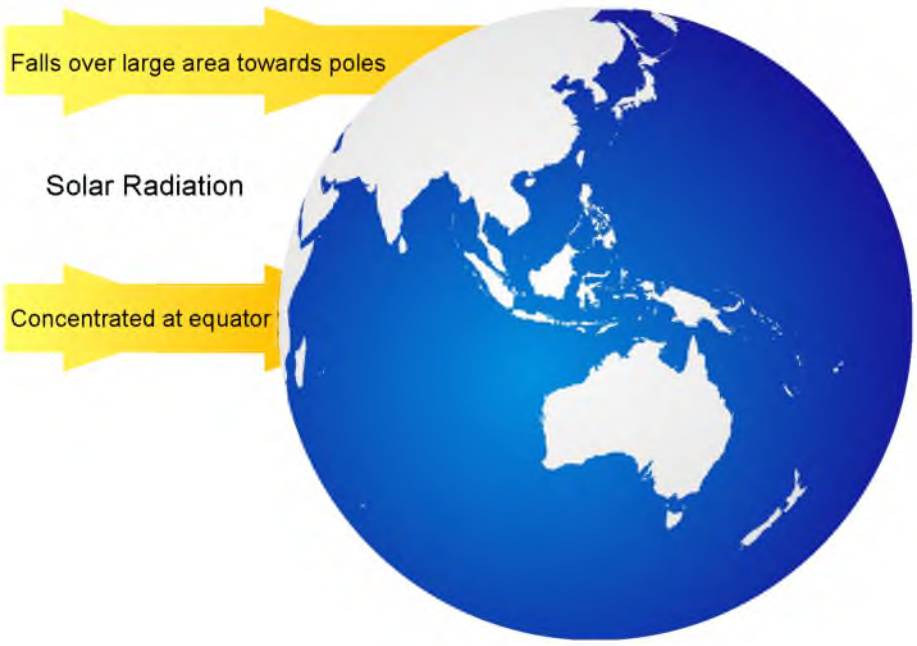

Figure 1.4: Illustration of the different solar radiation incident on the Earth's surface. Because of the sphericity of the Earth, the radiation at the poles is spread over a larger area than at the equator, resulting in a significantly lower insolation per square metre.

1.2.2 Coriolis Effect

Because of the Earth's continuous rotation, two points at different latitudes on the Earth's surface move at different speeds. If we take latitudinal slices at each of the two points, the resulting cross-sections will be circles, each with a different radius, R, and circumference. Since the Earth rotates 2π radians per day, its angular velocity (Ω, in radians per second), is constant at $2\pi/(24 \times 60 \times 60) = 7.27 \times 10^{-5}\ rad.s^{-1}$. The tangential velocity, ν, equal to $\nu = 2\pi R/t$ or $\nu = \Omega R$, of a point moving around the circumference of each cross-section will differ. At the equator, the Earth's radius is approximately 6370 km, resulting in a tangential velocity of 463 $m.s^{-1}$. At any other latitude, ϕ, the tangential velocity is

$$\nu = \Omega R cos\phi. \tag{1.1}$$

We can find that the tangential velocity at 30° latitude is 401 $m.s^{-1}$, much lower

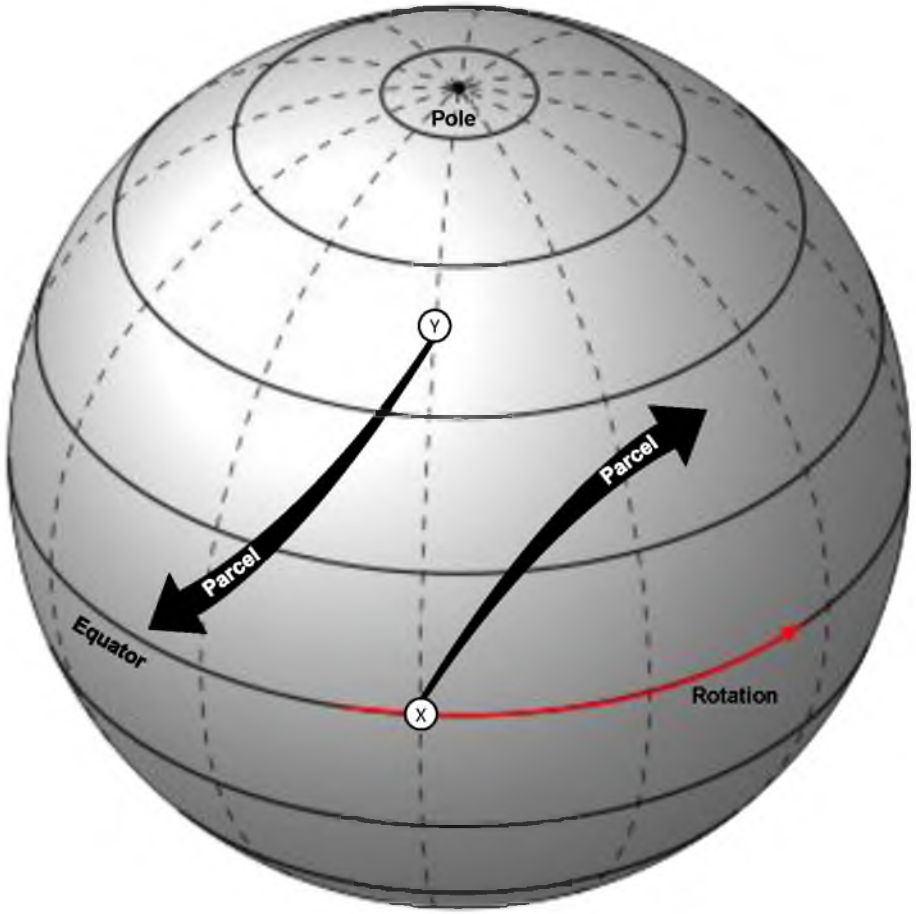

Figure 1.5: Illustration of the Coriolis effect. Points X and Y are located on the same longitude, however X has a greater distance to travel than Y in a given amount of time. As an air parcel moves poleward from X, it appears to speed up relative to the surface resulting in easterly movement. Conversely, equatorward transport from Y results in an air parcel appearing to slow down relative to the surface, thereby resulting in westward motion.

than what it was at the equator. Consequently, an air parcel moving from the equator to 30°, contains a surplus of momentum corresponding to a velocity of 62 $m.s^{-1}$. This surplus is actually just a matter of perspective. To explore this further, consider an air parcel moving from the equator to a higher latitude, as illustrated in Figure 1.5. The parcel that originates at the equator travels east with the Earth's rotation at its original speed of 463 $m.s^{-1}$. As it begins moving to higher latitudes however, the surface below is travelling at a continually slowing tangential speed. From the perspective of an observer on the surface, the air parcel appears to speed up, in the same direction as the Earth's rotation. Conversely, if an air parcel begins at a higher latitude and moves equator-ward, it keeps its original tangential velocity while the surface accelerates, resulting in a westward movement relative to the surface observer.

It is this effect that results in the major East-West circulation features observed in the global circulation cells, discussed below. The Coriolis effect also prevents air from moving unhindered between the equator to the pole, as would be expected by a simple Hadley circulation model. Consequently, a multi-cell model must be used to explain global atmospheric circulation - a three cell model being the best approximation for the Earth.

1.2.3 Global Circulation Cells

Global atmospheric circulation is made up of three primary cells, the Hadley, Ferrel and Polar cell, which extend from the equator to the poles in each hemisphere (Seinfeld and Pandis, 2006). Figure 1.6 summarises the annual average of these circulation cells and the effective surface winds arising in each cell from the Coriolis effect. In this section, these circulation cells and the forces from which they result will be discussed in terms of their annual average. Seasonal variations in the solar radiation - the primary force driving circulation - results in variations in the strength and locations of the circulation cells and their boundaries.

Starting at the equator, the high solar heating causes significant uplift. In the Southern Hemisphere, rising air moves south as it reaches the tropopause, until it begins to descend at around 30°S. From here, the pressure differential causes northward surface winds, closing the Hadley circulation cell. Horizontal pressure gradients in the Hadley cell are weak, resulting in little wind and consequently often known (in the past) as the doldrums. The magnitude of heat and moisture uplifted over the equator begins the atmosphere's largest heat redistribution process and also leads to the significant precipitation in the region. At the polar end of the circulation ($\sim$30° latitude), air cools and converges, producing a widespread, semi-permanent high-pressure system known as a subtropical high. As the dry free-tropospheric air

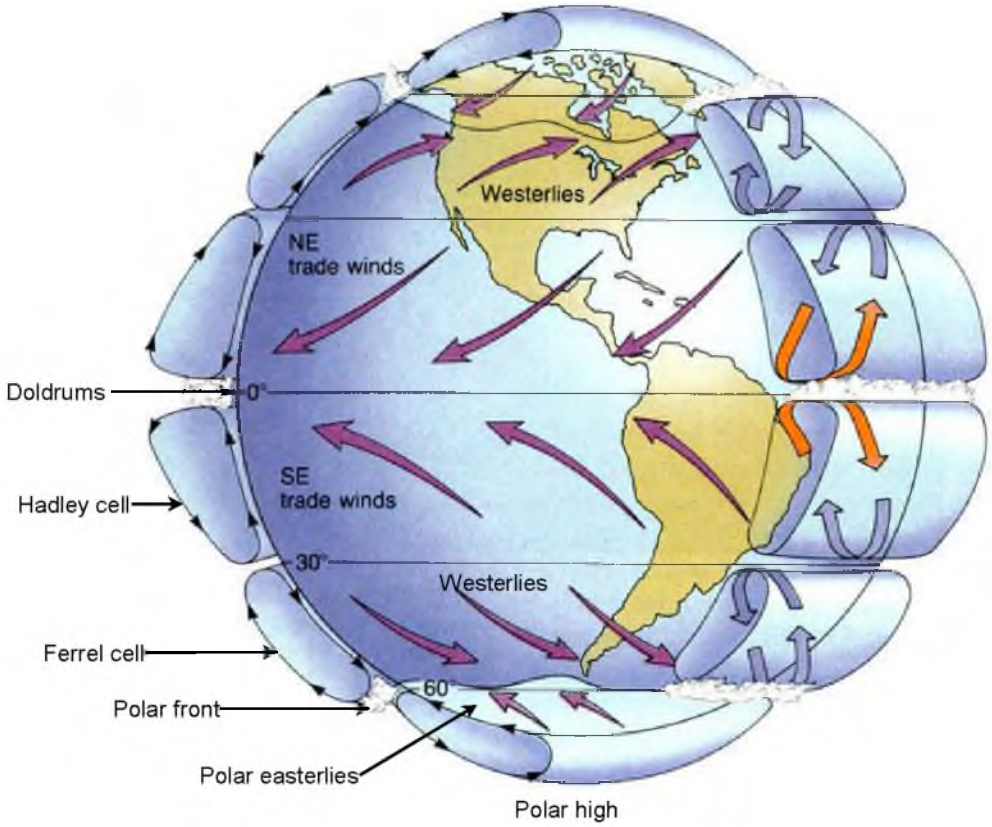

Figure 1.6: Global circulation as described by the 3-cell model. Air rises at the equator and falls at the poles, but occurs within 3-circulation cells: the Hadley, Ferrel and Polar cells. Note the characteristic surface winds, a result of the Coriolis effect. Image modified from original courtesy University of Rochester.

descends in the region, it warms adiabatically, resulting in clear skies, warm and dry climates and weak surface winds. These conditions lead to the global desert belts found at these latitudes, and because of the weak surface winds, these regions came to be known as the horse latitudes, since sailing ships that entered the region often had to throw off any horses on board to lighten the load.

Surface winds travelling back to the equator are directed by the Coriolis effect and so result in the easterlies characteristic of the Hadley cell. These easterly winds have come to be known as the trade wind belt, and allowed the establishment of trade routes across the Atlantic and Pacific oceans. The north-east trade winds of the northern Hadley cell, converge at the equator with the south-easterlies of the southern Hadley cell, resulting in an important region known as the intertropical convergence zone (ITCZ). This convergence assists in the uplifting in the region, and results in a widespread region of low pressure known as the equatorial low. This ascending, high moisture content air leads to significant convective cloud formation and high rainfall, resulting in a major belt of tropical rainforests.

The descending air at the horse latitudes is split into both equatorward and pole-

ward flows. As previously discussed, equatorward flows help complete the Hadley cell, however the poleward surface flows, occurring between 30° and 60° in each hemisphere, start the Ferrel cell circulation. Because of the Coriolis effect, this poleward surface air results in the characteristic westerlies of the mid-latitudes. As this mild air flow travels further poleward, it encounters cold equatorward moving polar air. Because of the significant temperature difference, these flows do not readily mix, and form a boundary known as the Polar Front. The strong convergence at this front pushes air aloft, resulting in the subpolar low and a strong band of storms and clouds. Once it reaches the tropopause, rising air divides, some moving equatorward to complete the Ferrel cell, while the remainder travels poleward. As the flows converge over the pole, they are cooled and descend, resulting in a permanent high pressure system over the pole, known as the polar high. This circulation, descent at the pole, equatorward surface flows, rising air at the Polar Front at around 60°, and high poleward flow, constitutes what is known as the Polar cell. Again, since surface flows are equatorward, the Coriolis effect results in Polar easterlies.

Although discussed briefly, this three-cell circulation model explains a vast array of the weather conditions observed around the world. This solar driven atmospheric circulation is an important concept to understand in order to decipher the drivers of our observations of aerosols in the Antarctic, in particular the circulation leading to the formation of the Polar front and the patterns in the Polar cell. It is important to remember that this three-cell model is a conceptual and time-averaged oversimplification of what occurs in reality though, and deviations in the circulation may arise because of the spatial resolution and time period being considered.

1.3 Atmospheric Aerosols

Atmospheric particulates - or aerosols - are a vital component of the Earth's atmosphere. Technically defined, the term aerosol refers to a colloidal system of fine solid particles or liquid droplets within an air or gaseous medium. In general usage however, this term is often used to refer only to the particulate component of the system, and ignores the medium within which it is suspended.

Aerosols are involved in many different atmospheric processes, making their study quite important to a variety of applications. They have significant effects on human health, being a major component of photochemical smog, and a transport pathway for pathogens and allergens (Pöschl, 2005; Stieb, Judek, and Burnett, 2002; Wichmann and Peters, 2000). They also provide an atmospheric surface which, combined with their spatially and temporally heterogeneous composition, make them important in many atmospheric chemical reactions including halogen radical release via sea salt chemistry, mercury cycling, nitrogen and sulfur chemical cycles and the

oxidation of organic molecules (Che et al., 2009; Finlayson-Pitts, 2009; Loukhovitskaya et al., 2009; Vlasenko et al., 2009; Herrmann et al., 2015; Ervens, 2015; Ervens, Turpin, and Weber, 2011). Aerosols also contribute significantly to the radiative balance (Figure 1.2) through a number of mechanisms, including scattering, reflection and absorption of incident radiation (aerosol radiation interactions), as well as through their role in cloud formation and the subsequent modification of their properties (aerosol cloud interactions) (IPCC, 2013; Menon et al., 2002; Ramanathan et al., 2001; Tao et al., 2012; Yu, Saxena, and Zhao, 2001).

Atmospheric aerosols are produced via two main mechanisms that are explored in detail in Section 1.5. Primary aerosols are emitted to the atmosphere directly, usually via mechanical means such as wind (e.g. dust), bubble bursting (e.g. sea salt) and combustion. Secondary aerosols are formed *in-situ* in the atmosphere by gas-to-particle conversion processes, such as oxidation chemistry to low volatility compounds.

Aerosols have two primary removal mechanisms: dry and wet deposition. Dry deposition is the process by which aerosols are deposited directly to the Earth's surface, and is the primary mechanism for removal of larger aerosols. Wet deposition involves the incorporation of aerosols into cloud droplets (also called scavenging) which, after growth into rain drops, precipitate back to the surface. These removal processes lead to relatively low atmospheric residence times (days to weeks in the troposphere) and combined with the diversity of sources, lead to their significant heterogeneity in space, time and composition.

A number of different aerosol properties can currently be measured, including number, mass and size concentrations and distributions, as well as chemical and optical properties such as chemical composition and optical depth. Number concentrations are generally dominated by sub-micron aerosol populations, since larger particles are often (but not always, for example sea salt aerosol) a coagulated population of smaller ones. Conversely, mass concentrations are dominated by the larger particles. This distribution has important ramifications for their roles in the various atmospheric process they are involved in, for example, an aerosol's size will determine its interaction with a given wavelength of light or its role in cloud formation.

Generally speaking, aerosol composition can be categorised into five primary types. These include sulfate, carbonaceous (black carbon and organic species), sea salt, dust, and the most recently identified, iodine. Each type of aerosol has distinctly different sources and radiative effects. For example, sulfate aerosols reflect incoming radiation, causing a cooling effect, while carbonaceous black carbon aerosol absorbs incoming radiation, resulting in atmospheric warming. Although it is useful to categorise aerosols, in the natural environment aerosols of one type rarely exist alone, but rather are present as mixtures of various types, often with a dominating

type (e.g. in the marine boundary layer of the open ocean, sea salt aerosol would dominate). Some aerosols are able to act as seeds for cloud droplet (cloud condensation nuclei, CCN) and ice crystal formation. Consequently, by their interaction and modification of clouds, these aerosols can have a significant effect on the radiative balance as well as on the hydrological cycle.

1.4 Aerosols and Radiation

The interaction of aerosols with radiation is an important aspect in any consideration of the radiative balance of the atmosphere. The interaction of aerosols with radiation can be differentiated into two main categories: aerosol radiation interactions (ARI; which consists of both scattering and absorbing interactions), and aerosol cloud interactions (ACI). These effects are summarised schematically in Figure 1.7. Scattering aerosols influence the radiative balance through elastically scattering incident radiation, immediately reflecting a portion of the incident radiation back to space. Absorbing aerosols absorb a portion of the incident radiation into the particle itself, which is subsequently converted into thermal radiation, which then interacts quite differently with the other components of the climate system (e.g. GHGs will now absorb its radiation). Aerosol cloud interactions involve the role of aerosols, in particular CCN and ice nuclei (IN), in the formation of clouds and the modification of their properties, which subsequently interact with radiation.

1.4.1 Aerosol Radiation Interactions

The composition of an aerosol population will determine the magnitude with which it will reflect or absorb radiation. In general, bright-coloured particles tend to reflect radiation in all directions, including back to space. Although some of this radiation is reflected down to the surface, the fraction that returns to space is removed from the Earth's radiation budget, and essentially creates a shadow over the surface, thereby cooling the surface. Since the most common aerosols are highly reflective (e.g. dust, sulfate and sea salt) (Seinfeld and Pandis, 2006; Tsigaridis et al., 2006), the local cooling effect created by these aerosols is spatially frequent, and together with atmospheric circulation and mixing processes, results in a regionally widespread net cooling on the climate system.

If the aerosol composition results in darker aerosols however, in particular black (or elemental) carbon, solar radiation is absorbed and converted into thermal energy. Initially, this absorption and conversion heats the aerosol layer and simultaneously reduces the radiation that reaches the surface, creating a cooling shadow. At the longer time scale, atmospheric mixing redistributes the thermal energy and the

cooling effect disappears. (IPCC, 2013)

Determining the direct radiative forcing requires knowledge of a number of key optical properties (single scattering albedo, specific extinction coefficient, and the scattering phase function), all of which are a function of wavelength and relative humidity, as well as the time varying atmospheric loading and geographic distribution of aerosol populations in both the horizontal and vertical dimensions. Although scattering aerosols will always produce a net cooling effect, the radiative forcing that results from these calculations depends not only on the aerosol composition but also on the underlying surface below and any other aerosols layers in the atmosphere. This is particularly true for absorbing aerosols, which won't just change the magnitude of the radiative forcing, but can also change from a warming to cooling effect or vice versa. For example, over dark surfaces such as oceans or dense forests, absorbing aerosols may exert a negative (cooling) radiative forcing, while over high albedo surfaces (e.g. deserts, ice, or above clouds), a positive (warming) radiative forcing can be observed. (IPCC, 2007)

It is important to mention that the direct interactions with radiation are wavelength dependent. For most aerosol populations, the size distribution is small enough that it interacts primarily with shortwave radiation, allowing longwave radiation to pass through. Longwave radiation only interacts directly with large aerosols in high concentrations at higher latitudes (IPCC, 2007). This preference for reflecting only shortwave radiation is one of the properties that leads to the net cooling effect of these direct aerosol-radiation interactions.

1.4.2 Aerosol Cloud Interactions

Cloud Condensation Nuclei (CCN) in the atmosphere provide a surface for water vapour to condense onto at atmospherically relevant relative humidity levels of just over 100%. Without CCN, the humidity necessary for droplet formation would need to be in the range of 200-300% (homogeneous nucleation) - a level never observed in the natural atmosphere. (Seinfeld and Pandis, 2006)

The interaction of clouds and aerosols is poorly understood. Aerosols have a number of different and highly complex effects on clouds, including affecting the cloud brightness (or reflectivity), cloud cover, lifetime, and precipitation (Topping and McFiggans, 2012). Many of these processes are summarised schematically in Figure 1.8.

Increases in CCN due to anthropogenic activity will result in an increase in the number, but a decrease in the size of cloud droplets - a result of dividing a finite water vapour reservoir between more condensation nuclei. This has a number of effects. Firstly, smaller droplets tend to reflect more incoming radiation, resulting in a net

increase in cloud albedo (the Twomey effect, (1974)). This cloud brightening results in significant cooling due to the reflection of incoming shortwave radiation, with no appreciable changes in outgoing long-wave radiation (infrared heat). This effect is complex and varies depending on the cloud height, thickness and temperature, with more cooling occurring from warmer, lower, thick clouds, than from higher, cooler, thin clouds. As the CCN number increases in a cloud, more but smaller droplets are formed, preventing larger droplets from coalescing. Lower coagulation rates means cloud droplets wont grow as readily into rain droplets that can precipitate out, resulting in lower surface precipitation (which has implication on the hydrological cycle), but more importantly for the radiative balance, longer cloud lifetimes result. These increased lifetimes, together with their high albedo, result in an increased net cooling effect for clouds with higher CCN concentrations. (Gantt et al., 2012; Rosenfeld, Wang, and Rasch, 2012; Sharon et al., 2006; IPCC, 2001; IPCC, 2007; Seinfeld and Pandis, 2006)

The magnitude of these effects is also dependent on the height of the cloud. Clouds low in the atmosphere are generally thicker and warmer than high clouds. This has two effects. Firstly, thicker clouds will reflect more short-wave radiation, resulting in increased cooling. Both clouds will be similarly transparent to thermal (infrared) radiation, however their respective thermal emissions will differ significantly because of their different temperatures. Consequently, the warmer low clouds emit more thermal radiation than the colder clouds above, adding to their higher cooling effect. (IPCC, 2001; IPCC, 2007; Seinfeld and Pandis, 2006)

Precipitation, and hence the hydrological cycle, are affected by aerosols via two primary mechanisms, both of which are currently not well understood (Lee et al., 2013; Tao et al., 2012). The first mechanism is related to the requirement of CCN for cloud formation and thus precipitation, while the second relates to the direct radiative climate forcing which causes variations in atmospheric dynamics. Numerous studies have found that low CCN number concentrations cause earlier (Tao et al., 2007) and more intense precipitation (Koren et al., 2012) and thus reduced cloud lifetimes (Rosenfeld et al., 2008). The atmospheric warming caused by absorbing aerosols can also prevent cloud formation by increasing evaporation rates from aerosol surfaces (IPCC, 2007). In an analysis of a 10-year dataset, Li et al. (2011) found that in clouds with a low, warm base containing both ice and water, enhanced aerosol loading increases the cloud top height and thickness. Rain frequency and rate were also found to change significantly with aerosol loading, dependent on cloud water content, with high aerosol loading causing more precipitation in high water clouds, but less in low water clouds. Additional effects can occur within mixed-phase clouds (those with both ice and liquid water present). Increases in ice nuclei in mixed-phase clouds, known as the glaciation effect, can increase the precipitation

efficiency, resulting in decreased cloud lifetimes and an overall warming influence on the surface below. The 'thermodynamic' effect results from delayed freezing by smaller droplets that leads to super-cooled clouds rising to colder temperatures. The radiative effect of the thermodynamic effect is currently not well quantified, and could be either positive or negative. (IPCC, 2007)

The composition of adjacent non-CCN aerosol populations may also have an effect on clouds. If black carbon aerosol is present within the cloud, *in-situ* heating can result in an increase in evaporation rates within the cloud. This 'cloud burn-off' process, would lead to a net warming effect, as the cooling effect disappears as the cloud does. Cloud physics and dynamics are also altered if the absorbing aerosols are present above the cloud, resulting in an increased static stability relative to the surface. The combination of these processes can lead to either a positive or negative radiative forcing, and its effect is not well understood. (IPCC, 2007)

A range of other effects have been observed to change with aerosol loading, with increases in CCN number concentrations leading to various changes. These include smaller and narrower cloud droplet size distributions, deeper mixed-phase regions, enhanced lightning activity, increases in cold cloud (below 0°C with both ice nuclei and supercooled liquid water presnt) precipitation processes and decreases in warm cloud (above 0°C) precipitation processes. These changes have numerous and significant effects on both the physical and chemical nature of the atmosphere. Despite the number of studies being undertaken in this area, numerous scientific organisations (IPCC, 2013; National Research Council, 2005; World Meteorological Organization et al., 2008) still recognise the low current understanding and requirement for significant further research in aerosol-cloud interactions. The radiative effects of the aerosol-cloud interactions are among the most important for a complete understanding and accurate estimation of the radiative balance.

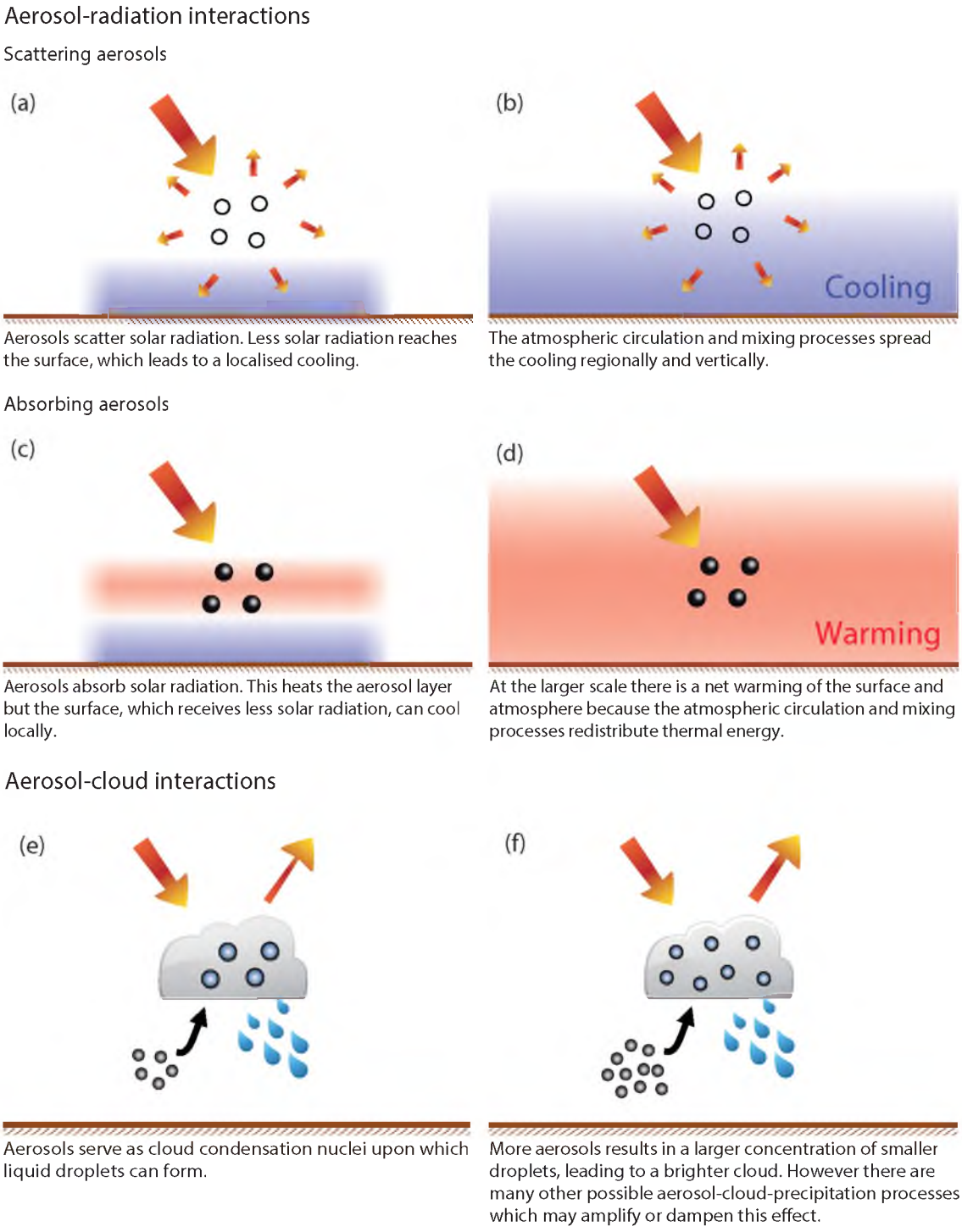

Figure 1.7: Overview of the interactions between aerosols and solar radiation. The direct interactions (a-d) are divided into instantaneous effects (left panels) and the overall impact after a response from the climate system (right panels). Aerosol interactions with clouds (e-f), are shown with both clean (left panel) and polluted (right panel) scenarios. Figure adapted from FAQ 7.2 of IPCC (2013).

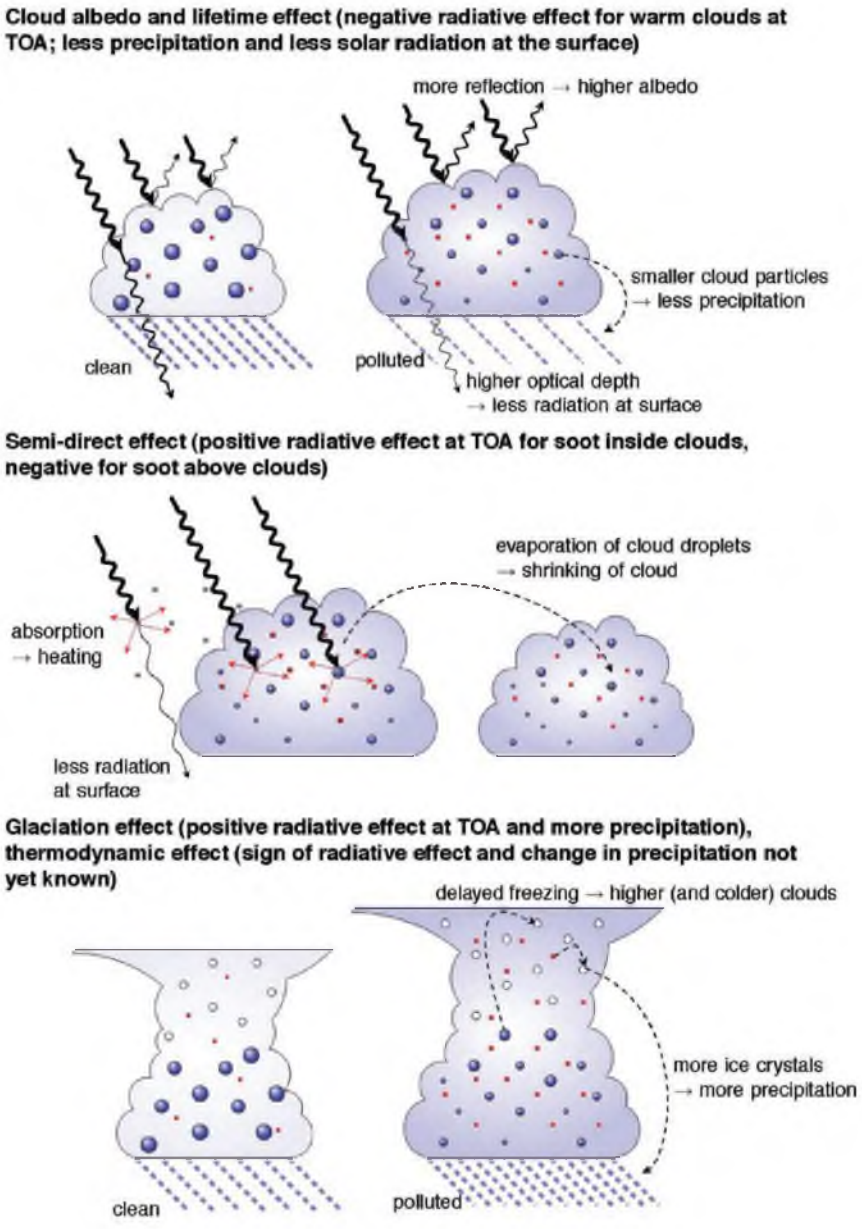

Figure 1.8: Summary of the effects of aerosols on clouds. TOA refers to top of the atmosphere. Figure courtesy IPCC (2007).

1.5 Aerosol Formation Mechanisms

There are a wide range of source mechanisms for producing atmospheric aerosols. In general, these mechanisms can be divided into two main streams: mechanical, where physical processes (e.g. wind) induce primary aerosol formation or release, and chemical, where gaseous species undergo reactions *in-situ* that result in secondary particles. Aerosols released directly to the atmosphere via mechanical processes are known as primary aerosols, while those formed from gas-to-particle chemistry are known as secondary aerosols. Atmospheric aerosols generally fall within the size range of a nanometre (nm), to tens of micrometers (μm), with secondary particles making up most of the sub-micron population (fine mode), and primary particles tending to be in the larger, super-micron size range (coarse mode). These two distinct modes are important because, in general, their properties are quite distinct in terms of growth, formation, removal processes, chemical compositions, optical properties, and health impacts. In this section, the different types of primary aerosols will be outlined briefly, after which the sources and mechanisms of secondary aerosol formation are discussed. (Seinfeld and Pandis, 2006)

1.5.1 Primary aerosols

Soil dust is a major component of primary aerosol and has both natural and anthropogenic sources. Mineral dust can be uplifted when wind acts upon soil particles. Arid and semi-arid regions are major sources of dust aerosols, particularly because they cover around one-third of the global land area. Additionally, areas which have been cleared or disturbed by human activities can become major dust sources. Dust aerosols are uplifted when the surface wind speed exceeds a threshold velocity, which varies depending on the region being considered, being a function of surface roughness, grain size and soil moisture. This source can be reduced when soil surfaces develop a crust, and increased when disturbed by things such as agricultural activity. Dust aerosols can be both absorbing and scattering, and can have significant climatic effects. Additionally, their composition often has a high content of iron, which after transport to iron-limited environments, can have important biological roles. Although intercontinental transport occurs frequently (e.g. Eguchi et al., 2009), their large size means they have a relatively short atmospheric lifetime compared to other atmospheric constituents, generally settling out gravitationally when the wind reduces. (IPCC, 2001)

Volcanic dust, or ash, isn't suspended into the atmosphere by the action of the wind, but rather by the pressure released during volcanic eruptions. Volcanic ash consists of pulverised fragments of rock, minerals and volcanic glass. Due to the energy associated with its release, volcanic ash gets injected high into the at-

mosphere, resulting in a wide spatial impact. The wide dispersal, together with the magnitude of aerosol mass, allows ash to have a number of impacts on society including human and animal health and disruptions to aviation, critical infrastructure (e.g. electrical power supply systems, telecommunications, water and waste-water networks), and primary industries (e.g. agriculture). The lower limit of primary volcanic dust emissions is around two orders of magnitude lower than emissions of soil dust. Despite this apparently small contribution, large explosive volcanic emissions can be significant, and can inject primary coarse aerosols into the upper troposphere and stratosphere where their lifetime can be up to 1 to 2 months, eventually being removed by gravitational settling. (IPCC, 2001)

Industrial dust is produced from numerous sources including transportation, coal combustion, cement manufacturing, metallurgy and waste incineration. Because of their impacts on air quality and health, and their conspicuous nature, these aerosols are highly monitored and regulated, resulting in significant recent reductions, particularly in developed nations. This regulation, together with their minimal optical activity ($> 1\ \mu m$ diameter), means that these aerosols have minimal climate relevance, although in highly industrialised developing nations where regulations are minimal, the sheer magnitude of aerosol loading could have significant climate impacts, not to mention the air quality effects. (IPCC, 2001)

Sea salt aerosol is produced via the action of wind across the sea surface. There are two primary mechanisms for their formation, both of which are heavily depended on wind speed. The first is the the bursting of air bubbles that have been entrained by wind stress during whitecap formation, while the second is the shear stress resulting in sea spray from wave tops. The generally coarse aerosol (ranging from 0.05 to 10 μm) resulting from this process is composed primarily of salt, and consequently, is both highly reflective and hygroscopic. These properties mean that these natural aerosols have significant direct radiative effects, but also are very efficient CCN, making them very important for ACI, particularly in marine regions where wind speeds are high and/or other aerosol sources are weak. (IPCC, 2001)

Biogenic aerosol consists of plant debris (cuticular waxes, leaf fragments, etc.), humic matter and microbial particles (bacteria, fungi, viruses, algae, pollen, spores, etc.). Estimates of biogenic aerosol loading are difficult, however measurements in temperate urban environments indicate that they can make up 10-30% of the total aerosol volume in both fine and coarse size modes. In densely vegetated regions (e.g. the moist tropics such as the Amazon), it is likely that this fraction is much larger. Humic substances make up much of the brown and black colours of the soils and decaying plant debris in biogenic regions. Its presence in biogenic aerosols results in light-absorption, which leads to the atmospheric warming discussed above. There is

some evidence that primary biogenic particles may also be able to act as both CCN and IN. Their importance in both ARI and ACI makes them a vital component of the atmosphere. (IPCC, 2001)

Biomass burning aerosols can be produced as primary emissions, but can also form from secondary processes. The fraction of biomass burning aerosols that are emitted as primary particles consist predominantly of carbonaceous aerosol, which includes both organic and black carbon, with organic carbon dominating the emitted population. Global emissions from biomass burning for organic and black carbon stand at 45-80 Tg/yr, and 6-9 Tg/yr, respectively. Although carbonaceous aerosols are present primarily in the sub-micron size fraction, the radiative effects differ substantially depending on their composition, with black carbon primarily absorbing solar radiation, while organic carbon scatters it. Given their sources, carbonaceous aerosols are limited primarily to terrestrial air-masses, and can have significant implications, both environmentally and on health, at the local to regional scale (e.g. during bush fires or smog events). The increasing anthropogenic emissions of black carbon, together with its key absorptive property that differs from most other aerosols, makes careful inclusion of these aerosols vital in any consideration of the climate system. (IPCC, 2001)

1.5.2 Secondary Aerosol Formation

Secondary aerosols are produced via a process known as gas-to-particle conversion. This process requires precursor gaseous species, already present in the atmosphere, to undergo *in-situ* chemical reactions that result in low volatility compounds that can nucleate into particles.

Precursor compounds can come from both natural and anthropogenic sources. Sulfuric acid is the gaseous species that is the precursor for sulfate aerosol, the most common secondary aerosol. Sulfuric acid can be produced from a number of sources. The two biggest chemical sources are SO_2, primarily from volcanoes and anthropogenic sources, and dimethyl sulfide (DMS), a biogenic emission primarily derived from marine phytoplankton. Since the sources of SO_2 relate mostly to either volcanoes or fossil fuel combustion, their source distribution and magnitude (in the case of combustion) can be well constrained, resulting in a relatively good representation in global models.

DMS emissions are more difficult to estimate because of the spatial and species heterogeneity of phytoplankton communities in the oceans. Calculating emissions relies on gridded climatologies (e.g. Kettle et al., 1999; Lana et al., 2011) that are based on an ensemble of measurements of ocean surface DMS concentrations published in the literature, together with a parameterisation of the ocean to air

gas transfer (e.g. Liss and Merlivat, 1986). The most recent monthly climatology of Lana et al. (2011) is based on around 25 000 observations around the globe. In many regions where measurements are difficult and therefore sparse, estimates are generated by assuming similarity to comparable biogeographic regions with adequate data coverage and by interpolation. This results in high uncertainties where data is sparse (such as in the Southern Ocean region).

Volatile Organic Compounds (VOCs) can be produced from a variety of natural and anthropogenic sources, and undergo chemical oxidation reactions that can result in low-volatility compounds that can homogeneously nucleate. Natural emissions of various organic species, for example isoprene and monoterpenes, can be significant (on the order of 5×10^2 Tgyr^{-1} (Guenther et al., 2012, and references therein)) and are common from both terrestrial and marine environments rich in flora. In addition to the continuous emissions that occur from day-to-day biological activity, biomass burning, in the form of wild fires, are a major source of the release of VOCs to the atmosphere, producing both black (or elemental) carbon and precursors for secondary organic aerosol. Anthropogenic emissions of VOCs are a factor of 10 less than natural sources, and originate primarily from the use and combustion of fossil fuels, but can also come from chemical industries such as the manufacture of paints and coatings, cleaning products and refrigerants. (Seinfeld and Pandis, 2006)

Nucleation chemistry involving iodine is the most recent mechanism for aerosol formation that has been discovered. This chemistry has only been observed at very local spatial scales but can produce incredibly high aerosol concentrations, numbering in the tens of thousands per cubic centimetre. The iodine oxides that lead directly to particle formation are chemically produced *in-situ* from halocarbons released from macroalgae. During low tide, macroalgae at coastal locations (the first observations of this chemistry were made at Mace Head in coastal Ireland (O'Dowd et al., 1998)) are exposed to the atmosphere. Under these stressful conditions, the macroalgae release a variety of compounds, some of which contain iodine. It is these halogen species, dominated by CH_2I_2, that are oxidised and lead to the formation of vast numbers of aerosol particles (on the order of 10^3, (O'Dowd et al., 1998)). Most observations of this chemistry have been limited to small spatial regions along the temperate coast (O'Dowd et al., 1998; O'Dowd et al., 2002a), with recent measurements showing reasonably low concentrations (< 1 ppt) of iodine oxide (IO), the key precursor of the nucleation chemistry, in the marine boundary layer throughout the globe (e.g. Gómez Martín et al., 2013; Prados-Roman et al., 2015). Recent research has shown significant concentrations of IO in the Antarctic region which may suggest its involvement at a more regional or hemispheric scale (Saiz-Lopez and Glasow, 2012). Additionally, IO can be produced from the oxidation of other iodine species, meaning that high concentrations of other species, such as

molecular iodine (I_2), could lead to aerosol nucleation.

Secondary aerosol formation, summarised schematically in Figure 1.9, can occur via numerous pathways and requires the nucleation of a cluster of molecules that remains thermodynamically stable until growth occurs. Classical nucleation theory reveals that the free energy of the system reaches a maximum, "the nucleation barrier", during nucleation, beyond which growth becomes spontaneous (Doyle, 1961; Middleton and Kiang, 1978; Raes, Saltelli, and Van Dingenen, 1992; Zhang, 2010). The rate of nucleation is dependent on the chemical make-up of the nucleus, as well as the identity and concentrations of condensing vapours (McGraw and Zhang, 2008). Nucleation itself, as well as initial stages of growth, are difficult because precursor vapours and young nuclei are readily absorbed by pre-existing particles. Particle formation processes are also affected by atmospheric mixing (Nilsson et al., 2001) and the magnitude of solar radiation (Hallar et al., 2011; Lee et al., 2003; Pirjola, 1999). Nucleation occurs via one of five major mechanisms: homogeneous nucleation involving binary mixtures of water and sulfuric acid (Kulmala and Laaksonen, 1990); homogeneous ternary nucleation involving water, sulfuric acid and ammonia (Kulmala, Pirjola, and Makela, 2000); ion-induced nucleation of binary, ternary or organic vapours (Yu and Turco, 2000; Lee et al., 2003); homogeneous nucleation of low-volatility organic vapours (Hoffmann et al., 1997); and homogeneous nucleation of halogen oxide species (Hoffmann, O'Dowd, and Seinfeld, 2001). Once formed, nuclei grow via the addition of condensible vapours or by coagulation with other particles.

1.5.2.1 Binary homogeneous nucleation

Although a broad definition, nucleation can be defined as either homogeneous or heterogeneous. Homogeneous nucleation differs from heterogeneous nucleation in that it does not require a surface onto which vapours can condense, but rather requires vapours to self-coalesce to form its own surface. In the context of aerosol nucleation, the heterogeneous process is not nucleation, but rather falls in the category of growth processes, but it has been included here because of its use throughout the literature particularly with regards to organic aerosol formation.

The nucleation that is most common in the atmosphere is understood through classical binary homogeneous nucleation theory. Details of this theory are omitted from this thesis for brevity, but can be found frequently in the literature (e.g. Seinfeld and Pandis, 2006; Kulmala and Laaksonen, 1990). The theory can be summarised as follows.

Homogeneous, homomolecular nucleation is impossible unless the vapour phase species is supersaturated. However, homogeneous heteromolecular nucleation - when two or more species are involved - can occur when participating species are present

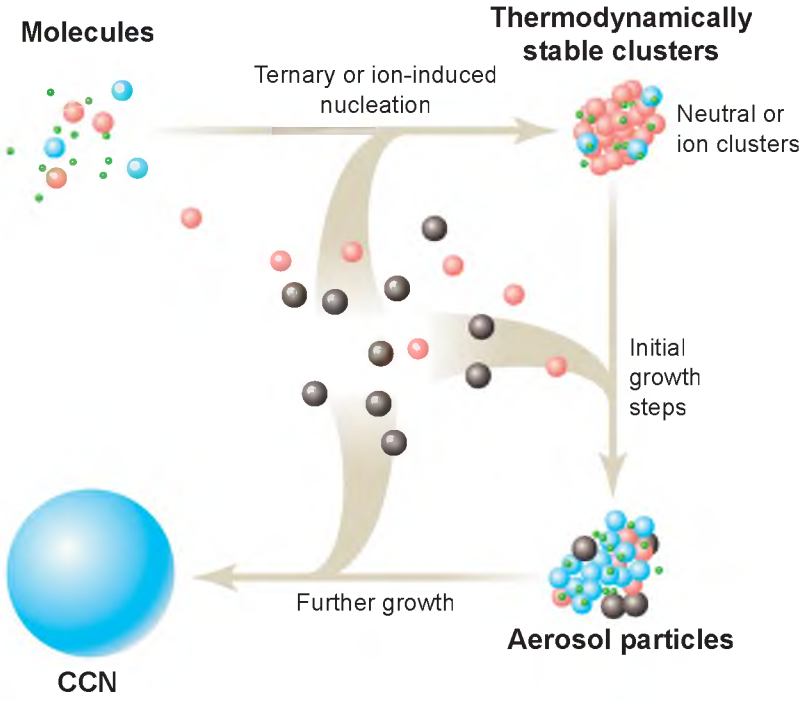

Figure 1.9: Gas-to-particle nucleation occurs to form stable clusters which, with the addition of further molecules, grow into aerosol particles. Growth and nucleation are inhibited by scavenging of gas molecules and nuclei by larger particles. Figure courtesy Kulmala (2003).

at concentrations below supersaturation (of the pure substance), provided all concentrations are supersaturated relative to the condensed droplet solution. The most commonly studied and most atmospherically important homogeneous heteromolecular nucleation mechanism is the binary nucleation between sulfuric acid and water.

As with any chemical reaction, nucleation will only occur spontaneously if the Gibbs free energy, ΔG, of nuclei formation is negative. The free energy of formation of a nucleus containing n_A molecules of species A and n_B molecules of species B is given by

$$\Delta G = n_A(\mu_{Al} - \mu_{Ag}) + n_B(\mu_{Bl} - \mu_{Bg}) + 4\pi r^2\sigma \tag{1.2}$$

where r is the radius of the droplet, σ is the surface tension, μ_{Al}, μ_{Ag}, μ_{Bl}, μ_{Bg} are the chemical potentials of components A and B in the mixed droplet (l) and in the gas phase (g), respectively. The difference in chemical potential between the liquid and vapour phases can be expressed as

$$\mu_{jl} - \mu_{jg} = -kTln\frac{p_j}{p_{j_{sol}}}, \qquad j = A, B \tag{1.3}$$

where k is the Boltzmann constant, T is the temperature in Kelvin and p_j is the partial pressure of component j in the gas phase and $p_{j_{sol}}$ is the vapour pressure of component j over a flat solution of the same composition as the droplet. The radius

r can be defined by the density, ρ, and number and mass (m_A and m_B) of molecules A and B using the relation

$$\frac{4}{3}\pi r^3 \rho = n_A m_A + n_B m_B \tag{1.4}$$

ΔG is only negative in the case when the $\mu_{jl} - \mu_{jg}$ term is, since the third term in Equation 1.2 is always positive. This case only occurs when both vapours A and B are supersaturated with respect to their vapour pressures over the resulting solution. Determining the radius and composition of the critical nucleus that results in spontaneous growth requires calculation of the minimum ΔG in the $n_A - n_B$ plane. The rate of formation of this critical nuclei, J, can be expressed as

$$J = Cexp(-\Delta G/kT) \tag{1.5}$$

where C is a (mainly) kinetic factor.

The H_2SO_4–H_2O system is a special case of binary homogeneous nucleation. In a humid volume of gas, H_2SO_4 molecules exist in various hydrated states: $H_2SO_4 \cdot nH_2O$. Consequently, nucleation of the H_2SO_4–H_2O system involves cluster formation between water and already hydrated H_2SO_4 molecules. In the atmosphere, over 95% of H_2SO_4 molecules are hydrated. The presence of hydrates reduces the rate of binary homogeneous nucleation of the H_2SO_4–H_2O system by a factor of $10^5 - 10^6$, compared to that in the absence of hydrates (due to reduced polarity). Despite this, only very small amounts of H_2SO_4 relative to water are required for nucleation to occur in the atmosphere. The nucleation rate of this system depends strongly on the concentrations of the condensing species (therefore absolute humidity) as well as temperature, meaning that uncertainties in the nucleation modelling are composed equally from those of measurements and from theory.

1.5.2.2 Ternary homogeneous nucleation

The binary nucleation mechanism described above explains aerosol formation in only certain parts of the atmosphere (Kirkby et al., 2011). In many parts of the troposphere, observed nucleation rates can exceed those predicted by the binary scheme, particularly those in the marine boundary layer and at some continental sites. In these locations, sulfuric acid concentrations are too low for binary nucleation, however they are suitable for ternary nucleation involving H_2SO_4–NH_3–H_2O. The ternary mechanism is important because it can explain the higher observed nucleation rates under typical sulfuric acid ($10^5 - 10^7$ $molec.cm^{-3}$) and ammonia (a few ppt) concentrations. The ternary mechanism's ability to nucleate at significantly lower concentrations than the binary scheme suggests that nucleation to detectable

sizes should be common, however under ambient conditions, condensational growth of ternary nucleated particles is around 1000 times slower (because of the lower condensable vapour concentrations required for nucleation), preventing more frequent occurrence (Kulmala, Pirjola, and Makela, 2000). This mechanism was first explored in detail by Korhonen et al. (1999) based on an extension of the classical theory summarised in the previous section, however other studies have contributed significantly (e.g. Coffman and Hegg, 1995; Kulmala, Pirjola, and Makela, 2000).

Incorporation of NH_3 into the classical theorem enhances the binary nucleation rate by several orders of magnitude provided NH_3 mixing ratios exceed around 1 ppt. Below this threshold, nucleation rates are similar to those produced by the binary mechanism. The mechanism is independent of relative humidity when concentrations of H_2SO_4 are below 10^8 $molec.cm^{-3}$ and NH_3 exceeds 5 ppt, suggesting it is important in a wide range of atmospheric scenarios. Similarly to the binary nucleation mechanism, the limiting factor is H_2SO_4, however as mentioned above, the nucleation threshold is around 1000 times lower than that for the binary scheme. (Korhonen et al., 1999)

The significant lowering of the activation energy required to reach a critical cluster can be illustrated with a case study. At 298 K, 52.3% relative humidity, 5 ppt NH_3 and 10^8 $molec.cm^{-3}$ H_2SO_4, the critical cluster using the ternary mechanism contains 18 molecules ($8\times H_2SO_4$, $4\times NH_3$ and $6\times H_2O$). In comparison, using the binary mechanism under the same conditions yields a critical cluster consisting of 130 molecules. (Korhonen et al., 1999)

1.5.2.3 Ion-mediated nucleation

Ion-mediated nucleation (IMN) is another mechanism that can explain the high observed nucleation rates that binary nucleation cannot predict (see Turco, Zhao, and Yu (1998); Yu and Turco (2000); Yu (2006); Yu and Luo (2010) and reviews by Enghoff and Svensmark (2008) and Seinfeld and Pandis (2006)). IMN is suggested to be important and ubiquitous throughout the troposphere. In general, the mechanism involves the natural ionisation of atmospheric gases, followed by electrostatic combination into molecular clusters that readily grow to aerosol nuclei.

Ions are generated continuously throughout the atmosphere from galactic cosmic rays at a rate of 2 $ion\text{-}pairs.cm^{-3}.s^{-1}$ at ground level, up to 20-30 $ion\text{-}pairs.cm^{-3}.s^{-1}$ in the upper troposphere. Ions can also be generated from local sources including radioactive decay, lightning and corona discharge. These ionisation processes produce both positive and negative ions. In the lower atmosphere, common positive ions include hydronium (H_3O^+), ammonium (NH_4^+) and a variety of organic ions, while the typical negative ions are dominated by ionized nitric acid (NO_3^-), sulfuric acid (HSO_4^-), methane sulfonic acid ($CH_3SO_3^-$), and malonic acid ($C_3H_3O_4^-$). Given

the relative concentrations of the parent molecules, it is likely that sulfuric acid ions will dominate in most environments. Once produced, ions quickly achieve a steady state with ambient vapours. These primary ions are readily attracted to one another, and to other charged clusters, through electrostatic forces, resulting in the formation of molecular clusters.

Once produced, ions present a pathway with a lower free energy barrier to nucleation due to the introduction of electrostatic forces. The chemical identity of the ion plays little part in the effect of the charged cluster, since it can be reasonably assumed that the critical nucleus contains tens to hundreds of molecules, meaning that the ion buried at the centre of this cluster has minimal influence of the properties of the surface. The effect of the charge, however, extends well beyond this shielding effect.

The introduction of a charge to the clustering system alters the balance between condensation and evaporation of molecules from the cluster surface. The effect of the ion is more pronounced on evaporating molecules, reducing evaporation rates significantly, with minimal changes to condensation rates (due to the effect of distance on Coulomb effects). The net effect is that fewer molecules are required to reach critical nucleus size - the point at which condensation rates are larger than evaporation - resulting in nucleation occurring faster than without the ions present.

Compared to homogeneous nucleation involving neutral clusters, IMN is favourable for a number of reasons. Firstly, the presence of ions in the nucleated molecular clusters results in much more thermodynamic stability compared to neutral clusters. Secondly, because of the strong dipole interaction between charged clusters and strongly dipolar precursor molecules, the rate of growth of ionic clusters via condensation and coagulation processes is significantly enhanced (e.g. Kirkby et al., 2011). This mechanism can allow nucleation to occur when sulfuric acid concentrations are too low for the traditional mechanisms, described above, to occur.

Recent chamber studies in the CLOUD chamber at CERN (European Organisation for Nuclear Research, Switzerland) have suggested that the IMN mechanism makes a minimal contribution at the global scale (compared to binary and ternary nucleation mechanisms), however it could be important regionally, particularly in the mid-troposphere or where particle concentrations are low (Almeida et al., 2013; Kirkby et al., 2011). Recent modelling studies suggest that this mechanism could be dominant in the Antarctic region where DMS emissions interact with the cosmic radiation that is focussed by the Earth's magnetic field (Yu and Luo, 2010).

1.5.2.4 Organic vapour nucleation

Nucleation from organic vapours is actually a misnomer since the process cannot actually occur without the presence of a seed particle. Consequently, this process is

more reflective of condensational growth at nanometre sizes than of pure nucleation. This process was first postulated by Hoffmann et al. (1997), however significant research has occurred since this paper (see reviews by Kanakidou et al. (2005) and Hallquist et al. (2009)), due largely to the vast array of species, both natural and anthropogenic, that have the potential to undergo a multitude of reactions before condensing into the aerosol phase.

Because of the large range of precursors, it is difficult to present a nucleation mechanism suitable for all organic species. For organic species to contribute to aerosol nucleation and growth, they must in general undergo gas phase oxidation to yield (typically oxygenated) products that have sufficiently low vapour pressures that can partition relatively easily from the gas phase to the aerosol phase. Products of this oxidation chemistry are often referred to as low- or non- volatile compounds, and when incorporated into aerosol, result in their widespread classification as Secondary Organic Aerosol (SOA).

The ability of organic vapours to contribute directly to nucleation is still under debate. Formation of large numbers (5×10^4 cm^{-3}) of new particles from organic precursors is routinely observed in laboratory studies that use moderate to high precursor concentrations (e.g. 20 ppb of α-pinene, a common proxy used for these studies), high ozone concentrations (e.g. 120 ppb) and no pre-existing particles (Kanakidou et al., 2005). However nucleation is relatively easily suppressed simply by introduction of moderate concentrations of seed particles - the vapours preferentially adhering to pre-existing aerosol surfaces rather than nucleating themselves (Kanakidou et al., 2005). Numerous field studies have reported nucleation events in both the boundary layer and free troposphere that have been suggested to be due to the nucleation of biogenic SOA compounds, particularly in remote areas (e.g. Marti et al., 1997; O'Dowd et al., 2002b; Kavouras and Stephanou, 2002). However, theoretical calculations of Gaman et al. (2004) concluded binary homogeneous nucleation of water-organic systems would not nucleate in the atmosphere. This idea is supported by the absence of nucleation events in the Amazon where biogenic VOC concentrations are very high while sulfuric acid concentrations are very low (Kanakidou et al., 2005). It is much more likely that in the real atmosphere, organics contribute significantly to the growth of particles after the initial nucleation - a property that could be important in the nucleation described in Chapter 5.

1.5.2.5 Iodine oxide nucleation

The mechanism of nucleation from IO was first described by Hoffmann, O'Dowd, and Seinfeld (2001), with numerous modifications made by a variety of studies (e.g. Jimenez et al., 2003; Saunders and Plane, 2005; Saiz-Lopez et al., 2011). The current understanding is outlined below.

The mechanism begins with the oxidation of a precursor gas, CH_2I_2 (which is the single most abundant iodine-containing compound released by macroalgaes (Hoffmann, O'Dowd, and Seinfeld, 2001)) or I_2. Once released, precursors are photo-dissociated, releasing iodine atoms which rapidly react with O_3 to form IO radicals such that:

$$\begin{aligned} CH_2I_2 + h\nu &\longrightarrow I + CH_2I \\ I_2 + h\nu &\longrightarrow 2\,I \\ I + O_3 &\longrightarrow IO + O_2 \end{aligned}$$

The reaction proceeding from IO to nucleation is summarised schematically in Figure 1.10. Once produced, IO undergoes self-reaction via two pathways, which result in the same final products,

$$\begin{aligned} IO + IO &\longrightarrow OIO + I\ (\sim 40\,\%) \\ IO + IO &\xrightarrow{M} I_2O_2 \longrightarrow OIO + I\ (\sim 60\,\%) \end{aligned}$$

OIO is highly photochemically stable, and can be readily lost to pre-existing particles that may be present. If pre-existing particle concentrations are low enough, OIO reacts with itself, or with IO such that

$$\begin{aligned} IO + OIO &\xrightarrow{M} I_2O_3 \\ OIO + OIO &\xrightarrow{M} I_2O_4 \end{aligned}$$

Futher reactions of I_2O_x (where $x = 2, 3 or 4$) compounds occur with O_3 throughout the mechanism, further oxidising the iodine

$$\begin{aligned} I_2O_2 + O_3 &\longrightarrow I_2O_3 \\ I_2O_3 + O_3 &\longrightarrow I_2O_4 \\ I_2O_4 + O_3 &\longrightarrow I_2O_5 \end{aligned}$$

I_2O_5 is thermodynamically stable and because of its large dipole moment, is highly condensible. At this stage, nucleation can occur by polymerisation of solid particles of pure I_2O_5, or via a competing polymerisation reaction that leads to particles of mixed compositions where the O/I ratio is less than 2 such that:

$$I_2O_x + I_yO_z \longrightarrow I_{2+y}O_{x+z}$$

where x = 2, 3 or 4, y = 1 or 2, and z = 1, 2, 3, or 4.

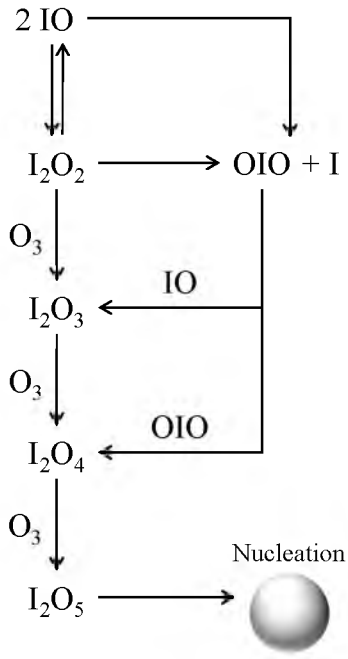

Figure 1.10: Summary schematic of the iodine chemistry that leads to aerosol nucleation. Adapted from lecture of Saiz-Lopez (2014).

Resulting aerosol nuclei are then likely to be composed of I_2O_5, and would grow by condensation of additional iodine compounds or other species, or coagulation processes. Importantly, since these nuclei are composed of I_2O_5, they are highly stable and hygrophilic (as opposed to I_2O_4), and have been found to readily accommodate other common species such as water, sulfuric acid, water, ammonia and organic species (see review by Saiz-Lopez et al. (2011)). The efficiency of nucleation, together with their interactions with other common atmospheric condensible vapours, makes them able to grow to sizes where they can be climatically active through both ARI and ACI.

1.5.3 Nucleation: a big unknown in aerosol science

There has been significant research into the formation mechanisms described above, as well as specific nucleation reactions pathways over the last 20 years or so. Some of the specific reactions that have been studied include: sulfuric acid pathways, alone (Covert et al., 1992; Sipilä et al., 2010), and in combination with organic aromatic acids (Zhang et al., 2004); low and semi-volatile biogenic organic compounds (Guo et al., 2012; Jung, Miyazaki, and Kawamura, 2013) or ammonium and nitrogen dioxide (Behera and Sharma, 2011); iodine oxide reaction pathways (O'Dowd et al., 2002c; Saiz-Lopez et al., 2006; Hoffmann, O'Dowd, and Seinfeld, 2001); and biologically emitted potassium salt as a seed for VOCs (Pöhlker et al., 2012). Despite this research, there is still great uncertainty in the fundamental chemical mechanisms and

composition of the nucleation occurring in the atmosphere (Zhang, 2010). Recent improvements in measurement technologies are helping reduce this uncertainty, allowing probing of nuclei to sizes as low as 1.5 nm - the approximate size required for spontaneous growth (Sipilä et al., 2010). Despite these improvements, many questions still remain about chemical mechanisms in various environments: including marine, urban, and biogenic air-masses, in polar, tropical and temperate ecosystems, and different atmospheric elevations - almost all being research fields not yet well established, particularly in the Southern Hemisphere where the research community and studies are more limited.

1.6 Aerosol Research in Antarctica and the Southern Ocean

Aerosol investigations in polar regions have been focussed primarily in the Arctic (Asmi et al., 2013; Collaud Coen et al., 2013). The earliest aerosol studies in Antarctica were as early as 1965 where CN concentrations were measured using expansion-type cloud chamber instruments (see review by Shaw (1988)). These early measurements were primarily driven by the aim to understand why, even in the most remote region of the Earth which is covered in a seemingly impervious multi-kilometre sheet of ice, that aerosols were present at all. Aerosols in this region provided a unique opportunity to study long-range atmospheric transport processes and to learn about cold, anthropogenic-free atmospheric chemistry.

Since then, research has continued throughout the continent. Given the logistical difficulties, expense of investigations in the Antarctic region, and typical funding variations for research in general, long-term measurements are relatively rare in the continent's 50 years of aerosol measurements (e.g. Virkkula et al., 2009; Ito, 1995), and the few intensive campaigns (e.g. Belosi et al., 2012; Davis et al., 2004; Davison et al., 1996) that have occurred have been limited primarily to the summer months when access is simpler.

Antarctica covers an area of over 13.7 million km^2, however permanent research stations servicing this region number only in the tens, meaning large spatial regions remain unsampled. Logistical limitations mean that most of these stations are located along the coast, however a number of major stations have been established on the Antarctic plateau such as South Pole and Dome Concordia (Dome C), typically with the goal of sampling deep ice cores. Research in the past two decades has evolved since the first studies, but still utilise the natural laboratory that Antarctica provides to understand a variety of atmospheric and cryospheric processes.

Unlike Arctic aerosols, which have major anthropogenic and biomass burning

sources (Brock et al., 2011), the remoteness of Antarctica makes it ideal for understanding a number of natural processes (Hara et al., 2011; Järvinen et al., 2013). This is particularly important in light of a recent study by Carslaw et al. (2013) that found that the largest gains in reducing the uncertainty in ACI - the largest uncertainty affecting climate projections - are achieved through understanding "pristine pre-industrial-like environments, with natural aerosols only".

One of the most important questions still under debate is the exact mechanisms and influence of different nucleation pathways (Kulmala et al., 2004; Kulmala, Lehtinen, and Laaksonen, 2006), an overview of those currently understood given in the earlier Section 1.5.2. Understanding how aerosols grow following nucleation, and whether growth occurs to climatically relevant sizes ($\geq 80\ nm$) where they can interact directly with radiation, or act as CCN, is also still an active area of research (e.g. Zhang et al., 2012; Gantt et al., 2012).

The role of absorbing aerosols in the radiative balance of polar regions, which are particularly sensitive to changes in climate, is also an important open question. Absorbing aerosols, such as black carbon, can heat the atmosphere above high albedo surfaces, and once deposited, can also reduce the surface's albedo, contributing to processes (which also includes changes to snow grain size) that result in melt pools on the ice surface, which in turn results in further reduction of the surface albedo (IPCC, 2013). Although these effects have been seen widely in the Arctic region where the anthropogenic influence, and consequently the loading of these absorbing aerosols, is higher (e.g. Stohl et al., 2013; Flanner, 2013; Goldenson et al., 2012), research into the significantly more pristine region of the Antarctic is more limited (e.g. Wolff and Cachier, 1998; Hansen et al., 2001).

Understanding aerosols in the Antarctic region and their sources and chemistry is also important in order to decipher past atmospheres and climates from ice core samples obtained from the continent. These paleoclimatological studies require a thorough and unambiguous understanding of the interactions between atmospheric processes and what is recorded in the snow-pack that becomes the ice cores used for interpretation (Bergin et al., 1998). Although measurements aimed at understanding these interactions have been conducted throughout the Antarctic region at both coastal sites (e.g. Wagenbach et al., 1998; Jourdain, 2002; Rankin and Wolff, 2003) and high plateau sites such as South Pole (Bergin et al., 1998; Arimoto et al., 2004; Davis et al., 2004, e.g.) and Dome C (e.g. Udisti et al., 2004), significant uncertainties remain in the scientific understanding of the paleoclimate.

Studies of aerosols in the last few decades have been primarily limited to permanent research stations on the coast or plateau (e.g. Asmi et al., 2010; Hansen et al., 2009; Hara et al., 2011; Ito, 1993; Järvinen et al., 2013; Koponen et al., 2003; Lai, Hoffman, and Xie, 2008; Pant, Siingh, and Kamra, 2011; Samson et al., 1990;

Virkkula et al., 2007; Weller et al., 2011) or where temporary field stations can be setup on permanent ice (e.g. Belosi et al., 2012). Generally speaking, these studies found that most aerosols and new particle formation events occurred in maritime air-masses, where significant precursor sources exist relative to air-masses originating from the Antarctic continent (e.g. Asmi et al., 2010; Belosi et al., 2012; O'Dowd et al., 1997; Shaw, 1988; Udisti et al., 2012; Yu and Luo, 2010). Only one study by Kyrö et al. (2013) found aerosols that originated from continental sources, with melt pond biota producing precursors to new particle formation.

Aerosols in marine air-masses that dominate the region are predominantly made up of coarse mode sea salt aerosol, however they also contain significant precursor compounds suitable for secondary aerosol formation. For example, Asmi et al. (2010) found that these maritime air-masses contained aerosols composed of both sulfuric acid and organic material. A range of formation mechanisms were discussed that could lead to these compositions, including both ion-induced and neutral cluster initiated. Most of the fine-mode aerosol in the Antarctic region is dominated by secondary sulfate aerosol (Ito, 1995) resulting from the oxidation of DMS which is released from the surface of the nearby oceans that hold concentrations higher than most around the globe (Lana et al., 2011). The Antarctic continent itself is almost entirely covered in a lifeless ice-sheet, meaning that precursor sources are limited to biological productive marine and sea ice regions or to a lesser extent, volcanic activity (Radke, 1982). Measurements of particle size distribution in continental Antarctica by Koponen et al. (2003) confirmed this idea, observing new particle formation and growth events only in marine/coastal air masses.

Despite the dominant origin of Antarctic aerosols being the Southern Ocean and sea ice regions surrounding the continent, there have only been a handful of measurements of aerosols and precursors in these areas. Our understanding of the Southern Ocean is primarily driven by just a few intensive campaigns, including the first Aerosol Characterisation Experiment (ACE 1) (Bates et al., 1998; Quinn et al., 2000; Quinn et al., 1998; Hudson, Xie, and Yum, 1998; Brechtel, Kreidenweis, and Swan, 1998; Weber et al., 1998) and the HIAPER Pole to Pole Observations (HIPPO) (Wofsy, 2011). Additional sporadic measurements have been made by numerous ships as either dedicated marine science voyages covering global spatial scales (e.g. Hu et al., 2013), or measurements made en-route to other locations such as the Antarctic continent (e.g. Koponen et al., 2002). Long-term measurements are rare and restricted to permanent stations with strong influence from the Southern Ocean such as Cape Grim (e.g. Ayers, Ivey, and Gillett, 1991).

Studies of aerosols directly over the sea ice are limited primarily to the Northern Hemisphere in the Arctic (Asmi et al., 2013; Collaud Coen et al., 2013; Covert et al., 1996; Shaw, 1982; Wiedensohler et al., 1996) and other smaller ice-covered seas

(Borrmann, Davidson, and Miller, 1987; Inoue and Toyota, 2005; Whitehead et al., 2012). There is only one similar aerosol dataset made in the entire Antarctic sea ice region. Davison et al. (1996) sampled air over the Weddell Sea region of the West Antarctic in the early summer period, and found that particle concentrations were similar to those measured at coastal stations, showing condensation nuclei concentrations around 500 cm^{-3} (see Chapter 3 text and Figure 3.5 for a detailed comparison). Given the maximal areal coverage of sea ice in the winter can be well above the area of the continent, reaching above 19 million km^2, this single aerosol dataset represents a severe and chronic undersampling.

The sparseness of measurements over Antarctic sea ice leads to significant uncertainty of aerosol properties and formation mechanisms in these regions, which needs to be remedied. Research also tends to be focussed in the West Antarctic, leaving the East Antarctic (0 to 180°E) with an even greater dearth of measurements. Additionally, the summer focus of almost all intensive research is likely to significantly bias our understanding of aerosols in the region. The combination of this summer bias and the dearth of aerosol observations in the East Antarctic region makes the spring-time measurements presented in this thesis important for validating and developing our understanding, and hence reducing the uncertainty, of many natural processes that may be occurring at both the regional and global scales.

1.7 SIPEXII

This thesis is based on measurements made during a marine science voyage made aboard Australia's flagship icebreaker, *Aurora Australis*, during the spring of 2012. The voyage was commissioned primarily for the second Sea Ice Physics and Ecosystems eXperiment (SIPEXII), with a number of smaller projects occurring simultaneously, including the atmospheric component, Project 4032, within which the studies presented here were made. Similar to the first SIPEX which occurred in 2007, SIPEXII was a multidisciplinary project aimed to characterise both physical and biological properties of the sea ice environment and the important interactions affecting the Southern Ocean ecosystems. The voyage involved more than 50 scientists from over eight countries. The 64 day round trip departed Hobart on September 14, which after stationary sea trials off the east coast of Tasmania was followed by a 5 day Southern Ocean traverse, reaching Antarctica's sea ice edge 9 days later. Once in the sea ice zone, the primary aim of the voyage was to moor the ship to large ($>$ 100 m) ice floes in order to setup temporary research "ice stations" from which scientists could alight onto the sea ice surface and conduct measurements. Although the aim was to have ten ice stations during the voyage, a total of eight were possible due to unfavourable weather patterns that trapped the ship numerous times for a

total delay of two weeks. The trajectory of the ship was such that it reached the ice edge at approximately 120°E then headed directly south, hoping eventually to reach the coastal polynya regions - an area of open water which is generally surrounded on one side by a continental ice sheet and on the other by sea ice, and which are often considered to be 'sea ice factories'. Unfortunately, due to the aforementioned delays and the need to re-supply Australia's Antarctic research stations (Mawson, Casey, Davis and the sub-Antarctic Macquarie Island), we were unable to reach the polynya region as it was decided to return to Hobart as quickly as possible.

Figure 1.11 shows an overview of the ship operations that occurred during SIPEXII. Numerous experimental surveys were performed from the two helicopters included on the ship, along with reconnaissance missions to determine the best route for the ship to take through the sea ice. The instrumented helicopters provided snow and ice thickness, surface topography, and sea ice motion and deformation over regional scales using high-resolution aerial photography, scanning LIDAR (LIght Detection And Ranging), infrared and microwave radiometers and scanning altimeters. Numerous disposable sea ice buoys, consisting of a sensitive accelerometer within a powered housing, were deployed onto ice floes which relayed information via satellite about sea ice movement and ocean currents. Additional buoys were deployed to measure the interactions between waves and the sea ice, gleaning insights onto wave propagation in the sea ice zone and its effect on floe-size distribution (Kohout et al., 2014).

A multitude of operations occurred during the ice stations. Remotely Operated Vehicles (ROVs) and Autonomous Underwater Vehicles (AUVs) were deployed under the ice surface to observe and film krill and other biology, as well as characterising the complex three-dimensional under-ice topography of the ice floes (Williams et al., 2014). The important krill populations were studied from small samples taken from below the ice and on the sea floor using customized pumping systems and light-traps. On top of the ice, sea ice was characterised in terms of properties such as type and thickness, snow cover, salinity and temperature. Many of these properties were obtained by analysing ice core samples. Included in these sampling and measurement regimes were algal communities within the sea ice, conductivity measurements, trace metal concentrations as well as a number of trace gas concentrations in the sea ice melt water, brine and underlying seawater, together with their emissions from the surface. Surface topography and wind blown snow was also characterised using sensors mounted on temporary masts and mobile laser based systems.

The scientific activities that occurred as part of the SIPEXII project were many and varied and as well as directing the ship track, consumed most of the time and resourced that were supplied for the voyage. Australian Antarctic Division (AAD) Project 4032 was the second priority of the voyage time, but didn't require

any special deviations from the voyage track specified by SIPEXII. Details of this project are described in the following section.

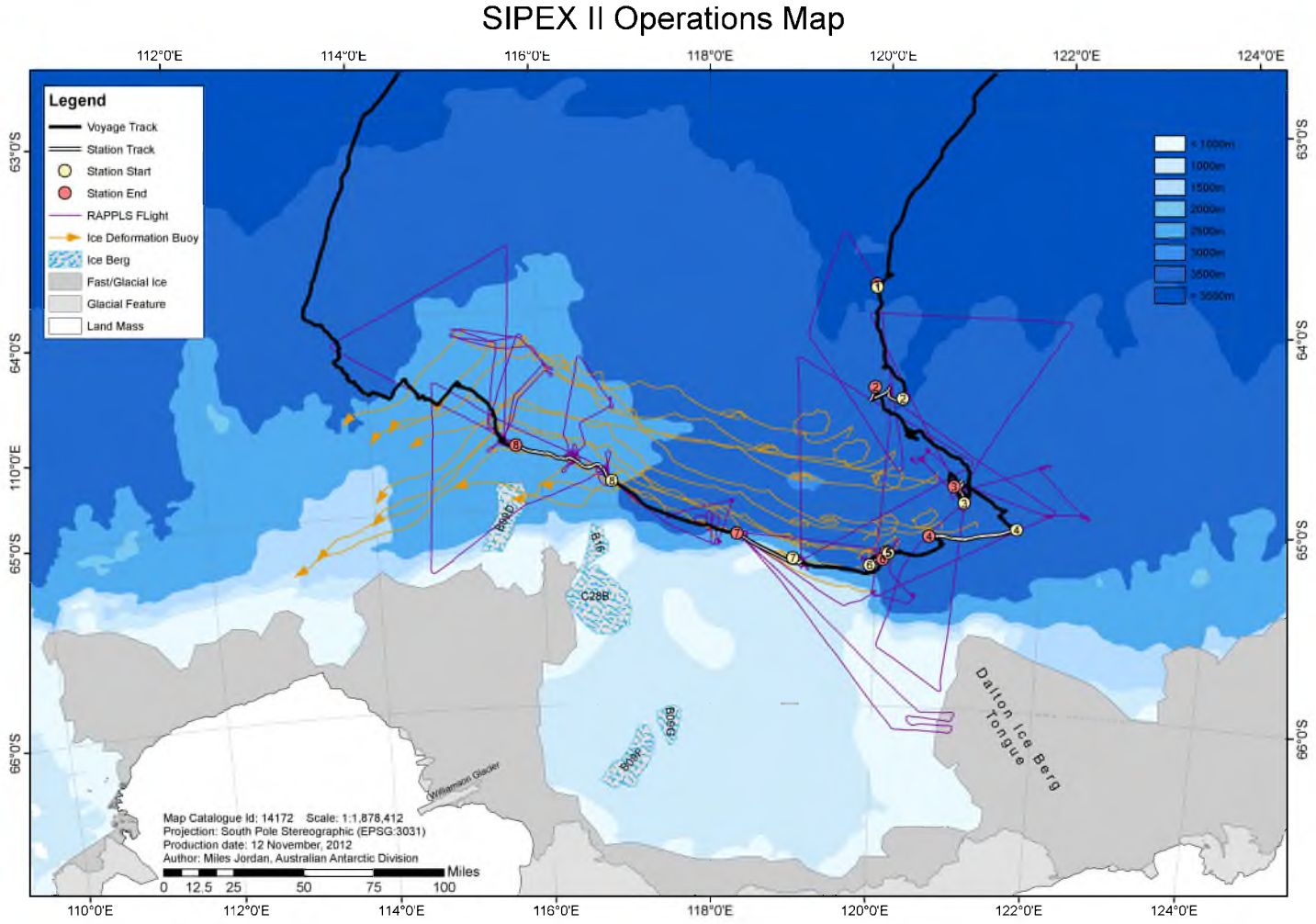

Figure 1.11: SIPEXII operations map within the sea ice zone off the coast of East Antarctica. The legend shows the continent and ice features, as well as GPS tracks of the ship and various instrumentation, including the general movement of the sea ice in a westerly direction around the continent (Ice Deformation Buoy, orange). Map courtesy Miles Jordan, Australia Antarctic Division.

1.7.1 AAD Project 4032: Atmospheric Measurements

The original proposal of AAD Project 4032 was titled "bromine control of the mercury flux into the biosphere of the Southern Ocean and Antarctic regions". The first observations of periods of Total Gaseous Mercury (TGM) depletion were reported in the Arctic in the months following polar sunrise, and were associated with simultaneous increases in mercury concentrations in the snow pack (Schroeder et al., 1998; Lu et al., 2001; Lindberg et al., 2002). The chemistry of these events, commonly described as Mercury Depletion Events (MDEs), is summarised schematically in Figure 1.12. These events are associated with the oxidation of Gaseous Elemental Mercury (GEM, Hg^0) which, with its 1 year atmospheric lifetime, is distributed globally from its multitude sources, of which between 25-50% is of anthropogenic origin (Biester et al., 2007; Holmes et al., 2010). This oxidation is initiated by the release of highly reactive bromine radicals that are released in large quantities in the polar spring (Bottenheim et al., 1990). The release of these radicals is found to correspond to the spatial distribution of young (1 year old) sea ice (Richter et al., 2002), and is proposed to be an autocatalytic release from sea salt on the snow pack that has accumulated over the polar night. This release is confined to the polar sunrise and their occurrence is rare in Antarctica after November (Temme et al., 2003a; Temme et al., 2003b). Once released to the atmosphere, bromine radicals readily react with both GEM and O_3, resulting in simultaneous depletion of both species. After oxidation, reactive mercury deposits onto the sea ice, which can subsequently methylate and enter the biosphere, which is particularly toxic during the extremely high primary productivity of spring-time. Although the deposition flux due to this chemistry has been determined in the Arctic to be 100 tons of mercury per year (approximately 30% of the total flux) (Ariya et al., 2004), no observationally constrained flux has been calculated for the Antarctic - a gap Project 4032 aimed to fill. Even basic measurements of this chemistry are rare in the Antarctic (e.g. Ebinghaus et al., 2002), and concurrent measurements of the microbial mercury response has never been performed (Barkay and Poulain, 2007). Measurements of mercury in the Antarctic in general are uncommon, with only a handful of coastal or continental measurements and two ship voyages, neither of which occurred in the polar spring (Dommergue et al., 2010; Pfaffhuber et al., 2012; Xia, Xie, and Sun, 2010).

As well as measuring the atmospheric component of mercury depletion events in the Antarctic, this project also aimed to characterise the biogeochemical cycle it initiates. To achieve these aims, a multitude of measurements were made of both the atmosphere and the microbial communities in the snow, sea ice and ocean. Mercury was measured by the use of a TGM analyser, which, due to operational constraints, could not be complemented by planned mercury speciation measurements.

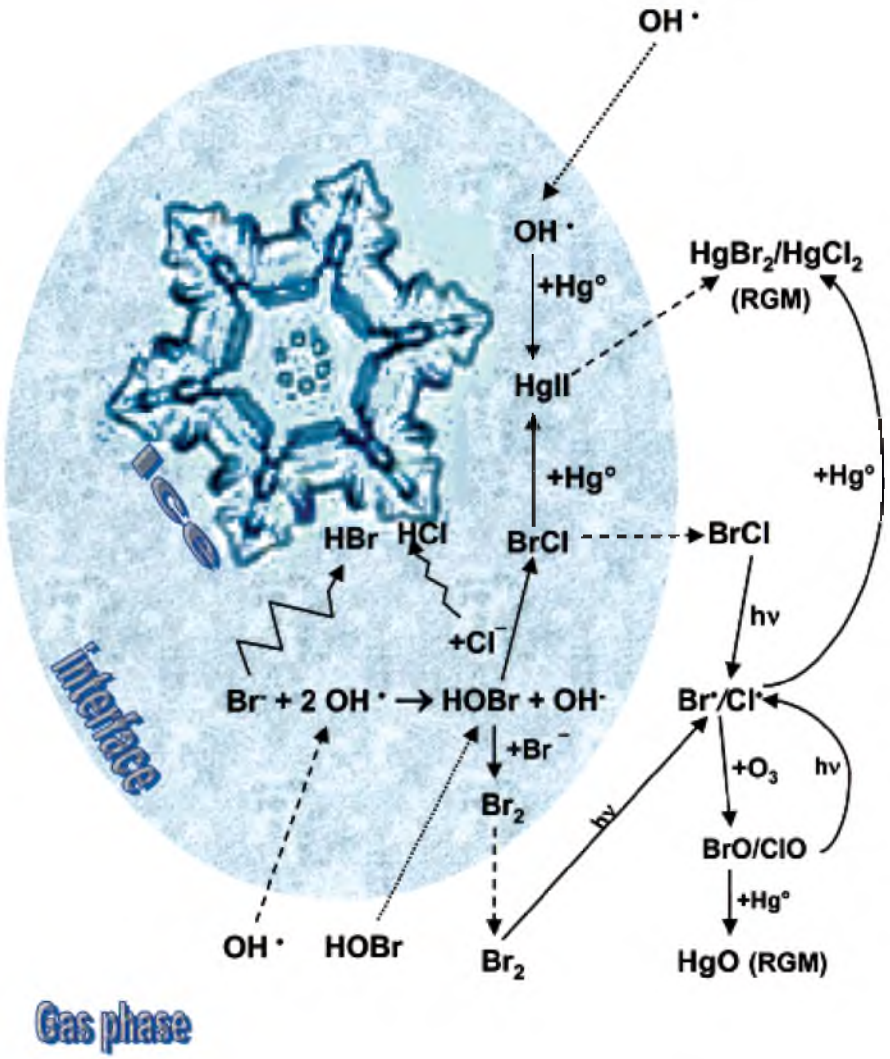

Figure 1.12: Conceptual diagram of the proposed Hg^0 oxidation reaction sequences based on the most favourable pathways from observations made at Barrow, in the Canadian Arctic. Dashed lines represent inter-phase transport; solid lines are reaction pathways. Schematic taken from Lindberg et al. (2002).

The MAX-DOAS (Multi-AXis Differential Optical Absorption Spectroscopy) was utilised to determine BrO mixing ratios in the lowest 4 km of the atmosphere, along with other species such as NO_2 and O_3, as well as aerosol extinction. O_3 was also measured *in-situ* using a standard ozone monitor. These core measurements were also complemented by the use of a Gas Chromatograph with Electron Capture Detector which provided concentrations of halocarbons which may be involved in the halogen chemistry being assessed. Additionally, my last-minute involvement in the project meant that aerosol instrumentation was able to be included which, along with providing useful information for possible heterogeneous chemistry with the mechanisms being investigated, also allowed an aerosol focussed project to be undertaken.

This thesis describes the results of the aerosol focussed study of the voyage

commissioned for the SIPEXII project. The aims of this study were to characterise, for the first time, the aerosol loading in the East Antarctic sea ice, as well as to investigate any new particle formation which could be occurring in the region. Although not part of the initial research proposal for Project 4032, this opportunistic project has shown to be a valuable addition to the original outcomes, as well as to both fields of Antarctic aerosols and aerosol nucleation mechanisms in general. The results of this project will be described in this thesis in the following manner. In Chapter 2, the experimental design and setup is outlined in detail along with data handling, analysis and uncertainty calculations. Chapter 3 describes the surprisingly high background aerosol populations discovered in the region and assesses the source regions and possible precursors leading to their formation. Results from global chemistry and transport models attempting to reproduce the high measured aerosol concentrations are described in Chapter 4. The chemistry and meteorological conditions associated with a single, but significant, new particle formation event are then discussed in Chapter 5. In Chapter 6, a succinct overview of the results and conclusions of this thesis is presented.

Chapter 2

Methods

The basis of this thesis was a dataset obtained during a campaign in the pack-ice off the coast of East Antarctica. The campaign was a marine science voyage, departing port in Hobart, that aimed at characterising the Antarctic sea-ice environment. During this voyage, numerous datasets were obtained by myself, project collaborators, and other scientific projects and infrastructure. All data from this project are archived separately at the Australian Antarctic Data Centre and references to archives are included at the end of each section describing the relevant dataset. This chapter outlines the general meteorological conditions, measurement platform, instrument setup and data analysis that is relevant for all the following chapters of this thesis. Since this project is a collaborative endeavour, a statement describing the various collaborator's contributions has been included in each relevant section.

2.1 Measurement Platform

The Australian Antarctic Division's flagship ice-breaker, Aurora Australis, is a 94.9 m multi-purpose research and resupply ship capable of breaking ice up to 1.23 m thick (Australian Antarctic Division, 2010). The Aurora Australis was commissioned for the Sea Ice Physics and Ecosystems eXperiment II (SIPEXII), a marine science voyage aimed at studying processes in the sea ice zone off the coast of East Antarctica. The voyage, shown in Figure 2.1, occurred between 14 September and 16 November, 2012 and involved a Southern Ocean traverse, and significant time (49 days) in pack ice. Ocean capable inlets allowed measurements of atmospheric trace gas species during the ocean crossing, with the addition of aerosol measurements within the sea ice zone (between 112°E - 122°E, and south of 61.5°S) between 23 September and 11 November. A detailed map of the various ship operations which occurred as part of SIPEXII is shown in Figure 1.11, and includes tracks while the ship is both underway and docked at an ice station and drifting with the pack ice.

Locations of measurement inlets and the spectroscopic tracking head (detailed

below) are shown in Figure 2.2 and 2.3. The aerosol inlet, located on the starboard forecastle, was setup away (∼40 m) from other atmospheric measurements for logistical reasons. This location difference is negligible for the studies here as: time and thus spatial averaging has been applied to data; the MAX-DOAS (tracker head pictured far right in Figure 2.2) data represents horizontally and vertically integrated concentrations over numerous kilometres and hundreds of metres respectively; and the sources of measured parameters are likely not highly heterogeneous at this small spatial scale in this region.

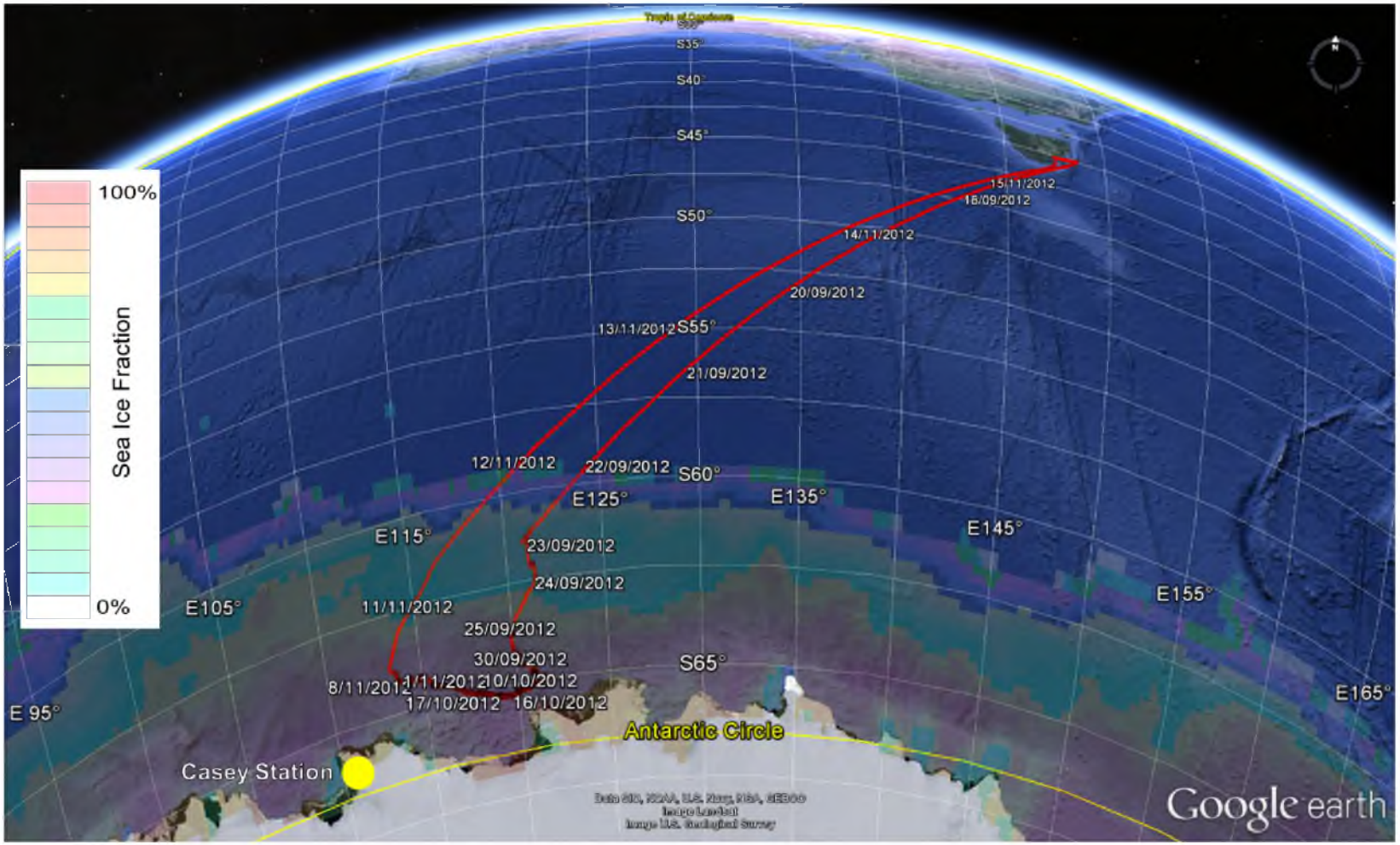

Figure 2.1: Ship track of the marine science voyage, SIPEXII. The voyage, that departed Hobart, Australia on September 14, arrived at the Antarctic ice edge (density shown by colours around the continent) on September 23 where it spent 52 days before returning to Hobart on November 16. The nearby Casey Station is labelled for reference. Sea ice concentrations data is derived from Extended Reconstructed Sea Surface Temperature (ERSST) Version 3b, October 2012 mean, with imagery from Google Earth.

Figure 2.2: Locations of various instruments and sample inlets on the ship. **A**: Aerosol inlet on the starboard forecastle approximately 11.5 m above sea level (ASL); **B**: inlets for instruments measuring halocarbons and gaseous elemental mercury, along with a windmill anemometer, were situated off the monkey deck directly above bridge, approximately 18 m ASL. The ozone inlet was located directly adjacent to B; **C**: the tracking head of spectroscopic instruments mounted on the same deck, viewing to the port of the ship at the same height of approximately 18 m ASL. During ice stations and ice breaking, the ship sat up to 2 m above the nominal sea height, resulting in variable inlet heights relative to sea level.

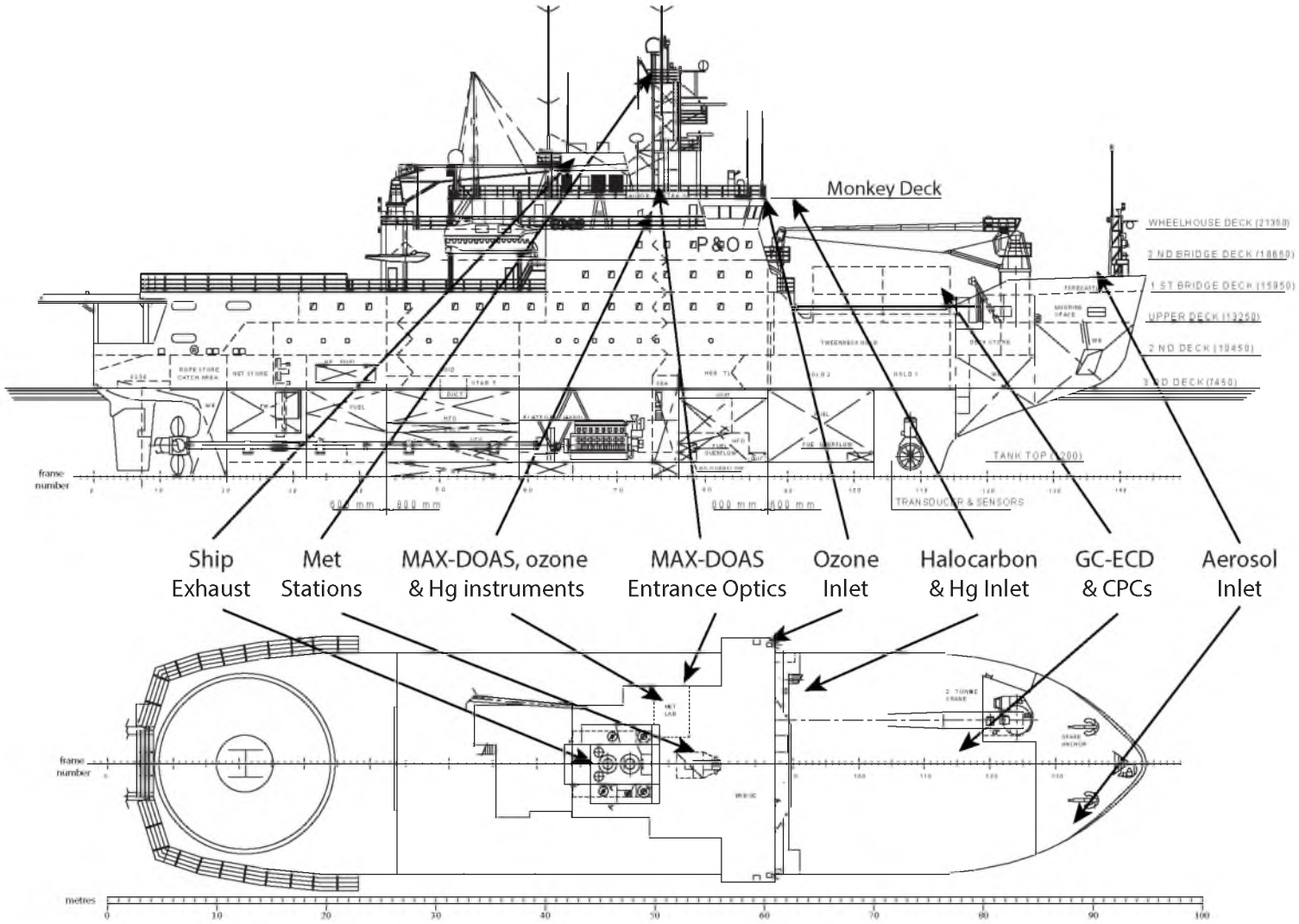

Figure 2.3: Locations of various instruments and sample inlets overlayed on a modified ship schematic obtained from the Australian Antarctic Division. Unless otherwise stated, units are in millimetres.

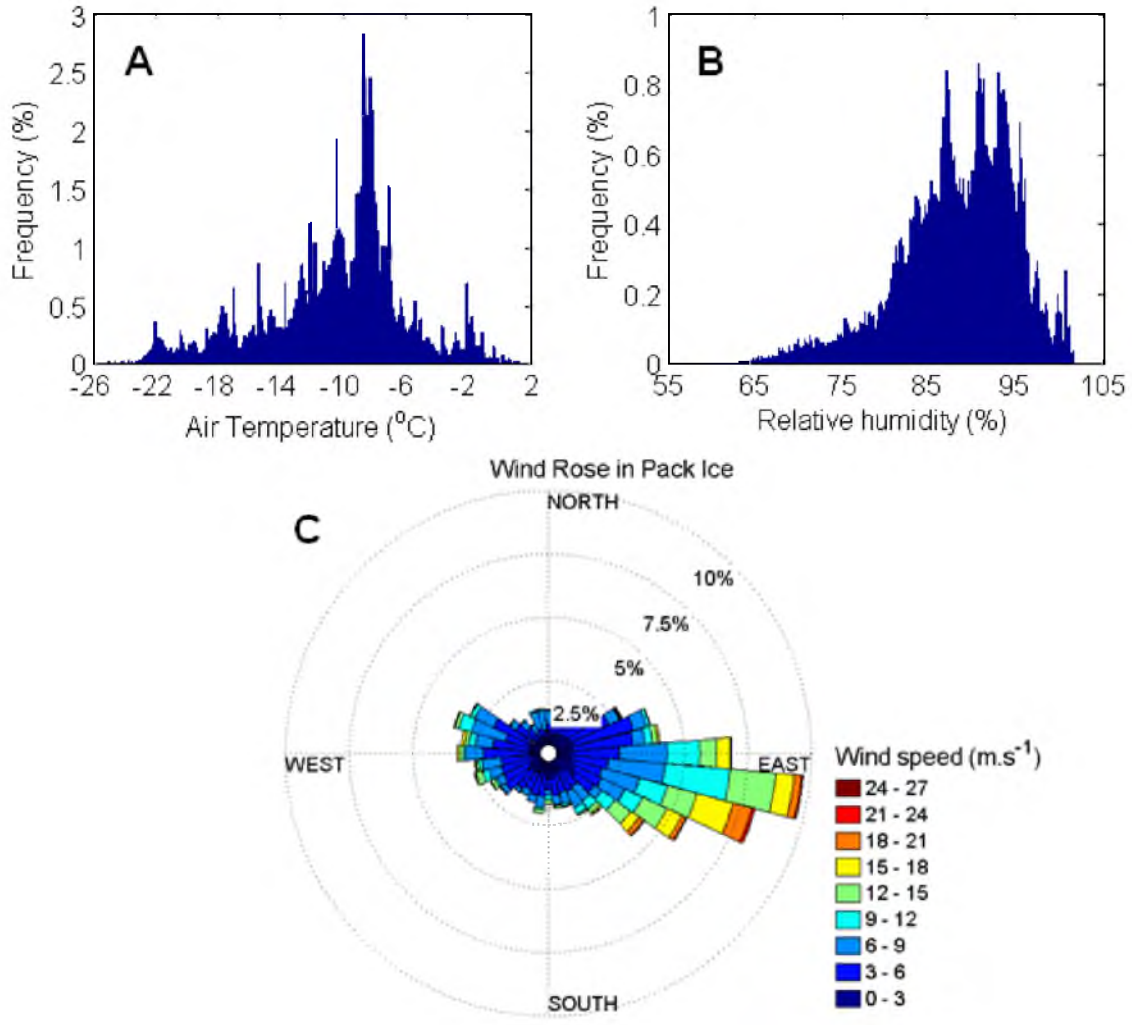

Figure 2.4: Meteorological statistics during the pack-ice section of the voyage. **A)** Air temperature (°C) histogram. **B)** Relative humidity (%) histogram. **C)** Wind rose showing the frequency (vector magnitude) of wind directions and their speeds (colours). The dominant easterly winds, characteristic of the surface winds of the Polar Cell, are clearly evident.

While in the sea ice, temperatures (Figure 2.4A) ranged from -25.4°C to 1.2°C, with a mean and median of -10.5°C and -9.7°C, respectively. Being a marine environment, the relative humidity (Figure 2.4B) remained high throughout the entire sea ice portion of the cruise, not dipping below 60%, and averaging 88%. Wind conditions ranged considerably, but were consistent with winds typical of polar regions. A wind rose of all observations in the sea ice (Figure 2.4C) shows the distinct easterly pattern characteristic of Polar Cell conditions. It is important to note that this wind rose is heavily weighted for southerly observations where most of the time was spent. This is further elaborated on later in the text Chapter 3 where the data is divided, into spatially different datasets, based on atmospheric air-masses, revealing two very distinct wind patterns.

Figure 2.5 shows the snowfall measured at the height of the ship's monkey-

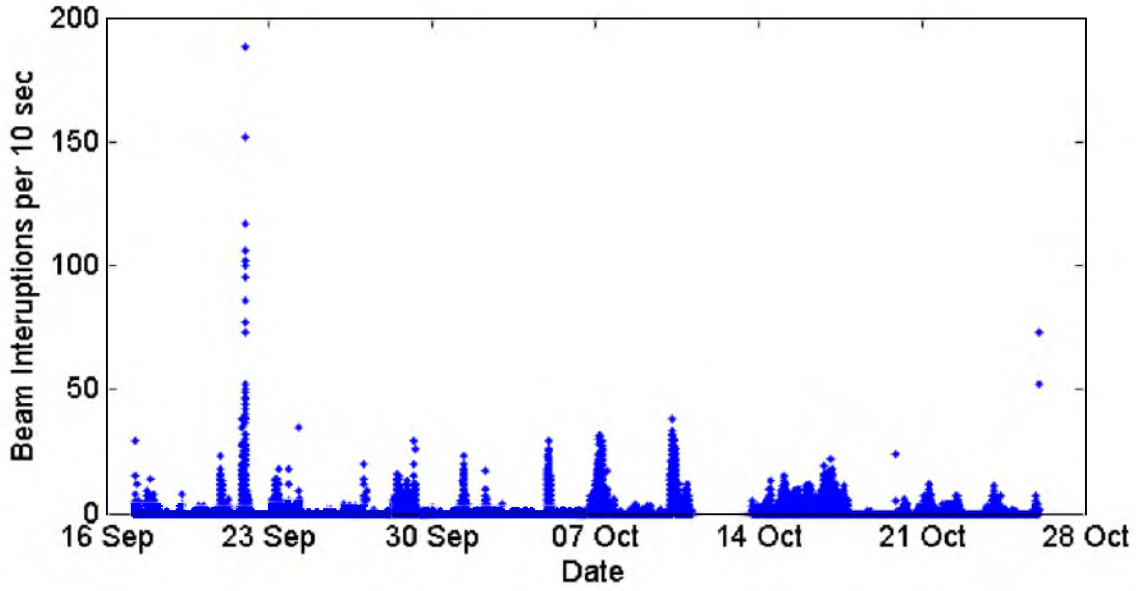

Figure 2.5: Falling snow measured as interruptions of a photoelectric sensor. Note the frequency of snowfall events throughout the cruise.

deck (above the bridge) as interruptions of a photoelectric beam given every 10 seconds. These measurements give the amount of falling snow, rather than accumulated snow. Given the high relative humidity, extreme weather conditions of the Southern Ocean and dominance of stratocumulus clouds in the the region, it is unsurprising that snowfall events were so common throughout the cruise. This high snowfall precipitation frequency also explains the deep snow cover over the sea ice.

It is useful to understand the surface topography around the measurements in order to determine its effect on atmospheric emissions and dynamics. Scientific investigations that directed the voyage focussed on large-scale (several hundred metre) sea ice floes that could be either first of multi-year floes. These floes moved dynamically with ocean currents and changing atmospheric conditions. It is within these dynamics that floe collisions occur, resulting in the rafting observed in Figure 2.6 that shows an example of sea ice surface topography. This rafting causes small-scale topography of only up to a few metres. Other than this rafting, the ice-scape has minimal topographical variation of atmospheric relevance. The ice surface was also covered in a significant layer of snow, which varied in depth, age and structure (e.g. could be powder, which allows wind-blown snow, a potential aerosol source; or melted and refrozen surfaces, which prevents wind-blown snow). The SIPEXII cruise was dominated by fresh snow at depths of over 1 m. Figure 2.6 also shows the most common cloud conditions, low lying marine stratocumulus clouds which were important for consideration of photochemistry and biology as well as when interpreting spectroscopic data (see Section 2.2.7).

Figure 2.6: Typical topography of sea ice surface shows little large scale topography that could affect atmospheric turbulence. Small scale topography, such as rafting (as observed in the photo), was common, but would be unlikely to produce affects on atmospheric turbulence that would be observable in atmospheric measurements taken aboard the ship. All the ice surface were covered in snow which ranged in depth but could be up to 1 m deep.

2.1.1 Ship Activities

The marine science voyage was a collection of projects funded by the Australian Antarctic Division (AAD). Atmospheric measurements occurred during the whole cruise, with the exception of the aerosol measurements which, due to inlet limitations, were only able to be conducted in the pack ice. These measurements had no particular spatial needs other than being within the sea ice zone. The major project on-board, SIPEXII, which assumed the majority of resources, primarily defined the ships heading, location and activities. Activities occurring as part of the SIPEXII project were generally confined to ice-stations - times when the ship was anchored to a sea ice floe and persons alighted the ship to make measurements. Activities that occurred outside the 8 ice stations (shown in Table 2.1) were limited to helicopter operations. It is important to consider the activities that occurred in order to determine conditions that may affect atmospheric measurements. Ice station activities included, but were not limited to: crane operations; movement of heavy gear around ice using quad-bikes and manual labour; large (approx. 1.5 m) and small (approx. 10 cm) diameter ice drilling with drills powered by both electric and diesel

motors; manual shovelling of snow and ice; Inflatable Rescue Boat (IRB) activities; and various other activities which included up to 50 people on the ice at any one time.

The other major influence on atmospheric measurements was the ship exhaust that was often active even while anchored to the sea ice (some experiments required the engine to be powered down to eliminate underwater acoustics). This exhaust included diesel combustion products, as well as incinerator products, and was the single largest contaminant to atmospheric measurements. Since this was a point source, and had distinct chemical markers (e.g. ozone depletion and high particle concentrations), identification of and subsequent filtering of the dataset was performed easily using wind direction and chemical data.

Table 2.1: Dates and locations of sea ice stations deduced from ship logs and ship speed. Information is approximate here because numerous periods were experienced where we were stuck in the ice before logistics decided to declare an ice-station.

Station Num.	Date (UTC, 2012) Start	End	Start Location	End Location
1	25 Sept 03:40	25 Sept 11:00	63.89°S, 119.90°E	63.88°S, 119.90°E
2	26 Sept 04:45	29 Sept 08:30	64.45°S, 120.25°E	64.40°S, 119.92°E
3	3 Oct 04:30	5 Oct 07:30	64.96°S, 121.03°E	64.89°S, 120.88°E
4	7 Oct 10:00	9 Oct 01:30	65.14°S, 121.09°E	65.14 °S, 120.63°E
5	12 Oct 10:30	12 Oct 23:00	65.29°S, 119.93°E	65.26 °S, 120.01°E
6	13 Oct 01:00	14 Oct 09:00	65.26°S, 120.01°E	65.26 °S, 120.09°E
7	20 Oct 01:00	23 Oct 22:00	65.26°S, 118.99°E	65.13 °S, 118.29°E
8	29 Oct 01:00	4 Nov 08:00	64.82°S, 116.75°E	64.68 °S, 115.69°E

2.2 Atmospheric Measurements

2.2.1 Meteorological and Underway Ship Data

The Aurora Australis has a number of fixed sensors attached to the vessel that continuously collect snapshot data on the marine, atmospheric and navigational conditions on average every 10 seconds. These data are known collectively as the

Underway dataset. A full list of parameters recorded as part of this dataset can be found in Reeve (2013), however those relevant to this thesis are included in Table 2.2. Instruments were deployed at various locations on the ship, depending on the parameter being measured. Wind anemometers were located on two separate masts (port and starboard) located fore of the ship exhaust protruding above the Monkey Deck at a height of approximately 30 m above sea level (depending on ship draft). The two masts ensured that accurate measurements were being taken when one of the instruments was being wind shadowed by the supporting structure. Identification of wind shadowing was performed by examining periods where the two datasets differed, and discarding the one with higher fluctuations that were indicative of small-scale eddies that occur in the lee of structures. Other meteorological parameters, such as air temperature and humidity were measured on the Monkey Deck, approximately 18.5 m above sea level. Marine data were recorded on water samples taken from an uncontaminated seawater intake located on the port aft of the ship's keel.

Measurements of fluorescence are an important proxy for the biological activity occurring in the marine environment, and thus the flux of organic biological products to the atmosphere such as dimethyl sulfide and isoprene. Fluorescence is directly related to the chlorophyll concentration and was measured continuously throughout the voyage with an on-board fluorometer as part of the Underway dataset. For effective use of the data and to enable comparison to other studies, fluorescence data was calibrated with High Pressure Liquid Chromatography (HPLC) chlorophyll data. Seawater samples were collected within the top 15 m of the water column. From these, sub-samples were collected by filtration of 2 L of seawater under low vacuum (< 50 kPa) onto 13 mm diameter GF/F filters (Whatman, Gottingen Germany) in low light conditions. The filters were frozen immediately using liquid nitrogen for later analysis at the Australian Antarctic Division, Kingston, Tasmania. Chlorophyll pigment extractions and analyses followed procedures of Mock and Hoch (2005), with modifications described by Wright et al. (2010). Calibration of fluorescence data was performed by Robert Johnson (Institute for Marine and Antarctic Studies, University of Tasmania, Hobart, Tasmania, Australia) as part of the Underway data analysis.

An extra 2D anemometer (Model 5305-AQ, R.M. Young, Traverse City, United States, provided by US Geological Survey) was installed alongside the inlet (see Figure 2.8) for Gaseous Elemental Mercury measurements (see 2.2.4) to allow for more accurate wind statistics for filtering of instruments located on the Monkey Deck. The anemometer was oriented with zero degrees taken as the fore of the ship. Mean wind speed and direction were recorded every 5 minutes using a data-logger (Model CR1000, Campbell Scientific, Logan, United States). Due to wind shadowing

Table 2.2: List of Underway data streams relevant to this thesis. A full list is included in the Appendices. All sensor heights are approximate, dependent on ship draft, and are given as values Above Sea Level (ASL).

Underway parameter	**Data category**	**Sensor location**
Time stamp	Navigational	N/A
Latitude (degrees)	Navigational	N/A
Longitude (degrees)	Navigational	N/A
Solar Radiation ($W.m^2$)	Meteorological	Mast, port and starboard (30 m ASL)
Accumulated Precipitation (mm)	Meteorological	Mast (30 m ASL)
Relative Humidity (%)	Meteorological	Mast, port and starboard (30 m ASL)
Air Temperature (°C)	Meteorological	Mast, port and starboard (30 m ASL)
Wind direction (degrees). Includes both raw and corrected for ship heading.	Meteorological	Mast, port and starboard (30 m ASL)
Wind speed (knots). Includes both raw and corrected for ship speed.	Meteorological	Mast, port and starboard (30 m ASL)
Salinity (PSU)	Marine	Port seawater intake
Sea Surface Temperature (°C)	Marine	Port seawater intake
Fluorescence (arbitrary units)	Marine	Port seawater intake
Ship heading (degrees)	Navigational	From GPS and gyroscope
Ship pitch (degrees)	Navigational	N/A
Ship roll (degrees)	Navigational	N/A
Ship speed over ground (knots)	Navigational	N/A

effects from the ship, wind directions from the stern of the ship led to erratic wind directions and speeds. These periods were coincident with measurements of ship plume so were able to be identified by their variance and filtered from the dataset. Comparison to the ship anemometers, where the effects of ship wind shadowing are minimised due to their height and position away from other structures, was also helpful in identifying and filtering these periods.

2.2.2 *In-situ* Aerosol Measurements

Measurements of *in-situ* aerosols were made using two Condensation Particle Counters (CPCs) measuring number concentration at two different size ranges: aerosols with diameters larger than 3 nm (CN_3, Model 3025A, TSI, Shoreview, MN, USA); and aerosols with diameters larger than 10 nm (CN_{10}, Model 3772, TSI, Shoreview, MN, USA). Measurements were made continuously from the same sample stream allowing calculation of the number of particles in the 3-10 nm size range (CN_{3-10}), a range representing new particles formed via gas-to-particle formation. Air was sampled from a 3 m high mast, shown in Figure 2.7, located on the starboard side of the forecastle (~9 m above sea level). Air was pulled continuously at a high flow rate of approximately 130 L.min^{-1} (to minimise loss via diffusion) through 17 m of 50 mm diameter antistatic (copper coil) polyurethane tubing and 2 m of 50 mm stainless steel pipe (for connection and extensions). A 1 m length of $\frac{1}{4}$" stainless steel tubing, oriented to minimize turns and thus aerosol loss via impaction, sampled from the primary flow and linked the outdoor sample line to the CPCs located inside an insulated shipping container laboratory. Approximately 1.7 m of flexible conductive tubing extended to a Y-piece which directed flow into each CPC. Additional downstream pumps were also used to boost sample flow through instruments, and to help to exhaust butanol through the waste air-stream.

The 3 m custom inlet (Figure 5) was designed for sea ice conditions - hosting an uncovered, downward facing opening protected from falling rain and snow, but containing no wave-protection thereby making it unsuitable for open ocean conditions. Consequently, aerosol measurements only began when ocean swell reduced in the sea ice zone on the 23 September, 2012 (finishing on the 24 October while still in the pack ice due to instrument malfunction and exhaustion of the butanol supply). The location of the inlet on the ship meant that wind directions between 150° - 270° (relative to the fore of the ship) were often contaminated with ship exhaust.

Quality control, data filtering and processing and inlet characterisations was an involved process for these instruments, primarily due to extreme laboratory conditions leading to instrument malfunction and long inlet lines causing sample loss that needed quantification. These processes are elaborated on in Section 2.3.

This dataset was obtained by a collaborative effort of co-investigators including myself, R. Schofield (University of Melbourne, Melbourne, Australia), and Melita Keywood and Jason Ward (CSIRO Marine and Atmospheric Research, Aspendale, Australia). The dataset is publically available at Humphries et al. (2014).

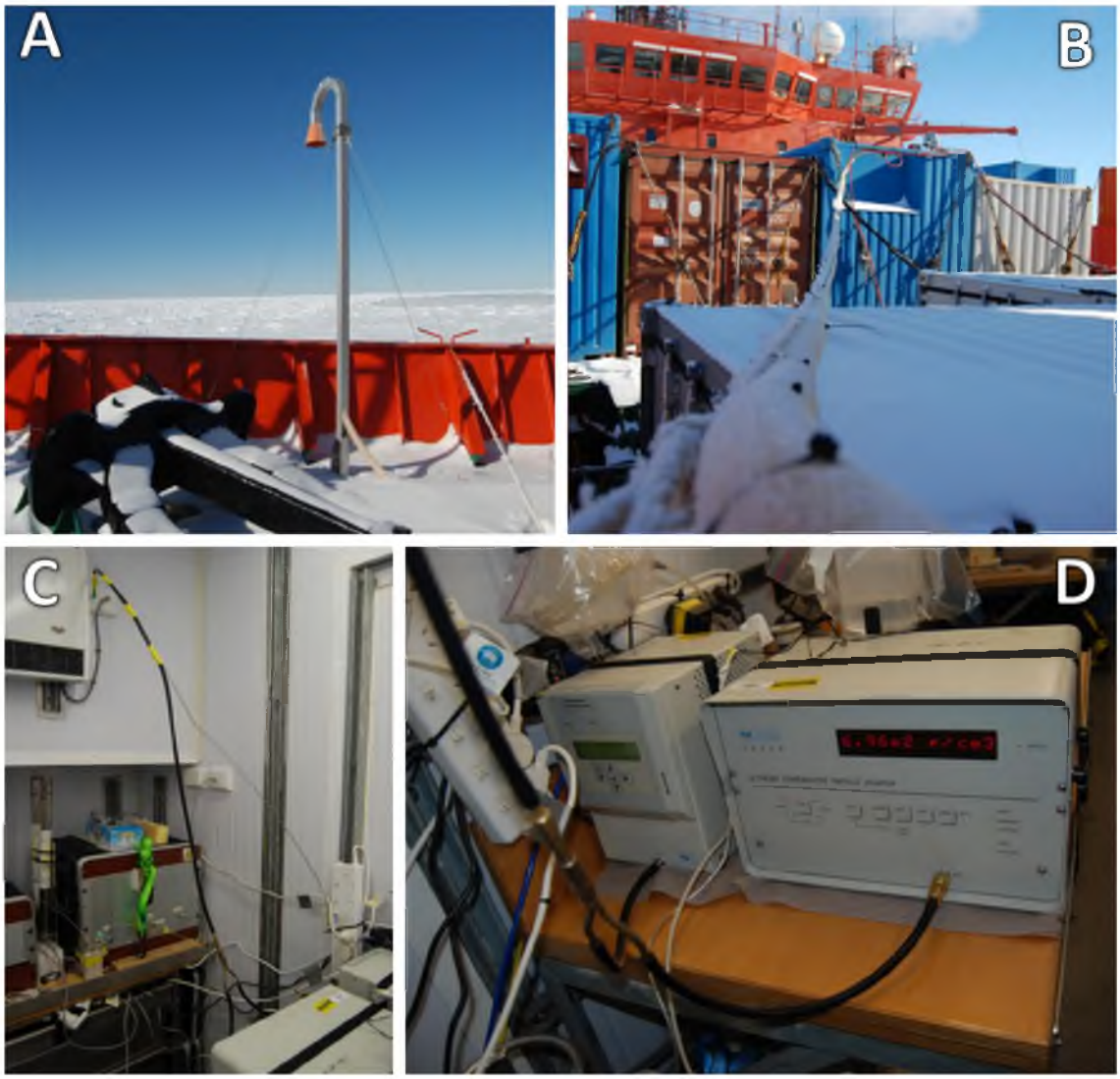

Figure 2.7: Aerosol inlet, sample line and instrumentation used on SIPEXII. **A**: The sample inlet was 3 m high on the starboard of the forecastle, as close to the edge as possible in order to reduce local contamination sources. **B**: Sample air was drawn through the 19 m of 50 mm diameter tubing at 130 L.min^{-1}. Bends in the sample line were kept to a minimum and sample flow rate kept high to minimise loss of large particles to impaction and small particles to diffusion, respectively. Air was sampled to the CPCs, inside the blue shipping container, off the primary flow which remained outside and led to the main pump. **C**: The 1/4" stainless steel tubing that sampled from the primary flow protruded through the container wall from which conductive tubing was connected. The bend radius of the conductive tubing was again kept to a minimum using guide-wire. **D**: The two CPCs (left: Model 3772; right: Model 3025) sampling from the same line after splitting with a copper Y-piece.

2.2.3 Ozone

Ozone (O_3) measurements were made continuously during all legs of the marine voyage, from September 14 to November 5, 2012. Ozone concentration (ppbv) was measured at a 1 minute time resolution using a commercial dual cell ultraviolet ozone analyser (Model 49C, Thermo Electron Corporation, Waltham, United States) on air sampled from the fore, port side railing of the Monkey Deck (Figure 2.2B). The sample inlet consisted of 30 m of 1/4" Teflon tube combined with an inline particle filter. Ozone loss through the inlet and filter was quantified and deemed to be negligible (Schofield et al., 2014d). Both before and after the voyage, calibration of the ozone monitor was performed to a traceable ozone standard (Schofield et al., 2014d). Each week during the voyage, a 30 minute instrument zero was performed by inserting an inline ozone scrubber that catalyses ozone destruction.

Ship exhaust contains high concentrations of NO_x which readily titrates ozone from the air. Since measurements aimed to characterise background values, rather than ship exhaust, it was necessary to filter raw ozone data for this influence. Data filtering was performed using wind statistics taken from a 2D anemometer located adjacent to the ozone inlet. The relative position of the sample inlet and the ship's exhaust meant that wind directions between 60° and 190° (taking the fore of the ship as 0°) were removed from the dataset. Data corresponding to wind speeds below 5 knots were also removed due to inhomogeneous air mixing at these speeds. Raw ozone values, as well as gaseous elemental mercury values (below), helped to validate the chosen parameters for the wind statistics mask. The parameters for this filtering were chosen by myself, A. Klekociuk (Australian Antarctic Division, Hobart, Australia) and I. Galbally (CSIRO Marine and Atmospheric Research, Aspendale, Australia).

This dataset was obtained as part of a collaborative effort involving myself, R. Schofield (University of Melbourne, Melbourne, Australia), I. Galbally and S. Molloy (CSIRO Marine and Atmospheric Research, Aspendale, Australia), and A. Klekociuk (Australian Antarctic Division, Hobart, Australia). Quantification of ozone loss and calibration was performed by I. Galbally and S. Molloy on-site at CSIRO Marine and Atmospheric Research, Aspendale, and details are therefore not included here. Data is publically available at Schofield et al. (2014d).

2.2.4 Total Gaseous Mercury (TGM)

Instrumentation commonly utilised for measurement of gaseous mercury species cannot distinguish between gaseous elemental mercury (GEM, Hg^0) and reactive gaseous mercury (Hg(II) compounds). Consequently, measurements are often reported as Total Gaseous Mercury (TGM), which is the addition of both GEM and

Hg(II) compounds. In most background air, TGM is composed primarily of GEM, and therefore these measurements are also often reported as GEM.

Measurements of TGM from boundary layer air during SIPEXII were made at 5 minute intervals continuously throughout the voyage between 14 Sept and 15 Nov, 2012. Air was sampled from a weather protected inlet positioned ~3 m off the front port side of the Monkey Deck, directly above the bridge (Figure 2.8). The inlet consisted of an inline filter to remove particulates, especially from ship exhaust, housed in a large (~30 cm diameter) stainless steel can to protect against rain, snow, sea spray and major impacts from nearby crane activity. Sample air was drawn through 35 m of heated Teflon sample tubing into the heated Met-Lab, where the Tekran 2537 mercury analyser (Tekran Instruments Corporation, Toronto, Canada) was located. Argon (Ar, 99.999% purity) was fed into the MetLab from separate gas cylinder storage (on the Monkey Deck), via $\frac{1}{4}$" Teflon tubing.

The Tekran analyser collected TGM on two parallel gold traps. During collection on one gold trap, TGM on the parallel trap was being thermally desorbed and detected by a cold vapour atomic fluorescence spectrometer. Calibration was performed every 24-48 hours using an internal Hg source. The internal calibration source was calibrated with an external mercury vapour standard prior to, and upon return to, the supplying laboratory (US Geological Survey).

This dataset had to be filtered to remove periods of instrument malfunction (i.e. faulty photodiode, lamp voltage adjustments and leaks in Argon line) and when wind directions caused sampling of ship exhaust, resulting in anthropogenic peaks in GEM concentration.

This dataset was obtained by a collaborative effort of co-investigators including R. Schofield, C. Gionfriddo and J. Moreau (University of Melbourne, Melbourne, Australia) and D. Krabbenhoft and M. Tate (US Geological Survey, Wisconsin, United States). Data quality control and filtering was performed by project collaborators and as such, details of this process are not included in this thesis. The publically available dataset can be found at Schofield et al. (2014a).

2.2.5 Halocarbons

Six *in-situ* halocarbons, including CH_3I, C_2Cl_4, CH_3CCl_3, $CHCl_3$, CH_2Br_2 (10-30% of identified CH_2Br_2 was $CHBrCl_2$ (Robinson et al., 2014)) and $CHBr_3$ were measured continuously throughout the voyage between 14 Sept and 15 Nov, 2012. The instrument (Gostlow et al., 2010), a Gas Chromatograph Electron Capture Detector (GC-ECD, μDirac, University of Cambridge, Cambridge, United Kingdom), was fed (1 L.min^{-1}) sample air from an inlet located inside the weather and impact protected inlet (Figure 2.8) on the Monkey Deck, alongside the GEM inlet (Figure

2.2B). Glass wool, serving as an inline filter, was inserted in the end of 60 m (2×30 m with 1 join) of 1/4" Teflon sample line that ran down to the instrument located in a modified shipping container on the foredeck. Carrier gases, He (99.995% purity) and N_2 (99.998% purity) for the GC-ECD were fed into the instrument container from an adjacent gas storage container via a ∼6 m length of 1/16" stainless steel tubing. Calibration air was drawn from a cylinder of dry air collected at Niwot Ridge (Colorado, USA) at an elevation of 3.5 km above sea level and enriched as needed with known concentrations of target compounds. The cylinder was supplied by the Earth System Research Laboratory (ESRL) within the National Oceanic and Atmospheric Administration (NOAA) so that the reported mixing ratios are linked directly to the NOAA halocarbon calibration scales. The cylinder was kept within the instrument container as this did not present a safety risk. Blanks and calibration chromatograms were run periodically after every 4 sample chromatograms, resulting in approximately 20 sample chromatograms each day.

The GC-ECD was designed as a robust, autonomous instrument for halocarbon measurements. Sample air was passed through a 20 mL absorbent tube, mounted across a 6 port, 2 position Valco valve, that quantitatively trapped compounds of interest. The absorbent bed was purged with He gas to remove oxygen before the sample was injected into the He carrier flow of the separation column via thermal desorption at 180°C. The separation column was first heated isothermally at 35°C for 5 minutes before heating at $8°C.min^{-1}$ to 145°C, resulting in separation of target compounds according to boiling point. The full chromatogram took ∼30 minutes to complete, after which the column was cooled back to 35°C ready for the next sample. Three types of chromatograms were run continuously throughout measurements in the following cycle: 4 samples, 1 blank, 1 calibration, 1 blank, then repeat. Due to undesirably cold laboratory conditions, column temperatures had to be increased to allow elution of higher boiling point products.

Processing of chromatograms, filtering for ship exhaust sampling, and quality control procedures (e.g. removal of unacceptably high baseline values due to power issues) was performed by colleagues at Cambridge University and details thereof are not included here. However details of the data processing followed those described by Gostlow et al. (2010). Measurements and logistics for this dataset were a collaborative effort between myself, R. Schofield (University of Melbourne, Melbourne, Australia), P. Johnston, K. Kreher and A. Thomas (National Institute of Water and Atmospheric Research, New Zealand) and N. Harris and A. Robinson (Cambridge University, United Kingdom). This dataset is publically available and can be found at Schofield et al. (2014b).

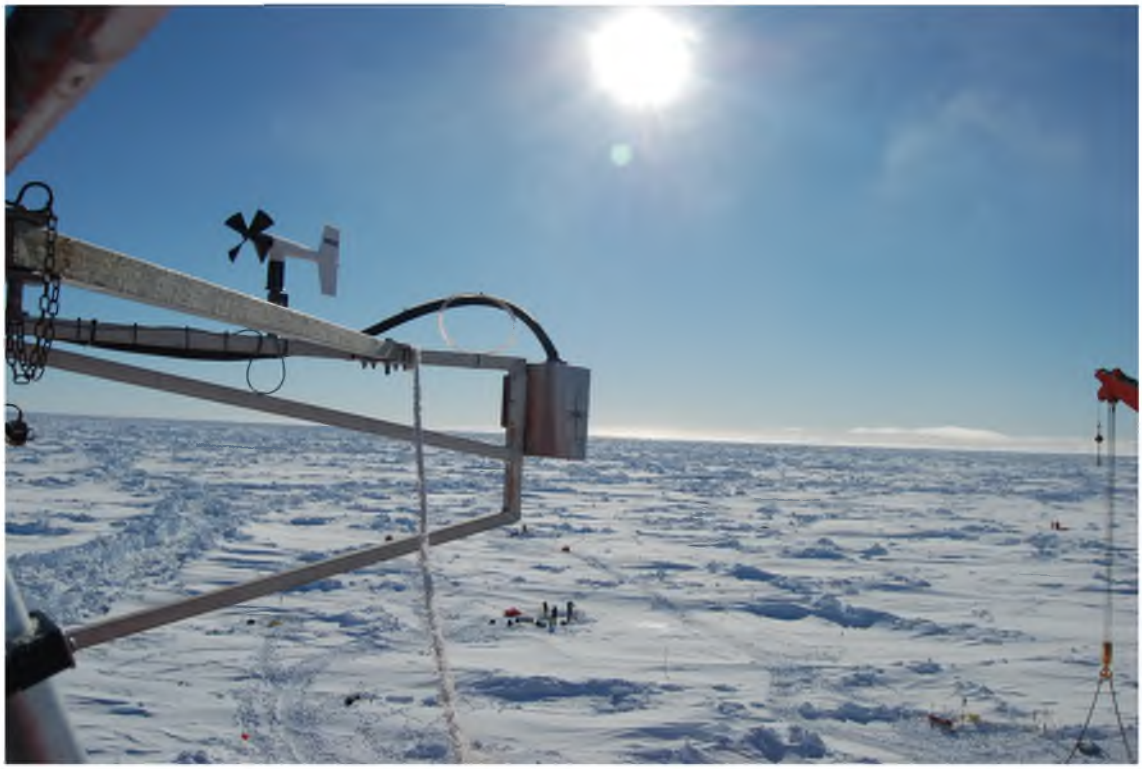

Figure 2.8: The sampling inlet (nicknamed "Ned Kelly") containing the sampling inlets for Gaseous Elemental Mercury measurements and halocarbon measurements using the GC-ECD. The inlet was suspended approximately 3 m off the Monkey Deck railing (seen in the left of the figure) on a retractable arm to allow for ease of maintenance. The 2D anemometer was fixed to the same arm.

2.2.6 Dimethyl Sulfide

Grab samples of Dimethyl Sulfide (DMS) were taken during the second half of the voyage, starting on the 18 Oct and continuing until the 31 October. On average, 3 grab samples were obtained daily at around 2300, 0400 and 0900 (UTC, after breakfast, lunch and dinner local time). Grab samples were taken by opening previously evacuated (0.01 - 0.07 mbar) glass flasks (1.350 L and 1.910 L) in the atmosphere to be sampled. An example of the sampling location is show in Figure 2.9. Samples were taken from the bow of the ship, as high as possible, and at a position intended to avoid sampling ship air.

Samples were analysed immediately after collection on-board using a Gas Chromatograph (GC, Model 450-GC, Varian, Middelburg, The Netherlands) equipped with a pulsed flame photometer (PFPD) and a purge and trap system. He (99.995% purity) was used as the carrier gas, with hydrogen and synthetic air as burning gas in the detector. These measurements were not prearranged but rather opportunistic based on available instrumentation and expertise (E. Damm, Alfred-Wegener-Institut, Bremerhaven, Germany). The GC used is not the common instrument for

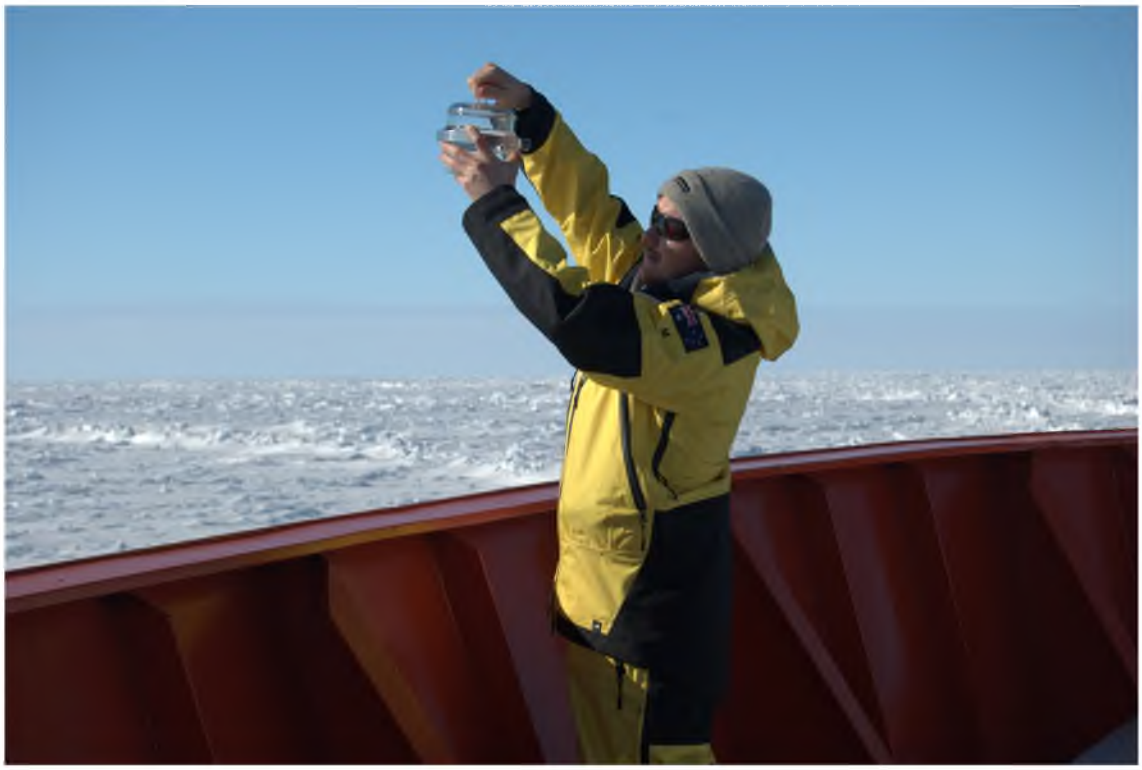

Figure 2.9: Flask sampling for DMS analysis was performed by manually opening evacuated flasks at the bow of the ship when wind directions avoided ship contamination.

atmospheric DMS measurements, but rather was designed for analysis of DMS concentrations in seawater samples (up to 0.5 nM). Consequently, atmospheric samples needed pre-concentration with longer purging time (and thus volume). Sample flasks were purged for up to 45 minutes with helium in a cryotrap (using liquid nitrogen) to pre-concentrate eluents. The sample loop was then moved from the liquid nitrogen dewar to a warm water bath for injecting into the GC to retrieve chromatograms that were converted to atmospherically relevant mixing ratios (pptv).

Although these DMS measurements were not a planned part of the voyage, results provided an a priori for aerosol modelling. Unfortunately due to the unsuitability of the instrument for atmospheric samples, results of these measurements were unsuitable for more comprehensive use. E. Damm (Alfred Wegener Institute, Bremerhaven, Germany) performed the data processing and analysis.

2.2.7 Spectroscopic Measurements of Aerosols and Reactive Gases using MAX-DOAS

Profiles of the boundary layer trace-gases were measured using Multi-AXis Differential Optical Absorption Spectrometry (MAX-DOAS). The MAX-DOAS collects spectra of scattered sunlight at different elevation angles above azimuth and uses

the Beer-Lambert law, combined with inverse modelling, to retrieve trace-gas concentration profiles. The retrieved trace-gases depend on the chosen wavelength measurement window (e.g. ultra-violet or visible window) and whether particular species have molecular absorption bands in that region.

The instrument used on the voyage was designed and built in-house at the National Institute of Water and Atmospheric Research (NIWA, Lauder, New Zealand). The instrument consisted of a Czerny-Turner type ISA HR320 (Horiba Scientific, Kyoto, Japan) flat-field spectrograph with a focal length of 320 mm and an aperture ratio of F/4. The array detector was an Hamamatsu C7042 detector head with S7032–1007 sensor chip (Hamamatsu Photonics, Hamamatsu, Japan). The back-thinned chip allows light to enter from the rear of the silicon substrate, substantially increasing the quantum efficiency over the full spectral range, particularly in the UV region (<400 nm), which is important for good signal-to-noise ratio for the focus species, BrO. To reduce dark current noise associated with thermally excited electrons, the detector was cooled to 253 K using a Peltier cooler. Detector signals were passed to computer via a 16-bit analogue-to-digital converter card. Entrance optics consisted of an angled telescope mirror that reflects the measured light through a focussing lens onto the entrance of a quartz fibre optical bundle leading into the spectrograph. The field of view of the telescope is approximately 0.5°.

The spectrometer was setup to scan two wavelength regions in the ultraviolet-visible (UV-Vis) region with a variable resolution spread over the pixel array CCD. The two regions were: 323-348 nm in the UV, retrieving NO_2, O_3 (two fitting regions), O_4, BrO and HCHO; and 416-443 nm in the visible, retrieving NO_2, H_2O, O_4 and IO.

Spectra were measured at multiple viewing angles: 1, 2, 3, 4, 6, 8, 15, 30 and 90° in the open water and first week of sea ice (14 Sept - 5 Oct, and 12 - 15 Nov) and -5, 1, 2, 4, 6, 8, 15, 30 and 90° in the ice (5th October – 12 Nov) above the horizon. The -5° viewing angle was added to test a recently described method for the retrieval of gas concentrations in the snowpack (Frieß et al., 2010), however analysis of this data is out of the scope of this thesis. Viewing angles were maintained throughout the voyage using the in-built stepper motor that actively corrected for the ship's roll using an accelerometer mounted to the ship's superstructure. The 90° data was used as the reference viewing angle during data processing. Due to the spectroscopic nature of this technique, data was filtered when reference spectra contained high amounts of NO_2 (a signature of ship exhaust). The entrance optics were also cleaned daily with lint-free paper towel.

Obtaining this dataset was a collaborative effort. Measurements and logistics were undertaken by almost all co-investigators including R. Schofield (University of

Melbourne, Melbourne, Australia), K. Kreher[a], P. Johnston and A. Thomas (National Institute of Water and Atmospheric Research, Lauder, New Zealand) and myself. Quality control and processing of spectra into Differential Slant Column Densities was performed by P. Johnston, while inverse modelling to retrieve vertical profiles was performed by T. Hay (previously at NIWA, Lauder, New Zealand). A significant gap (~2 weeks) in data occurred during the voyage due to hard-drive failure in the controlling computer. This issue was fixed on board at which point measurements resumed. The dataset is publically available and can be found at Schofield et al. (2014c).

2.3 Aerosol Data Analysis

2.3.1 CPC Calibration and Filtering

In-situ aerosol number concentrations from the two CPCs were calibrated for two factors: instrument flow rate (Section 2.3.1.1) using independent inlet flows measured throughout the cruise; and aerosol inlet transmission efficiencies (Section 2.3.1.2). Data were then filtered for physical events noted in the log (e.g. flow calibrations), before the data was resampled in the time dimension from second to minute resolution. This resampling involved calculating minute concentration means (assuming data is normally distributed), and propagating uncertainties. Aerosol data is then aligned with meteorological and ship data, ready for filtering for removal of pollution events from ship and scientific operations.

Relative wind directions between 150° and 270° (assuming 0° is the fore of the ship) were used to identify data where ship exhaust plume was being measured directly. Polluted data were further identified using statistics from the time resampling (standard deviations, minimum counts, maximum concentrations and maximum uncertainties). Data which was within 3 minutes of identified polluted events were filtered to allow for clearing of sample lines and differences between locations of instrument inlets and meteorological stations. Obvious outliers still remaining in the data were then filtered if they lay outside ten standard deviations from the previous 15 minute smoothed measurements.

Sampling of recirculated ship exhaust was also a potential source of contamination to the dataset. Recirculated ship exhaust can be defined as that which didn't directly go from the ship stack to the measurement inlet, but which still has influence from the chemistry which it had undergone. Ship exhaust contains high concentrations of oxides of nitrogen (NO_x) which quickly titrates O_3 from the air-mass, resulting in O_3 concentrations close to zero which slowly recover over a

[a]now at Bodeker Scientific, Alexandra, New Zealand

number of hours (Chen et al., 2005). Ozone data, already filtered for direct influence, was analysed for any significant deviations below background values, none of which were found. After filtering for recirculation and direct influence, the resulting dataset could be said to represent the clean, background atmosphere.

2.3.1.1 Flow calibration

For the CPCs to report aerosol concentrations, the raw signal counts per second are converted to counts per volume through knowledge of the instrument flow rate. Any changes in flow rate then, directly affect reported concentrations. Both instruments used a fixed capillary that could not be altered, so inlet flow was measured periodically for post-measurement calibration. It was found that the flow rates of both instruments increased throughout the campaign, likely due to changing efficiencies of common pumps downstream of the instruments. The time dependent calibration factor was determined by a linear regression to measured flow rates and the root mean square (RMS) error of this fit was used as the uncertainty of the calculation. The calibration factors were applied to each instrument via the following equation:

$$[CPC]_{flowCal}(t) = [CPC]_{raw}(t) \times \frac{Flow_{desired}}{Flow_{meas}(t)} \tag{2.1}$$

where t is time, $[CPC]_{flowCal}(t)$ is the flow calibrated aerosol concentration (cm^{-3}), $[CPC]_{raw}(t)$ is the uncalibrated aerosol concentration, $Flow_{desired}$ is the prescribed flow for each instrument, and $Flow_{meas}(t)$ is the time varying measured flow rate. Table 2.3 summarises the data used for flow calibration and resulting uncertainties.

Table 2.3: Flow rates measured for each CPC along with root mean square deviation (RMSD) from linear regression.

	CPC3772 ($Flow_{desired} = 1.0\ cm^3.min^{-1}$)	**CPC3025** ($Flow_{desired} = 1.5\ cm^3.min^{-1}$)
Day number	$Flow_{meas}\ (cm^3.min^{-1})$	
267	0.9304	1.610
274	0.9330	1.667
276	0.9437	1.697
298	0.9629	1.810
RMSD	0.0031	0.013

2.3.1.2 Characterisation of Inlet Transmission Efficiencies

The inlet used for aerosol sampling was experimentally characterised for transmission efficiencies (i.e. sample loss) for ambient aerosols ranging between 4 nm and 20 μm. Due to available resources, absolute transmission efficiencies were unable to

be determined experimentally. Instead, transmission efficiency was approximated relative to a standard laboratory inlet (described below). The two inlets were setup adjacent to one another and connected to a common inlet and instrumentation. Two ball valves provided switching of inlets every 10 minutes to allow for pseudo-continuous measurements of ambient air for comparison. This time resolution was suitable to capture changing atmospheric conditions, provided measurements of a range of aerosol conditions, and also allowed sufficient time for line clearing and instrument stabilisation between inlet switches.

An overview of the design of the characterisation experiment, setup at CSIRO laboratories in Aspendale, Australia, is shown in Figure 2.10. The reference laboratory inlet was setup to minimise sample losses in order to better approximate an absolute transmission efficiency. The length, number and degree of bends of the reference inlet was minimised to achieve this, using only about 1 m total length of $\frac{3}{8}$" metallic tubing with a 10 cm bend radius at the inlet entrance for weather protection. The campaign inlet was setup to emulate as close as possible the geometry present on the ship, while also taking into account that the two inlets had to be adjacent to each other during characterisation. This meant the sample line had one extra bend in it than what was present in the experimental setup, but the degree of this bend was kept as low as possible to reduce wall loss. Due to the large volume of the campaign inlet, air was flushed through it continually using the same pump used on the voyage, and the instruments sampled from this flow. A common sample line was setup between ball valves and the instruments.

Efficiencies were determined by measurements of the aerosol size distribution of number concentrations using 3 instruments: two Scanning Mobility Particle Sizer Spectrometers (SMPS) which measured size distributions from 4-150 nm (NanoSMPS; CSIRO Marine and Atmospheric Research, Aspendale, VIC, Australia) and 14 – 600 nm (SMPS; TSI Incorporated, Shoreview, MN, United States), and an Aerosol Particle Sizer (APS; TSI Incorporated, Shoreview, MN, United States) measuring aerosol size distributions between 0.5 – 20 μm. These instruments gave a good idea of transmission efficiencies over a significant size range, including both new particles formed via gas-to-particle conversion, and older or mechanically formed particles in the large size range.

Analysis

Data was first categorised by sample inlet (reference or SIPEX inlet) and filtered for when neither inlet could be assigned (i.e. when both ball valves were open during transition). The mean particle number was calculated for each size bin for each 10 minute inlet period, resulting in one mean size distribution for each 10 minute period. The inlet efficiency (IE) was then calculated for each non-zero size bin across

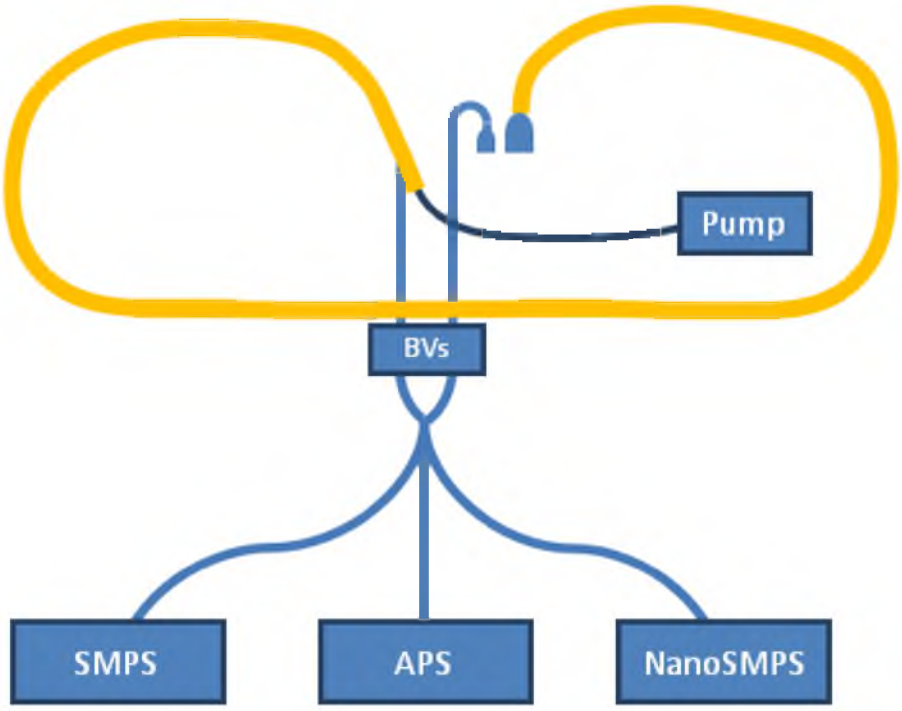

Figure 2.10: Experimental setup for characterisation of inlet efficiencies. Air was continuously flushed through a 50 mm diameter SIPEXII inlet (yellow) at a rate of ~130 L.min^{-1}. Air was sampled every alternate 10 minutes from this flow, with sampling from the reference inlet (blue) occurring in the alternate 10 minutes. Choice of inlet was controled by the ball valves (BVs) which connected the two inlets to a common inlets which fed into the 3 instruments (NanoSMPS, SMPS and APS, described above) that measured continuously for aerosol size distributions from 4 nm - 20 μm.

the entire time series such that

$$IE = \frac{SIPEX}{0.5(Ref_{before} + Ref_{after})}$$

The resulting time IE matrix was then analysed via a bootstrap sampling method to get the most likely value and the uncertainty. The bootstrap method involved taking a histogram of the sample data, fitting a Lorentzian function to the histogram, and taking the peak of the Lorentzian as the most likely value. The median and 2σ (based on median absolute deviation (MAD), such that standard deviation = 1.4826 MAD) of the resulting n sized array of bootstrap results was used as the IE and uncertainty respectively. The same bootstrap process was performed on each dimension of the IE matrix to determine if the IE changed with respect to both time and size.

The overall IE was calculated by the bootstrap method to be 0.88 ± 0.02 ($\mu \pm 2\sigma$). Figure 2.11 shows how the IE was stable with respect to time, and how the IE varied based on size and instrument.

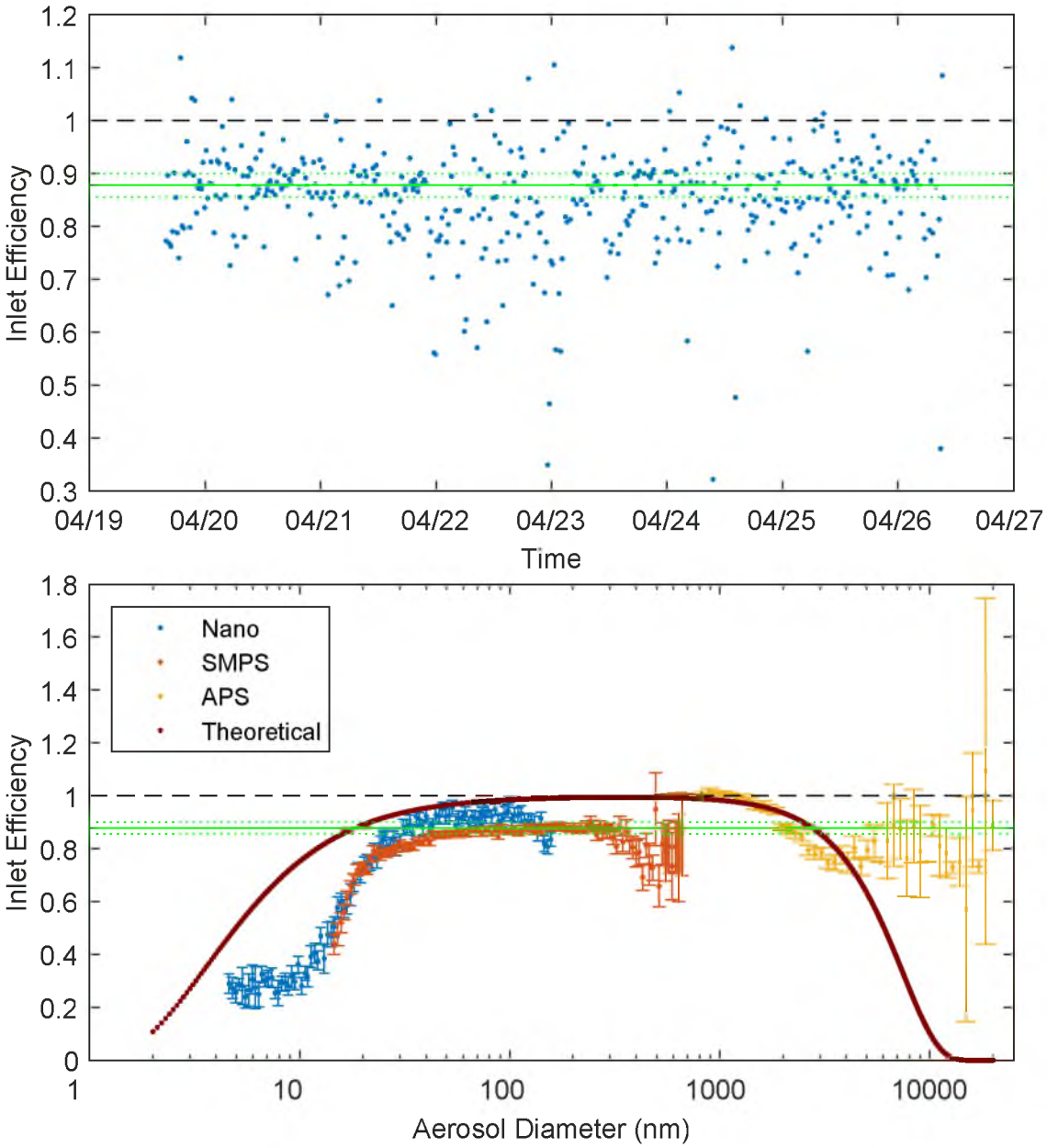

Figure 2.11: Top: Median Inlet Efficiencies (IE) of the size distributions plotted as a function of time period show the IE varies considerably, but remains within the 50% uncertainty. **Bottom**: Inlet Efficiencies (median) with respect to aerosol diameter (log scale) from the 3 different instruments used to cover the size range of 4 nm - 20 μm, together with theoretically calculated efficiencies (detailed below). The horizontal lines represent the overall IE with calculated 2 sigma error bars, with the black line a 100% efficiency reference line. The lower end trend is expected due to diffusion of smaller particles in the longer inlet line, resulting in loss of smaller particles to inlet walls. A similar effect is noted for the APS data (red), where the offset is due to efficiency differences in instruments, larger uncertainties are found at the higher sizes due to the small number of particles measured, and the descreasing trend in IE at the larger sizes due to losses caused by gravitational separation and inertial losses when sample air moves around a corner too tight for the given aerosol size.

Theoretical Absolute Inlet Efficiency

In addition to experimentally deriving an inlet efficiency relative to a standard reference inlet, the absolute inlet efficiency was calculated theoretically using the two aerosol loss calculators: the first described by Weiden, Drewnick, and Borrmann (2009), while the second was written by Baron, P.A. and is available online (http://aerosols.wustl.edu/AAARworkshop08/software/AEROCALC-11-3-03.xls). Both calculators gave similar results. These tools utilise relevant empirical and theoretical relationships found in the literature, and account for the most important sampling and transport effects encountered during typical sampling inlets such as those used in this study. The calculation involves breaking the inlet up into various segments, and describing each segment in terms of its flow rate, length and diameter and angles of inclination and curvature. The breakdown of the SIPEXII inlet, together with the parameters used for each calculation are outlined in Figure 2.12. The calculation was made across the size range of 2 nm to 10 μm (above which the transmission of particles becomes negligible).

It is important to note that the type of flow regime that exists within the inlet (i.e. turbulent, laminar, or transition), determines what calculations are utilised[b]. Currently, the transition regime does not have any reliable empirical or theoretical formulations associated with it that could be included in the calculation. Consequently, calculations that fall in the transition flow regime are assumed to be laminar flow to enable a final calculation.

Results from the calculation are presented in Figure 2.13. Inlet efficiencies between 10 nm and 1 μm are found to range between 0.75 - 1, similar to that calculated experimentally. Above around 2.5 μm, transmission falls off quickly, reaching about 0.1 at 10 μm. Given the low number concentrations of aerosols in this size range that would be expected in this environment, the higher inlet uncertainty in this micron size range would have negligible effects on this dataset.

Below 10 nm, calculated inlet efficiencies decrease quickly, changing approximately linearly from 0.15 and 0.75 for the size range from 2.5 and 10 nm, respectively. The effect of this on the current dataset could be significant, given number concentrations in this size range dominate much of the dataset. Since our size information is a single bin between 3 and 10 nm, it is best to approximate an inlet efficiency that can be applied to the whole size bin. To do this, information about the size distribution is required. Weber et al. (2001) measured free tropospheric size distributions of sub-micron aerosols in the Southern Ocean and found a peak in this size range at around 4.5 nm, which from our calculations would correspond to an

[b]Unfortunately, this problem of inlet flow regimes is a problem that faces many aerosol inlets, and using tools such as the Particle Loss Calculator in the design of an inlet can help improve these problems.

inlet efficiency of 0.45. Given the range of inlet efficiencies in this size range, the best estimate of inlet efficiency for this 3-10 nm size range is 0.45 ± 0.3.

Comparison of the theoretically calculated inlet efficiencies to those determined experimentally reveals that above 10 nm, experimental and theoretical results agree relatively well. Consequently, the experimentally derived transmission efficiency of 0.88 ± 0.02 was deemed suitable for this size range and was applied to the data. Inlet efficiencies for sizes below 10 nm were found to differ considerably between experimental and theoretical calculations. Given the uncertainty surrounding theoretical calculations (given the flow regime issue described above), as well as the high uncertainties associated with experimentally derived values in this size range, it was determined that neither of these values was preferable. Because of this, it was decided that the factor of $0.88^{+0.02}_{-0.5}$ (determined experimentally from the full size range) would be the best guess of inlet efficiency for this size range too, with the confidence intervals taking into account the increased uncertainty.

Because of the assumption, aerosol number concentrations in this thesis should be considered as a lower bound for actual number concentrations. If theoretical calculations are correct, then CN_{3-10} number concentrations could be up to 70% higher (depending on the size distribution in this range), which could result in an increase in CN_3 concentrations of approximately 50% (under the assumption of 70% of the population being in the CN_{3-10} size range, as was observed in this study and outlined in Chapter 3).

Section No.	Flow rate ($L.min^{-1}$)	Tube length (m)	Tube diameter (mm)	Angle of inclination[1] (°)	Angle of curvature[2] (°)
1	130	1	50	-	180
2	130	2.5	50	90	0
3	130	1	50	-	90
4	130	2	50	0	0
5	130	0.75	50	-	25
6	130	0.75	50	-	10
7	130	11	50	15	0
8	2.65	1	6.3	0	0
9	2.65	0.5	6.3	-	75
10	2.65	0.7	6.3	75	0
11	2.65	0.02	6.3	60	45
12	2.65	0.03	6.3	60	0
13	2.65	0.02	6.3	60	45
14	2.65	0.5	6.3	-	60

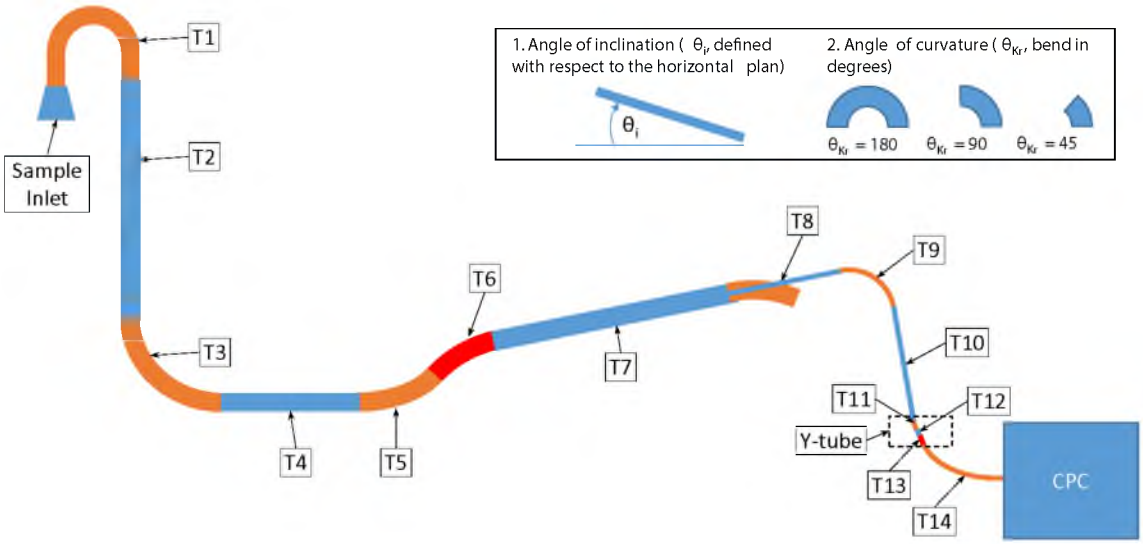

Figure 2.12: Breakdown of the aerosol inlet used for the calculation of the theoretical inlet losses. Colours are used to distinguish between sections and numbering refers to the table above which includes all the parameters required for the calculation. The included key visually explains some of the terms required for the calculation.

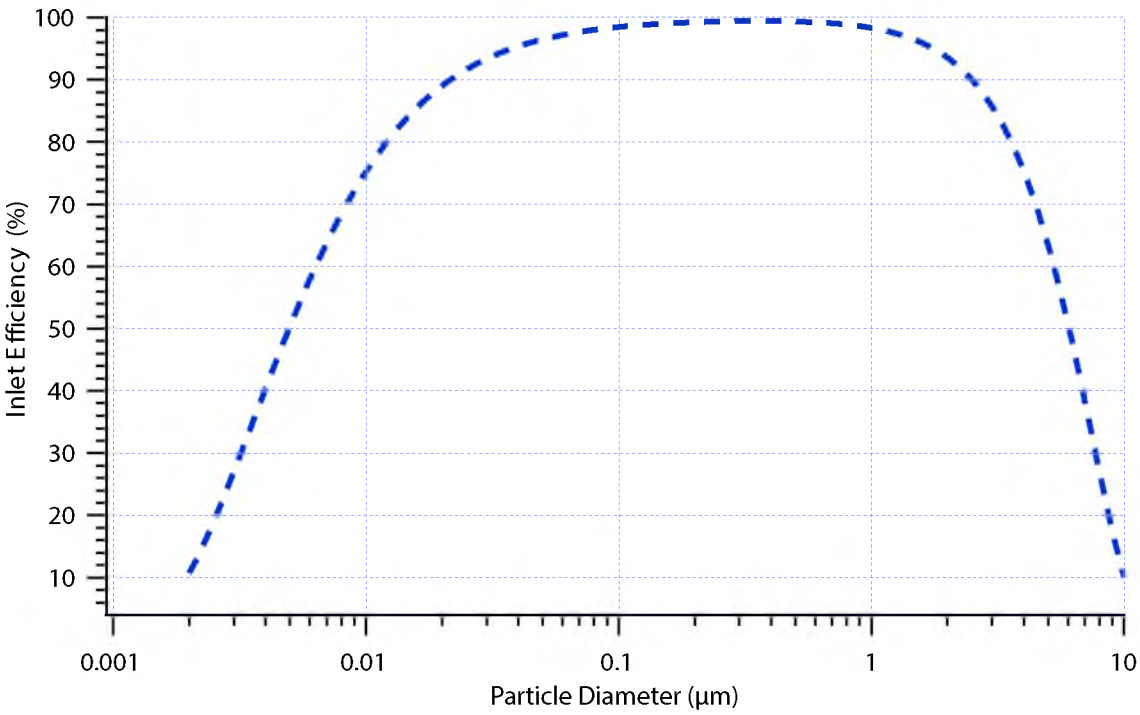

Figure 2.13: Theoretically calculated inlet efficiency (%) over the range of 2 nm to 10 μm performed with the calculator described by Weiden, Drewnick, and Borrmann (2009). Note that the flow conditions of this inlet are in the transition regime for which the calculation is not valid. Laminar flow is assumed in tube sections with this regime.

2.3.2 Calculating Nucleation Mode Particles

Nucleation mode particles are those with a diameter of 3-10 nm. Calculation of this was a simple subtraction of measurements of the number of particles above 10 nm (CN_{10}) from those above 3 nm (CN_3). This calculation is performed under the reasonable assumption that the counting efficiency of both CPCs is the same for particles larger than 10 nm diameter (Wiedensohlet et al., 1997).

2.3.3 Uncertainty Analysis

Raw data output from the instruments is given as a count of pulse signals recorded on the photodetectors. At low concentrations (<10 000 cm^{-3}), pulse signals are well defined (pulse width 3.3 μs) and the uncertainty associated with the output data is defined by simple counting statistics (TSI, 2002), such that:

$$\Delta CN_{raw} = \sqrt{CN_{raw}} \tag{2.2}$$

where ΔCN_{raw} is the statistical error of the raw total count data, CN_{raw}. Since all filtered data in this measurement set lies below 10 000 cm^{-3}, this simple definition of counting uncertainty is employed.

Further uncertainty is introduced at both flow and inlet calibration steps, as well as when data is resampled from second to minute time resolution. The uncertainty introduced at each calibration step is outlined in their respective detailed sections (2.3.1.1 and 2.3.1.2). It is reiterated here that because this study is looking primarily at the trends and relative changes, the absolute aerosol concentration is not emphasised, and therefore the inlet efficiency uncertainty is not included in the error propagation as this would dominate the uncertainty and would remove deciphering of relative trends. However, inclusion of this inlet uncertainty imposes only a lower bound on the reported concentrations, with significantly smaller lower bound uncertainties compared to upper bound. Excluding the inlet uncertainty, the relative error resulting from counting and calibration uncertainties is given by:

$$\frac{\Delta CN_{cal}}{CN_{cal}} = \sqrt{\left(\frac{\Delta CN_{raw}}{CN_{raw}}\right)^2 + \left(\frac{\Delta Flow_{meas}}{Flow_{meas}}\right)^2 + \left(\frac{\Delta Cal_{inlet}}{Cal_{inlet}}\right)^2}$$

where, ΔCN_{cal} is the uncertainty in calibrated concentrations, CN_{cal}. $\Delta Flow_{meas}$ is the root mean square deviation of the linear regression of the measured flow rates (equal to 0.0031 and 0.013 $cm^3.min^{-1}$ for CPC3772 and CPC3025, respectively) while $Flow_{meas}$ is the median of the linear regression for each minute (approximately 0.94 and 1.7 $cm^3.min^{-1}$ for each instrument respectively). Cal_{inlet} and ΔCal_{inlet} are the calibration factor and associated uncertainty obtained through inlet character-

isation experiments and is instrument independent, having values of 0.88 and 0.02, respectively.

The uncertainty introduced in the time resolution resampling is given as

$$\Delta CN_{min} = \frac{\sigma}{\sqrt{n}} \tag{2.3}$$

where ΔCN_{min} is the uncertainty of the mean minute concentration, σ is the minute standard deviation, and n is the number of measurements used to calculate each minute value (i.e. typically 60). The relative error is then

$$\frac{\Delta CN_{min}}{CN_{min}} = \frac{\sigma}{CN_{min}\sqrt{n}} \tag{2.4}$$

Combining the calibration and resampling errors, the relative error of the final concentration, CN, becomes

$$\begin{aligned}\frac{\Delta CN}{CN} &= \sqrt{\left(\frac{\Delta CN_{cal}}{CN_{cal}}\right)^2 + \left(\frac{\Delta CN_{min}}{CN_{min}}\right)^2} \\ &= \sqrt{\left(\frac{\Delta CN_{raw}}{CN_{raw}}\right)^2 + \left(\frac{\Delta Flow_{meas}}{Flow_{meas}}\right)^2 + \left(\frac{\Delta Cal_{inlet}}{Cal_{inlet}}\right)^2 + \left(\frac{\sigma}{CN_{min}\sqrt{n}}\right)^2}\end{aligned}$$

However, since the relative counting error simplifies to

$$\frac{\Delta CN_{raw}}{CN_{raw}} = \frac{1}{\sqrt{CN_{raw}}}$$

The absolute error of CN can be expressed as

$$\Delta CN = CN\sqrt{\frac{1}{CN_{raw}} + \left(\frac{\Delta Flow_{meas}}{Flow_{meas}}\right)^2 + \left(\frac{\Delta Cal_{inlet}}{Cal_{inlet}}\right)^2 + \left(\frac{\sigma}{CN_{min}\sqrt{n}}\right)^2}$$

The above error analysis was performed for each CPC separately. Calculation of nucleation mode particles (CN_{3-10}) was a simple subtraction calculation, resulting in an uncertainty of

$$\Delta CN_{3-10} = \sqrt{(\Delta CN_3)^2 + (\Delta CN_{10})^2} \tag{2.5}$$

Resulting uncertainties for each instrument are presented in Figure 2.14. Uncertainties for all final products were dominated by counting statistics and were generally below 10% for typical measured concentrations. It is important to note that because inlet loss calibrations were performed relative to a reference inlet, rather

than an absolute scale, values reported here are a lower bound of true atmospheric values.

Dataset	CN_3	CN_{10}	CN_{3-10}
Mean Uncertainty (%)	4.1	6.2	8.7
Standard Deviation of Uncertainty (%)	1.5	1.8	8.9
Median Uncertainty (%)	3.8	6.4	6.8
Median Absolute Deviation (%)	1.2	1.5	4.4
Maximum Uncertainty (%)	10.8	13.0	89.0

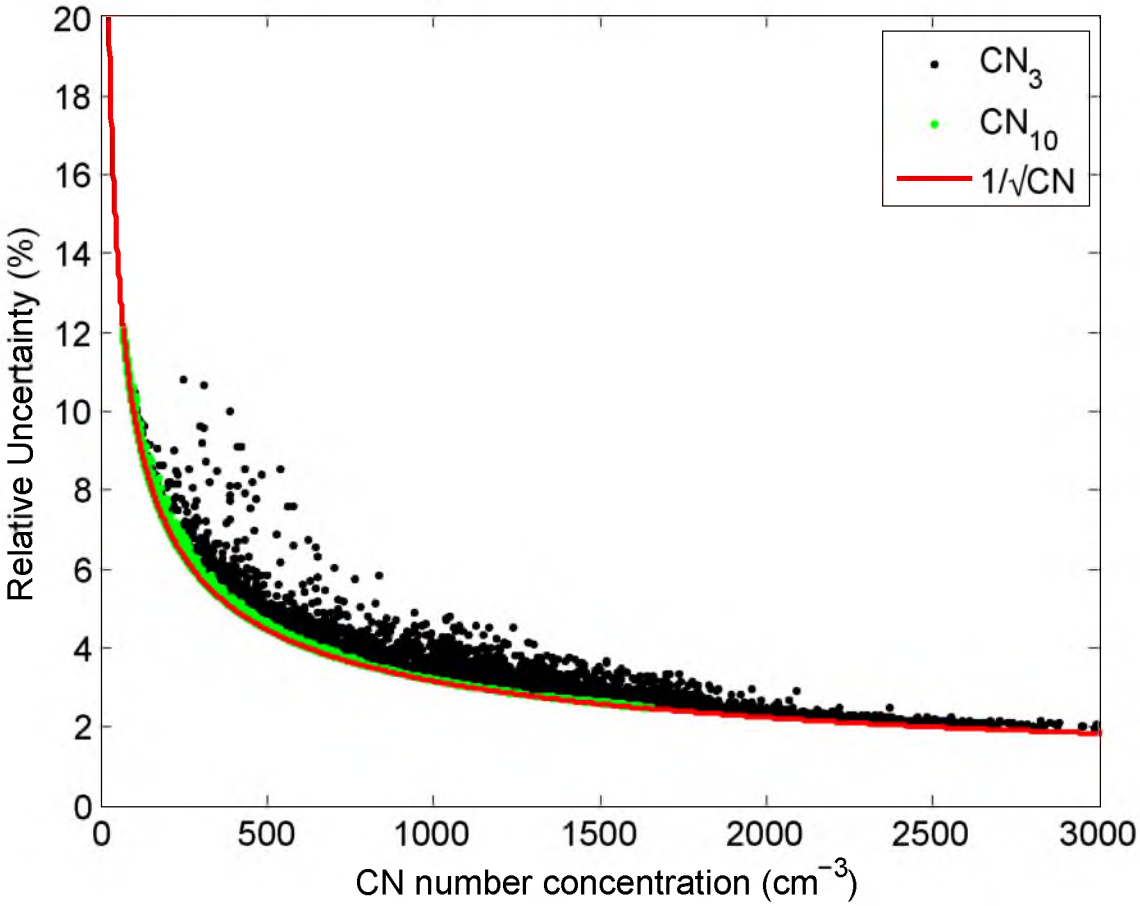

Figure 2.14: The relative uncertainty (%) of CPC measurements as a function of calibrated number concentration. The trend is driven primarily by counting statistics that vary inversely with the square root of concentration (shown in red). Statistics are given in the table above.

Chapter 3

Background Polar Cell Aerosols

Abstract

This chapter describes the unexpectedly high concentrations of sub-micron aerosols that were observed during the SIPEXII voyage in the sea ice off the coast of East Antarctica during the spring of 2012. Background CN_3 concentrations measured in the boundary layer were found to exhibit a 10-fold increase moving across the Polar Front, with mean Polar Cell concentrations of 1130 cm^{-3} - higher than observed anywhere else in the Antarctic and Southern Ocean region. Modelling studies (Chapter 4) suggest aerosol nuclei formed in the Antarctic free-troposphere are not a result of common sulfur chemistry. Aerosol growth information suggested these aerosols were not formed locally, and extensive trajectory analyses revealed a air-masses had been in the free troposphere only a few days prior to measurement, suggesting this as the source region. Sea ice boundary layer air-masses were also found to travel equator-ward, transporting young aerosol nuclei and nucleation precursors to the Southern Ocean, where nuclei grow by condensation, coagulation and cloud processing to climate relevant sizes. One of the most important findings of this work was the distinct difference of the sea ice atmosphere relative to adjacent continental or Southern Ocean air-masses. This previously unrecognised aerosol load could yield cloud condensation nuclei (CCN) currently missing in the Southern Ocean in climate models.

Publication and Author Contributions

This chapter is currently in the final stages of preparation for submission to Atmospheric Chemistry and Physics and the contributions of the various authors is as follows. Ruhi Humphries wrote the manuscript, led the overall data analysis and interpretation, ran the instruments during the field campaign and performed quality control on aerosol data. Andrew Klekociuk (Australian Antarctic Division, Australia) performed the trajectory modelling and validation, and together with

Simon Alexander (Australian Antarctic Division, Australia) and myself, interpreted trajectory data. Robyn Schofield (University of Melbourne, Australia) led AAS Project 4032, and was instrumental in the field campaign and data analysis. Melita Keywood and Jason Ward (CSIRO Ocean and Atmospheres Flagship, Australia) provided aerosol instrumentation and technical support. Ian Galbally and Suzie Molloy (CSIRO Ocean and Atmospheres Flagship, Australia) provided and installed the ozone monitor, and Ian Galbally, Andrew Klekociuk, and Ruhi Humphries did quality control for ozone. Paul Johnston, Karin Kreher and Alan Thomas (National Institute of Water and Atmospheres, New Zealand) built the MAX-DOAS instrument and processed the data. Matthew Woodhouse (CSIRO Marine and Atmospheres Flagship, Australia) ran the global model (Chapter 4). Andrew Robinson, Neil Harris (University of Cambridge, UK) and and Alan Thomas provided the GC-ECD instrument. Andrew Robinson and Neil Harris performed GC-ECD data quality control and running algorithms. Robin Schofield, Melita Keywood and Stephen Wilson provided academic support. All authors contributed to the editing of the manuscript.

3.1 Introduction

Reconciling the radiation budget over the Southern Ocean poses one of the greatest challenges for current climate models. Current state-of-the-art models, compared in the international Atmospheric Chemistry and Climate Model Intercomparison Project (ACCMIP), underpredict the AOD in the Southern Ocean (Shindell et al., 2013), suggesting a missing source of aerosols in the region. This missing aerosol affects our understanding of both aerosol radiation interactions (ARI) and aerosol cloud interactions (ACI), along with aerosol and cloud chemistry and properties, and consequently, how these processes are represented in models.

The hostile marine and sea ice environment of the Southern Ocean make measurements in this region difficult. The dearth of observations results in a poor understanding of environmental parameters, including aerosol and cloud properties. Current knowledge suggests that the aerosol loading of this pristine area is made up primarily of sea-salt and secondary inorganic aerosols. The spatially sparse aerosol studies in the Antarctic and Southern Ocean region have focussed primarily on these aerosols, and often miss the difficult-to-measure ultrafine aerosols, which are recently formed from gas-to-particle conversion and dwell in the size range of one to tens of nanometres. This size range is too small for effective interaction with radiation, making measurements using current generation remote sensing technologies such as satellites (which have the advantage of minimal spatial limitations), near impossi-

ble. Measurements utilising *in-situ* technologies have been able to measure ultrafine aerosols down to 3 nm for over a decade, with further improvements in size range (down to 0.5 nm) occurring in recent years (Kulmala et al., 2012). Investigations of the chemistry of ultrafine aerosols in this region, then, can only occur through *in-situ* measurements, which due to logistics are expensive and rare.

The current dataset, obtained as part of the SIPEXII marine science voyage, consists of measurements of number concentrations of ultrafine aerosol in the Antarctic sea ice. This dataset provides a rare opportunity for understanding natural aerosol processes in an environment almost free of anthropogenic influences, and to gain further insights into the identity of a missing aerosol source in the region and help to reconcile the differences between models and measurements.

3.2 Methods - Understanding Atmospheric Circulation

Full details of the measurements made during SIPEXII are detailed in Chapter 2, however an understanding of the atmospheric circulation systems influencing the measurements became necessary during data analysis. To this goal, trajectory modelling studies were performed in collaboration with Andrew Klekociuk (Australian Antarctic Division), details of which are outlined below.

3.2.1 Trajectory Modelling

The HYbrid Single-Particle Lagrangian Integrated Trajectory (HYSPLIT) model (Draxler and Hess, 1998) calculates simple air parcel trajectories within given meteorological fields. Each trajectory traces released air parcels through time and provides three-dimensional locations every 3 hours for the given runtime. The model can be run either backwards or forwards in time for different purposes. In this study, backward trajectories were utilised to investigate source locations, while forward trajectories were used to understand the broader impact of measured constituents.

Input meteorological fields can be one of two types: modelled or reanalysis. Modelled meteorological fields are calculated completely from numerical weather and climate models. Reanalysis datasets utilise data assimilation systems to nudge model simulations to archived observations. Modelled fields are useful for future predictions or where, for any other reason, observational data doesn't exist. For simulations of the past, reanalysis data is preferred as it represents a world closer to reality.

In this study, trajectories were calculated in repetition using three different reanalysis datasets: the ERA-Interim reanalysis (Dee et al., 2011), the Global Data

Assimilation System (GDAS) analysis (Kanamitsu, 1989), and the National Center for Environmental Prediction/National Center for Atmospheric Research (NCEP/NCAR) reanalysis (Kistler et al., 2001). The model was setup to utilise reanalysis data at 1.5° horizontal resolution and was run in vertical motion mode. An increased resolution of 0.75° was tested in a sensitivity study and resulting circulation patterns were unaffected. The model utilised surface invariant geopotential, 10 m surface U and V winds, 2 m surface temperature, and U, V, W[a], temperature and humidity on pressure levels from 1000 to 100 hPa (excluding 125 hPa to adhere to download restriction on data servers). Each trajectory calculation provided hourly three-dimensional air parcel locations for a total time-span of up to 10 days. Trajectories were initiated at the ship's location for every hour of the cruise at heights of 10 m (above mean sea level) and from 500 m to 4000 m at 500 m intervals.

Additional trajectory analyses were run in order to determine both the seasonal and spatial variability of the circulation observed during the voyage. The starting locations of these trajectories, referred to as virtual sea ice stations, are shown graphically in Figure 3.1. Seasonal variability was assessed from a single starting location near the cruise location, highlighted in blue in the figure. Trajectories, run using ERA-Interim meteorology, were initiated every hour from (65°S, 120°E) at a height of 10 m above mean sea level, spanning 2010 to 2012. Highlighted in green in the figure are the starting locations used for the assessment of spatial variability. These locations were chosen to span the continent at 30 degree longitudinal intervals and to remain within the sea ice region at approximately equal distances from the coast. This resulted in starting locations in western longitudes (0 to -180°) being situated at 70°S, while trajectories initiated from eastern longitudes (0 to 180°) started from 65°S. Further trajectories were initiated from the same starting locations around the continent, and run in forward mode in order to investigate the potential spatial impact of measured constituents.

Full trajectory datasets are publically available though Schofield and Klekociuk (2014).

3.2.2 Meridional Mass Stream function

The meridional mass stream function is used to provide a quantitative description of the mass flow of any fluid. When the fluid being considered is the atmosphere, the stream function helps to identify overturning cells in general circulation patterns. More specifically, the meridional mass stream function used here provides an Eulerian zonal mean description of the overturning cells in general atmospheric circulation along the meridional plane.

[a]U and V are horizontal components of wind velocity, while W is the vertical.

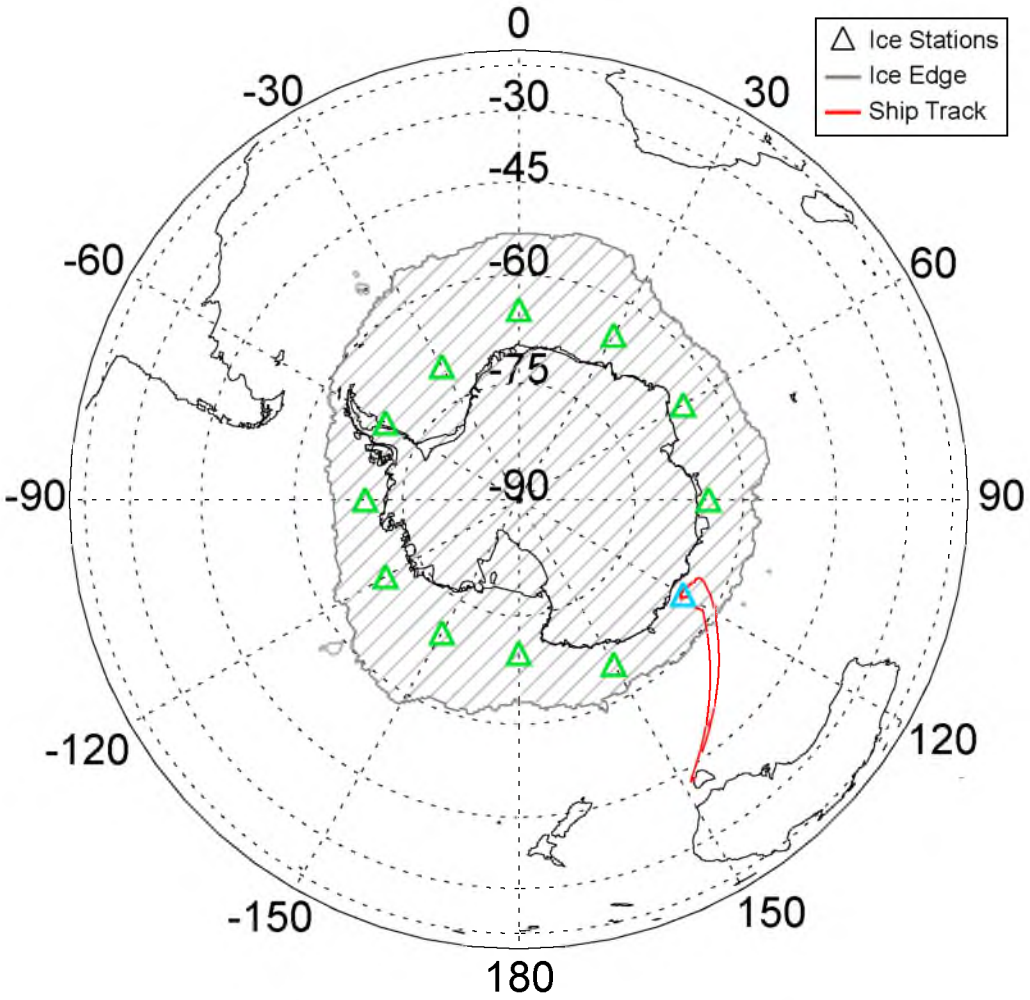

Figure 3.1: Ice stations used as starting locations for trajectory analyses (green) with the blue triangle being the basis of long-term and detailed analyses. The part of the ship track (red) inside the sea ice extent (grey) is the starting location for ship based trajectory analyses.

The meridional mass stream function was calculated to independently confirm the circulation patterns identified from trajectory analyses using HYSPLIT, and therefore results have not been explicitly included in the main text, however sample results are included in Appendix Figure A.8. Calculations in this study utilised the NCEP/NCAR reanalysis dataset as input data for analysis.

3.3 Results

3.3.1 Aerosols and the Polar Front

Number concentrations of *in-situ* aerosols were observed in the East-Antarctic sea ice region at two size ranges, those with diameters > 3 nm (CN_3) and > 10 nm (CN_{10}). Taking the difference between these datasets results in CN_{3-10}, a parameter

that describes the number of particles with diameters between 3 and 10 nm - those recently formed via gas-to-particle conversion. As the voyage moved further south, a sharp jump in aerosol number concentration was observed. In Figure 3.2 (and in Appendix Figure A.1), the order of magnitude jump in CN_{3-10} and doubling of CN_{10} aerosols is clearly observed, with the transition occurring between 64.39°S and 64.46°S (29th September). Unfortunately, confirmation of this step change feature was unable to be confirmed as the ship moved north out of the Polar Cell, due to instrument malfunction and exhaustion of working fluid while south of the Polar Front. Mapping the concentrations to the ship's GPS location, shown in Figure 3.3, gives a similar picture, but reveals that the transition period identified in Figure 3.2 coincides with westerly drift of the ship with minimal latitudinal movement. This longitudinal drift leads to the poorly defined boundary (i.e. a mixture of concentration magnitudes are found at the same latitude labelled as the Polar Front) observed in the latitudinal plot. Given the latitudinal gradient, the change in aerosol concentration observed during this westerly drift is likely to be the result of the Polar Front being latitudinally non-uniform at that location and time (i.e. it extends longitudinally).

Discussed in detail in Section 1.2 and summarised schematically in Figure 1.6, are the general atmospheric circulation features occurring in each hemisphere that are suggested to explain these step changes. The circulation in each hemisphere consists of 3 primary circulation cells: the Hadley, Ferrel and Polar cells. The boundary between the Ferrel and Polar cells, also known as the Polar Front, is a dynamic boundary which lies at approximately 65°S in the Southern Hemisphere. The observed step change in aerosol concentration with latitude is consistent with the measurement platform moving from the Ferrel cell, where low aerosol concentrations are observed, across the transition of the Polar Front into the Polar cell, where enhanced concentrations were present.

The proposed location of this boundary, identified from the aerosol record, was tested using *in-situ* meteorological data. Both atmospheric circulations cells have characteristic surface winds determined by the Coriolis effect, with the Ferrel Cell having dominant westerlies and the Polar Cell having dominant easterlies (Figure 1.6). Utilising this feature, wind roses were constructed for both Ferrel and Polar cells using data obtained from north and south of the boundaries identified in the aerosol record, respectively. These wind roses, shown in Figure 3.4, showed the expected surface wind directions, confirming the proposition of the step change in aerosol concentrations being caused by movement of the measurement platform from the Ferrel cell to the Polar cell.

Aerosol	Polar Cell Conc. (cm^{-3})				Ferrel Cell Conc. (cm^{-3})			
Size Range	Mean	Median	IR	MAD	Mean	Median	IR	MAD
CN_{3-10}	774	536	667	242	52	45	21	10
CN_3	1130	816	972	345	224	196	39	20
CN_{10}	351	256	286	100	194	141	53	22

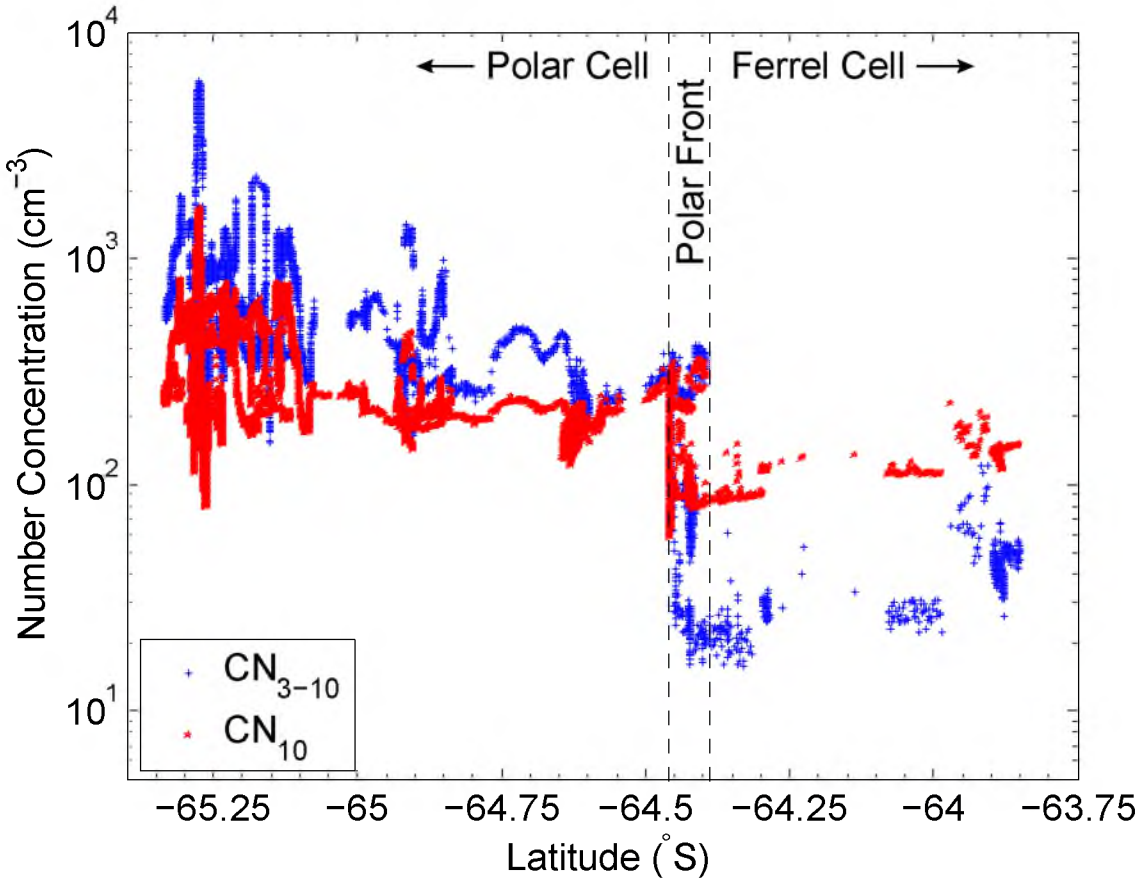

Figure 3.2: Ship-based measurements of aerosol above the sea-ice show a sharp jump in aerosol number concentration moving south across the Polar Front. The locations of the Polar Front and Polar and Ferrel Cells are labelled. Statistics of aerosol concentrations within each cell (mean, median, interquartile range (IR) and median absolute deviation (MAD)) are given above.

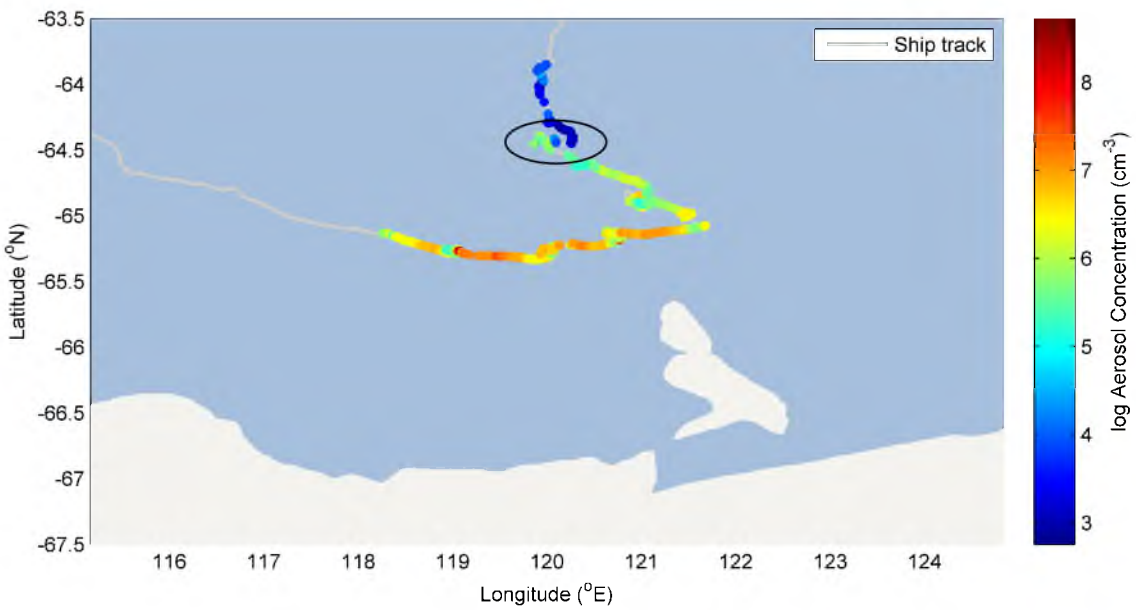

Figure 3.3: Number concentration of CN_{3-10} measurements overlaid on the ship's GPS track (grey). The sudden change from dark blue to lighter colours (circled) reflects the order of magnitude step change in concentration observed in the record. The transition occurs on approximately the same latitude, with higher concentrations on the westerly side. This could be due to an uneven Polar Front.

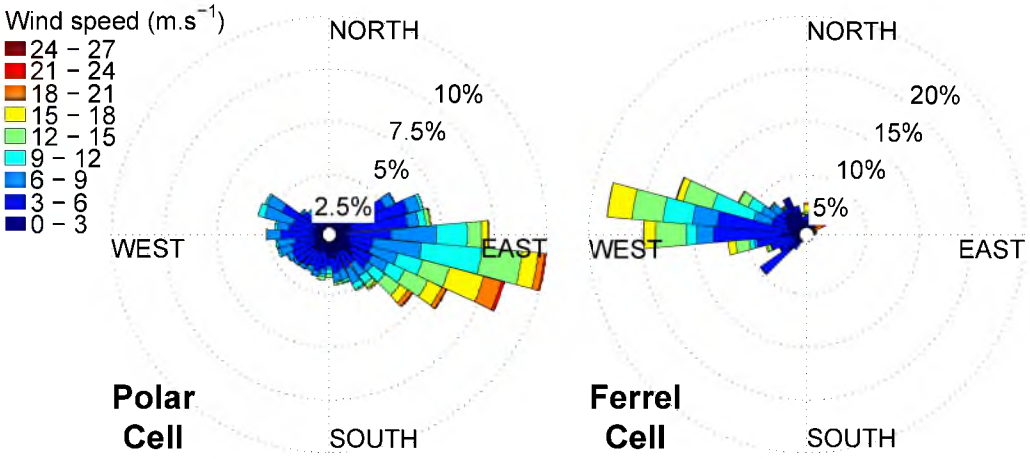

Figure 3.4: Wind roses from the ships *in-situ* meteorology data confirm the Polar Front location proposed from *in-situ* aerosol data. The data used for the Polar Cell wind rose is that subset where latitudes were south of the Polar Front identified from the aerosol record (see Figure 3.2), while the Ferrel Cell wind rose are those north of that boundary.

Although the location of the Polar Front can be confirmed by *in-situ* meteorological data, initial identification from this data is difficult. It is likely that measurements of aerosol concentration in the boundary layer is a novel method for locating the Polar Front by *in-situ* observations (provided local anthropogenic influences, such as ship exhaust, are removed).

3.3.2 Unprecedented Polar Cell Aerosol Concentrations

Sub-micron aerosol number concentrations measured in the Ferrel Cell during this voyage were about half of those observed during other measurements in the Southern Ocean marine boundary layer (e.g. Brechtel, Kreidenweis, and Swan, 1998; Wiedensohlet et al., 1997), with median CN_3 concentrations of 196 cm^{-3} ($\bar{x} = 224\ cm^{-3}$). In the Polar Cell however, the striking step change (Figure 3.2) resulted in median CN_3 concentrations of 816 cm^{-3} ($\bar{x} = 1130\ cm^{-3}$). Except for one new particle formation event which resulted in measured CN_3 concentrations over 7500 cm^{-3} (described in Chapter 5), background aerosol CN_3 concentrations generally ranged between 500 and 2000 cm^{-3}, with not infrequent periods above 2600 cm^{-3}.

A summary of Antarctic aerosol number concentrations published in the literature is depicted graphically in Figure 3.5, with the associated table included in Appendix A.1. The Antarctic and Southern Ocean region is a chronically undersampled region. Most measurements occur either in the relatively easy to access Southern Ocean north of the sea ice edge, or at continental and coastal Antarctic locations where permanent research stations exist.

Compared to our spring East Antarctic measurements, the only other measurements in Antarctic pack-ice (Davison et al., 1996) occurred in early summer in the West Antarctic and found background CN_3 to be 400-600 cm^{-3}, with local new particle formation events responsible for short-term peaks up to 4000 cm^{-3}. Similar concentrations were recently reported (Belosi et al., 2012) on the Nansen Ice sheet glacier (74°30′ S, 163°27′ E, 85 m above sea level). This region of fast ice (ice attached to the continent) in East Antarctica showed concentrations in December similar to those of Davison et al. (1996). In contrast to maximum concentrations in the thousands, measurements at the coastal Neumayer Station (Weller et al., 2011) and South Pole (Park et al., 2004) showed average summer CN_3 maxima of around 724 cm^{-3} and 150 cm^{-3}, respectively. It is important to note that in the Antarctic region, CN_3 concentrations show a small peak in spring, with an annual maximum in summer (Weller et al., 2011; Virkkula et al., 2009).

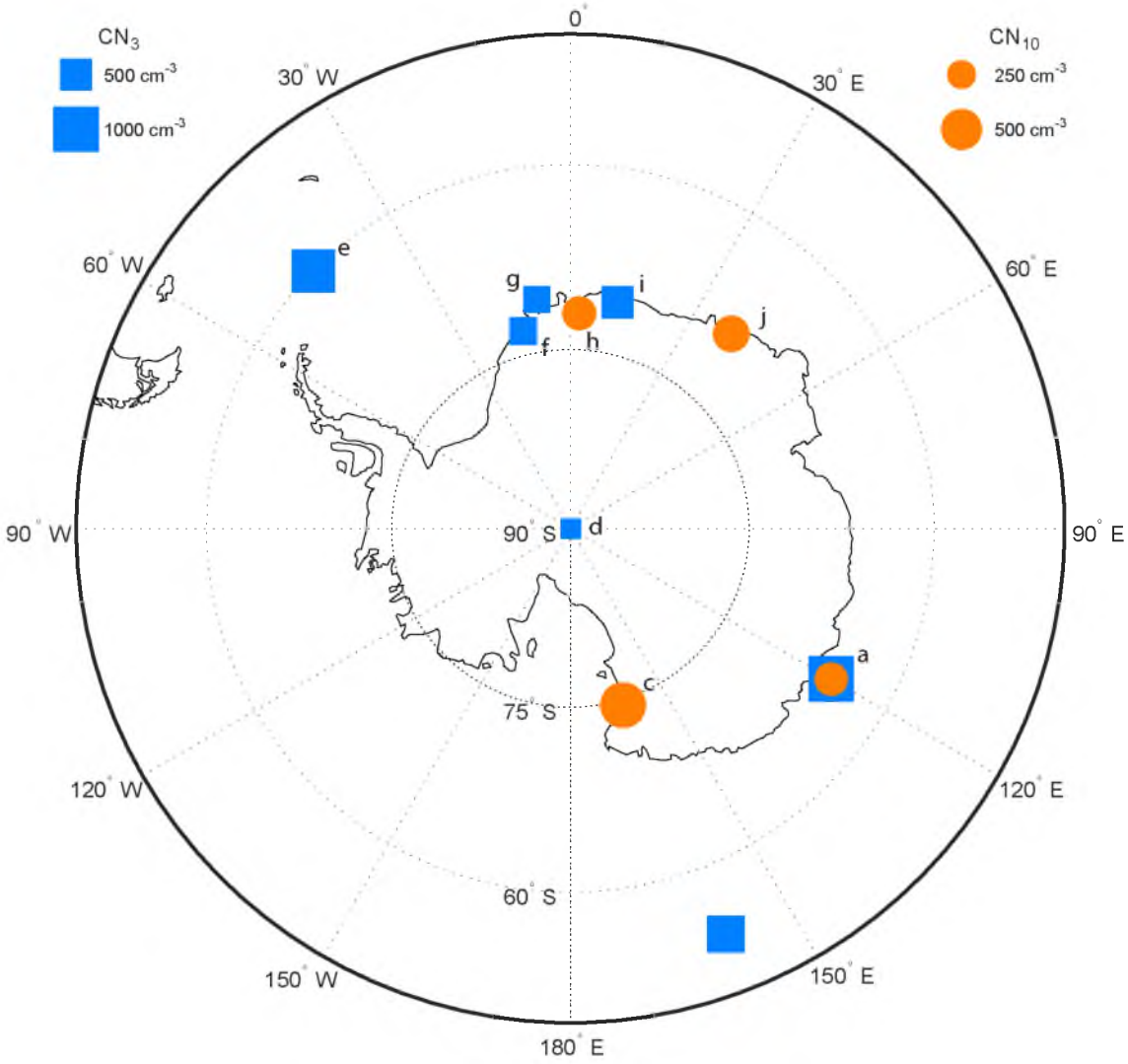

Figure 3.5: Graphical representation of CN_3 (square) and CN_{10} (circle) measurements around Antarctica and the Southern Ocean. The size of the shape is proportional to the average reported from measurements. Lettered labels refer to the following: a - this study; b - Brechtel, Kreidenweis, and Swan (1998); c - Belosi et al. (2012); d - Park et al. (2004); e - Davison et al. (1996); f - Asmi et al. (2010); g - Weller et al. (2011); h - Hansen et al. (2009); i - Pant, Siingh, and Kamra (2011); j - Hara et al. (2011).

3.3.3 Aerosol Growth

To investigate the unusually high aerosol number concentrations measured in the sea ice, an investigation into the growth of the aerosol populations was undertaken. Typically, enhanced aerosol concentrations are a result of local particle formation, and therefore signs of growth are visible in the dataset, provided suitable measurements are available (Davison et al., 1996). The measurements available on SIPEXII provided two datasets that allowed probing of aerosol growth: CN_{3-10} and CN_{10}. Changes in these datasets that occur simultaneously are due to various factors. If both datasets are increasing and decreasing at the same time, then the measured population can be assumed to be in steady state, that is, the number of particles growing into the CN_{3-10} size bin equals the number leaving and entering the CN_{10} size range. This steady state is often achieved when this size flux is zero, as is the case when particles are not growing. If there is a delay between changes in number concentration in each of the size ranges, then it can be assumed that aerosol populations are changing in modal size. If there is no delay, the steady state exists and aerosol populations, rather than being formed locally, are more likely to be transported from elsewhere.

Further examination of particle number concentrations showed that, except for the single *in-situ* new particle formation event described in Chapter 5, no signs of aerosol growth were observed. If aerosols were formed nearby, it would be expected that the increase in CN_{10} were delayed relative to CN_3 as particles grew. Figure 3.6 shows an excerpt of the background aerosol record which includes a large fluctuation in number concentrations that could be mistaken for a particle formation event (detailed analysis of this event is given in Appendix A.4). Closer examination of this event reveals that the two size ranges vary simultaneously, suggesting the aerosol population is in a steady growth state, likely with no growth occurring. This pattern of simultaneous changes between datastreams is common to all but the one observed new particle formation event (described in Chapter 5). Growth particularly at these size ranges is generally observed unless air-masses are removed from their source. It is reasonable to conclude then, that precursor species emitted locally (see Section 3.3.8) are not immediately contributing to aerosol growth or formation.

It is likely then, that the measured aerosols were formed elsewhere, and grew until the precursor reservoir is depleted, before being transported into the region where they were measured. Comparison of population characteristics suggests that measured aerosol number concentrations are too high to be explained by entrainment from the stratosphere (Stohl and Sodemann, 2010) and are not typical of polar populations, but are instead characteristic of populations formed in the free troposphere (polar populations have mean diameters around 150 nm and number concentrations

in the tens or hundreds, whereas free tropospheric populations generally have mean diameters around 10 nm and number concentrations in the thousands, (Seinfeld and Pandis, 2006)). In order to elucidate the source region of the measured aerosol populations, further work, in the form of a (back) trajectory analysis, was performed.

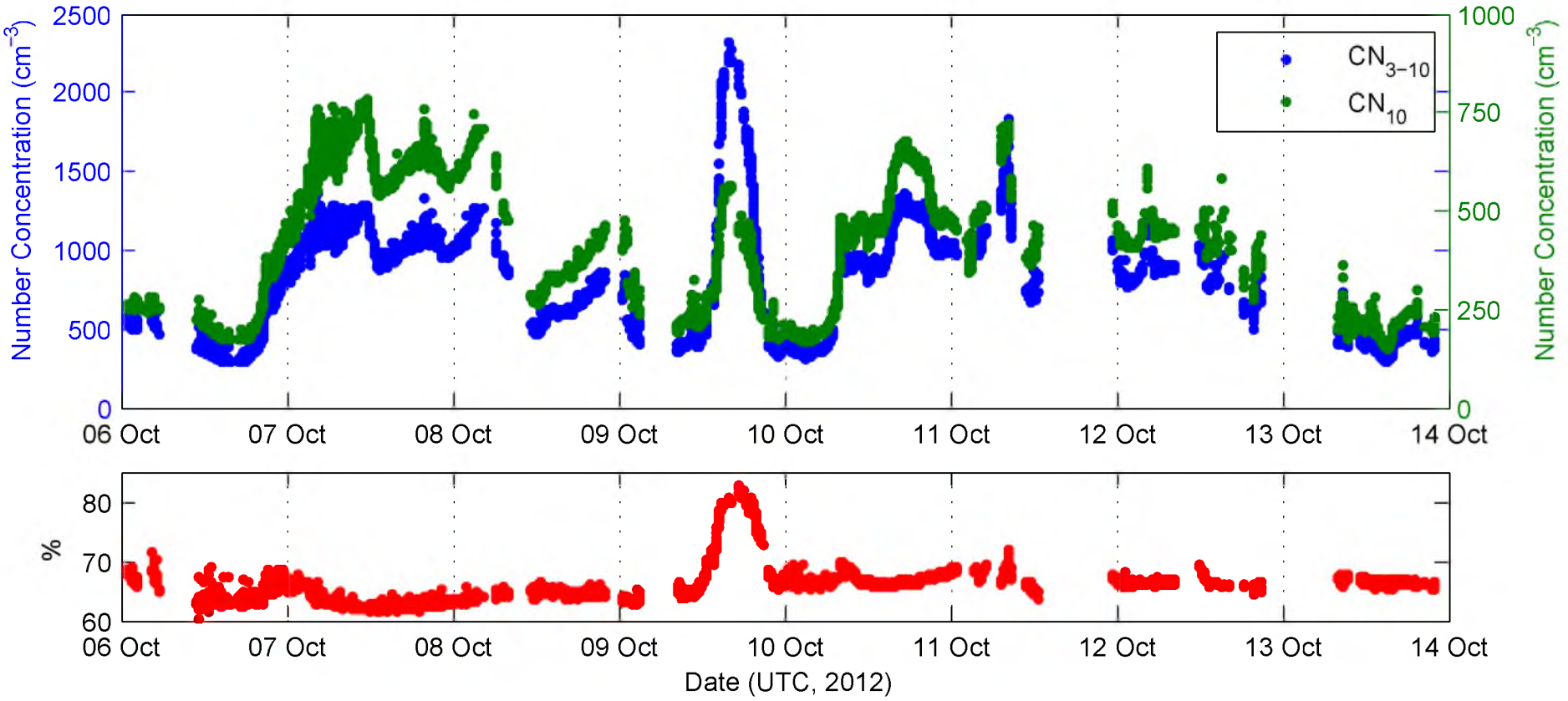

Figure 3.6: Example of background aerosol populations. Number concentrations of CN_{3-10} (blue) and CN_{10} (green) are observed to vary simultaneously, reflecting steady state or no growth. The 9th October showed the largest fluctuations in background populations, and was likely caused by a change in air-mass (see section A.4). Fluctuations in the percentage CN_{3-10}/CN_3 (lower panel, red) is likely due to the time difference between the end time of nucleation and growth processes in different air-masses, with higher percentages representing growth ceasing more recently.

3.3.4 Backward Trajectories

Trajectory analyses were used to investigate aerosol transport and source regions of the aerosols dataset. When run backwards in time, trajectories allow the spatial air-mass history to be derived using meteorological models that are driven by global observational reanalysis datasets. At the high latitudes of the Antarctic, these reanalysis datasets rely on sparse meteorological measurements, and as such, contain high uncertainty. Because of this, five day trajectories were preferred for most interpretation, while 10 day trajectories contained additional information that was interpreted with caution (similar to Scarchilli, Frezzotti, and Ruti (2010)). A more detailed analysis of the reliability and robustness of conclusions drawn from trajectory data is outlined in Section 3.3.4.1.

Results from trajectory calculations (the details of which are outlined in Section 3.2.1) revealed that before being measured, air parcels had travelled north from above the continent until the Antarctic coast where they descended to the sea ice surface and turned sharply to move with the dominant Polar Cell easterlies. Both forward and backward trajectories were found to support the Polar Front location proposed from *in-situ* aerosol and meteorological data.

A more detailed investigation was performed by separating trajectories released from voyage locations into their dimensional (temporal and latitudinal, longitudinal and vertical spatial) components and viewing the mean of each component as a function of altitude and latitude. In Figure 3.7, the dimensional components are observed with some surprising features. Most prominently, a well-defined downward flow is observed that transports free-tropospheric air from above the Antarctic continent to the sea ice, beginning its descent at around 70°S and reaching the surface just off the Antarctic coastline, where it travels westward with Polar Cell easterlies. Just north of this downward flow, air ascended in the Polar Front, travelling south as it approaches the tropopause - a feature confirmed by forward trajectories (Section 3.3.9) and present with all reanalysis datasets used. Major circulation features were confirmed through independent analyses of the meridional mass stream function (results shown in Appendix Figure A.8).

Trajectory information suggests this atmospheric transport occurs in a semi-closed circulation. This circulation begins in the sea ice, ascending in the Polar Front until it approaches the tropopause where it travels south towards the Pole. At the Pole it descends slightly, turns back north and remains high until descending in the downward flow where it returns to the sea ice surface. Time information from trajectories suggest that this round trip takes roughly 10 days.

Further analyses were performed to ascertain how long trajectories were in contact with the sea ice surface - the most likely region of surface emissions - in order

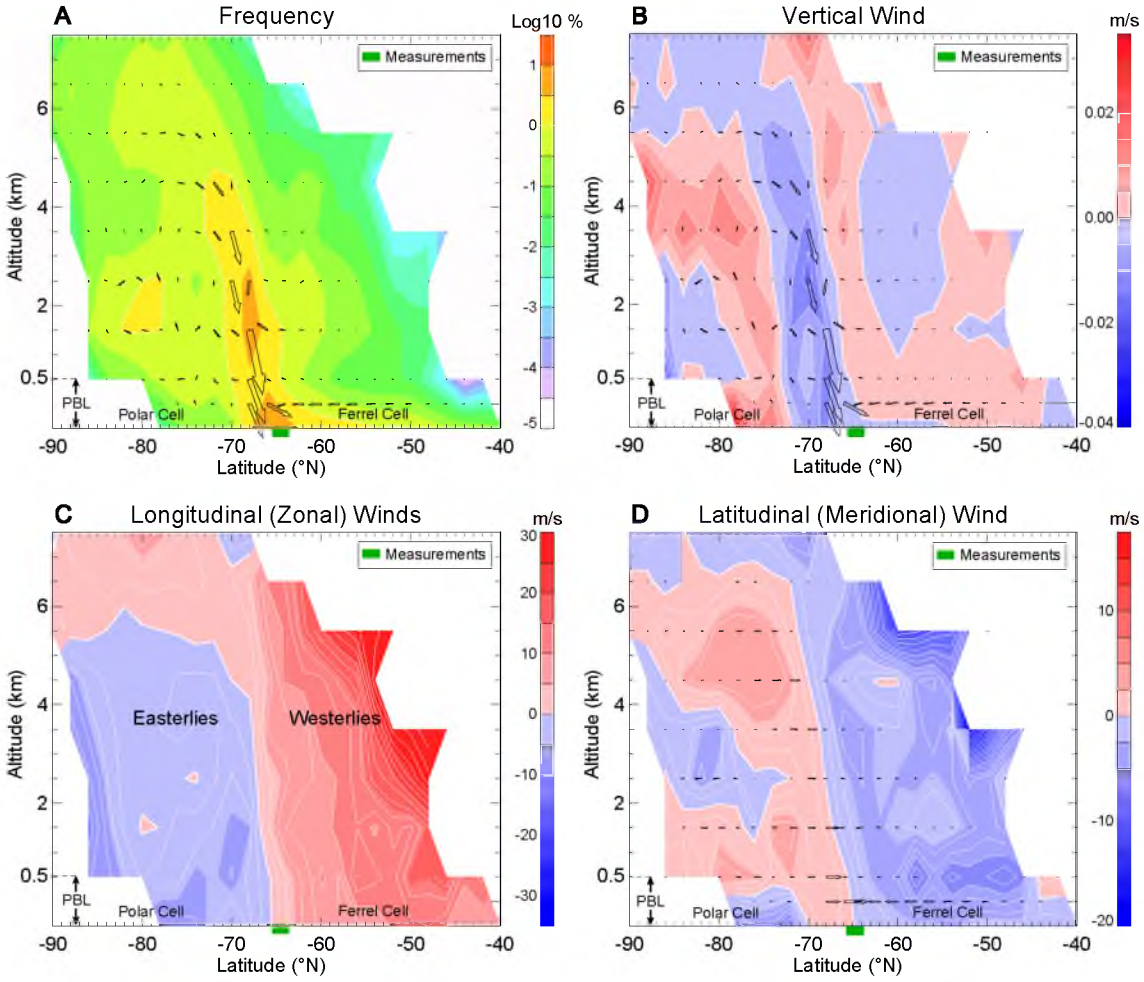

Figure 3.7: The dimensional components of 10-day back trajectories released at 10 m height every hour from sea ice voyage locations (green mark on x-axis), plotted latitudinally against altitude above mean sea level. The dimensional components include **A:** the frequency component (i.e. the number of times a trajectory passes through a given grid box), plotted in log scale; **B:** vertical wind, red colours indicating upward motion and blue downward; **C:** zonal wind, red is westerlies, blue is easterlies; **D:** meridional wind, red is equatorward flow, blue is polar flow. Overlayed with the two-dimensional weighted vector plot, **A** and **B** clearly show the downward flow from the free troposphere. Plot **D** is overlayed with meridional only weighted vectors. Plots **C** and **D** show the well-defined Polar Front and winds characteristic of both Polar and Ferrel Cell circulation systems. Consideration of plots **B** and **D** reveals the lower tropospheric circulation above the Antarctic continent.

to assess the source loading. It was found that after travelling north and descending from the upper troposphere, trajectories on average spent 36 hours in contact with the sea ice surface before being measured, generally travelling west with the polar easterlies. Since aerosol growth is not observed (Section 3.3.3), any precursors emitted in this region are not chemically activated for condensation resulting in either nucleation or growth. Given this information, the presence of oxidised species capable of condensation only occurs after the time calculated from sea ice contact,

giving a lower bound on the time necessary for emission, oxidation and nucleation to occur. The round trip time of 10 days gives the corresponding upper time bound for these processes, along with additional growth time.

Trajectories run from 2010-2012 at virtual sea ice locations around the continent (see Figure 3.1 for start locations, and Appendix Figure A.5 for results of this analysis) show that this circulation pattern is a dominant feature at all East Antarctic locations, and to a lesser degree in West Antarctic longitudes. Trajectories started at lower latitude locations (e.g. upto 52°S) showed similar circulation patterns, suggesting a significant influence to, and from, the Antarctic free-troposphere. A detailed seasonal analysis (e.g. Appendix Figure A.6) found that this circulation occurs almost year-round, with the weakest features apparent in summer.

A number of factors are likely to be responsible for these circulation features having not been previously identified. The latitudinal approach used in this analysis, along with the sea ice trajectory starting location are both important factors. The seasonal cycle of this circulation is also likely to contribute to why these important features have been missed, since most campaigns in the Antarctic occur in the summer months when access to the continent is logistically simpler. Additionally, a large fraction of research in the region is focussed around the Antarctic Peninsula where this newly described circulation feature is at its weakest.

3.3.4.1 Reliability of Input Meteorology for Trajectories

The reliability of reanalysis datasets is a legitimate concern in any assessment of atmospheric circulation. In the Antarctic region, surface measurements are relatively sparse compared to other parts of the globe. However the global coverage of satellite measurements for the surface and lower atmosphere during our period of interest is relatively uniform (Bracegirdle and Marshall, 2012). Uncertainties in trajectory analyses magnify the longer they run, so that 10 day trajectories may not contain significantly more information than 5 day trajectories, and may in fact be misleading. Additionally, the starting location of trajectories may affect their reliability, particularly when starting locations are within the lower boundary layer. Some trajectory models (e.g. BADC Trajectory Service) terminate when the modelled air-parcel touches the surface, likely because of this high uncertainty.

We assessed the reliability of these factors by running simulations with various input reanalysis datasets, running times, and starting heights. Examples of results from these studies are shown in Figure 3.8. Input reanalysis datasets tested include ERA-Interim, Global Data Assimilation System (GDAS) and National Center for Environmental Prediction (NCEP) reanalysis. Running times tested were 5 and 10 days, while starting heights included 10 m, 100 m, 500 m then every 500 m up to 4 km. It was found that changing the input meteorology, starting heights and runtime

made no significant difference to the inferences about average circulation patterns, giving some level of confidence to conclusions.

Trajectory Run	Trajectory Contact Time (hours)			
	Free Troposphere	Mixed Layer	Sea Ice	Ice Sheet
ERA-Interim, 240 hrs, 10 m (A)	158.4	80.5	110.3	101.8
ERA-Interim, 120 hrs, 10 m (B)	61.4	57.6	61.1	48.4
NCEP, 240 hrs, 10m (C)	152.4	86.5	82.7	127.0
ERA-Interim, 240 hrs, 500 m (D)	175.9	63.1	125.8	72.2

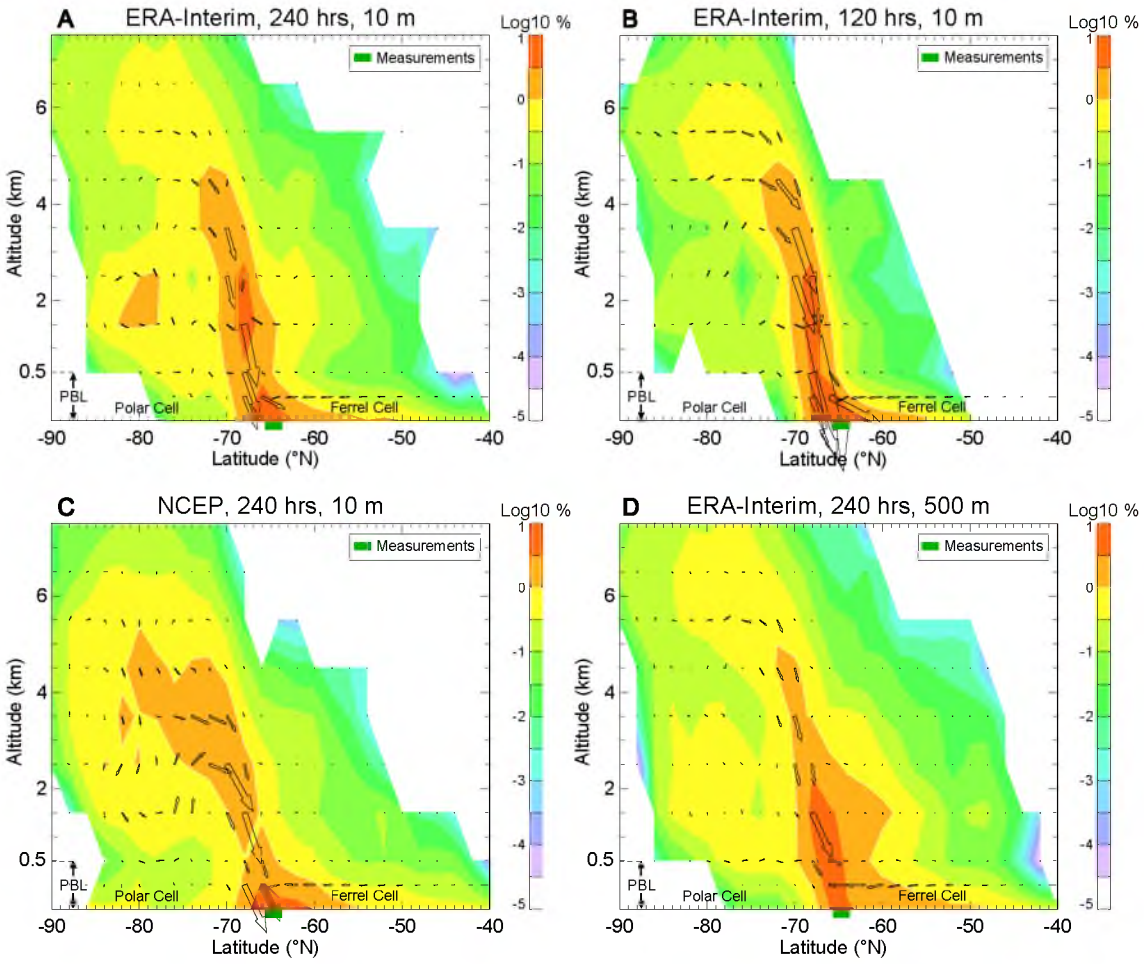

Figure 3.8: Assessment of reliability of trajectory analyses in the Antarctic region using plots similar to those described in Figure 3.7. **A**: Longitudinally averaged cross section showing grid frequency of 10 day back-trajectories using ERA-Interim reanalysis, released at 10 m above sea level for every hour of the voyage, with two-dimensional vectors weighted by number of points at each location. **B**: As in **A**, but for 5 day trajectories. **C**: As in **A**, but using NCEP reanalysis. Analyses with GDAS reanalysis produced patterns similar to ERA-Interim. **D**: As in **A**, but using a starting point of 500 m. Varying any of these parameters creates minimal changes in final trajectories, giving confidence in the conclusions of circulation. The table above outlines average contact time with various aspects of the atmosphere and surface. Note the sum of the free-troposphere and mixed layer contact times does not equal the total time due to the necessary data removal and rounding.

3.3.5 Aerosol nucleation: free-troposphere or boundary layer?

Back-trajectories analyses, together with the absence of signs of growth within the background population suggests that aerosols measured in the sea ice region have come from the Antarctic Free Troposphere (AFT) within the previous five days, with transport along the sea ice in the 36 hours (average) before measurement. Although this is the probable explanation based on evidence presented thus far, it is worthwhile discussing in more detail why boundary layer nucleation is unlikely.

There are a number of reasons that make boundary layer nucleation unlikely, including lack of signs of aerosol growth, homogeneity of the sea ice region, low measured levels of biological activity during the sea ice voyage transects, and results from modelling studies.

Although detailed information about the size distribution was not measured, the two measured size bins are in the range of nucleation and initial growth, and have been used in numerous previous studies and long-term measurement programs to assess new particle formation (see review by Kulmala et al., 2012). The instruments employed in this study allow deduction of aerosol growth between 3 and 10 nm diameters. If a delay is observed between the increase in CN_3 and CN_{10}, then growth between the two sizes can be concluded under the assumption that the air-mass being sampled is constant throughout the analysed period. If there is no delay between changes in the two size-bins, we can deduce that there is no growth between the two sizes. Growth above 10 nm almost invariably occurs after particle formation. Consequently, if nucleation were occurring nearby, it would be unlikely that an increase in the number of 10 nm particles would not be observed with this measurement technique. If nucleation were to occur, but growth only occurred to a size below the detection at 10 nm, we would expect a change in the ratio of CN_3 and CN_{10} particles, that would again be detected through this method. This change in ratio occurs only twice in the dataset, once associated with a local new particle formation event, and once a result of a change to an air-mass that brought populations more recently from the Antarctic free-troposphere that resulted in less time for growth to occur via coagulation (see Section 3.3.6). Other than the new particle formation event described in Chapter 5, the aerosol record showed no signs of growth, and as such, nucleation is concluded to occur elsewhere.

Determining the location of nucleation requires an assessment of meteorological conditions and trajectory analyses. In general, the upwind location within the previous 36 hours (average) was the sea ice region to the east of the measurement location. The measurement voyage itself spanned over 400 km of sea ice latitudinally, and longitudinally spanned from the ice edge to within 50 km of the continent. Sea ice conditions were homogeneous on the broad scale, with surprisingly low biological

activity throughout the whole voyage (see Section 5.3.7.1). Given this homogeneity, upwind regions were unlikely to differ significantly from those observed on the cruise track, and therefore, no obvious sources were apparent from which boundary layer nucleation was possible.

After the mean 36 hours within the sea ice boundary layer, trajectories found that air-masses had come from the AFT where nucleation is proposed to occur in this study. Aerosol populations also more closely resembled free-tropospheric populations, compared with typical polar or stratospheric concentrations due to the predominance of ultrafine particles (Seinfeld and Pandis, 2006). Periods of higher aerosol concentrations were found, through back-trajectory analyses, to occur when air-masses had more recently been in the AFT compared to periods of low concentration (explored in detail in the following section), adding evidence for free-tropospheric nucleation compared to boundary layer nucleation.

Finally, results from global chemistry and transport modelling based on known processes (described in Chapter 4) suggest that boundary layer nucleation mechanisms contribute minimally to aerosol concentrations compared to free-tropospheric nucleation, with final concentrations being well below those observed in the field.

It is more likely then, that nucleation in the AFT can explain the observed number concentrations compared to boundary layer nucleation. Circulation timescales of up to 10 days (determined by trajectories) are reasonable for transporting non-growing secondary aerosols, particularly given the low temperatures that would reduce evaporation of the aerosol cluster (see Appendix A.3 for details of aerosol lifetimes).

3.3.6 Variations in Background Aerosol

The cause of the variability of Polar Cell aerosol number concentrations was investigated by comparison with meteorological, *in-situ* O_3 and trajectory data. No visible relationship of air temperature, relative humidity, or O_3 was found with aerosol variations, however qualitative relationships were found to exist with atmospheric pressure and wind speed, suggesting the influence of cyclones.

In Figure 3.9, a positive correlation is observed between CN and latitude. Considering the air-mass originates from the south (described in previous sections), it is plausible that this trend is a proxy for time (and hence distance) since nucleation. Under this assumption, air-masses measured further north can be approximated to be older, meaning aerosol populations have had more time to grow via coagulation, thereby reducing number concentrations. This effect would result in a more pronounced change in CN_{3-10} (as a function of latitude) than would be observed in the CN_{10}, as is observed in Figure 3.9.

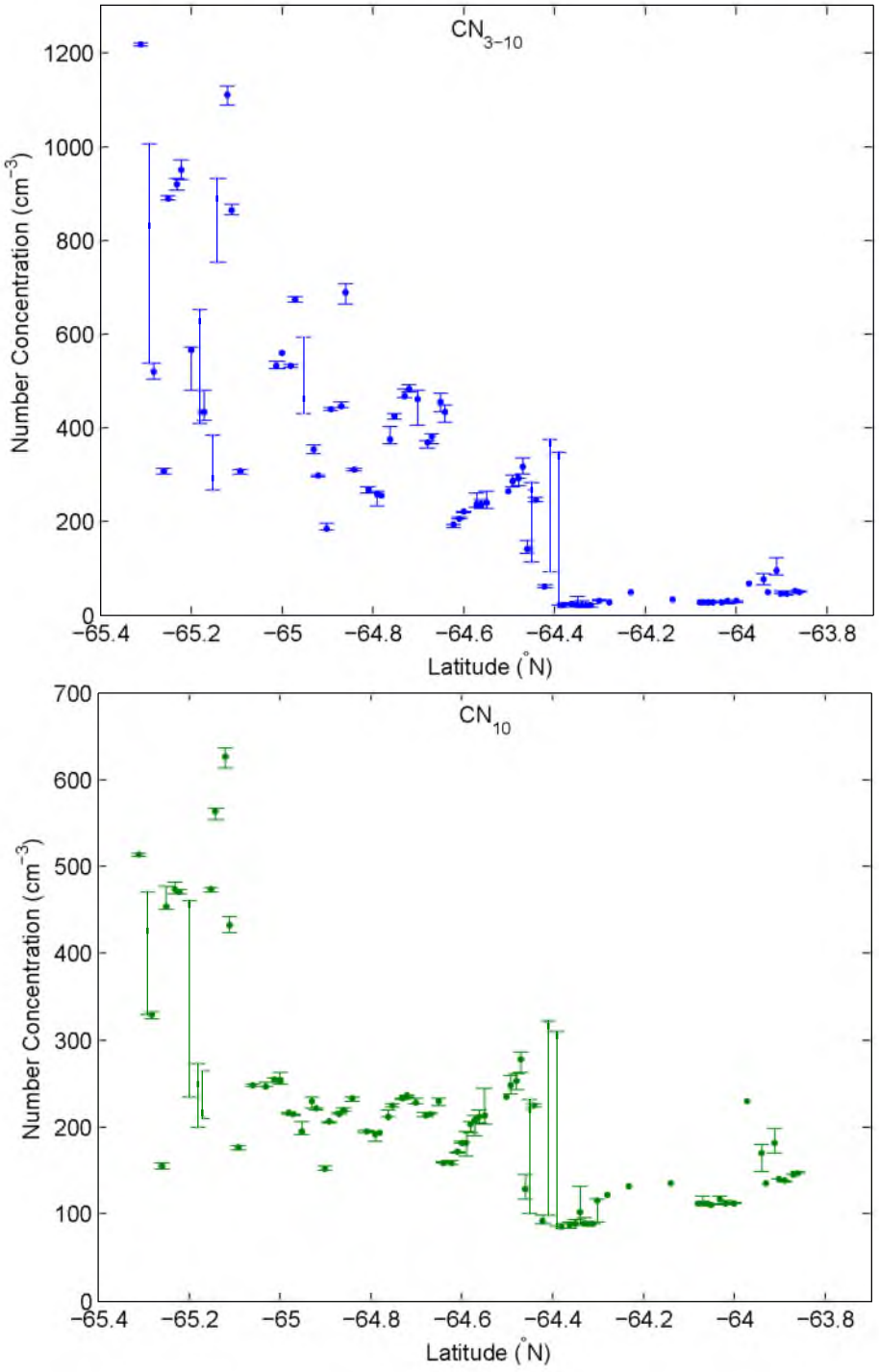

Figure 3.9: Correlation between latitude and the median number concentrations of values binned at each 0.01° for both CN_{3-10} (top) and CN_{10} (bottom). Within the Polar Cell, CN_{3-10} concentrations are observed to increase with latitude, while the same trend in CN_{3-10} data is weaker. Linear regressions applied to data south of the marked Polar Front yield R^2 values of 0.51 and 0.39 for CN_{3-10} and CN_{10}. Confidence intervals are calculated at the 95th percentile using medians such that the lower and upper limits are given by the difference between the median value the values at the $n/2 - 1.96\sqrt{n}/2$ and $1 + n/2 + 1.96\sqrt{n}/2$ ranked values, respectively.

At the shorter timescale (hourly-daily), number concentrations varied by over 1000 cm^{-3}. In Figure 3.10, the variability in the aerosol record (excluding the new particle formation event on the 18th October) is shown to vary inversely with the number of hours an air-mass has been in contact with the sea ice prior to measurement - a parameter calculated from trajectories. This relationship seems only to exist for data after the 4th October. While this is apparent in the time series data, correlations, shown in Figure 3.11, show only a weak inverse relationship. Despite this, the visibly similar trends observed in the figure suggest that this relationship could contribute to the variability in the aerosol record. If true, this relationship could be caused by three things: the sea ice contact parameter could be a proxy for time since being in the free-troposphere; increased coagulation due to surface proximity; or the surface acting as an aerosol sink.

To investigate whether the sea ice contact parameter is a proxy for time since being in the free-troposphere, further back-trajectories were calculated to compare air-mass history during periods of high and low aerosol number concentrations. This analysis used the HYSPLIT trajectory model and found that during periods of high aerosol concentrations, air-masses had more recently come from the AFT compared to periods of lower aerosol concentration (results shown in Appendix Figure A.12). This results in less time for the aerosol populations formed in the AFT to reduce in number concentration via coagulation. It is likely then that passing cyclones cause faster transport of AFT air-masses to the sea ice boundary layer where the measurements occurred (further discussion of this point has been included in Appendix A.6). The latter two options, increased coagulation due to enhanced turbulence resulting from surface wind shear, as well as the increase surface sink, could be working together with the air-mass transport to cause the observed trends.

The latitude and passage of cyclones could explain a large portion of the variation in the background aerosol record but do not explain it entirely. It is likely that a number of other yet to be discovered factors are influencing this variability and further measurements are required to determine their complex interactions.

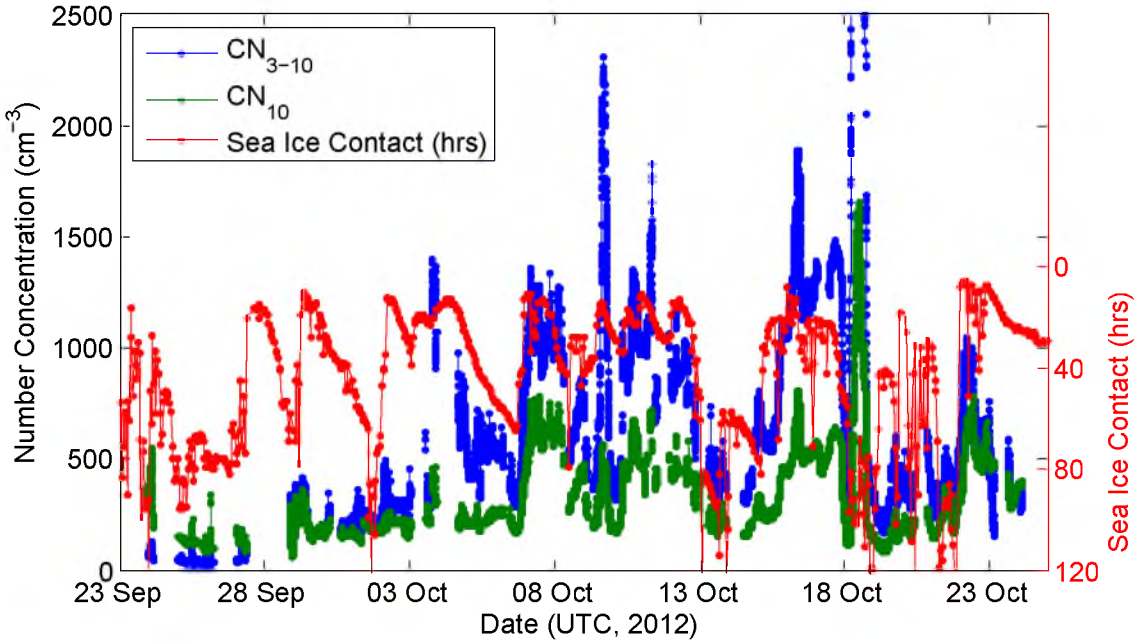

Figure 3.10: Time series of CN_{3-10} and CN_{10} compared to sea ice contact times. Note, the y-scale of contact times have been inverted and restricted to better show the correlation with number concentrations.

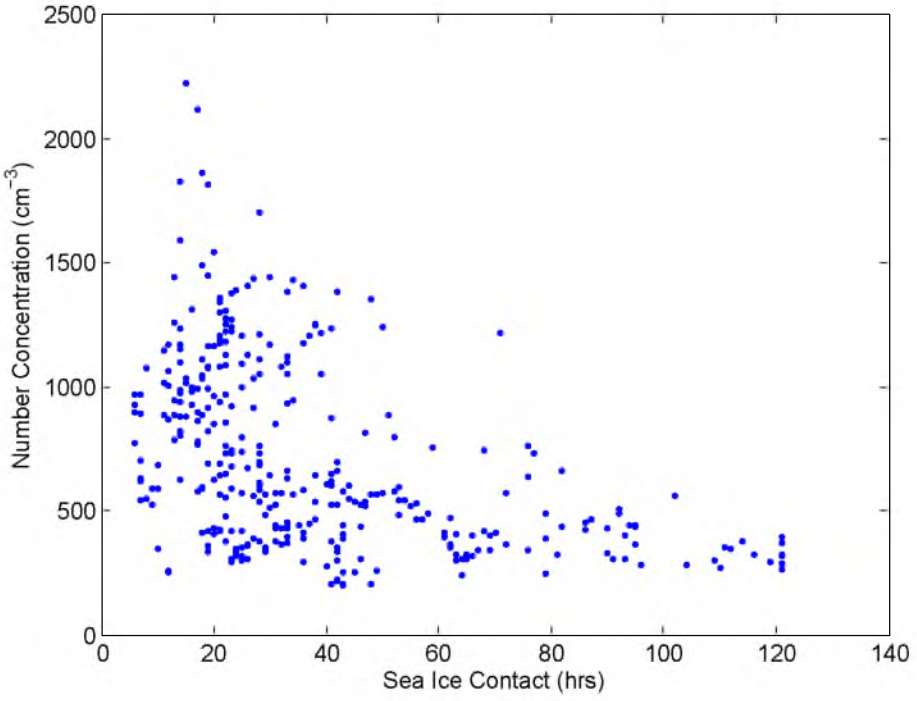

Figure 3.11: Scatter plot showing the weak inverse relationship between sea ice contact and CN_{3-10}.

3.3.7 The Antarctic Free Troposphere: a common nucleation reservoir

Free-tropospheric aerosol nucleation is common throughout the global atmosphere (e.g. Ito, 1993; Clarke et al., 1998; Raes, 1995), and has been proposed by numerous studies to explain Antarctic surface aerosol measurements (Virkkula et al., 2009; Ito, 1993; Ito, 1995; Asmi et al., 2010; Järvinen et al., 2013; Koponen et al., 2003). However, as discussed above, surface aerosol concentrations resulting from FT nucleation reported in these studies are far lower than our Polar Cell concentrations.

Since the well-defined downward motion at ~70°S is strong relative to other vertical motion in the region (and compared to expected sedimentation rates of ~1 $m.day^{-1}$ for 0.1 μm radius particles of 3 $g.cm^{-3}$ at 5 km altitude), it is possible that a large fraction of the nuclei formed in the AFT are transported via this mechanism predominantly into the East Antarctic sea ice region. Given the similar characteristics (e.g. size distribution) of aerosol populations measured around the continent (see references cited above), it is likely that the free-troposphere is a common reservoir for the entire Antarctic region. Therefore, the aerosol population remaining after transport to the East Antarctic sea ice region is likely to advect to the continental surface where the other measurements were made. Although this idea of a common reservoir has been suggested previously, most notably by Ito (1993), the discovery of the circulation and significant aerosol number concentrations over the sea ice region suggests the common AFT nucleation source is much larger than previously estimated.

Our forward trajectories, run as part of the HYSPLIT analysis, found that almost half of all air-masses originating in the sea ice region, and a significant fraction of those originating in the Southern Ocean, all around the continent, ascend and move south into the Antarctic FT as part of the Polar Front circulation. This circulation transports emissions from the surface up into the AFT from all around the continent, creating the significant precursor reservoir that is necessary for the common AFT nucleation that could explain aerosol concentrations measured in this study and those measured at permanent continental stations.

3.3.8 Potential Precursors

The circulation system that exists in the Antarctic region, as revealed by our trajectory analyses, means that precursors emitted from around the continent can combine into a common reservoir from which nucleation can occur and lead to the high aerosol number concentrations observed in the sea ice region. It is therefore useful to evaluate precursor concentrations measured around the continent, based on both SIPEXII measurements and those reported in the literature.

Aerosols and their precursors in the Antarctic originate predominantly from marine and sea ice areas, with only one recent continental study reporting aerosols sourced from local melt-pond cyanobacteria (Kyrö et al., 2013). In the Antarctic region, aerosol mass concentrations are dominated by coarse mode (> 1 μm) sea salt formed mechanically by wind shear on ocean surfaces or brine in the sea ice. Although low overall (see Section 3.3.2), number concentrations in the Antarctic are primarily dominated by sulfate aerosol (Korhonen et al., 2008; Shaw, 1988; Hara et al., 2011; Weller et al., 2011).

As described in this study, CN_3 number concentrations in the Antarctic sea ice region are surprisingly high compared to previous measurements outlined earlier in this chapter (see Figure 3.5). Numerous studies (discussed in detail below) have described the large concentrations of various aerosol precursors observed in this region, including sulfur, iodine and organic species - some of which are higher than observed anywhere else on Earth. These large concentrations are likely to be a result of the high biological activity in this region (Moore and Abbott, 2000), resulting in emissions such as dimethyl sulfide (DMS; CH_3SCH_3), halogenated and non-halogenated organic species, as well as inorganic halogen species.

Sulfur is abundant in this region in the form of DMS. It is a major secondary metabolite, being emitted by marine phytoplankton in the surface ocean, which upon saturation, is released to the atmosphere (Stefels et al., 2007). Figure 3.12 shows global DMS emissions based on climatology from Lana et al. (2011). The Southern Ocean is a major DMS source, accounting for 62% of the global atmospheric DMS flux, with the highest sea-surface DMS concentrations in the sea ice zone off the Antarctic coast (Levasseur, 2011; Bates et al., 1992; Lana et al., 2011). Consistent with their biological origin, seasonal cycles of DMS show maxima in summer, with mean concentrations at coastal locations of almost 300 pptv (Read et al., 2008; Savoie et al., 1992; Legrand et al., 2001; Berresheim et al., 1998; Minikin et al., 1998). In Southern Ocean air, average concentrations of around 100 pptv have been measured at Cape Grim, Tasmania (Ayers et al., 1997), and free tropospheric particle production associated with photochemically produced H_2SO_4 has also been observed (Weber et al., 1999). In the Southern Ocean, the flux of DMS to the atmosphere averages 9.4 $\mu mol.m^{-2}.d^{-1}$ (Curran and Jones, 2000), but can reach as high as 30 $\mu mol.m^{-2}.d^{-1}$ in summer (Lana et al., 2011). Measurements of DMS flux in the Antarctic sea ice are less frequent, yet those that have been made have found significant emissions that vary depending on ice-type: multi-year sea ice - 11 $\mu mol.m^{-2}.d^{-1}$(Zemmelink et al., 2008); pack ice - 54 $\mu mol.m^{-2}.d^{-1}$; fast ice - 16 $\mu mol.m^{-2}.d^{-1}$; ice edge - 12 to 23 $\mu mol.m^{-2}.d^{-1}$; and fast ice cracks and breakouts - 6 to 84 $\mu mol.m^{-2}.d^{-1}$ (Trevena and Jones, 2012). These sea ice flux emissions are significant and currently unaccounted for in global models, where sea ice is treated

as impermeable for DMS to pass from the surface-waters below (e.g. Lana et al., 2011).

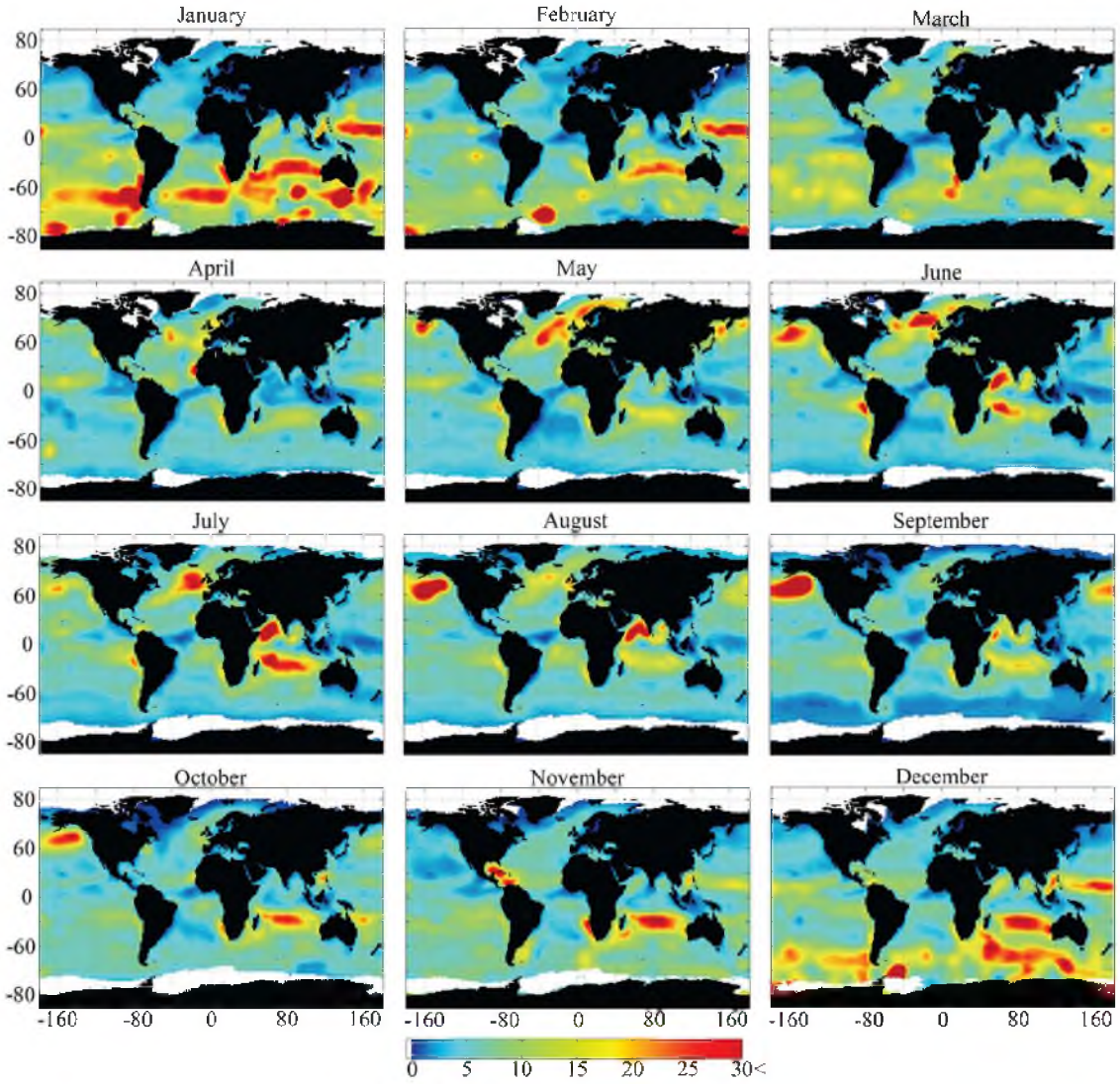

Figure 3.12: Monthly climatology of fluxes of DMS ($\mu mol.m^{-2}.d^{-1}$) based on climatologies of ocean concentrations from Lana et al. (2011). Scale is capped at 30 $\mu mol.m^{-2}.d^{-1}$ for readability.

Organic compounds can serve as precursors to aerosol nucleation and growth, with products known as Secondary Organic Aerosol (SOA). These emissions can come from various sources depending on the location being considered. In marine environments, biogenic organic matter is largely produced by phytoplankton, with dissolved compounds escaping to the atmosphere through wave breaking mechanisms (O'Dowd et al., 2004; Middlebrook, Murphy, and Thomson, 1998; Meskhidze and Nenes, 2006). Ocean phytoplankton are also known to produce non-methane hydrocarbons, in particular isoprene (Bonsang, Polle, and Lambert, 1992; Milne et al., 1995; Broadgate, Liss, and Penkett, 1997). Isoprene emissions are large enough that atmospheric concentrations in the remote Southern Ocean have been measured

as high as 60 pptv (Yokouchi et al., 1999).

Organic emissions produced by phytoplankton in the Southern Ocean, and presumably in the sea ice zone, could be a significant factor in nucleation and/or growth of aerosol populations in this region. Although measurements of fluorescence (a proxy for chlorophyll concentrations and therefore phytoplankton) during SIPEXII, presented in detail in Chapter 5, show negligible biology, pronounced biological activity is common in numerous locations in the Antarctic marine environment (e.g. Hu et al., 2013), suggesting biological emissions could be important for aerosol precursors.

For aerosol nucleation to occur from DMS or organic species, they must first be oxidised. Precursor oxidation can occur by UV radiation, or via numerous species including OH, O_3 and halogens. As summer approaches, incoming solar radiation increases, thereby increasing the photolytically oxidising UV radiation. Concentrations of O_3 measured during SIPEXII are consistent with Southern Hemisphere patterns, remaining high in the spring at around 28 ppb. OH concentrations have been measured at concentrations ranging from $0.1 - 2 \times 10^6 molec.cm^{-3}$ (Mauldin et al., 2001; Bloss et al., 2007; Jefferson et al., 1998; Kukui et al., 2014; Creasey et al., 2003), similar to the global average and measurements found in mid-latitude and tropical locations (e.g. Prinn et al., 1987; Prinn et al., 1995; Taraborrelli et al., 2012).

Halogen species in general are known for their highly reactive nature in polar atmospheres. Chlorine, bromine and iodine have been implicated as significant ozone depleting substances in both the troposphere and stratosphere, and have an important role in the oxidation of mercury, DMS and organic species (Saiz-Lopez et al., 2007a; Abbatt et al., 2012; Glasow and Crutzen, 2004). Halogen species can also change the atmosphere's oxidising capacity by interacting with the HO_x cycle and thereby affecting the OH budget (Sjostedt et al., 2007). Halogens, in particular iodine, have also been shown to be active precursors to aerosol nucleation (O'Dowd et al., 2002c). A scheme of the iodine chemistry leading to aerosol nucleation is presented in Appendix A.13. Major emissions of halogens and halogen containing species have been recorded in the Antarctic region and, as with DMS, are likely to have a common biological source.

During SIPEXII, concentrations of CH_3I, an iodine source and proxy for higher iodocarbons (Yokouchi et al., 2011), were measured by GC-ECD at levels below 0.2 pptv. In contrast to these low concentrations, Reifenhäuser and Heumann (1992) measured CH_3I in the Antarctic Peninsula up to 7.9 pptv. The difference of these measurements is consistent with the lower biological activity observed in East Antarctica compared to the Antarctic Peninsula, particularly at this time of year (Moore and Abbott, 2000). This biological gradient may also not fully reflect the

iodine budget in a particular location, with measurements in Weddell Sea recording molecular iodine (I_2), which can be emitted inorganically from the snowpack (Saiz-Lopez and Glasow, 2012), at concentrations of 12.4 pptv while iodocarbons were all below 0.2 pptv (Atkinson et al., 2012). Iodine oxide (IO) has been measured throughout the Antarctic region using a range of techniques. Measurements made during this study using MAX-DOAS show concentrations up to 1 pptv (see Chapter 5 for details). Boundary layer *in-situ* measurements have been made at numerous surface locations at concentrations of up to 10 pptv at Neumayer Station (Frieß et al., 2001), 7 pptv in the Weddell Sea (Atkinson et al., 2012), and 20 pptv at Halley Station (Saiz-Lopez et al., 2007a), the latter of which is the highest IO concentration recorded anywhere in the atmosphere. IO can also be measured remotely via satellite based instruments. Satellite data shows IO spread significantly throughout the Antarctic atmosphere, concentrating in particular in the West Antarctic during spring, and the East Antarctic sea ice during summer, creating a significant, spatially distributed IO source spanning a large part of the year (Schönhardt et al., 2012; Schönhardt et al., 2008; Saiz-Lopez et al., 2007b).

Although still an open question, the release mechanism required to obtain these concentrations of iodine compounds in the Antarctic region is likely to be unrelated to biology, but a result of release from the snowpack (Saiz-Lopez and Glasow, 2012; Frieß et al., 2010). Halogen compounds are often emitted by similar mechanisms, some of which are independent of biology, including sources such as hypersaline brine surfaces on young sea ice, frost flowers, surface hoar adjacent to refreezing leads, saline snowpacks and sea-salt aerosol (Stephens et al., 2012; Douglas, 2005; Kaleschke, 2004; Simpson et al., 2007; Foster et al., 2001; Saiz-Lopez and Glasow, 2012). The independence of halogen sources from biology is consistent with the seasonal cycle of halogen oxides at Halley Bay (Saiz-Lopez et al., 2007a), shown in Figure 3.13, which shows maxima in spring when biological activity is still low.

The involvement of halogen species in the oxidation of sulfur and organic species has also been proposed in a number of investigations. Saiz-Lopez et al. (2007a) found that IO was involved in the rapid oxidation of DMS at Halley Station. A number of studies have also found that BrO, which is autocatalytically released in similar concentrations to IO in the polar atmosphere, was the most important oxidant of DMS in this environment (Saiz-Lopez et al., 2007a; Breider et al., 2010). Comparison of the co-located spatial distribution of DMS emissions and IO and BrO concentrations could lead to a significant oxidised precursor reservoir in the Antarctic troposphere.

A number of organohalogen species were measured during SIPEXII which showed their general abundance. Bromine species such as CH_2Br_2 and $CHBr_3$ (Figure 3.14) were measured at concentrations reaching over 2 pptv and 6 pptv, respectively,

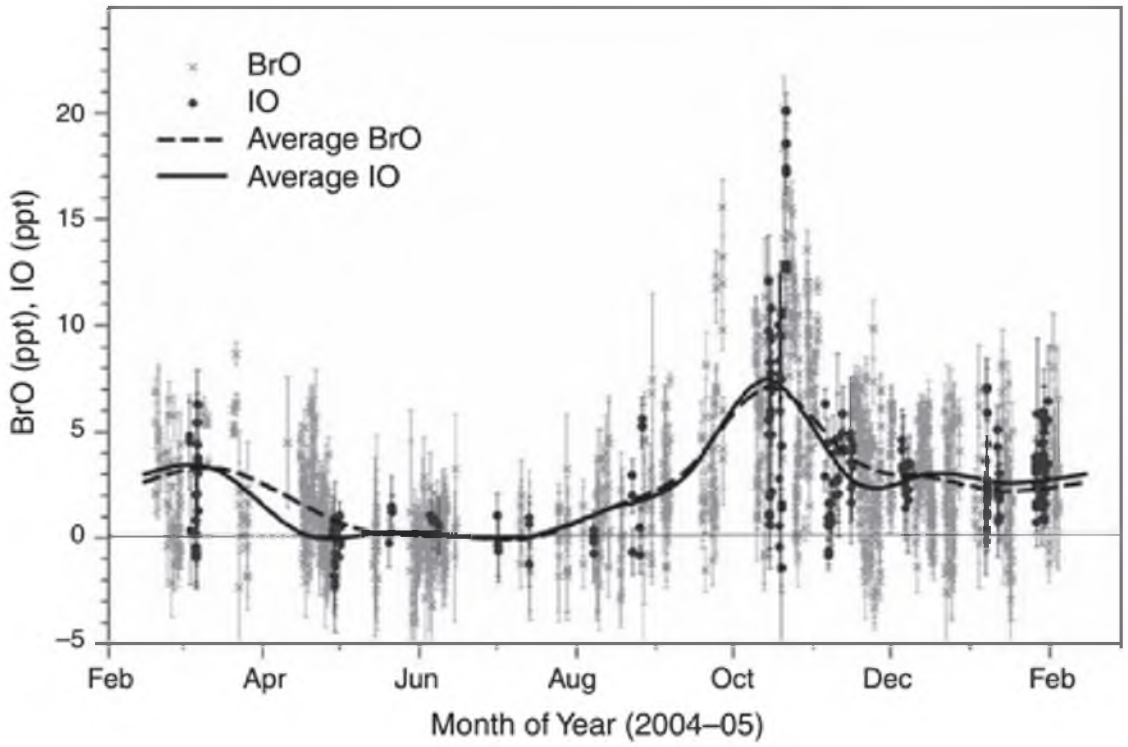

Figure 3.13: Long-path DOAS measurements from Halley Station, West Antarctica show the seasonal cycle of halogen species, BrO and IO peaks in spring, suggesting non-biologically driven production. Image courtesy Saiz-Lopez et al. (2007a).

reaching their maxima in the sea ice region. Chlorine species were also measured with concentrations of $CHCl_3$ reaching over 12 pptv. It is clear that the Antarctic atmosphere is rich in halogen species which can have a significant impact on the oxidative capacity of the atmosphere, creating oxidised species which can nucleate into aerosol particles, as well as themselves being important to particle growth.

It is evident that aerosol precursors are abundant in the Antarctic, with particularly high emissions from the sea ice region. In particular, measurements reveal that polar regions are abundant in biologically driven emissions such as DMS and that the Antarctic region is a global iodine hotspot. As mentioned previously, seasonal cycles of aerosols generally show maxima in summer with a smaller peak in spring. Comparison of this cycle with that of precursor cycles suggests that the high spring aerosol concentrations observed in this study are a result of inorganic iodine emissions rather than the commonly attributed biological DMS precursor. The identity of the precursor species was investigated further by utilising a global chemistry and transport model. The results of this modelling study are outlined in Chapter 4.

Regardless of the identity of the precursor species, consideration of high precursor concentrations around the continent, together with the circulation revealed by trajectory analyses, suggest that a large reservoir of precursor species exists from

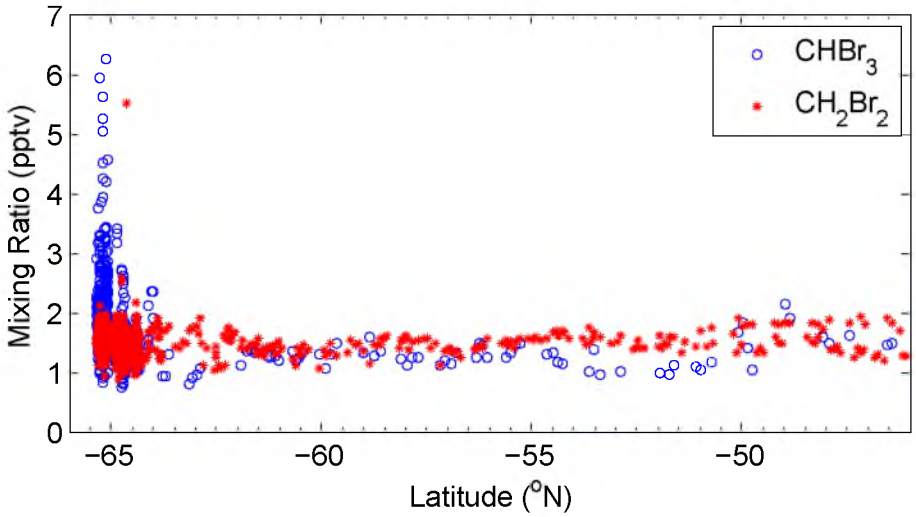

Figure 3.14: $CHBr_3$ and CH_2Br_2 concentrations (pptv), measured during SIPEXII using GC-ECD show maximum concentrations in the sea-ice region south of approximately 62°S.

which aerosol nucleation can occur in the free troposphere above the continent. As discussed in the following section, aerosols in the free-troposphere are likely to have come from the sea ice region, and thus are likely to be dominated by sub-10 nm particles. Using this study's median Polar Cell concentrations, and assuming the same size distribution, air-masses reaching the free troposphere are likely to have a pre-existing surface area below 8 $\mu m^2.cm^{-3}$, sufficiently low so as not to suppress nucleation (other studies suggest surface areas below 5-25 $\mu m^2.cm^{-3}$ is necessary for nucleation) (e.g. Covert et al., 1992; Raes, 1995; Clarke et al., 1998). Trajectory analyses constrain the chemistry occurring here to a timeframe of between 36 hours and 10 days. This time-frame is consistent with atmospheric lifetimes of the two primary precursor candidates, iodine (Saiz-Lopez et al., 2011; Abbatt et al., 2012) and sulfur (Chin et al., 1996).

3.3.9 Forward Trajectories

As discussed in Chapter 1, natural aerosols have both direct and indirect effects on the radiative balance, being able to reflect or absorb radiation directly (depending on their composition), or influence cloud formation and properties, respectively. Given the likely sources outlined in Section 3.3.8, aerosols formed in this circulation mechanism are likely to be composed of sulfate and iodine (as discussed above), and therefore highly reflective. Since the surface albedo of the Antarctic continent and sea ice is similar to that of natural aerosols and clouds, changes in albedo due to these natural aerosols is likely to produce negligible changes in the radiative balance. If, however, natural aerosols are effectively transported north to locations where surface albedo is low, such as the Southern Ocean and ice-free landmasses,

radiative changes from ARI and ACI caused by these aerosols could be significant.

In order to investigate this idea, 10-day forward trajectories were initiated at 10 m height (AMSL) from sea ice locations (Figure 3.1) around the continent. Results from these trajectories are shown in Figure 3.15. What is immediately apparent from the results is the significant spatial extent, covering much of the Southern Ocean, to which air-masses reached within the 10 day trajectories. Not infrequently, air-masses are found to reach as far north as 30°S. Northward moving air-masses are found to ascend slightly, likely in the Polar Front, and travel above the planetary boundary layer (PBL) in the lower troposphere, preventing their observation in our dataset north of the Polar Front and explaining the aerosol concentration step change of Figure 3.2.

A more detailed analysis of trajectory location was performed to determine the percentage of air-masses that cross the edge of the sea ice region without returning. This analysis gives a more robust measure of the impact of aerosols measured in the sea ice region. Results of this analysis (table in Figure 3.15) found that after 7 days, almost 50% of air-masses had been transported north of the sea ice edge into the low albedo Southern Ocean region, while the remainder ascend and travel south in the Polar Front and subsequent circulation.

Figure 3.16 divides the impact of the calculated forward trajectories into numerous vertical layers. This perspective confirms a number of aspects of the circulation over the continent suggested by back-trajectories. Looking at the forward trajectories as a function of height and spatial coverage, the Polar Front transport is observed, and moves south. Observing back-trajectories from this slab-atmosphere perspective (Appendix A.5) reveals similar patterns. Although the various reanalysis datasets are not entirely independent, using multiple methods and data sources to come to the same general conclusions on circulation features greatly enhances the robustness of the conclusions of the circulation mechanism occurring over Antarctica and its surrounds.

Based on these forward trajectories, transport of air-masses from the sea ice region to areas where surface albedo is low, does occur. For aerosols to interact with radiation and clouds though, they must first grow to climatically relevant sizes (>80 nm). Growth of freshly nucleated particles to these sizes has been observed in the region (e.g. Koponen et al., 2003; Virkkula et al., 2006). The absence of nanoparticles in observations in the Southern Ocean boundary layer (Weber et al., 1999) also suggests that if aerosol populations are being transported from the Antarctic region to the Southern Ocean, as is suggested by trajectories, that background nanoparticles have grown significantly.

In general, this growth can occur via numerous processes including coagulation of pre-existing aerosols, or condensation of vapours. In these northward moving

Age (days)	1	2	3	4	5	6	7	8	9	10
Outside (%)	2.9	15.9	26.6	35.1	39.7	43.6	47.4	48.0	48.9	49.9
Lost (%)	0.6	4.1	7.8	12.1	17.2	22.4	28.1	33.9	41.7	49.9

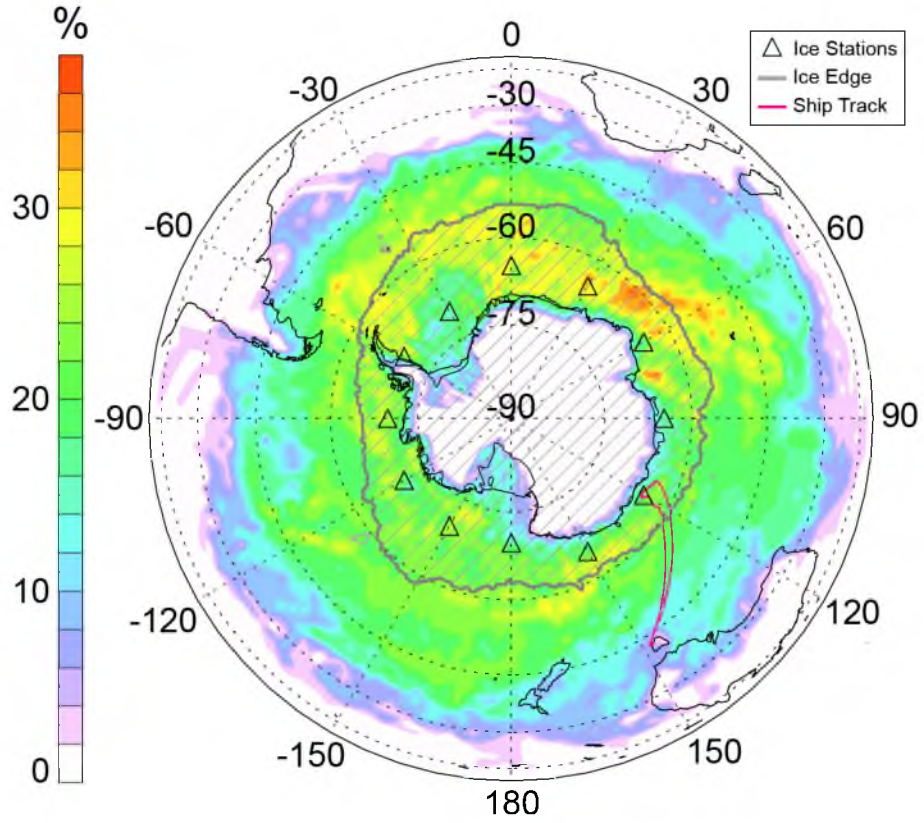

Figure 3.15: Ten-day forward trajectories from all ice stations for October 2012 show the extent to which air-masses originating in the sea ice travel north of the ice edge to the low albedo Southern Ocean. The table above classifies trajectories with age and as either *outside* - those outside the sea-ice edge on the given day; or *lost* - those which do not re-enter the sea-ice zone after the given days. Trajectories are released at 10 m height from virtual sea ice stations around the continent (triangles) for every hour of October 2012. The number of times any trajectory hourly location passes through a given horizontal grid box (integrated over 0-500 m altitude) is presented (colours) as a fraction of the total number of trajectories released.

air-masses, both of these processes could be occurring. For condensation to occur though, vapours are required, and as discussed in Section 3.3.3, these air-masses have already been depleted of precursors in the Antarctic troposphere before measurement. However, as discussed above, the sea ice region is one of the most productive regions for precursor emissions. Since these air-masses travelling to the Southern Ocean first pass via the productive sea ice region, it is reasonable to think they are re-enriched in precursor species that during northward transport, are oxidised and can contribute to condensational growth. These air-masses that have been enriched

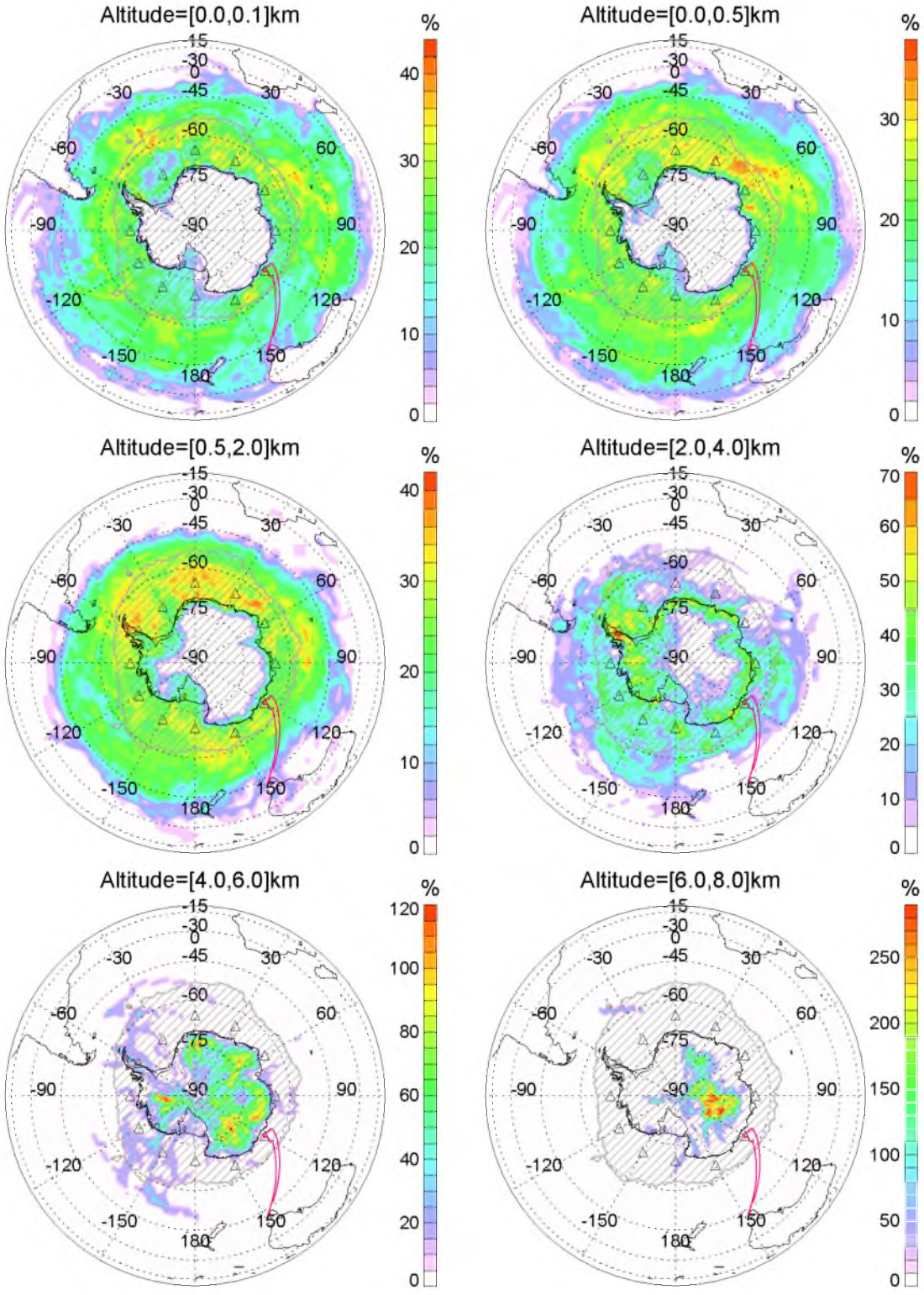

Figure 3.16: As in Figure 3.15, but includes numerous atmospheric altitude layers where [0.0,0.1] km refers to the integrated layer from 0 to 100 m above sea level. The two different transport pathways from the sea ice are observed, with northern transport to lower latitudes staying in the lower troposphere and Polar Front transport moving south in the higher altitudes.

in precursors, are found to split into two primary flows: one ascending with the Polar Front and moving south, and the second ascending above the MBL and moving north (therefore resulting in the low aerosol number concentrations observed north of the Polar Front in our dataset). It is likely then, that precursors ascending in the Polar Front are involved in both nucleation and growth chemistry (given the low aerosol surface area), while those moving north are oxidised and contribute primarily to aerosol growth. It is quite plausible then, that aerosols formed in this circulation scheme are able to grow to sizes where they could contribute substantially to the radiative budget of the Southern Hemisphere.

3.4 Summary and Discussion

The aerosol formation mechanism, described above as a combination of circulation patterns and chemistry, is summarised schematically in Figure 3.17. The magnitude of aerosol number concentrations reported here represents populations that are an order of magnitude higher than those currently simulated in global models over the Antarctic sea ice, suggesting a significant missing source present in our understanding of aerosol loading in this region. Depending on the precursor identity, closing the gap between simulations and observations could involve correction of transport factors, increasing known sources, or incorporation of new (halogen) chemistry.

3.4.1 Uncertainties

It is important to remember here that although an initial interpretation of the factors influencing the aerosol loading in the East Antarctic sea ice region was possible using the available data, the global datasets (e.g. ERA-Interim) utilised inherently have significant uncertainties, largely due to the sparseness of measurements in the region. As such, these results are far from conclusive but rather, suggest the need for further more detailed investigations. For example, many of the conclusions of this chapter are based on trajectory modelling, rather than measurements. These trajectory models utilise global meteorological datasets to provide information on the history of the air-mass affecting a particular location or region. Although these datasets are the best product available for such studies, they are based heavily on measurements, and where these measurements are sparse, such as over oceans or over and around Antarctica, resulting uncertainties can be significant. Consequently, the major circulation features affecting the Antarctic region are far from concluded and require significant long term, higher spatial density, measurements to understand further. Despite this, the understanding derived from this study is still useful as a first approximation, and is consistent with aerosol size distribution data, as well as

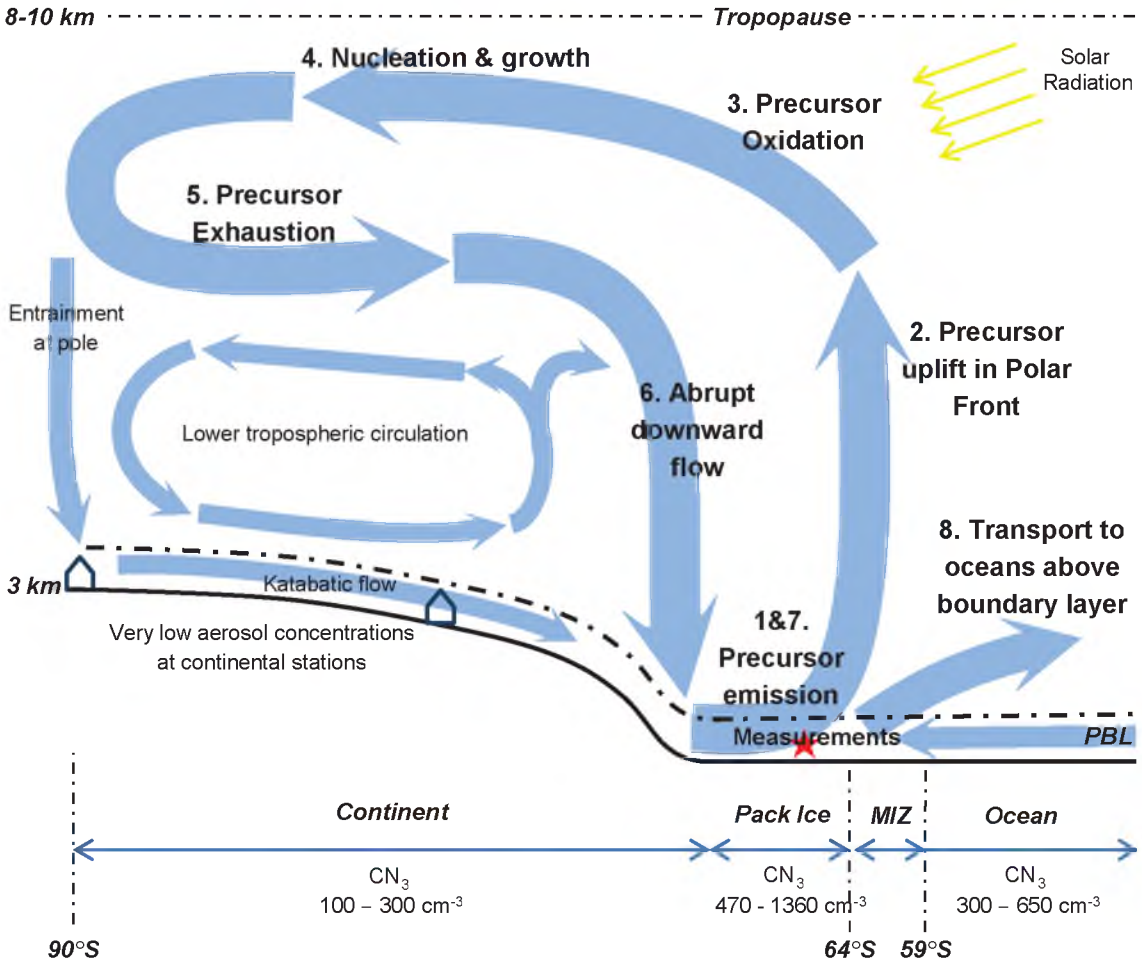

Figure 3.17: Proposed circulation and aerosol formation scheme over the Antarctic region. Precursor species emitted (**1**) in the biologically productive pack ice region and Marginal Ice Zone (MIZ), are uplifted with the Polar Front to the upper troposphere (**2**) where they are oxidised (**3**), likely by OH, O_3 or UV, to form a regional reservoir of aerosol precursors from around the continent. Air is transported south as aerosol formation begins (**4**) before descending at the pole. While the bulk air-mass stays high and moves north, a small portion moves to the polar surface, providing aerosols and precursors to the Antarctic continent. As the dominant air-mass moves north, the precursor reservoir is exhausted (**5**), halting aerosol formation and growth. Formed, non-growing aerosol populations within the air-mass descend abruptly at about 70°S (**6**) before reaching the sea-ice surface at the Antarctic coast. As the air-mass travels across the sea ice, it is re-enriched by unactivated precursor species (**7**). As aerosol populations ascend within this Polar Front, 50% are transported north to lower latitudes (**8**) where, with further addition and activation of precursors species, they continue to grow, interacting with radiation both directly, and indirectly by acting as CCN. Quoted aerosol number concentrations are ranges from the literature (continent Weller et al., 2011; Park et al., 2004 and ocean Weber et al., 1999) and 25th and 75th percentiles from this study (pack ice).

the spatial distributions of aerosols in the region derived from the literature.

The sparseness of data also significantly affects conclusions about source regions, since datasets such as those presented by Lana et al. (2011) are based on a limited number of measurements, particularly in the Southern Ocean and Antarctic regions. These datasets are 'filled in' using interpolation methods, however are weighted heavily to the handful of measurements made, which may be biased based on the discretion of potential authors in publishing all the available datasets (e.g. low concentrations may not be that interesting, so aren't published or made publically available). As such, conclusions made in this thesis about sources are purely speculative and further measurements and modelling work is necessary for conclusive evidence on this.

3.4.2 Sensitivity to climate change

The magnitude of measured aerosol number concentrations represents a previously unrecognised loading that could act as a significant source of aerosols and CCN to the Antarctic and Southern Ocean regions, potentially having substantial impacts on the radiative balance of the whole Southern Hemisphere. If true, the formation scheme, and thus the resulting aerosol concentrations, are likely to be sensitive to numerous factors, including the strength of emission sources, the locations of sea ice emissions, and circulation locations and patterns, all of which could change with future variations in the climate system.

As the climate changes, precursor emissions, particularly those associated with biological activity, could vary radically. For example, DMS is the most common precursor of summer aerosol in Antarctica and is emitted by marine phytoplankton in the ocean which, as surface waters saturate, results in a flux to the atmosphere. The species of phytoplankton greatly influence the magnitude of DMS production, with some species, such as *Phaeocystis*, being highly efficient producers due to harbouring high levels of the precursor dimethylsulphoniopropionate (DMSP) and having the enzyme able to perform the chemical conversion of DMSP to DMS (e.g. Stefels et al., 2007, and references therein). Phytoplankton growth is, as with any biological community, sensitive to numerous environmental conditions such as ocean temperature, ocean pH, and light and nutrient availability.

Recent modelling studies (Levasseur, 2011; Cameron-Smith et al., 2011) have found that with increased climate warming, phytoplankton communities shift poleward in the Southern Ocean due to changes in temperature, mixing, nutrient and light regimes. This shift moves diatom communities poleward, leaving flagellate-dominated communities, rich in DMSP, to thrive in the middle latitudes. The study also assumes shrinking Antarctic sea ice with climate warming, which favours growth of DMS producing *Phaeocystis* species at high latitudes. Overall these studies sug-

gest that as the ocean warms with climate change, DMS emissions from the Southern Ocean increase by around 30% between 30°S and 50°S, and up to 170% south of 60°S by 2100.

Although thorough in some aspects, the modelling studies above are still approximations of reality and, as with all current projections of future climate, cannot consider the complete complex system (Gattuso and Hansson, 2011; Doney et al., 2009). Factors such as ocean acidification and climate warming have commonly been considered as uncoupled consequences of increased atmospheric CO_2. Observational-based relationships between pH and DMS concentrations were established by Six et al. (2013) and used to perform Earth system model climate simulations in order to determine changes in future DMS emissions. They report that as ocean acidification increases, global DMS emissions decrease by an estimated 18($\pm$3)% by 2100 compared with pre-industrial times.

The spatial distribution of DMS emissions is also determined by light and nutrient availability, which in the Antarctic region are both affected by sea ice extent and volume. Changes in sea ice cover in the Southern Hemisphere are influenced by two major factors: climate change, and the recovery of the stratospheric ozone hole (Thompson et al., 2011). As climate change intensifies, sea ice extent in the Arctic is reducing, yet in the Antarctic, the reverse affect is occurring (Parkinson and Cavalieri, 2012), the causes of which are still under debate (Sigmond and Fyfe, 2014; Bitz and Polvani, 2012; Bintanja et al., 2013; Holland and Kwok, 2012). Things get even more complicated upon consideration of the recovery of the stratospheric ozone hole, which because of its complex interactions with radiation and atmospheric dynamics, can result in either increases or decreases in sea ice in the Antarctic (Thompson et al., 2011). These changes in ice extent and density can dramatically alter the chemical environment and nutrient and light availability in this highly biological productive region, resulting in further uncertainty in the distribution and strength of DMS emissions in this region.

Atmospheric dynamics and circulation can also be affected by both the recovery of the stratospheric ozone hole and climate change. Changing the general dynamics of the atmosphere through longer-term variations in the radiative balance could change the location of the Southern Hemisphere's Polar Front and other circulation patterns, such as those described in this work. The recovery of the hole in the stratospheric ozone layer, for example, will reduce the amount of incoming radiation reaching the surface, therefore producing a surface cooling effect, and pushing the Polar Front equatorward (Thompson et al., 2011). The reverse effect occurs with climate warming caused by greenhouse gas increases, with numerous studies, using a variety of methods, reporting a widening of the Hadley Cell circulation, and thus a poleward shift in Polar Front (Seidel et al., 2008; Lucas, Timbal, and Nguyen,

2014; Davis and Rosenlof, 2012; Choi et al., 2014; Thompson et al., 2011).

The high aerosol loading, if a result of the aerosol formation scheme outlined in Figure 3.17, will depend on the co-location of strong emission sources (such as those found in the Antarctic sea ice zone) and the Polar Front, which transports emissions into the free troposphere where nucleation chemistry can occur. A decoupling of these features, caused by opposing changes caused by anthropogenic influences such as those described above, could significantly influence this natural aerosol formation scheme. If changes were dramatic enough to completely turn off this formation mechanism, the large net cooling effect of these aerosols through both ARI and ACI would cease. Since these aerosols are transported to a wide area, the resulting warming may be a regional or hemispheric phenomenon, and could result in a new and prominent negative feedback mechanism of anthropogenic climate change.

3.4.3 Influence on regional physics and chemistry

Aerosols are necessary for cloud formation in all parts of the atmosphere, including the stratosphere where Polar Stratospheric Clouds (PSC) form. PSCs are a vital component of the formation of the stratospheric ozone hole, making the CCN onto which they form important. If aerosols formed through the mechanism described in this chapter were to make it into the stratosphere, then they could contribute directly to PSC formation and thus ozone degradation. Wang et al. (2008) have reported a correlation between Antarctic PSC occurrence and deep tropospheric cloud systems, suggesting that these cloud systems not only cool the lower stratosphere, favouring PSC formation, but also transport lower tropospheric air to the lower stratosphere, providing a pathway to the stratosphere for Antarctic free tropospheric aerosols. Since stratospheric ozone destruction is a seasonal process, the seasonality of the aerosol formation processes, combined with the lifetimes of aerosols in the stratosphere, would be important considerations to determine the impact this mechanism has.

Recent modelling work by Schofield and Fisher (2014) attempted to simulate elemental mercury (Hg^0) in the boundary layer to compare to atmospheric measurements made as part of SIPEXII. Model results showed very good agreement during periods in the Ferrel cell, but almost no correlation to measurements within the Polar Cell. Heterogeneous aerosol chemistry is a well known, but poorly understood atmospheric science involving a multitude of gaseous species (Subir, Ariya, and Dastoor, 2012). Given the distinctly different aerosol loading in the Polar Cell that is not currently simulated in global models, it is possible that heterogeneous chemistry is occurring with the Hg^0, and that this chemistry isn't currently understood or captured in the model. Further studies to understand this complex chemistry are

required.

Currently, the sources of CCN in the Southern Ocean are uncertain, with both local sources and long-range transport possible. Some modelling studies have attributed most of the CCN to sea salt (Pierce and Adams, 2006; Merikanto et al., 2009), however modelling and limited observational studies suggest that the majority of CCN in the Southern Ocean are nucleated in the free-troposphere from DMS and continental sulfate sources, before being entrained into the boundary layer (Korhonen et al., 2008; Clarke et al., 1998). It is possible that precursors, produced in the sea ice region, and aerosols produced by the scheme described in this chapter, are transported north to the Southern Ocean where they nucleate and grow, respectively, resulting in the observed CCN loading of the region.

The largest contribution to the uncertainty of the effective radiative forcing by aerosols is caused by uncertainties in pre-industrial natural aerosols (Ghan et al., 2013; Carslaw et al., 2013). In the Southern Ocean, processes that lead to CCN properties are poorly understood (Marchand et al., 2014), and current modelling simulations underestimate general aerosol loading and cloud properties (Russell et al., 2013). The proposed aerosol nucleation scheme described in this work, may dramatically decrease the uncertainty associated with natural aerosols in this region.

The measurements reported here represent the first aerosol focussed study in the East Antarctic sea ice region. Measurements in this study reveal that this region shows a distinctly different atmospheric character compared with both adjacent regions of the Antarctic continent and the Southern Ocean. The distinct atmospheric character, combined with the dearth of measurements in the region, highlights the importance of further study through long and short-term measurement programs and modelling studies. These studies are important for understanding a large spatial region, but are particularly crucial because of the impact this region has on the vast Southern Ocean. This study's findings of the highest measured spring-time aerosol concentration could be a significant missing piece of the puzzle of Southern Hemispheric atmospheric chemistry.

Chapter 4

Modelling Background Sub-micron Aerosols

Abstract

A global chemical transport model, GLOMAP, is utilised to try to further understand the drivers and impacts of the unexpectedly high aerosol concentrations described in Chapter 3. In the Antarctic region, secondary aerosol is produced primarily by the high regional emissions of dimethyl sulfide (DMS). The control simulation, which utilised the most recent DMS climatology of Lana et al. (2011), was unable to reproduce the observed number concentrations, being an order of magnitude too low. The control model was then modified to allow a flux of DMS through the sea ice - a change that is supported by measurements in the literature. This perturbation increased number concentrations by a factor of two over the continent, however in the sea ice region, concentrations increased by only 40%, well below that necessary to match observations. These model results were compared to others found in the literature that utilised the ion-mediated nucleation (IMN) mechanism (Yu and Luo, 2010) which has been reported to be particularly important in polar regions. Simulations using the IMN mechanism drastically increased number concentrations, yielding similar values in summer compared to our spring-time observations, however simulated spring-time values were still a factor of three too low. Both model simulations are driven by the seasonal cycle of DMS, and the temporal offset of number concentrations suggests that non-DMS chemistry, possibly involving iodine, is most likely responsible for the spring-time observations.

Author Contributions

This modelling work was performed in collaboration with Matthew Woodhouse from CSIRO Marine and Atmospheric Research (Aspendale, Victoria, Australia). Experimental design was performed primarily by myself, in consultation with M. Wood-

house. Simulations were coded and run by M. Woodhouse, remotely at the University of Leeds. Analysis of output data was performed by myself, and interpretation was validated in consultation with M. Woodhouse. Additional modelling data was also obtained from previous studies by Yu and Luo (2010).

4.1 Introduction to Atmospheric Models

Atmospheric models incorporate the current scientific understanding of the atmosphere into a computer algorithm which simulates the conditions of the Earth's atmosphere. They can be used to understand specific processes, and by comparison to real world observations, can help identify weaknesses in the scientific understanding of the world around us. By iteratively running models and comparing them to real-world observations, scientific understanding, and thus our ability to model the atmosphere, constantly improves.

Although an approximation to the actual atmosphere, models have the advantage over measurements in that they are not as limited in space and time and can give information on processes or locations were measurements are difficult. Given it is an approximation, care must be taken when interpreting model data, particularly in locations that are validated by a low number of, or no, measurement data, such as the Antarctic and Southern ocean region. Models have the advantage that measurements performed in the field, in laboratories, or in theoretical calculations, are all synthesised into a single understanding of the atmosphere which can then be tested.

The atmosphere is a complex system, and modelling such a system is difficult. To get a best estimate of the atmosphere in a model, a number of factors must be considered including dynamics, *in-situ* chemistry and emission and removal processes. Treatment of these factors varies between models, and full treatment of a given process is often weighed against computing time and costs, resulting in simpler parameterisations.

4.1.1 Modelling Antarctic Aerosol Processes

The modelling experiment undertaken in this study aimed to answer two primary questions concerning the results described in Chapter 3:

1. What is the chemical nucleation mechanism leading to the observed number concentrations?

2. What is the impact of these high aerosol concentrations on the radiative balance of the Antarctic and Southern Ocean region?

To answer these, a number of smaller questions must first be asked, the responses to which will determine our ability to answer the primary questions. Some of these include:

1. Do the chemical schemes currently included in state-of-the-art models produce the observed number concentrations in the Antarctic sea-ice? And does the model replicate the important meteorological transport in this region?

2. If the answer to 1 is "no", then can we perturb the model system by adding a new source, based on observations published in the literature, that still utilise the known chemistry and thereby replicate the observations?

The results of this modelling study were able to partially answer the first of these primary questions. However, to answer both questions, it was determined that significant model development was necessary which was beyond the scope of the present thesis. Nevertheless, results from the model did prove useful in understanding the chemistry in the Antarctic region. These results will be outlined below.

4.2 Model Description and Setup

In this section, an overview of the model configuration is given before details of each sub-component is outlined. Acronyms may not be defined in the overview paragraph (for the sake of brevity) but will be outlined in later sections where appropriate.

This study utilised the GLObal Model of Aerosol Processes microphysical aerosol scheme (GLOMAP; utilising the modal version) (Mann et al., 2010; Mann et al., 2012) within the United Kingdom Chemistry and Aerosol sub-model (UKCA) of the Met Office Hadley Centre Global Environmental Model (HadGEM3). The tropospheric chemistry-aerosol configuration of HadGEM3-UKCA was identical to that used by Mann et al. (2014), but was updated to version 8.4 of the Unified Model which included full coupling for radiative forcing via aerosol-radiation (Bellouin et al., 2013) and aerosol-cloud interactions (West et al., 2014), and improved aerosol scavenging (Kipling et al., 2013). Model resolution was 1.25° in latitude and 1.875° in longitude, with 38 vertical levels extending to approximately 85 km. Meteorology was nudged to the ERA-interim dataset. Sea-surface dimethyl sulfide (DMS) emissions were calculated online from the Lana et al. (2011) DMS climatology and the Liss and Merlivat (1986) sea-air flux parameterization. The binary homogeneous sulfuric acid nucleation parameterization of Kulmala, Laaksonen, and Pirjola (1998) was used in conjunction with the organic-mediated boundary layer nucleation parameterization of Metzger et al. (2010). The baseline simulation included

no DMS emission through sea-ice. As part of the study, DMS emission from sea-ice was included, proportional to the underlying seawater DMS concentration, derived implicitly from the literature (Trevena and Jones, 2012; Nomura et al., 2012).

The simulations presented here were run from 2007 through 2009 with a 4 month spin-up. At the outset, simulations were designed to run up to the end of 2012, with output temporal resolution at the model's full capacity of 3 hour time steps during the SIPEXII campaign period (September - November, 2012), and monthly averages at all other times. Unfortunately, bugs in the code (likely the end of one of the input datasets) prevented simulations running past the end of 2009. Since this bug had been observed before, it could be confidently concluded that data up to this point was unaffected and could be used in the analysis. This meant that comparison to SIPEXII data was not possible. This didn't prove to be a major limitation in addressing the scientific questions though, since all the available model data showed similar seasonal patterns and underlying datasets showed no deviations that would result in any significant perturbations from these trends. The same simulations are currently being setup to run on Australia's global weather model, the Australian Community Climate and Earth-System Simulator (ACCESS), to repeat the experiments without missing data and to help further develop this model.

4.2.1 HadGEM3

Version 3 of the Hadley Centre Global Environment Model (HadGEM3, http://goo.gl/M5LWZc) comprises a family of models that include a range of complexity levels, all within a common framework. HadGEM3 includes a coupled ocean-atmosphere configuration that can be a simple ocean-troposphere type, or an Earth-system type that could include dynamic oceans, vegetation, biology, atmospheric chemistry and sea ice dynamics. Each of these components is itself its own sub-model, with the atmospheric physics being driven by the Unified Model (UM), and composition and chemistry driven by UKCA. In HadGEM3, ocean modelling is performed by NEMO (Nucleus for European Modelling of the Ocean, http://www.nemo-ocean.eu/), and sea ice is prescribed by CICE (Community Ice CodE, http://oceans11.lanl.gov/trac/CICE), with coupling performed by the OASIS coupler (https://verc.enes.org/oasis). Further details of the atmospheric components of HadGEM3 are outlined below.

4.2.2 The Unified Model

The Unified Model (UM, http://goo.gl/Fu3wgJ) is a numerical modelling system developed and used by the United Kingdom Met Office. The UM models weather and climate, and is fundamentally designed to be a 'seamless' solution to

simulations at a range of time and spatial scales, requiring a simple configuration change for the desired scale, rather than a whole different model. Ocean and surface ice fields can be prescribed or the UM can be coupled with a variety of ocean and ice models, enabling earth system modelling. Meteorology can either be modelled entirely, or 'nudged' using reanalysis data of observational data (e.g. ERA-Interim).

The model spatial resolution is graphically depicted in Figure 4.1, with detailed vertical resolution outlined in Table 4.1. This study used a resolution of 1.875 degrees and 1.25 degrees in longitude and latitude respectively, with 38 vertical levels (up to approximately 39 km) scaled on a hybrid sigma-pressure grid (terrain following lower levels with a transition point well above land topography to pressure defined levels). Meteorology was nudged to ERA-Interim datasets, and prescribed AMIP-II sea-ice fields and sea-surface temperatures were utilised (described below).

4.2.3 UKCA

The United Kingdom Chemistry and Aerosol (UKCA, ,http://www.ukca.ac.uk) model simulates atmospheric composition and chemistry in both the troposphere and stratosphere. It is primarily run within the Hadley Centre Global Environment Model (HadGEM) which incorporates the UM. UKCA comprises of a comprehensive set of chemical reactions, emissions and deposition processes. The scheme simulates O_x, HO_x and NO_x cycles, the oxidation of numerous hydrocarbons as well as active photochemistry.

The model has the capacity to include the GLOMAP aerosol sub-model which enables sulfur nucleation chemistry. The sulfur chemistry included in this study was concerned primarily with the emissions of DMS and therefore, the sulfur chemistry scheme, in particular the DMS-SO_2-H_2SO_4-aerosol formation scheme, was enabled. Prescribed DMS emissions were necessary to initiate this chemistry and were updated to the most recent climatology based on Lana et al. (2011).

4.2.4 GLOMAP

GLOMAP (the GLObal Model of Aerosol Processes) (Mann et al., 2010; Mann et al., 2012) is an aerosol microphysics model that is built into several host models that provide other parameters such as meteorology and composition (in this study, we used the UM and UKCA as the host model). It is one of a new breed of aerosol models that accounts for both the mass and number distributions of aerosol populations, enabling modelling of particle growth and composition and the simulation of more realistic aerosol cloud interactions (via changes in both primary and secondary CCN).

GLOMAP comes in two versions: bin resolved (GLOMAP-bin) and modally

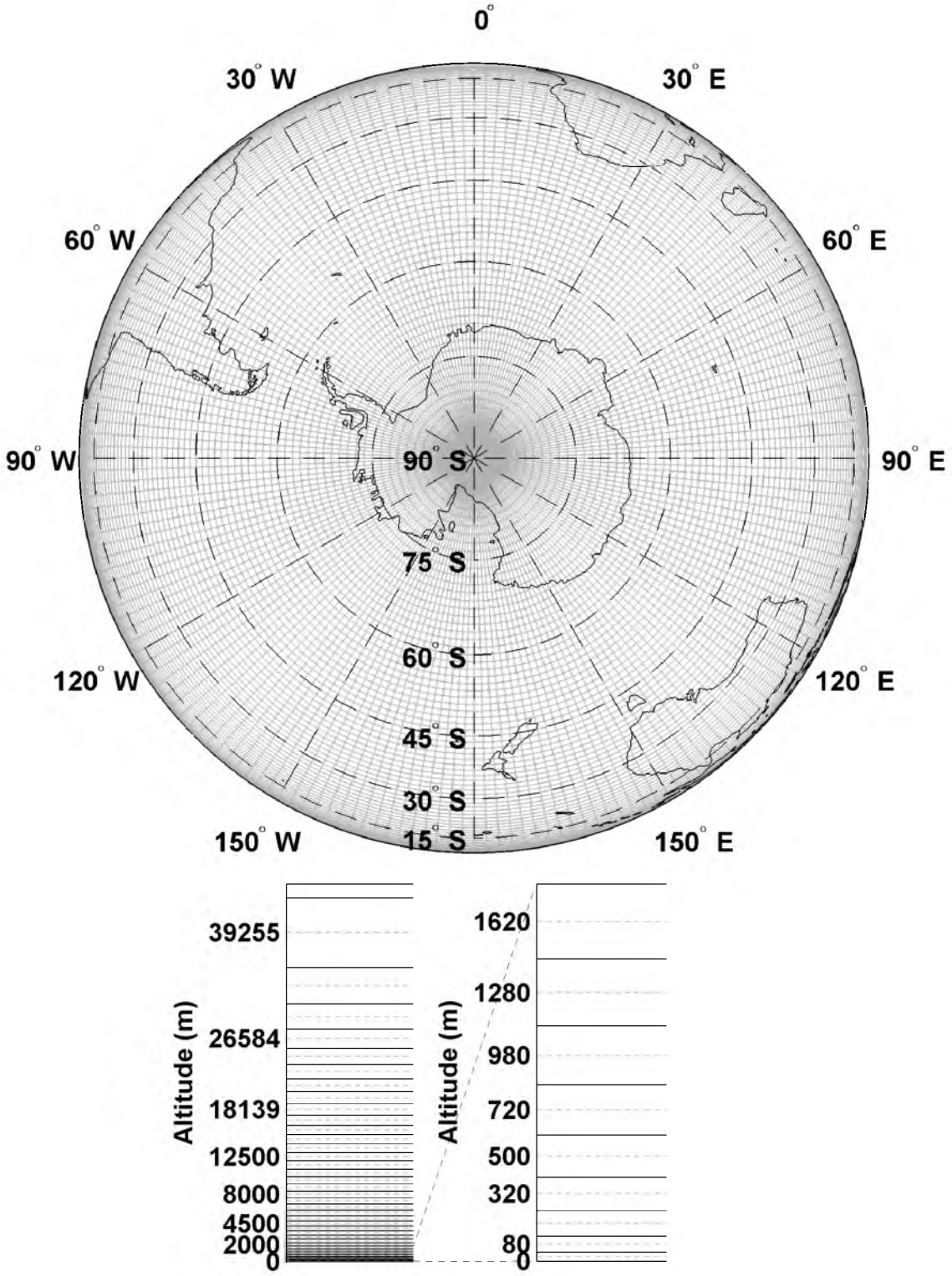

Figure 4.1: Model grid projections.

resolved (GLOMAP-mode). Bin resolved gives high resolution size distribution information at the price of computation time. The modal version, used in this study, includes aerosol microphysics with dynamically varying particle size, but instead of being binned, particle size distributions are parameterised by a series of log-normal

Box #	Mid Point	Lower Boundary	Upper Boundary	Box height
1	20	0	40	40
2	80	40	120	80
3	180	120	240	120
4	320	240	400	160
5	500	400	600	200
6	720	600	840	240
7	980	840	1120	280
8	1280	1120	1440	320
9	1620	1440	1800	360
10	2000	1800	2200	400
11	2420	2200	2640	440
12	2880	2640	3120	480
13	3380	3120	3640	520
14	3920	3640	4200	560
15	4500	4200	4800	600
16	5120	4800	5440	640
17	5780	5440	6120	680
18	6480	6120	6840	720
19	7220	6840	7600	760
20	8000	7600	8400	800
21	8820	8400	9240	840
22	9680	9240	10120	880
23	10580	10120	11040	920
24	11520	11040	12000	960
25	12500	12000	13000	1000
26	13520	13000	14040	1040
27	14581	14040	15122	1082
28	15695	15122	16268	1146
29	16875	16268	17483	1215
30	18139	17483	18794	1311
31	19503	18794	20212	1417
32	20990	20212	21769	1557
33	22626	21769	23483	1715
34	24458	23483	25433	1950
35	26584	25433	27734	2301
36	29219	27734	30704	2970
37	32909	30704	35113	4409
38	39255	35113	43396	8283

Table 4.1: Approximate model altitude box heights (rounded to nearest metre). Note that these heights are only a guide as the grid is terrain following, leading to compression of the lower levels as terrain height increases.

modes, each covering defined regions of the particle radius range (see Table 4.2). Because of this parameterisation, GLOMAP-mode becomes computationally efficient enough to enable integration into coupled aerosol-climate simulations such as those

run in this project.

The modal schemes used here carries aerosol component masses and number concentrations in 7 modes, with aerosol composition divided into a number of different bins including sulfate (SU), black carbon (BC), particulate organic matter (POM), sea salt (SS), dust (DU) and water (WT). Each mode that covers a defined particle radius range, also has a prescribed composition which is outlined in Table 4.2.

Table 4.2: Standard aerosol configuration for GLOMAP-mode. Size ranges for each mode are described with the geometric mean diameter, D. Adapted from Mann et al. (2010).

Mode	Size Range	Composition	Soluble?
Nucl-sol	$D < 10\ nm$	SU, POM	Yes
Aitken-sol	$1\ nm < D < 100\ nm$	SU, BC, POM	Yes
Accum-sol	$100\ nm < D < 1\ \mu m$	SU, BC, POM, SS, DU	Yes
Coarse-sol	$D > 1\ \mu m$	SU, BC, POM, SS, DU	Yes
Aitken-ins	$10\ nm < D < 100\ nm$	BC, POM	No
Accum-ins	$100\ nm < D < 1\ \mu m$	DU	No
Coarse-ins	$D > 1\ \mu m$	DU	No

The host chemical transport model (in this case, HadGEM3-UKCA) calculates transport and the majority of gas phase chemistry, while GLOMAP itself simulates aerosol processes including size-resolved primary particle emissions, new particle formation, condensation, coagulation, cloud processing, dry deposition, sedimentation, and both nucleation and impaction scavenging. Full details of how these processes are included in the model are outlined by Mann et al. (2010). As part of the aerosol process calculations, GLOMAP includes a handful of gas phase chemical reactions that are important for the sulfur (and organic) chemistry being considered during this study. These reactions are outlined in Table 4.3.

Table 4.3: Gas phase chemistry used in GLOMAP-mode as described by Mann et al. (2010). An involatile organic species, SEC-ORG, is generated from monoterpene (MONOTER) oxidation at 13% yield following reaction rates for α-pinene.

Reaction	Reference
$DMS + OH \longrightarrow SO_2$	Atkinson et al. (1989)
$DMS + OH \longrightarrow 0.6SO_2 + 0.4DMSO$	Pham et al. (1995)
$DMSO + OH \longrightarrow 0.6SO_2 + 0.4MSA$	Pham et al. (1995)
$DMS + NO_3 \longrightarrow SO_2$	Atkinson et al. (1989)
$CS_2 + OH \longrightarrow SO_2 + COS$	Pham et al. (1995)
$COS + OH \longrightarrow SO_2$	Pham et al. (1995)
$SO_2 + OH + M \longrightarrow H_2SO_4$	Pham et al. (1995)
$MONOTER + OH \longrightarrow 0.13SEC\text{-}ORG$	Atkinson et al. (1989)
$MONOTER + NO_3 \longrightarrow 0.13SEC\text{-}ORG$	Atkinson et al. (1989)
$MONOTER + O_3 \longrightarrow 0.13SEC\text{-}ORG$	Atkinson et al. (1989)
$HO_2 + HO_2 \longrightarrow H_2O_2$	Jones et al. (2001)

4.2.5 Input Datasets

A number of additional datasets were required to run the model including sea ice and emission data. Many of these datasets are based on observational data and therefore allow the model to simulate conditions closer to reality than without them. The relevant datasets included in this study are outlined below.

4.2.5.1 ERA-Interim Reanalysis

The European Centre for Medium-range Weather Forecast (ECMWF, Reading, UK, http://goo.gl/FZVM8o) is a research institute and operational service that produces and disseminates numerical weather predictions for its 34 member states. The institute produces a multitude of products, including climate reanalysis datasets. These datasets utilise forecast models and data assimilation systems to reanalyse archived observations, resulting in global datasets describing the recent history of the earth system, including the atmosphere, land surface and the oceans. Reanalysis data provide a multivariate, spatially complete and coherent record of the global atmospheric circulation and are often considered to produce the closest global dataset to reality. Archived observations assimilated into the reanalysis product range considerably in terms of spatial and temporal coverage as well as in the accuracy and precision of measurement. These observations can range from point *in-situ* surface observations to modern high-resolution satellite data sets and everything in-between. The final product has global coverage and contains the best estimates of climate variables including atmospheric parameters such as air temperature, pressure and wind

at different altitudes, and surface parameters such as rainfall, soil moisture content and sea surface temperatures.

The ECMWF Re-Analysis Interim (ERA-Interim) dataset is a publicly available, global atmospheric reanalysis that runs from 1979, and is continuously updated in real-time. It produces output at a 3 hour time-resolution, and has a spatial resolution of approximately 79 km spaced on a reduced Gaussian grid, with 60 vertical levels from the surface up to 0.1 hPa. The atmospheric model is also coupled to an ocean-wave model for improved output. Further details of the ERA-Interim dataset are outlined by Dee et al. (2011).

4.2.5.2 DMS Climatology

The recently published DMS climatology of Lana et al. (2011) was used in this study, being updated from the previously included climatology of Kettle et al. (1999). This updated climatology utilises the 3 fold increase in observational data points in the global surface ocean DMS concentration database over the last decade (15 000 to 47 000 data points). Both interpolation and extrapolation methods are applied to the discrete data to produce spatially coherent geographic maps for each month of the 12 month climatology. The most significant concentrations in this dataset are at high latitudes. It is important to note that the concentrations at the higher latitudes, particularly in the southern hemisphere, are often based on only a few data points that gives rise to some potentially inaccurate representations in these regions. Resulting sea surface concentrations are shown in Figure 4.2, which lead to the previously presented (Figure 3.12) emissions calculated using the parameterisation of Liss and Merlivat (1986).

4.2.5.3 AMIP-II Sea Ice and Sea Surface Temperature dataset

The Atmospheric Model Intercomparison Project (AMIP) is a standard experimental protocol for global Atmospheric General Circulation Models (AGCMs). AMIP allows a framework for systematic analysis of model output and includes almost universal participation of the international climate modelling community since 1990.

AGCMs are constrained by sea surface temperatures and sea ice. AMIP sea ice and Sea Surface Temperature (SST) data are sourced from passive satellite measurements (provided by ECMWF, NCEP, and UK Met Office) and are supplied in two distinct sets - observational and boundary conditions. The observational data set provides monthly mean data from satellite based measurements, while the boundary conditions linearly interpolate between monthly means to enable suitability for model input.

The AMIP-II dataset is an updated version of the AMIP-I dataset. It is available

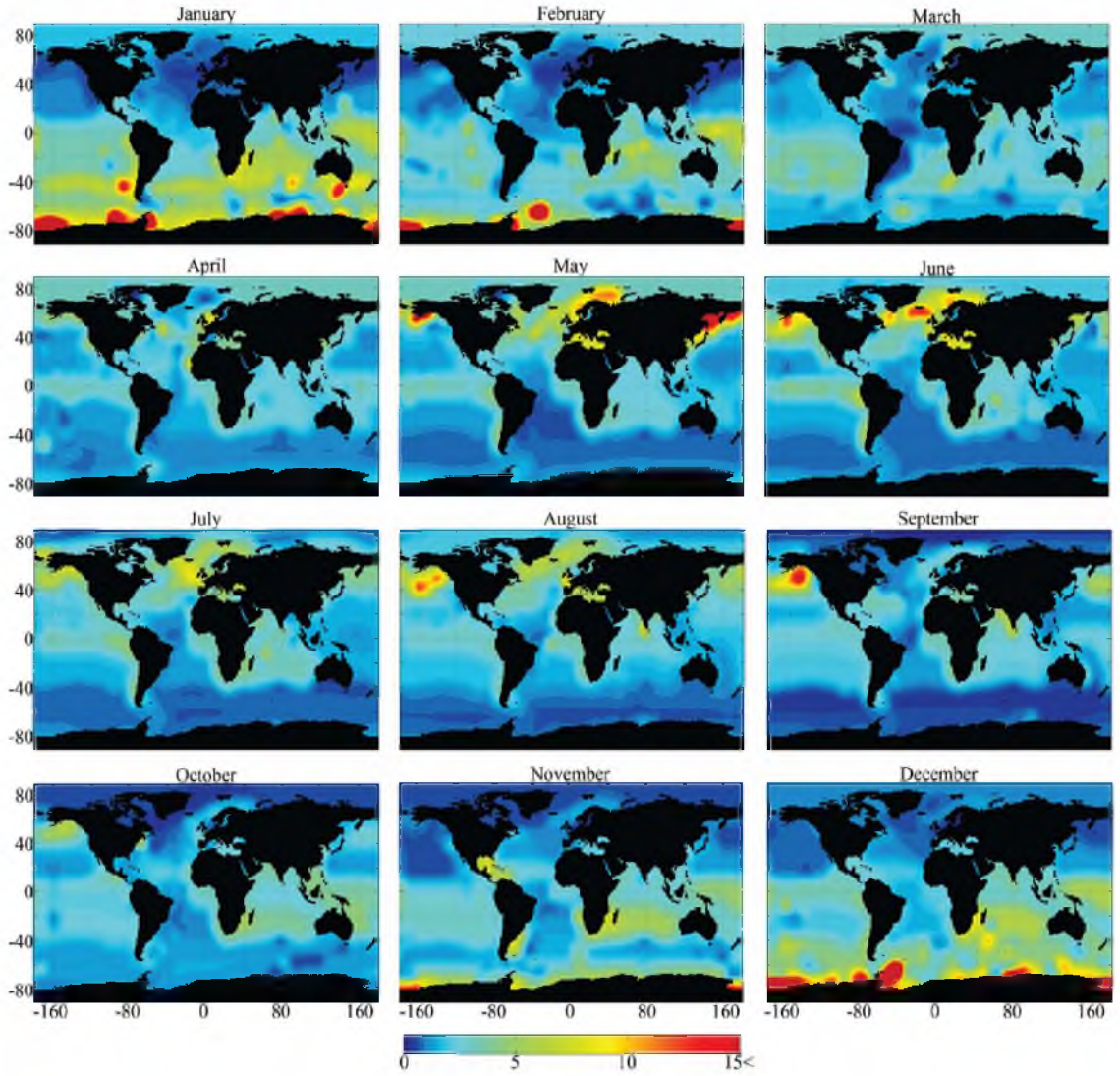

Figure 4.2: Monthly climatology of surface ocean DMS concentrations (nM) based on climatologies of Lana et al. (2011). Scale is capped at 15 nM. Emissions based on these ocean concentrations are shown in Figure 3.12.

at a spatial resolution of $1° \times 1°$ and at various temporal resolutions from one day out to monthly, both sufficient for this study. Further details of this dataset are out of the scope of this study but can be found online (http://goo.gl/NXvpz2).

4.2.6 Model Simulations

As part of this model study, we are aiming to validate the circulation features described in Chapter 3 as well as determine whether known processes can explain the significant particle concentrations observed in the Polar Cell. We hypothesise from back-trajectory calculations that the process responsible for aerosol nucleation is occurring around the continent and although not the only candidate, the most likely precursor is DMS. Due to the limitations in chemistry schemes associated with running this global model, DMS chemistry was the only chemical mechanism

able to be tested to try to explain the measurements. Since most aerosol studies in the Antarctic identify sulfur as the main aerosol component (see Chapter 3), this limitation may not be significant.

A number of different simulations were run to assess the impact of DMS chemistry on the aerosol loading in the region. These simulations included a control run, which was found not to reproduce observed number concentrations, and perturbed runs, which aimed to reproduce observations by changing the DMS loading in the region with varied emissions.

4.2.6.1 Control run

The control run aimed to set a baseline with the setup and input parameters outlined above, and determine what aerosol loading could be produced in the sea ice region with the standard emissions and nucleation chemistry included in the model. It is important to understand how the DMS emission is calculated in the model to enable an effective perturbation to be made. The standard emission code (Algorithm B.1) calculates emissions online from the DMS ocean concentration climatology and the sea-air flux parameterisation of Liss and Merlivat (1986) for each grid box such that,

$$DMS_{E_{comb}} = L_f.DMS_{E_{land}} + (1 - L_f).DMS_{E_{ocean}}.(1 - I_f) \tag{4.1}$$

where $DMS_{E_{comb}}$, $DMS_{E_{land}}$, $DMS_{E_{ocean}}$ is the total, land and ocean emissions of DMS respectively and L_f and I_f are the fractions of land and ice in a given grid box, respectively. The calculation sets emissions from land to zero and uses sea ice fraction to mask DMS emissions from the ocean. In the sea ice region, this setup results in the fraction of a given grid-box that is covered in sea ice to have zero emissions. It is this latter characteristic of the model, an assumption of zero flux through sea ice, that is utilised to alter the system in the perturbation simulations.

4.2.6.2 Perturbing the system

The magnitude of aerosol concentrations measured in this study is higher than any previously observed in the Antarctic and Southern Ocean region. Because of this, it is likely that modelled concentrations are too low, and that an additional source of aerosols is required. Since measurements show that sulfur aerosols are the most common in the region, and sulfur chemistry is included by default in the model due to its ubiquity throughout the global atmosphere, it is sensible to add a source of DMS to the model in order to perturb the system.

It would be desirable to include a perturbation that is local to the region of interest. Any perturbation made to the flux parameterisation or DMS climatology would have global affects and could be unrealistic. The zero flux through the sea

ice that the model assumes has the potential to be altered to more realistic values that also have the ability to provide an additional source localised only to polar regions. A search of the literature reveals a number of measurements that show a non-negligible gas flux (e.g. CO_2 and DMS) through the sea ice (Semiletov et al., 2004; Nomura, Yoshikawa-Inque, and Toyata, 2006; Nomura et al., 2010; Zemmelink et al., 2006; Loose et al., 2011; Miller et al., 2011; Papakyriakou and Miller, 2011).

The flux of DMS from the sea ice is a complex process that involves *in-situ* production from biological communities within the ice itself, diffusion from sea water beneath the ice, and transport between sea water, ice, brine and atmosphere (e.g. Levasseur, Gosselin, and Michaud, 1994; Tison et al., 2010; Curran and Jones, 2000; Semiletov et al., 2004; Zemmelink et al., 2008; Trevena and Jones, 2012). The parameterisations of DMS and sea ice in the model provided limited options as to the implementation of a flux from the sea ice. DMS is included in the model only as surface sea water concentrations, while sea ice is parameterised only as grid fraction, with no specification of properties such as age, thickness or snow cover. Consequently, a flux was approximated that was proportional to the underlying sea water DMS concentrations. This flux parameterisation was approximated based on literature values (Table 4.4) and a reasonable first guess for an upper limit emission factor was 1.6 $\mu mol.m^{-2}.d^{-1}$ for every 1 nM ocean DMS concentration. This factor was calculated as the average (outliers excluded) of the high emissions found in the literature (Trevena and Jones, 2012). Additional sensitivity studies were conducted using a factor of 10 and 100 lower emission factors that reflected the lower end of literature estimates (e.g. Nomura et al., 2012). The resulting formulation becomes,

$$DMS_{E_{comb}} = L_f.DMS_{E_{land}} + (1-L_f).DMS_{E_{ocean}}.(1-I_f) + I_f.DMS_{conc}.I_{DMSflux}.I_{DMSscalar} \quad (4.2)$$

where DMS_{conc} is the concentrations of DMS in the underlying surface ocean, $I_{DMSflux}$ is the literature derived flux of DMS through the sea ice, and $I_{DMSscalar}$ is a factor that allows simple scaling of this flux. The altered code is presented in Appendix Algorithm B.2.

Interestingly, DMS concentrations are likely to be higher in water under sea ice (compared to open ocean) because of biological communities resident in the sea ice (Nomura et al., 2012). It is factors such as these that are not currently included in the DMS climatology but serve, together with better parameterisations of sea ice type and thickness, as areas of future model development.

Table 4.4: Standard aerosol configuration for GLOMAP-mode.

DMS Ocean Concentration (nM)	**DMS Flux** $\mu mol.m^{-2}.d^{-1}$	**Ice Type**	**Reference**
2.9-11.2	< 1	Fast ice	Nomura et al. (2012)
9	16	Fast ice	Trevena and Jones (2012)
31	54	Pack ice	Trevena and Jones (2012)
3	27	Ocean	Trevena and Jones (2012)
2	3	October mean	Trevena and Jones (2012)
16	23	November mean	Trevena and Jones (2012)
31	45	December mean	Trevena and Jones (2012)
7	6	January mean	Trevena and Jones (2012)
36	23.1	Sea ice leads	Zemmelink et al. (2005)
N/A	23.1	Polynia (partial ice cover)	Tortell et al. (2012)
N/A	11	Multi-year ice floe	Zemmelink et al. (2008)
	$< 1 - 30$		
N/A	9.4	seasonal ice zone	Curran and Jones (2000)
	1.7-49		

4.3 Results

4.3.1 Control Run

Figure 4.3 shows the CN number concentrations in both an aerial map projection and a latitudinal cross-section for two months, taken as case-studies, that represent the spring and summer. These two case studies are good representations of the spatial distribution of simulations across seasons and between years, and represent the upper limit of the magnitude of inter-annual variability of model results (Appendix Figures B.1 and B.2). If these upper limit case studies are not comparable to experimental results, then it is highly unlikely that the current model parametrisations can reproduce observations.

Surface number concentrations are found to be low in the region, with regional maxima (south of 50°) of ~300 cm^{-3} and local hotspots in the Ross Sea (approx. 77°S, 165°E) of over 500 cm^{-3}. Over the sea ice however, number concentrations during the summer maximum reach barely above 100 cm^{-3}, with springtime concentrations well below that.

Cross-sections show that concentrations above 3000 cm^{-3} exist in the free-troposphere above the continent, where previous studies (e.g. Ito, 1993) and measurements in this study (Chapter 3) have proposed nucleation in the region to occur. These significant concentrations are restricted to the free-troposphere and are not observed to go far below 3 km. Surface concentrations are found to be an order of

magnitude lower.

It is important to remember that the model simulations are nudged to the same dataset as the back-trajectories of Chapter 3 that revealed the free-troposphere as the likely source region. Small signals are occasionally present in the cross-sectional CN plots (e.g. Figure 4.3B) that may indicate the presence of the important downward flow near the coast, although these patterns are very weak. The low concentrations at the surface then, are likely a combination of insufficient precursor sources, and incorrect transport. There is little that can be done to correct the transport in this study, however an additional source of DMS can be added relatively simply.

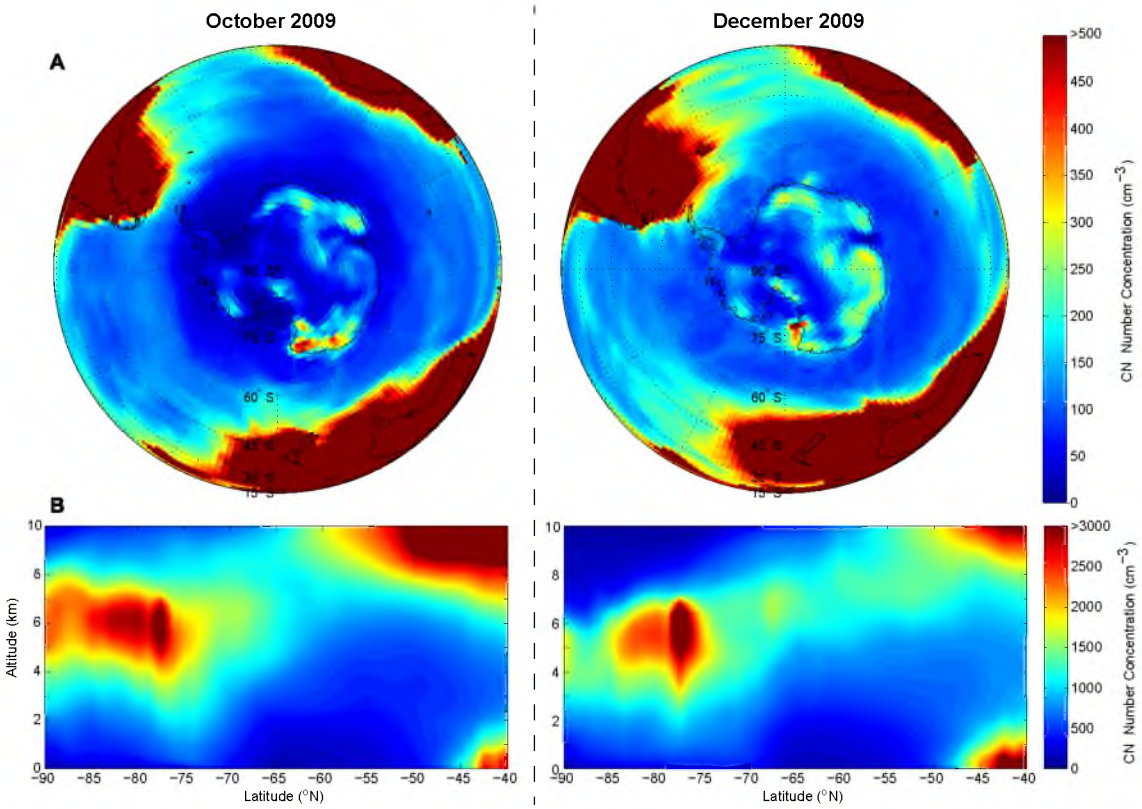

Figure 4.3: Total CN number concentrations output from the model for two months of the year, including spring (October), as measured, and the annual maximum in summer (December). **A:** Aerial view of the surface layer (0-40 m above ground level) aerosol shows concentrations locally only reach up to 500 cm^{-3}, with regional maxima up to 300 cm^{-3}. High concentrations are limited to the continent and predicted concentrations above the sea ice are below 100 cm^{-3}. **B:** Latitudinal cross-section of aerosol number concentrations with altitude (km above surface), showing the Eastern hemisphere only (0-180°E). High number concentrations are observed in the free-troposphere above 3 km altitude, indicative of nucleation. No such concentrations are observed below this. Note that the spring 2009 plot shows anomalously high concentrations in the free troposphere, with some years only just reaching above 1000 cm^{-3}. Note that both plot types are cut off to show Antarctic concentrations, resulting in saturation over other continents, and the scale is different between map and cross-sectional plots.

4.3.2 Adding a sea ice flux

The control simulations, and the configuration currently present in the commonly used model version, assumes there is a zero flux through the sea ice. Figure 4.4 shows both the DMS seawater concentration, together with the sea ice fraction that would act as a mask for DMS emissions from underlying concentrations. The fluxes that result from these ocean concentrations are shown in Figure 4.5 together with the additional emissions that are introduced by making the sea-ice permeable. The effect of the sea ice mask on control emissions is observed clearly, with a significant areal coverage around the Antarctic continent having zero emissions in this simulation.

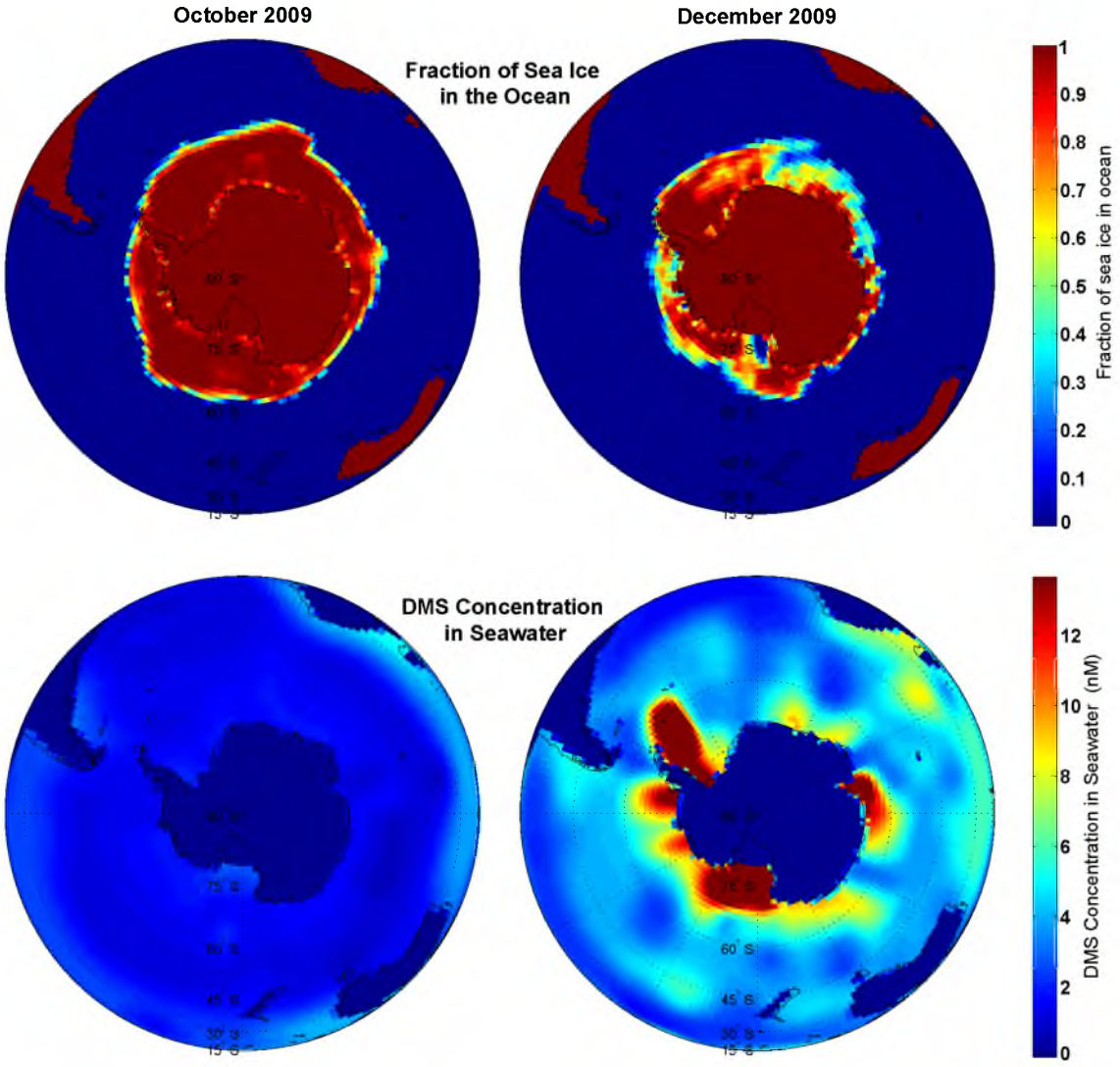

Figure 4.4: Sea ice fraction and DMS concentration in seawater. Sea ice fraction is a result of dynamics and AMIP-II sea ice data, while DMS concentrations are directly from the Lana et al. (2011) climatology. In the control code, the sea ice masks ocean emissions. Although sea ice fraction is lower in the summer, DMS concentrations are much higher, resulting in maximum emissions Dec through Feb.

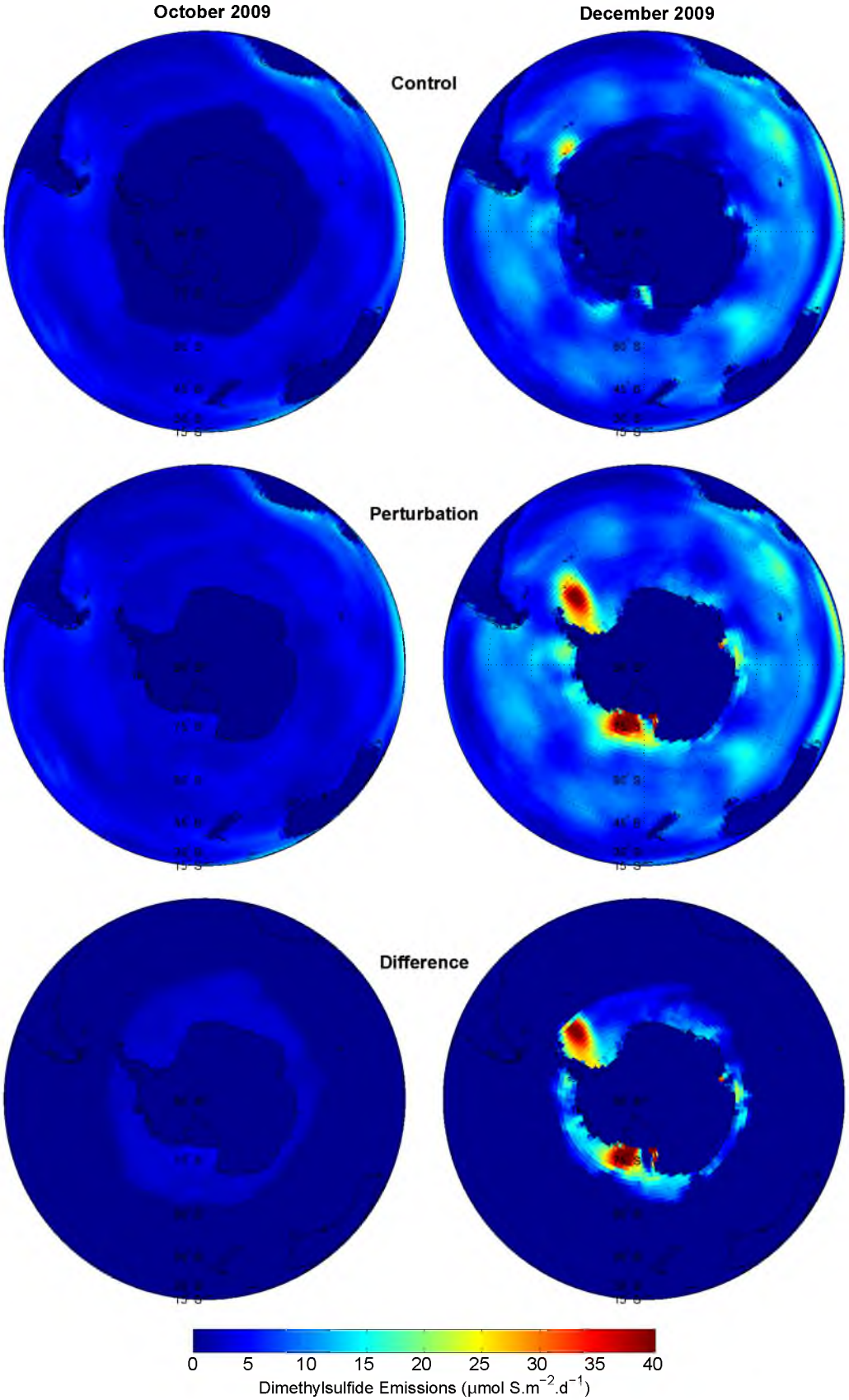

Figure 4.5: DMS emissions from the model for the two focus months of October and December 2009. Top: The control run with the sea ice mask. Middle: The perturbation run with the sea ice made permeable. Bottom: Absolute difference between the perturbation and control run, showing the significant emissions added, particularly in December when high concentrations of ocean DMS are present.

The addition of a parameterisation to enable permeable sea ice results in emissions from this region that are comparable in magnitude to those of the surrounding ocean. This suggests that the magnitude of the parameterisation is such that it is, to a first approximation, as if the sea ice isn't there at all. This is unrealistic for a sea ice average, and is more reflective of what would be expected from emissions from melt pool or leads, rather than the identified pack ice emissions of Trevena and Jones (2012).

Additional sensitivity studies were conducted that reduced the DMS flux by factors of 10 and 100 relative to the unrealistically high baseline flux. Both simulations found increases in CN number concentration less than ~5% above the control simulation (where number concentrations are in the range of 100 cm^{-3}), which is insufficient to explain observations. Consequently, the unrealistically high DMS flux was used, rather than the lower emission scenarios, to test and compare to measurements. If this scenario could not reproduce the observed aerosol number concentrations, then it could reasonably be concluded that DMS nucleation chemistry, with the current understanding of sources, is insufficient to explain observations. Consequently, an additional source of DMS (other than a sea ice source), different precursors or alternative chemical mechanisms must be required to explain the observed number concentrations.

An assessment of the CN number concentrations resulting from the high emission simulation is shown in Figure 4.6. It can be seen that over the entire Antarctic region, the average CN number concentration changes by a maximum factor of 2, and this change occurs over the continent or in hotspots over the coast. Changes in the sea ice region around the continent increase by up to 40%, with lower increases in the East Antarctic region.

This begs the question - if significant increases in DMS emissions to the atmosphere do not have an appreciable change in CN number concentrations, then where is all the additional sulfur going? Figures 4.7 and 4.8 show the breakdown of the CN number concentration into its size modes for the two case study months. It can be seen that the largest relative increases occur in the nucleation mode, with moderate increases in the Aitken mode, and minimal changes in the accumulation mode. Assuming a given size for each mode (Nucleation: 8nm; Aitken: 80 nm; Accumulation: 200 nm), a back-of-the-envelope calculation reveals that the mass increase in the accumulation mode at the surface is four orders of magnitude larger than in that of the nucleation mode. This is supported by model output of sulfate mass mixing ratio in each of the three modes, shown in Appendix Figure B.3 and B.4, which shows the most significant increases occur in the accumulation mode. This suggests that the sulfur added to the system from the increased DMS flux results in a greater number of larger particles, rather than the increase in nucleation

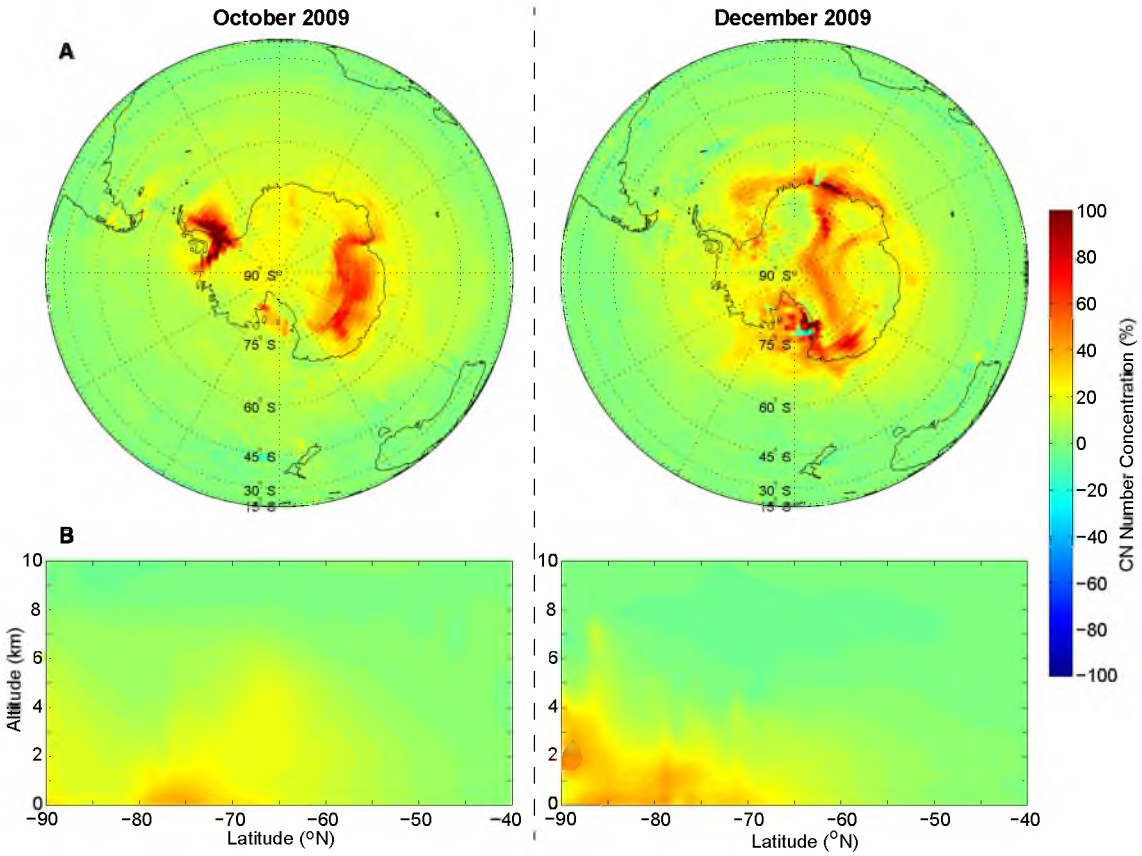

Figure 4.6: As in Figure 4.3, except colours show the percentage difference between CN number concentration produced with the additional DMS flux through sea ice at the full rate of 1.6 $\mu mol.m^{-2}.d^{-1}$ for every 1 nM ocean DMS concentration. Again, the plots in B are for East Antarctica only.

mode particle number concentrations.

Since GLOMAP utilises the binary homogeneous nucleation mechanism, vapours either condense homogeneously, resulting in nucleation, or onto pre-existing particles, resulting in growth. GLOMAP has not been validated extensively in the ultra-clean environment of the Antarctic and Southern Ocean regions, and so it is likely, given the results presented here, that the partitioning of condensible vapours between nucleation and condensation is unrealistic under these conditions. It may be the case that binary homogeneous nucleation is the dominant mechanism in the region, and that its parameterisation is incorrect for the conditions, or that an alternate nucleation mechanism may be dominating.

As discussed previously, baseline CN number concentrations are a factor of 10 lower than the average of those measured in the sea ice region. Since the largest flux resulted in a maximum change in aerosol number concentration of a factor of 2, and this change was not in the measured region, where changes were much lower, it can be reasonably concluded that even with an unrealistically high perturbed DMS flux, the default nucleation mechanism (i.e. binary homogeneous nucleation) included in this, and most global chemistry and transport models, is insufficient to explain

aerosol number concentrations in the Antarctic region. It is possible that a different nucleation mechanism is dominant in the Antarctic region however, and this idea is explored in Section 4.3.3.

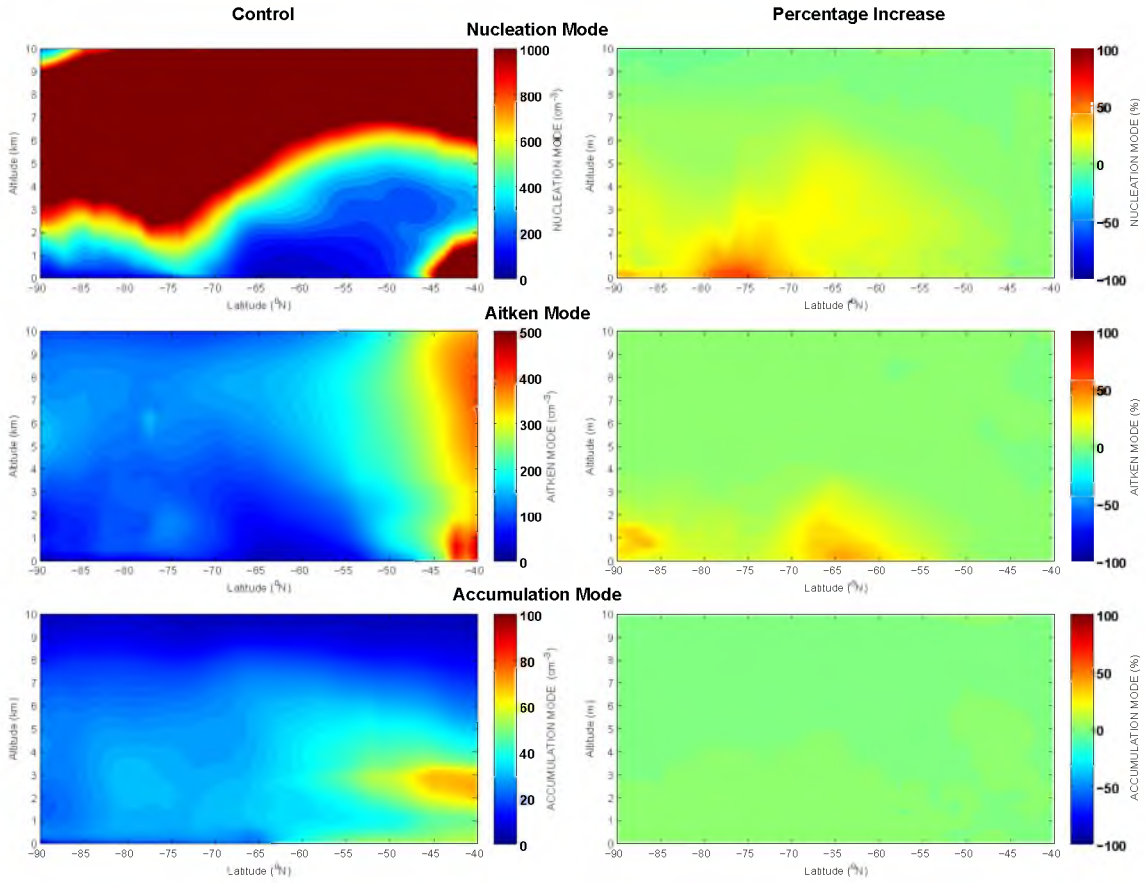

Figure 4.7: A breakdown of the changes in number concentration in each of the three modes that would be affected by the increased DMS flux. In the left column is the total number concentration in each mode, while the right column contains the percentage change compared to the control simulation. Data shown are for East Antarctica only and are from October 2009.

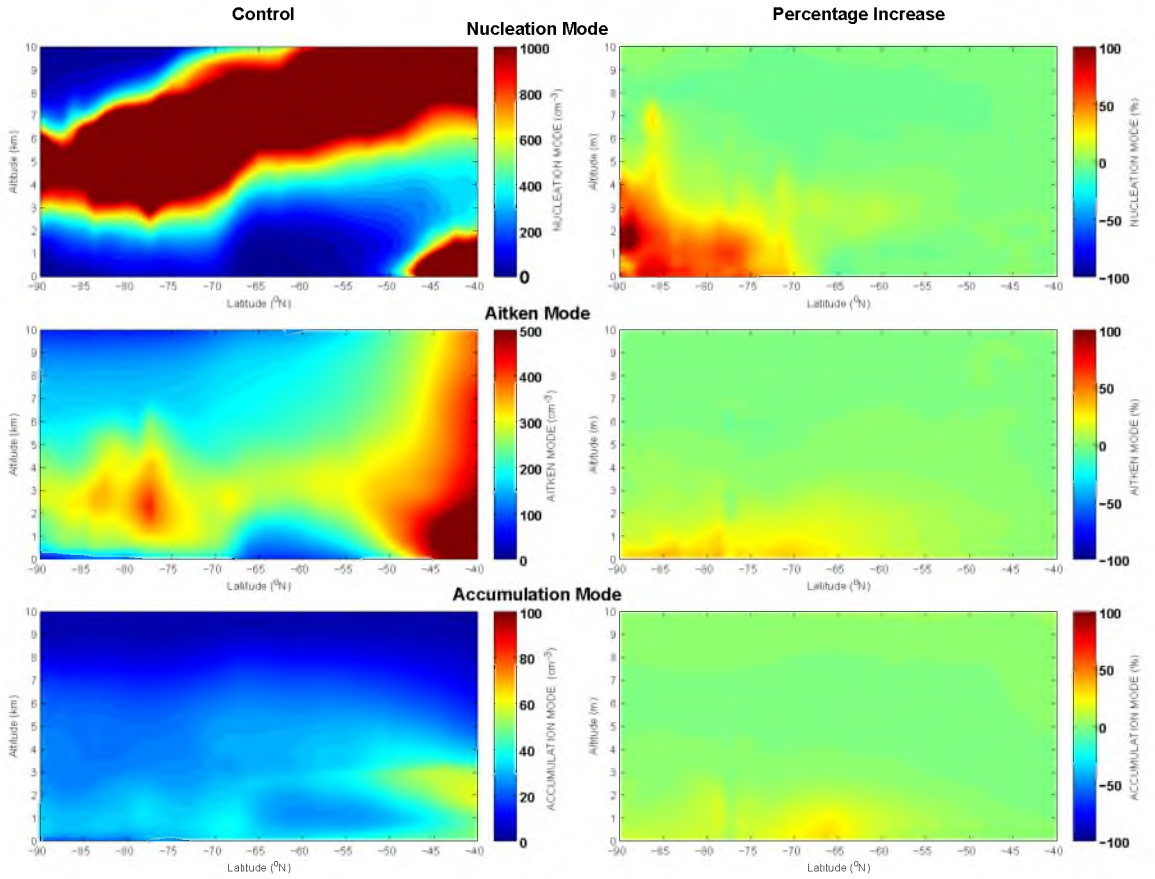

Figure 4.8: As in Figure 4.7 but for December 2009 data.

4.3.2.1 Assessing circulation patterns

Despite modelled aerosol number concentrations at the surface being well below those measured during SIPEXII, simulations exhibited sufficiently high number concentrations in the free-troposphere above the continent. Indeed, free tropospheric concentrations are high enough ($\geq 3000\ cm^{-3}$) that, if circulation patterns were as back-trajectories from Chapter 3 suggest (in particular, the steep downward flow that brings free-tropospheric air to the sea-ice surface), then the current DMS loading could be sufficient to explain observations ($\sim 1100\ cm^{-3}$ October 2012 mean). Figure 4.9 shows the vertical component of wind velocity averaged latitudinally over the East Antarctic region (0-180°E). The Polar Front is immediately apparent in the figure, with a broad expanse of rising air north of 70°S (extending to 65°S at the surface). South of the Polar Front, descending air is observed over the continent. These general patterns are similar to those observed in the meridional mass-stream analysis discussed in Section 3.2.2. However, the crucial, well-defined downward flow observed in the back-trajectory analysis outlined in the previous Chapter is absent in the plots. This could be due to a number of factors, including resampling of spatial resolution of the data, or the method by which nudging is implemented in the model. Regardless of the reason, the absence of this flow means that the

high free-tropospheric aerosol concentrations do not reach the sea ice region where measurements occurred. Instead, the broad descending air south of 65°S is likely to carry some of the free-tropospheric populations, resulting in the highest simulated surface concentrations occurring over the continent. Additionally, given this broad descending air extends over ~15° of latitude, compared to ~5° for the well-defined flow, concentrations would be diluted in at least twice the volume of air (depending on the exact flow structure), resulting in significantly lower surface concentrations.

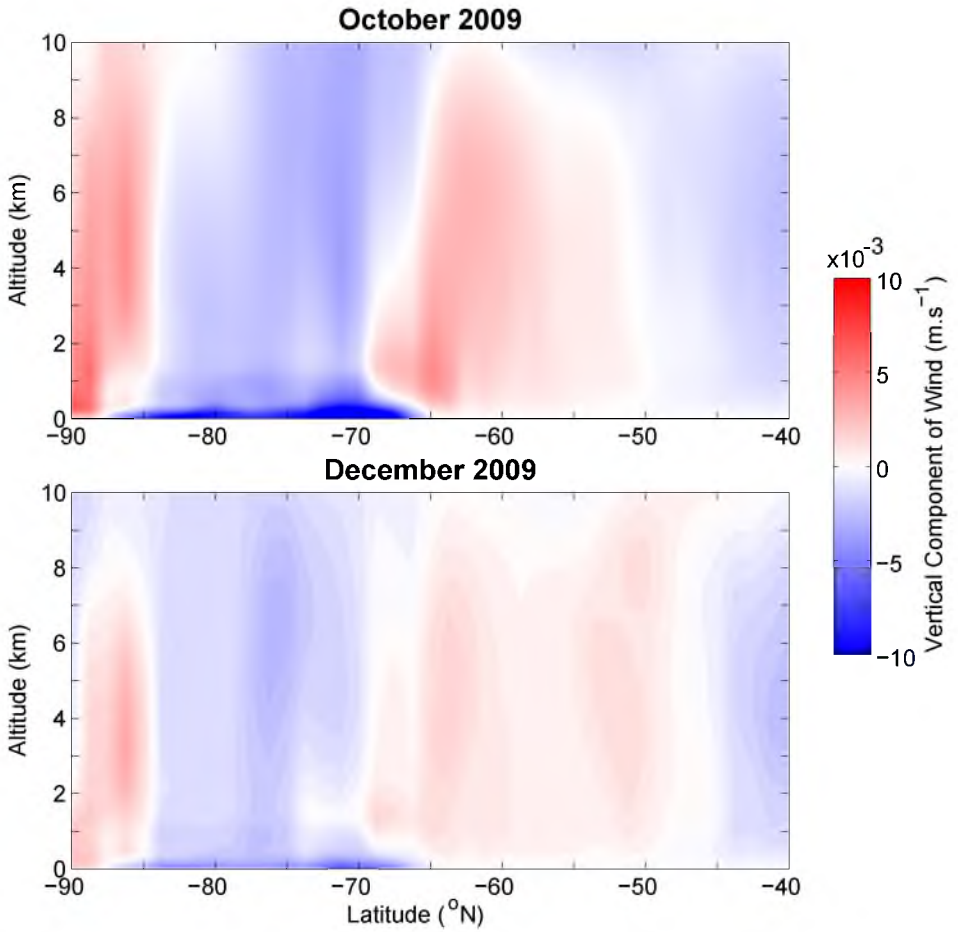

Figure 4.9: Vertical component of the wind averaged from East Antarctic longitudes only for the two case-study months. Red colours indicate upward motion while blue depicts descent.

There is some evidence, however, that could indicate the transport is occurring. Figure 4.10 shows the change in number concentration of the soluble portion of the accumulation mode aerosol - a subset of the CN that is in the 100 nm<D<1 μm size range and where the added sulfur species would reside after growth (as outlined in Table 4.2). The figure, which restricts data to the East Antarctic longitudes only, shows a distinct increase in number concentration (up to 30%) localised primarily to the sea ice region, similar to the distribution envisaged from measurements. Although the number concentrations are still far too low, this pattern would be

consistent with the scenario of free-tropospheric nucleation followed by growth and transport to the sea ice region. However it could also be the case that the additional sea ice emissions nucleate and grow locally, without transport. This second option is less likely because growth to these sizes generally takes longer (particularly given measured populations were observed not to be growing significantly) than the time that transport processes would allow for populations to remain in this region (discussed in detail in Chapter 3). These data suggest that transport patterns are consistent with trajectories, and that nucleation and growth chemistry is too fast and results in small changes in number concentrations at larger sizes, rather than the observed high number concentrations of smaller particles.

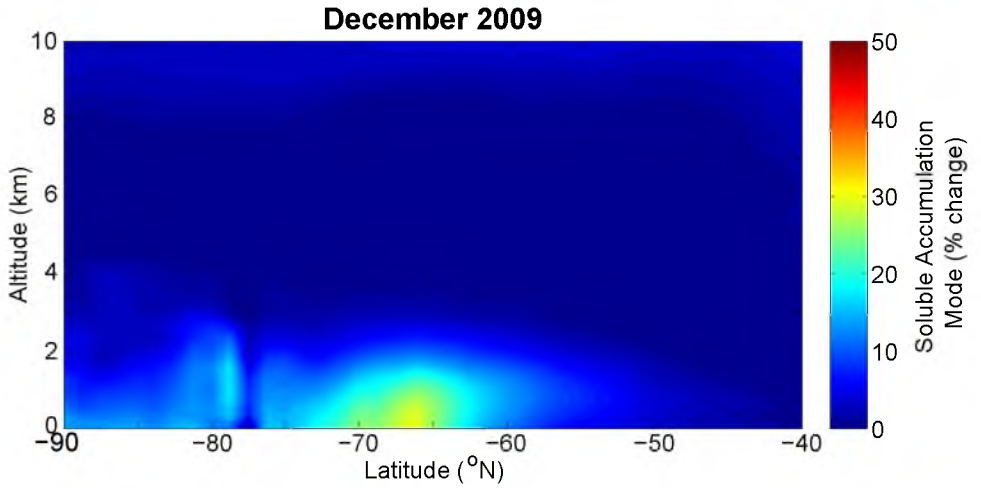

Figure 4.10: Latitudinal cross-section of the percentage change in number concentration of the soluble component accumulation mode aerosol particles from the increased flux. The plot includes East Antarctic longitudes only but clearly shows localisation in the sea ice region closest to the continent.

Given both trajectories and the global model are being driven by the same reanalysis dataset (ERA-Interim), it should follow that the circulation patterns are the same. Since the downward flow is so striking in trajectory results, it is particularly surprising that it is absent in the raw meteorological data. It is unknown though, how the meteorology is altered by the various forcings within the model, and therefore whether the resulting wind fields are similar to the original input data. To quantify any difference, it would be ideal to export the model's meteorological data that has been nudged to ERA-Interim, then re-run the trajectory analyses and compare to the original. Unfortunately this process was logistically and technically challenging (required other people for data export and handling) and would have taken a disproportionally long time-frame to complete. Although a necessary part of future model validation, undertaking this level of analysis would not have added significantly to the present study. This is primarily because the chemistry of the model

was still able to be tested by changing the data analysis slightly by the following method.

The model's circulation (Figure 4.6) is found to transport air from the Antarctic free troposphere directly down to the continent's surface, rather than to the sea ice (as suggested from trajectories). Because of this, concentrations measured in the sea ice during SIPEXII can also be compared with those found at the continent's surface in model simulations. These comparisons must be performed carefully, taking into consideration dilution factors (transport into a larger volume over the continent compared to what would be likely from the transport suggested by back-trajectories), and assuming adiabatic transport (the model calculates concentrations in a pressure independent unit, similar to mixing ratios, which are then converted to cm^{-3} for visualisations). If these comparisons still result in concentrations that are far too low, then it is very unlikely that DMS is responsible. Results from this comparison are included along with simulations from an alternative nucleation mechanism that may be important in the Antarctic region.

4.3.3 Ion-Mediated Nucleation

As discussed in Chapter 1, there are a variety of currently proposed mechanisms for secondary aerosol formation from gaseous precursors. The current parameterisation utilised in GLOMAP (Mann et al., 2010) assumes a binary homogeneous nucleation mechanism which assumes a nucleation rate, J, that follows Kulmala, Laaksonen, and Pirjola (1998) as:

$$J = exp\left\{Alog\left(\frac{S}{S_{crit}}\right) + BX_{al} + C\right\} \tag{4.3}$$

where S is the molecular concentration of sulfuric acid vapour, X_{al} is the sulfuric acid mole fraction at the critical radius ($= D + 0.012logS$), and S_{crit} is the value of S above which nucleation occurs, calculated as

$$S_{crit} = exp\left(14.5125 + 0.1335T - 10.5462RH + 1958.4\frac{RH}{T}\right) \tag{4.4}$$

where T is the air temperature, RH is the relative humidity (between 0 and 1) and the coefficients A, B, C and D are calculated as in Kulmala, Laaksonen, and Pirjola (1998).

Although this mechanism has been shown to perform well throughout most of the atmosphere, there is some evidence to suggest that an alternate mechanism, ion-mediated nucleation (IMN), could be important in the troposphere (Turco, Zhao, and Yu, 1998; Yu and Turco, 2000; Yu, 2006; Yu and Luo, 2010). This mechanism

relies on atmospheric ions that are generated from interactions with the natural flux of cosmic radiation. Although recent studies have suggested that the IMN mechanism makes only a minor contribution to atmospheric nucleation as a whole, it is suggested to be important in the mid-troposphere and when particle concentrations are low (e.g. in the polar regions) (Almeida et al., 2013; Kirkby et al., 2011).

A recent global modelling study by Yu and Luo (2010) assessed the importance of the IMN mechanism in the Antarctic region using cosmogenically ionised H_2SO_4 from DMS precursors. Results from this study showed that this mechanism was able to reproduce CN_{10} number concentrations measured at the German Antarctic research station Neumayer (70°40'S, 8°16'W) - concentrations which are similar to measurements at many other coastal stations on the continent. Contributions of secondary particles from the IMN mechanism at Neumayer were found to range between 40 and >70%, much higher than in other locations around the globe. It is possible that this higher contribution is a combination of the lower overall aerosol loading, combined with the higher cosmic radiation flux that would be present at the poles.

The author of this study, Fangqun Yu, provided modelled data for the SIPEXII location during the simulated time period. Monthly averages of CN_3 and CN_{10} data were provided for the grid box closest to (65°S, 120°E) for 2006 and 2007 from the dataset published in Yu and Luo (2010), and using a modified version of the model (different version of the chemical model, GEOS-Chem) for 2012 which didn't produce any results that differed from the previous model version with any statistical significance.

A comparison of the annual cycle at (65°S, 120°E) from the 3 years of data from both GLOMAP (2007-2009) and IMN (2006, 2007, 2012) global models is shown in Figure 4.11. The figure shows that the IMN mechanism dominates at this location, producing an order of magnitude higher concentrations than the binary-nucleation mechanism of GLOMAP. Even if the transport is incorrect (as discussed in Section 4.3.2.1), and concentrations from a variety of continental surface locations are used for comparison (grey traces in figure), concentrations produced by GLOMAP are far below what the IMN mechanism can produce.

Despite the IMN mechanism generally performing better than GLOMAP in terms of reproducing number concentrations in this region, neither model could reproduce the spring peak in the seasonal cycle observed in the Antarctic region (e.g. Gras, 1993; Hara et al., 2011). The average aerosol number concentrations recorded during the spring-time SIPEXII, plotted as part of Figure 4.11, were factors of 3 and 16 higher than those simulated using the IMN and GLOMAP mechanisms, respectively.

It is likely that in reality, both the IMN and binary homogeneous nucleation

mechanisms are occurring simultaneously in the atmosphere. However, since the GLOMAP model currently cannot simultaneously run both of these mechanisms, testing whether this makes a notable difference is out of the reach of the current simulations and would require significant work to incorporate into the model. A first approximation to test the effect of both simulations occurring would be to simply add the results of the two simulations together. Because of the low overall CN number concentrations simulated, in particular by GLOMAP, this still puts the simulated CN number concentrations well below observed number concentrations, and points to another mechanism or species responsible for the measured spring-time peak.

The seasonal trends of both the models were found to follow the same general pattern, with a maximum in summer, consistent with the DMS precursor source. Although the maximum of the GLOMAP simulation was an order of magnitude lower than SIPEXII measured concentrations, the IMN simulations produced summer maxima within the range of those observed. It is possible then, that the timescales of transport and chemistry within the model are incorrect. However, this is unlikely because true timescales of both chemistry and transport relevant for these processes are likely to be significantly shorter than the two month offset observed between these similar modelled and measured concentrations.

It can be reasonably concluded then, that sulfur chemistry, regardless of which of the currently formulated mechanisms is utilised, is unable to reproduce the spring-time number concentrations observed during the SIPEXII voyage. Given the magnitude of the difference between observed and modelled concentrations simulated using the binary homogeneous nucleation mechanism in GLOMAP, as well as the fact that the ternary mechanism relies largely on sulfuric acid concentrations (Bellouin et al., 2013), it is unlikely that future plans to incorporate ternary homogeneous nucleation mechanisms, which incorporate ammonia and amines into the nucleation chemistry, would would make a considerable difference to these results.

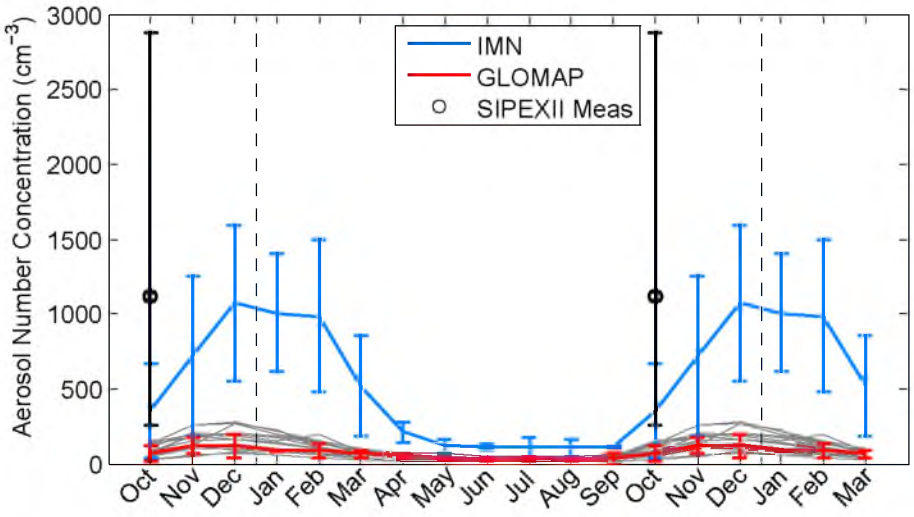

Figure 4.11: Three year climatologies of CN_3 number concentrations derived from models compared with measurements from SIPEXII (black). The red trace represents modelled surface concentrations at the SIPEXII location (65°S, 120°E), together with 14 different East Antarctic continent surface locations (grey) that show that concentrations are far too low throughout the continent, ruling out transport as an issue. The blue trace represents the same SIPEXII approximated location but derived using a different model that utilises the Ion-Mediated Nucleation (IMN) mechanism (Yu and Luo, 2010). Error bars on both red and blue traces represent 2 standard deviations of the three year data. The range of values observed during SIPEXII (excluding outliers due to local particle formation) is shown in black, along with the average (despite data not being normally distributed) to enable comparison to model and literature data. Note that the first and last 3 months of the year are repeated to show the seasonal cycle more clearly.

4.3.4 Implications for the Radiative Balance

Unfortunately, since number concentrations could not be reproduced in the sea ice region using any of the tested configurations, an assessment of the radiative impact of the measured enhanced aerosol loading could not be performed. Although it would be a valuable extension of the study, arbitrary modification of the code to force the observed aerosol number concentrations (e.g. by increasing the prescribed nucleation rate) could result in undesired and unrealistic changes in aerosol loading in other regions, making it impossible to determine the cause of resulting changes in radiative impact. For example, altering the general nucleation rate to match Antarctic sea ice concentrations would likely result in increases in aerosols in the Southern Ocean region. Any consequent changes in radiative forcing in the Southern Ocean region then, would be a result of the combination of Antarctic outflow and unrealistically high *in-situ* Southern Ocean aerosol concentrations. Future model development is necessary in order to reproduce the concentrations observed during this study. These developments may include modifications of the sulfur chemistry

scheme and how it responds to various spatial areas (which could include more complex temperature parameterisations or additional sources), or could incorporate a new source (discussed further in Section 4.4). These modifications were deemed precursory to any reasonable analysis of the radiative impact of the high aerosol number concentrations.

4.4 Discussion and Summary

The modelling studies described in this chapter show that the precursor that is generally attributed to Antarctic aerosols, DMS, is unable to reproduce the high aerosol number concentrations observed during the spring-time SIPEXII voyage described in Chapter 3 using known chemical mechanisms. In the Antarctic region, both mechanisms tested (binary homogeneous nucleation and IMN) are driven by emissions of DMS from the surface oceans based on either Lana et al. (2011) or Kettle et al. (1999). Both of these DMS climatologies show similar seasonal cycles, with minimal concentrations until December when concentrations reach their maximum before dropping in March. This driving pattern is then found, unsurprisingly, to be reflected in the modelled aerosol concentrations. Unless spring-time measurements of DMS in the Antarctic (no reliable atmospheric measurements were made during SIPEXII, however other DMS measurements are discussed in Section 3.3.8) are an order of magnitude lower than reality, which is unlikely, it can be reasonably concluded that DMS-H_2SO_4 chemistry is not responsible for the observed number concentrations.

The other major mechanisms for nucleation in the atmosphere involve amines, organic and iodine precursors. Measurements of ammonia and amines in the Antarctic region shows significant variability, leading to significant uncertainty remaining for the region's nitrogen budget (Legrand et al., 1998; Gras, 1983). However, the primary sources of these compounds (combustion and bacterial decomposition of plant matter in soils and animal excreta) are minimal in Antarctica and are primarily limited to penguin rookeries (Legrand et al., 1998). Organic compounds such as isoprene can be emitted by various phytoplankton communities (e.g. Moore, Oram, and Penkett, 1994; Shaw, Chisholm, and Prinn, 2003). At the regional scale being considered however, these organic compounds only become significant when strong phytoplankton blooms occur (e.g. Hu et al., 2013). Since phytoplankton blooms, and biological activity in general, are intimately linked to DMS concentrations, it is likely that seasonal cycles are similar, and therefore, that organic precursors are unlikely to contribute to the spring-time loading observed here. Further discussion of organic precursors can be found in Chapter 3.

As discussed in earlier chapters, iodine precursors can produce significant num-

bers of secondary particles. Although iodine precursors are generally spatially restricted, a number of studies have found an abundance of precursors in a wide geographic are of the Antarctic region, with concentrations revealing Antarctica as a global hotspot (Atkinson et al., 2012; Saiz-Lopez et al., 2007a; Frieß et al., 2001; Schönhardt et al., 2012; Schönhardt et al., 2008; Saiz-Lopez et al., 2007b). The seasonal cycle of these iodine concentrations, shown previously in Figure 3.13, are found to peak in the spring-time. This seasonality is consistent with the spring-time peak observed in numerous Antarctic aerosol records (e.g. Weller et al., 2011; Virkkula et al., 2009; Bigg, Gras, and Evans, 1983), as well as the measurements made in this thesis. Although it is mere speculation at this point, the proven nucleation mechanism, as well as the abundance of precursors at the correct time of year, makes iodine the most likely precursor for spring-time aerosol in the Antarctic region.

As part of future developments of the GLOMAP model, work with Matthew Woodhouse (CSIRO Oceans and Atmosphere Flagship) is currently planned to incorporate iodine inventories, chemistry and nucleation mechanisms into the model. Similar work is also occurring, under the supervision of Alfonso Saiz-Lopez (CSIC), to incorporate the iodine scheme into another global model - the Community Atmospheric Model with Chemistry (CAM-Chem, http://goo.gl/PCIRVs). This work is likely to drastically improve model simulations of secondary aerosol formation, particularly in the Antarctic and Southern Ocean regions.

Although the radiative impacts could not be determined in this study, the future developments (described above) will hopefully provide more reasonable simulations of particle number concentrations in the Antarctic region that can then lead to reasonable calculations of radiative forcing and thus the impact of these measured high concentrations.

Results from this modelling study provided more questions than answers, and primarily just showed that DMS precursors cannot explain the observed aerosol number concentrations. Future work in model development, as described above, as well as further measurements of atmospheric composition are necessary to more completely understand what is driving the aerosol number concentrations observed in the region. Measurements should consist of both long and short term measurement programs, and include both gaseous and aerosol composition, as well as other atmospheric dynamics parameters (e.g. boundary layer height) in order to better understand the large scale circulation patterns influencing the region.

Chapter 5

A Nucleation Event over Antarctic Sea-Ice

Abstract

Only one particle formation event was observed during the 32 days of aerosol measurements in the Antarctic pack ice. This event occurred on the only day to exhibit extended periods of global irradiance in excess of 600 $W.m^{-2}$. Number concentrations of particles larger than 3 nm (CN_3) reached almost 7700 cm^{-3} in the single air-mass within a few hours of clouds clearing, and grew at rates of 5.6 $nm.hr^{-1}$. Formation rates of 3 nm particles were in the range of those measured at other Antarctic locations at $0.2 - 1.1 \pm 0.1$ $cm^{-3}.s^{-1}$. Our investigations into the nucleation chemistry found that there was insufficient precursor concentrations for known halogen or organic chemistry to explain the nucleation event. Modelling studies utilising known sulfuric acid nucleation schemes could not reproduce both particle formation or growth rates. Surprising correlations with Total Gaseous Mercury (TGM) were found that, together with other data, suggest a Hg catalysed photochemical nucleation mechanism may be responsible for aerosol nucleation. Given the very low vapour pressures of the Hg species involved, this nucleation chemistry is likely only possible where pre-existing aerosol concentrations are low and both TGM concentrations and global irradiance levels are relatively high ($\sim$1.5 $ng.m^{-3}$ and $\geq$600 $W.m^{-2}$, respectively), such as those observed in the Antarctic sea ice boundary layer or in the global free-troposphere, particularly in the Northern Hemisphere.

Author Contributions

A modified version of this chapter has recently been submitted to Atmospheric Chemistry and Physics and the contributions of the various authors is as follows. Ruhi Humphries wrote the manuscript, led the overall data analysis and interpretation, ran all instruments, except the Tekran, during the field campaign, performed

quality control on aerosol, and ran the box model and interpreted the results. Robyn Schofield (University of Melbourne, Australia) led AAS project 4032, and was instrumental in the field campaign and data analysis.Melita Keywood and Jason Ward (CSIRO Ocean and Atmospheres Flagship, Australia) provided aerosol instrumentation. Jeffrey Pierce (Colorado State University, United States) provided the box model, and assisted in its commissioning. Caitlin Gionfriddo (University of Melbourne, Australia), Michael Tate and David Krabbenhoft (United States Geological Survey, United States) provided, ran and performed quality control on Hg data. Ian Galbally and Suzie Molloy (CSIRO Ocean and Atmospheres Flagship, Australia) provided and installed ozone instrumentation while Ian Galbally, Suzie Molloy and Andrew Klekociuk, and Ruhi Humphries performed quality control. Paul Johnston, Karin Kreher and Alan Thomas (National Institute of Water and Atmospheres, New Zealand) provided the instrument, technical support and analysis of data from the MAX-DOAS. Andrew Robinson, Neil Harris (University of Cambridge, UK) and and Alan Thomas provided the GC-ECD instrument. Andrew Robinson and Neil Harris performed GC-ECD data quality control and running algorithms. Robert Johnson (Institute for Marine and Antarctic Studies, University of Tasmania, Australia) produced chlorophyll data from fluorescence measurements. Stephen Wilson (University of Wollongong, Australia) and Ruhi Humphries calculated $OH^{\bullet}$ concentrations. Robin Schofield, Melita Keywood and Stephen Wilson provided academic support. All authors contributed to the editing of the manuscript.

5.1 Introduction

Aerosol nucleation is ubiquitous throughout the atmosphere, with frequent burst events occurring in the boundary layer, known as new particle formation (NPF) events. In the continental boundary layer, where precursor sources are significant, NPF events are relatively common (Kulmala et al., 2004). In the marine boundary layer (MBL) however, NPF-precursor source strengths are lower and significant background aerosol populations exist (e.g. wind-produced sea-salt) which scavenge precursor vapours, preventing gas-to-particle nucleation. Consequently, only a handful of NPF events have been observed in the remote MBL (e.g. Covert et al., 1996; Koponen et al., 2002; Heintzenberg et al., 2004). The Antarctic sea ice region has many characteristics of the remote MBL, however the concentration of background wind-produced aerosol populations is significantly reduced due to the ice barrier between the ocean and atmosphere. Consequently, NPF events in the Antarctic sea ice boundary layer could be more likely than the MBL, given precursors and other favourable environmental conditions (e.g. oxidants, high humidity) are present.

The aerosol record described in this thesis represents one of the longest aerosol records in the Antarctic sea ice region. The majority of this aerosol record is characterised by minimally-growing background aerosol populations, currently thought to have been transported through the region after formation in the free troposphere above the Antarctic continent, as described in Chapter 3. Despite the significant variations observed in the full aerosol record (Figure 5.1), only minimal indirect evidence was found for growth in the majority of these cases (e.g. air-mass history). Only one event occurred during the measurement period that showed evidence of it being a NPF event. Presented in this chapter is the characterisation of this NPF event through analysis of measurement data together with modelling studies. The changes in aerosol concentration are assessed for rates of formation and growth as well as possible nucleation mechanisms.

5.2 Methods

A detailed overview of the instrumentation utilised in the campaign is given in Chapter 2. A number of additional methods were used for the investigation of the new particle formation event, which included trajectory modelling, calculation of $OH^{\bullet}$ concentration, as well as the utilisation of a box model to investigate nucleation chemistry. Details of these methods are outlined below.

5.2.1 Trajectory Analyses

Back-trajectories were calculated using NOAA's HYSPLIT (HYbrid Single-Particle Lagrangian Integrated Trajectory) model (Draxler and Hess, 1998). The trajectories were calculated using the standard Global Data Assimilation System (GDAS) meteorological data available via the web-interface and confirmed with the NCEP reanalysis dataset. Vertical motion was calculated using model vertical velocity mode. Trajectories were initiated at heights of 10, 500 and 1000 m above sea level at the ship's location during the time surrounding the 18th October particle formation event. Trajectories were restricted to 72 hours, which limited the uncertainty of the calculations inherent from input meteorology that are calculated from sparse observations in the region (as discussed in Chapter 3). Each calculation estimated hourly three-dimensional air-parcel locations within the specified time-frame.

5.2.2 Hydroxyl Radical, $OH^{\bullet}$

$OH^{\bullet}$ concentration on the 18th October was calculated from values of $J(O^1D)$[a]. $J(O^1D)$ was not measured directly, however using the relationship modified from

[a]The rate of ozone photolysis to produce $O(^1D)$ which in turn results in $OH^{\bullet}$.

Wilson (2014), it can be calculated such that:

$$J(O^1D) = 2\left(\sum_i A_i exp\left(-\frac{B_i}{cos\theta}\right)\right)\left(\frac{O_3^{sat}}{300}\right)^{-RAF} \quad (5.1)$$

where θ is the solar zenith angle, O_3^{sat} is the total ozone column retrieved from satellite for the measurement day, and A_i, B_i and RAF (the Radiation Amplification Factor) are derived experimentally and are given in the literature (Wilson, 2014; Creasey et al., 2003). The total column ozone is utilised in this equation as it determines the level of UV radiation available for photolysis at the surface. The equation given by Wilson (2014) is suitable for low albedo regions, such as the Southern Ocean, however over the dense pack ice, the high albedo surface increases the actinic flux (the quantity of light available from all directions at a point in the atmosphere) significantly. The multiplication factor of two leading the equation is used to roughly correct for this elevated albedo. O_3^{sat} was derived from OMI satellite measurements (http://www.esrl.noaa.gov/) to be 441 Dobson units during the event day. Under the assumption of clear sky, this resulted in a $J(O^1D)$ of 1.2×10^{-5} s^{-1}.

The $OH^{\bullet}$ concentration was calculated directly from values of $J(O^1D)$ using the method described by Creasey et al. (2003). At low concentrations of NO_x and non-methane hydrocarbons, the primary source of $OH^{\bullet}$ is the UV photolysis of ozone in moist air:

$$O_3 + h\nu(\lambda{<}345nm) \xrightarrow{J(O^1D)} O(^1D) + O_2$$
$$O(^1D) + H_2O \longrightarrow 2\,OH^{\cdot}.$$

The rate of primary $OH^{\bullet}$ production, $P(OH)$, is given from these two equations such that

$$P(OH^{\cdot}) = 2J(O^1D)[O_3]f \quad (5.2)$$

where f is the fraction of $O(^1D)$ that reacts to generate $OH^{\bullet}$ (approximated to a value of 0.1 (Creasey et al., 2003)), $[O_3]$ is the measured concentration of O_3 during the period (28 ppb), and $J(O^1D)$ is as previously defined.

The primary loss mechanisms of $OH^{\bullet}$ in the atmosphere are via reaction with CO and CH_4 to produce HO_2:

$$CO + OH^{\cdot} \longrightarrow HOCO$$
$$OH^{\cdot} + CO \longrightarrow H + CO_2$$
$$H + O_2 \xrightarrow{M} HO_2$$

and

$$OH^{\cdot} + CH_4 \longrightarrow CH_3 + H_2O$$
$$CH_3 + O_2 \xrightarrow{M} CH_3O_2$$

where M is a third body. Using the approximation that the photolysis of ozone is the only source of $OH^{\bullet}$, the steady state expression for $OH^{\bullet}$ concentration is given by,

$$[OH^{\cdot}] = \frac{P(OH^{\cdot})}{\sum_i k_{OH^{\cdot}+i}[i]} = P(OH^{\cdot})\tau \tag{5.3}$$

where i are the sinks of $OH^{\bullet}$ and $k_{OH^{\cdot}+i}$ is the rate constant for the reaction between $OH^{\bullet}$ and i. Ignoring the minor contributions from sinks such as HCHO, H_2 and CH_3OOH, the $[OH^{\bullet}]$ can be approximated using values of [CO] = 6.0×10^1 ppb and $[CH_4]$ = 1.8 ppm (http://ds.data.jma.go.jp/gmd/wdcgg/) and values of k obtained from the literature (Sander et al., 2011), The resulting $OH^{\bullet}$ concentration is estimated to be 3.4×10^6 $molec.cm^{-3}$. This is in good agreement with estimates using the relationship described by Rohrer and Berresheim (2006). This high value is driven primarily by the high surface albedo. Direct measurements (as opposed to the calculations made here) around the Antarctic region (both continental (Mauldin et al., 2001) and coastal Bloss2007, Kukui2014) report similarly high OH concentrations, giving some confidence that our calculations are within realistic ranges.

5.2.3 Box Modelling

The nucleation and growth chemistry of the NPF event was investigated using a box-model version of the TwO-Moment Aerosol Sectional (TOMAS) microphysics algorithm (Adams and Seinfeld, 2002; Pierce and Adams, 2009a; Pierce and Adams, 2009b). Described in detail by Chang et al. (2011), this version of TOMAS is configured to simulate the number and mass of particles by nucleation, condensation and coagulation processes within 44 log-normally spaced size bins spanning dry diameters between 0.5 nm and 10 μm. TOMAS currently includes gas phase sulfur chemistry (DMS, SO_2 and H_2SO_4) based on work by Chin et al. (1996), which has been shown to work well compared to other schemes in the Arctic (Karl et al., 2007). The chemical mechanism utilised in the model is outlined in Table 5.1. Given the similar polar environmental conditions, the mechanism should be suitable for the Antarctic environment of this study.

Recent work has posited the importance of methanesulfonic acid (CH_3SO_2OH; MSA) in nucleation and condensational growth processes, particularly in the marine environment (Bzdek, Ridge, and Johnston, 2011; Dall'Osto et al., 2012; Dawson et

Table 5.1: Sulfur chemical mechanism (Chin et al., 1996) before nucleation.

Reaction	**Rate Coefficient**, $(cm^3 molecule^{-1} s^{-1})$	**Note**
$H_2S + OH \longrightarrow SO_2 + ...$	$6.3 \times 10^{-12} e^{\frac{-80}{T}}$	
$DMS + OH \longrightarrow SO_2 + ...$ (H abstraction)	$9.6 \times 10^{-12} e^{\frac{-234}{T}}$	
$DMS + OH \longrightarrow 0.75\,SO_2 + 0.25\,MSA + ...$ (OH addition)	$\frac{1.7\times10^{-42} e^{7810/T}[O_2]}{1+5.5\times10^{-31} e^{7460/T}[O_2]}$	
$DMS + NO_3 \longrightarrow SO_2 + ...$		a
$DMS + X \longrightarrow SO_2 + ...$		b
$SO_2 + OH_{(g)} \longrightarrow H_2SO_4 + ...$	$\left\{\frac{k_0(T)[M]}{1+k_0(T)[M]/k_\infty(T)}\right\} 0.6^{\{1+[log\frac{k_0(T)[M]}{k_\infty(T)}]^2\}^{-1}}$ with $k_0 = 3.0 \times 10^{-31} \times \left(\frac{300}{T}\right)^{3.3}$ and $k_\infty = 1.5 \times 10^{-12}$	
$SO_2 + H_2O_{2(aq)} \longrightarrow H_2SO_4 + ...$		c
$OCS + h\nu, OH, O \longrightarrow SO_2 + ...$		d

[a] Assumed to be limited by the rate of NO_3 formation at night from the $NO_2 + O_3$ reaction.
[b] X is an additional oxidant assumed to react with DMS at the same rate as OH and NO_3 combined.
[c] Assumed to proceed to completion (titrate the limiting regent) in cloud air over the 4-hour time step.
[d] Specified loss rate of OCS as a function of altitude.

al., 2012; Bork et al., 2014). A simplified inclusion of MSA into TOMAS was performed such that MSA produced from DMS oxidation was identified as H_2SO_4 in the model, and added to the condensing H_2SO_4 reservoir, essentially increasing the nucleation and condensational growth rates. This is a reasonable parameterisation for an upper bound of the effects of MSA given its much higher vapour pressure compared to H_2SO_4. The growth of particles larger than 3 nm by MSA should be equivalent to H_2SO_4 as both are essentially non-volatile when condensing to particles of this size (Davis et al., 1998). This simple parameterisation is sufficient for the aims of this study and a full parameterisation of MSA nucleation and growth mechanisms should be performed as part of future work. Consequently, the sensitivity of the model to included MSA parameterisations were not quantified. However, results from this inclusion, although increasing growth rates, did not change the overall conclusions associated with these modelling results.

The TOMAS model includes two different nucleation mechanisms that were utilised for this study. The first is a simple activation nucleation parameterization to predict nucleation rates such that $J_{nuc} = A[\mathrm{H_2SO_4}]$ where J_{nuc} is the nucleation rate and A is an empirical parameter (Sihto et al., 2006). This linear dependence is based on the theory that stable, but sub-critical clusters exist that require the addition of a single sulfuric acid molecule to reach critical size where stable condensational growth

can occur. This mechanism, although simplified, allows easy scaling of nucleation rates. The second mechanism calculates rates and critical cluster properties using the ion-mediated nucleation mechanism (Yu and Turco, 2000; Yu, 2006; Yu, 2010). This mechanism presumes that charged molecular clusters condense around natural air ions, resulting in nucleation and growth rates significantly faster than neutral counterparts, and can produce nucleation in situations where traditional nucleation mechanisms are unfavourable. Other sulfuric-acid based schemes (e.g. binary or kinetic nucleation) were not tested because they either produce similar (kinetic) or smaller (binary) nucleation rates than the ones tested here (Yu et al., 2010). Although the model employed does not explicitly simulate schemes of sulfuric acid with ammonia, amines or organics, development to include these schemes was not deemed necessary for this study because of the low concentrations that are likely in the East Antarctic sea ice region where we were far from the region's biggest (although still small in the global context) sources of biological activity (see Section 5.3.7.1) and the continent (e.g. Legrand et al., 1998; Davison et al., 1996; Ayers and Gras, 1980; Gras, 1983).

A range of typical input variables to the TOMAS box model, shown in Table 5.2, was used to account for uncertainties in the nucleation rate. The model was initialised with a pre-existing aerosol size distribution (single or dual mode distributions with variable modal median diameter and number concentration with a fixed width, σ, of 2 (Chang et al., 2011) which is unit-less in log-normal space) and concentrations of DMS and $OH^{\bullet}$ that spanned the likely values in the field. Simulations were performed with A factors ranging from 10^{-10}, suitable for clean polar environments, to 10^{-6}, those found to suit continental locations (Chang et al., 2011). The pre-existing aerosol is assumed to have the density and hygroscopic growth properties of ammonium bisulfate - an assumption with minimal effect compared to changes in size distribution (Chang et al., 2011). The box presumes a pulse of DMS emission, followed by zero emissions (such as would be found in a rising air-mass). This is unlikely to be representative of measurements and is one of the constraints/uncertainties given careful consideration in the interpretation of results. Initial concentrations of MSA, SO_2 and H_2SO_4 are assumed to be zero, and MSA and H_2SO_4 are the only included condensable vapours (i.e. no species such as organics were included) and are assumed to have the same condensable properties. Three estimates of MSA fraction produced from DMS oxidation were used including 0.1, 0.3 and 0.5 (Chen et al., 2012). $OH^{\bullet}$ was kept constant throughout the simulation, with concentrations chosen to span likely values, as well as extremes for model validation. Cloud cycling is not accounted for in the model. Simulations were run for 24 hours, which spans more than the total time a constant air-mass was present over the measurement site. Over 1000 simulations were run, including all permutations

of the model inputs (listed in Table 5.2), inclusion of MSA condensation and the two nucleation mechanisms.

Table 5.2: Range of model input parameters to test sulfur chemistry.

Parameter	Tested Values
Background aerosol concentration (cm^{-3})[a]	100[b], 200, 400[c], 500, 600, 1000
Background mode size (nm)	0.5, 1, 1.5, 2, 3, 10, 30, 50, 100, 150, 300
[OH] (molecules.cm^{-3})	10^5, 2×10^5, 4×10^5, 7×10^5, 10^6
Initial [DMS] (pptv)	100, 200, 300, 400, 500, 600, 700, 800
A (s^{-1})	$10^{-10}, 10^{-9}, 10^{-8}, 10^{-7}, 10^{-6}$

[a] Can be approximated to CN_3.
[b] Based on our experimental measurements of number concentrations of particles >10 nm immediately before formation.
[c] Based on our experimental measurements of number concentrations of particles >3 nm immediately before formation.

5.3 Results

The NPF event will be outlined in the following manner. Trends in aerosol data are first described to give a general overview. After determining the air-mass influences throughout the period, the formation and growth rates, as well as the loss mechanisms and rate, are quantified. The chemistry of nucleation is then investigated. This is performed first by investigating correlations of aerosol data with photochemical indicators after-which the chemistry is assessed to determine whether known mechanisms can explain observations.

Figure 5.1[b] shows a time series of aerosol parameters CN_{3-10}, CN_{10}, and CN_{3-10}/CN_{10} ratio for both the entire dataset as well as 10 days of the voyage encompassing the 18th October, 2012. The parameter CN_{3-10}/CN_{10} has been shown previously (Warren and Seinfeld, 1985; Covert et al., 1992) to allow new particle formation to be easily distinguished from background concentrations. Particle concentrations on the 18th October are observed to be significantly higher than the background concentrations experienced throughout the remainder of the voyage. Background concentrations had a maximum CN_3 of 2800 cm^{-3} (median and mean of 767 and 939 cm^{-3}, respectively) and a CN_{3-10}/CN_{10} ratio value that varied minimally around two (Figure 5.1). The particle formation event on the 18th October was the only one during the full 32 day measurement period that showed both rapid increases in particle concentrations (> 1000 $cm^{-3}.hr^{-1}$) beyond background values and evidence of growth. The ratio CN_{3-10}/CN_{10} showed very little variation throughout the

[b]Note: all times quoted are in UTC, and solar midday is around 04:00 UTC.

record (reaching a maximum of 4.8 at any other time), but increased by almost an order of magnitude near the start of the event to a maximum of 16.4, decreasing as particles grew to diameters larger than 10 nm. This was further evidence confirming the attribution of the event as *in-situ* particle formation rather than fluctuations in background populations.

One other high concentration period was observed on the 9th October but showed no evidence of growth. Analyses of growth indicators and back-trajectories determined this was likely associated with variations in the age of air-masses which supply background aerosol concentrations to the region. Further analysis of this period is outlined in Appendix A.4.

A more detailed view of the 18th October formation event is plotted in Figure 5.2. At the peak of the event, CN_{3-10} number concentrations reached above 6100 cm^{-3} within a few hours, while CN_{10} concentrations reached above 1600 cm^{-3} ($CN_3 \approx 7700\ cm^{-3}$). A breakdown of the event is given as follows, with numbering referenced in Figure 5.2. An air-mass change, at the beginning of period **I**, resulted in CN_3 number concentrations dropping from ~2000 cm^{-3} to 390 cm^{-3} just prior to the event, well below average for the entire dataset. After an overcast morning, clouds cleared at **II**, providing the highest levels of solar radiation observed throughout the 32 day measurement period. At **III**, number concentrations of CN_{3-10} began to increase rapidly, with no simultaneous increase in CN_{10} (remaining at background values of 120 cm^{-3}), suggesting nucleation. About 1.25 hours later, period **IV** began with growth into the CN_{10} size range, increasing their number concentrations and simultaneously decreasing the rate of increase of CN_{3-10}. Further increases in number concentrations of CN_3 ceased at the beginning of period **V**, likely the result of nucleation rates slowing (due to decreased solar radiation) to the same rate as growth into the CN_{10} size bin (observed from the continued increase in CN_{10} during period **V**). At the beginning of **VI**, particle concentrations in both size bins began to decrease (likely the result of coagulation together with reduced nucleation) coincident with sunset(i.e. zero solar radiation). The rate of decline significantly increased during period **VII** due to an air-mass change (determined below), ending in background concentrations approximately eight hours after nucleation ceased. Variability in number concentrations, in particular the highlighted peaks, are suggested to be fluctuations in background concentration due to their simultaneous variation in both size bins and their absence in CN_{3-10}/CN_{10} ratio data.

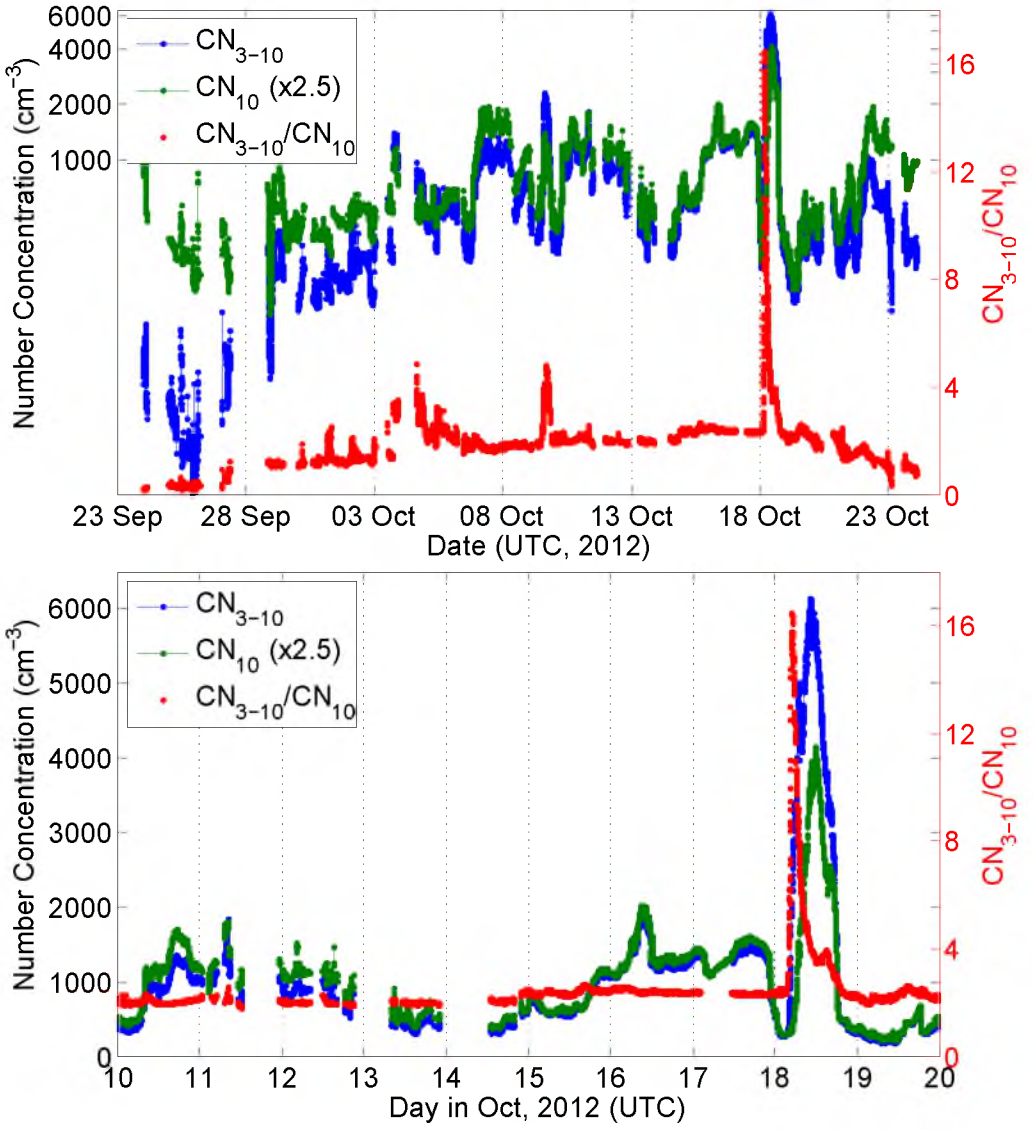

Figure 5.1: Aerosol data from the two different size ranges and the ratio between the two that reflects when new particle formation occurs. **Top**: Full aerosol record (log scale) from measurements that began on the 23 September when the ship entered the marginal ice zone where sea swell reduced enough to allow erection of the aerosol inlet. Measurements ended on the 25 October due to instrument malfunction. **Bottom**: Aerosol parameters for a 10 day subset surrounding the significant concentrations on the 18th October.

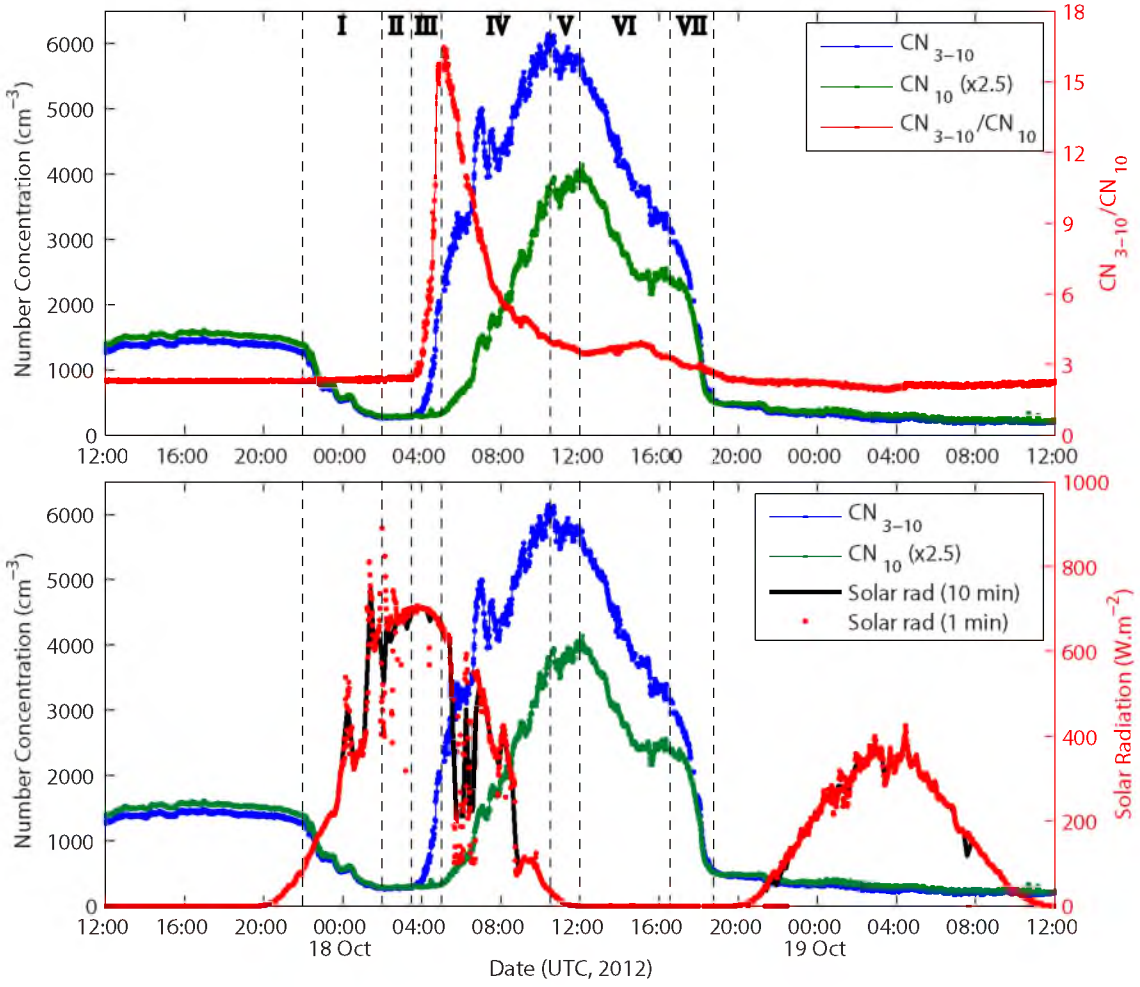

Figure 5.2: *In-situ* new particle formation event observed on the 18th October. Top: aerosol data with the CN ratio data. Bottom: aerosol data with 1 minute and 10 minutes means of solar radiation (global irradiance) data. Labels are described in the main text.

5.3.1 Identifying a Single Air-mass

To understand the changes in aerosol data, the various influences on the air-mass must be characterised to determine possible sources, sinks and other changes. This is done by consideration of sea ice conditions, measured *in-situ* meteorological data, calculated back-trajectories, and ancillary composition data such as O_3 and Total Gaseous Mercury (TGM). In this section, the air-mass influence is determined by discussing the evidence available including physical and atmospheric conditions, trajectory investigations and coincident *in-situ* gas and aerosol concentrations.

Sea ice and Meteorology: During the days surrounding the formation event, the ship was stuck, drifting with the pack ice due to weather patterns that caused convergence of the ice floes into a lead-free region that was determined by helicopter survey, to stretch for at least 20 km in each direction. This expanse of homogeneous, low-profile and generally multi-metre thick surface suggests minimal source contribution from the (ice or ocean) surface since fluxes through the ice are low (e.g. Nomura et al., 2010) and leads are rare or non-existent.

A selection of meteorological data is included in Figure 5.3, with further data included in Appendix C.1. Just prior to the event, relative humidity (RH) decreased from around 96% to 85%. This change occurred simultaneously with a drop in background aerosol concentrations, and is likely the result of recirculation over the local region where the fractional area of leads (the source of high humidity in the area) is close to zero during the period of measurement. Interestingly, air-temperature was found to be inversely proportional to RH during the start of this event, increasing slightly from -8°C to -7°C, with a 2°C variance around the higher temperature. This pattern does not result in a constant absolute humidity. This pattern of decreased RH and slightly increased temperature is consistent with other measurements of NPF in the MBL (e.g. Covert et al., 1992).

Although wind direction was consistently from the east in the days preceding, during and after the event, changes in RH and air temperature began simultaneously with the drop in aerosol number concentrations, suggesting a change in air-mass. High frequency fluctuations in wind direction can be explained by the calm conditions experienced during the event - the slow wind speeds making wind anemometers sensitive to temporally small changes in wind direction.

Wind speed was found to be below 7 $m.s^{-1}$ throughout the event, with high wind speeds up to 20 $m.s^{-1}$ 24 hours before the event, consistent with the passage of a low pressure system (967 hPa), and after the event, corresponding to the passage of a high pressure ridge (1000 hPa). These calm conditions could suggest ship emissions were being sampled, however the lack of anthropogenic signatures in other data streams (e.g. O_3 or high frequency particle concentration fluctuations) indicated

background air was measured. Other measurements (Raes, 1995; Clarke et al., 1998) found similar low wind speed conditions were necessary for nucleation in the MBL due to lower pre-existing aerosol surface area because of reduced wind-induced sea-spray aerosol. Sea-spray aerosol is unlikely to be important in the sea ice region because of reduced exposed ocean, however aerosols from blowing snow (Yang, Pyle, and Cox, 2008) and frost-flowers (Rankin, Wolff, and Martin, 2002) could occur in higher winds. These aerosols would scavenge vapours and prevent nucleation, making the low wind speed similarly important for low pre-existing aerosol numbers in this environment.

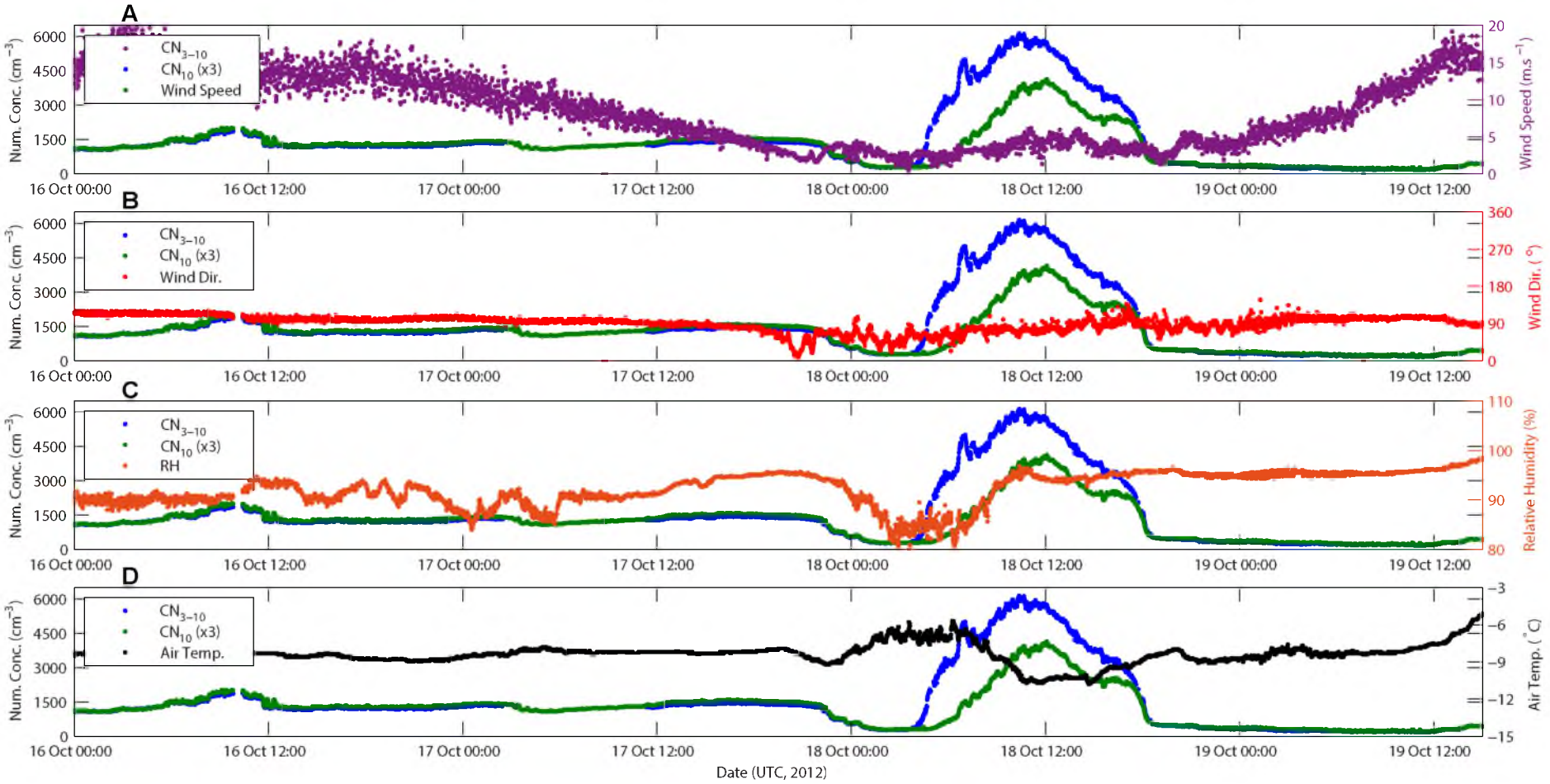

Figure 5.3: A selection of meteorological parameters measured during the new particle formation event (aerosols plotted for reference). **A**: wind speed ($m.s^{-1}$), **B**: wind direction (° from north), **C**: relative humidity (%), **D**: air temperature ($°C$). Further meterological parameters, including pressure and snowfall, are given in Appendix C.1.

Back-Trajectories: Figure 5.4 shows back-trajectories terminating at 10 m above mean sea level for the period spanning the formation event. Although *in-situ* wind direction is consistently from the east during this period, 72 hour trajectories show significant changes in air-mass history. During the high aerosol concentrations prior to the event, easterly winds brought air that had been in the free-troposphere only 36 hours prior to measurement that was representative of background populations (Chapter 3). The air-mass change identified in period **I** of Figure 5.2 and the first red track of Figure 5.4A, shows the first signs of air changing direction within the 12 hours prior to the event. The lower aerosol concentrations just prior to the event were found to correspond to air-masses that had recently come from the region north-west of the measurement location. During the period of increasing CN (Figure 5.4B), trajectories were found to 'recirculate' around this north-west region for about 24 hours, before being measured. This gives a meso-scale (~500 km) spatial bound to the chemistry and conditions leading to the formation event, rather than the local-scale. A change from this recirculation occurs at approximately 1500 (UTC, Figure 5.4C), when the decreasing aerosol concentrations began to plateau before a sudden decrease, caused by an abrupt change in air-mass history that increased influence from areas further west of the recirculation region. Additional trajectories with a range of starting heights and an alternate meteorological dataset confirm the general conclusions described here, and are included in Appendix C.2. Overall, trajectories support the conclusion that a single air-mass influenced the measurement location throughout the period of interest, and that this air-mass came from the north-west.

O_3: Independent measurements of atmospheric components, such as O_3, can help in identifying air-mass influence. Although trajectories show the circulation never exactly passed over the ship prior to measurement, uncertainties in the trajectory modelling mean that it is possible that air-masses have been influenced by the ship's own emissions. Recirculated air would be expected to be depleted in O_3 due to its full titration with high NO_x emissions from the ship exhaust (this chemistry removes reduces O_3 down to a few ppb from air travelling directly from the exhaust to the sampling inlet only a few tens of metres away). In Figure 5.5, O_3 can be seen to be relatively constant throughout the nucleation period at approximately 27.5 ppb, with abrupt changes occurring at times previously identified (via CN and trajectory data) as air-mass changes. The constant concentrations between these abrupt changes then, is reflective of the influence of a single air-mass and confirms previous conclusions.

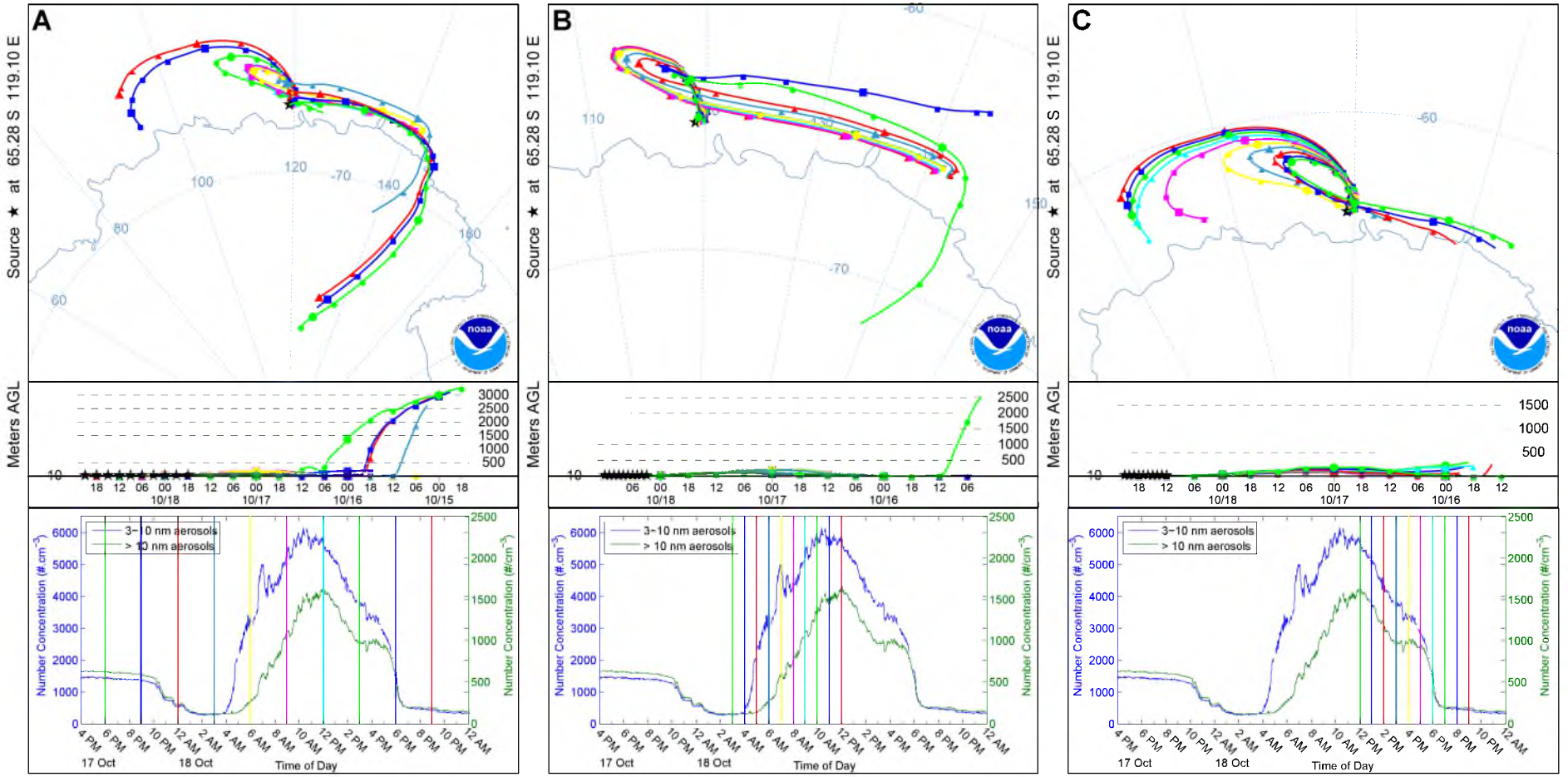

Figure 5.4: 72 hour back trajectories, calculated using NOAA's HYSPLIT model and driven by GDAS meteorological data, during the 18th October particle formation event. Coloured lines in the lower plots correspond to colours in trajectory plots and show the release time of the trajectory relative to the particle concentration time-series. **A**: Ten trajectories, one released every three hours, spanning the entire event from 17 Oct 18:00 to 18 Oct 21:00. **B**: Ten trajectories, released hourly, spanning the increase in particle number concentration, between 03:00 and 12:00 18 Oct. **C**: Ten trajectories, released hourly during the decrease in particle number concentration to background between 12:00 and 21:00 18 Oct. All times are in UTC.

Total Gaseous Mercury (TGM): TGM is another independently measured atmospheric component that shows (Figure 5.5) significant and simultaneous change with air-mass changes identified previously. Despite the recent establishment of a number of continuous monitoring stations, background TGM concentrations are still relatively rare in the Southern Hemisphere (Slemr et al., 2015). Despite short-term spikes above 1.5 $ng.m^{-3}$, our measurements generally showed background values ranging from 0.7 to 1.1 $ng.m^{-3}$, similar to the most recent Southern Hemisphere values that range between 0.8 and 1.1 $ng.m^{-3}$ (Slemr et al., 2011; Slemr et al., 2015). During the period being discussed however (Figure 5.5), concentrations increased from less than 1.0 $ng.m^{-3}$ up to 1.5 $ng.m^{-3}$, remaining at these conditions for a sustained period relative to previous spikes, before returning back to background values less than 1 $ng.m^{-3}$, coincident with the ending air-mass change. This corroborates the previous inference of a single air-mass identified to be influencing the event.

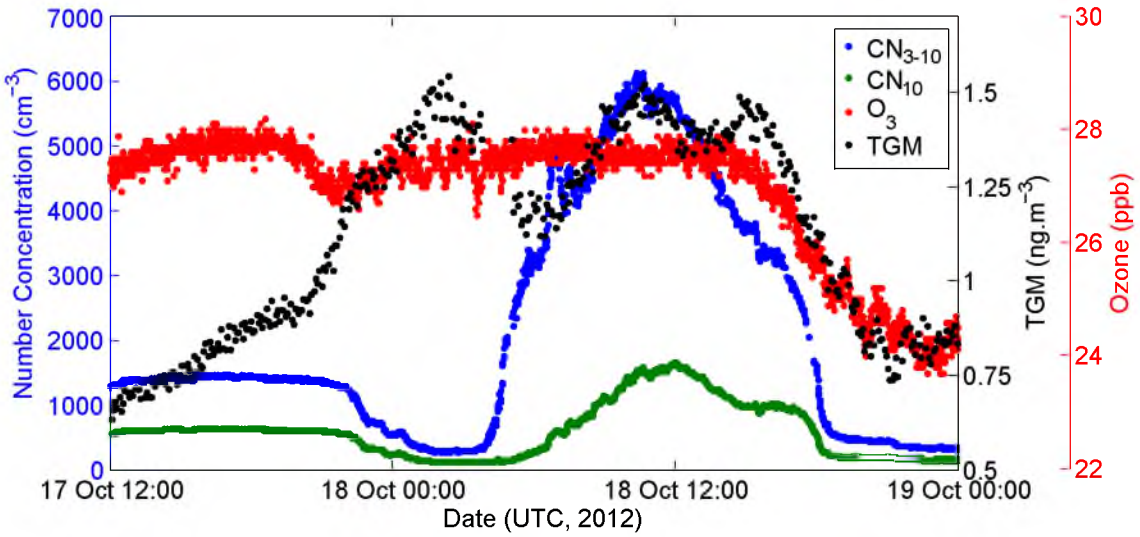

Figure 5.5: Time series of O_3 and TGM during the nucleation event, with aerosol concentrations included for reference. O_3 is observed not to deviate from around 27.5 ppb throughout the nucleation and growth period of the event. During the same period, TGM concentrations within the single air-mass influence during the event, were found to vary around a value of approximately 1.5 $ng.m^{-3}$, a significant increase compared to a median value (± MAD) of 1.0 $ng.m^{-3}$ for the whole voyage. The simultaneous decrease occurring at the end of the event corresponds to the return of particle concentrations to background values resulting from an air-mass change.

Aerosols: If nucleation is occurring at the meso-scale, steady or slowly changing aerosol trends will be observed in particle concentration. Conversely, if events are occurring over the scale of 10s of metres, sudden and large fluctuations in number concentration would be expected on short timescales on the order of seconds to

minutes. The generally steady trends in aerosol number concentrations during this event support the conclusion of a meso-scale homogeneous air-mass.

A single air-mass: Since a single air-mass is influencing the measurement site, it can be concluded that the physics and chemistry over this meso-scale is largely homogeneous. Consequently, during this NPF event, conclusions about the growth of aerosols and changes in atmospheric composition from measurements from our stationary site can be made confidently without worrying that variability is a result of changing air-mass.

5.3.2 Particle Formation Rates

Particle formation rates are important in quantifying many chemical and physical processes in the atmosphere. The technology for measuring nucleating clusters directly has only recently been developed (Jiang et al., 2011a; Jiang et al., 2011b; Vanhanen et al., 2011), and its measurement is not yet widespread. Previous to this recent development, measurements could only detect aerosols greater than 3 nm diameter. Kulmala et al. (2004) summarises the established methods that allow calculation of the formation rate, J_D, of particles of diameter D. The diameter, D, corresponds to the instrument detection limit, which in this study equals 3 nm. Mathematically, J_D is equal to the flux of particles past the size D because of their growth:

$$J_D(t) = \left.\frac{dn(D,t)}{dD}\right|_D \times \left.\frac{dD}{dt}\right|_D \tag{5.4}$$

where t is time and $n(D,t)$ is the particle number size distribution. To apply Eq. 5.4, the particle number size distribution and the growth rate at size D must be known, both of which are rarely available. The instantaneous formation rate, $J_D(t)$, is rarely calculated, but instead, an average formation rate, J_D, is calculated over some time interval Δt. The choice of Δt is arbitrary, but is usually calculated over the formation event or some shorter period. Taking a time average, a new relation can be written such that

$$\left.\frac{\Delta N_{D,D_{max}}}{\Delta t}\right|_{obs} = J_D - \left.\frac{\Delta N_{D,D_{max}}}{\Delta t}\right|_{self-coag} - \left.\frac{\Delta N_{D,D_{max}}}{\Delta t}\right|_{coag-scav} - \left.\frac{\Delta N_{D,D_{max}}}{\Delta t}\right|_{trans} \tag{5.5}$$

where $N_{D,D_{max}}$ is the total particle number concentration in the size range $[D, D_{max}]$ and D_{max} is the maximum size the critical clusters can reach because of their growth during Δt. The first term on the left hand side of Eq. 5.5 is the observed change in $N_{D,D_{max}}$ during Δt and can be obtained from measurements. The second and third terms on the right hand side represent the loss of particles in the size range $[D, D_{max}]$ by self-coagulation and coagulational scavenging to larger pre-existing

particles (with $D > D_{max}$), respectively. The last term represents the influence of air mass transport on $N_{D,D_{max}}$. This term may become important in particular locations and at particular periods during an event.

When the effects of both coagulation and transport are small compared with particle production, Eq. 5.5 reduces to

$$J_D \approx \left.\frac{\Delta N_{D,D_{max}}}{\Delta t}\right|_{obs}. \tag{5.6}$$

This is often an excellent approximation when air-masses are relatively clean and homogeneous, when background particle concentrations are low (reducing scavenging), or when nuclei particle number concentrations is very high ($> 10^5 cm^{-3}$). Given air-masses in the Antarctic and Southern Ocean regions satisfy these conditions well, calculation of the nucleation rate using this equation should be a very good approximation for our dataset.

The instrumentation utilised in this thesis was capable of measurements down to 3 nm diameter, and gave measurements of number concentrations of particles between 3 and 10 nm diameters. This meant that J_3 could be calculated directly using Eq. 5.6 with $[D, D_{max}]$ defined as [3, 10] (units of nm). To ensure the assumptions hold true, the time period used for calculation was carefully considered, and was determined using the clear nucleation period identified using the linear period of increasing ratio data in Figure 5.6. Using this time period and diameter limits, Eq. 5.6 becomes

$$J_3 \approx \frac{\Delta N_{3,10}}{\Delta t} = 0.5 \pm 0.1 \ cm^{-3}s^{-1} \tag{5.7}$$

where the uncertainty has been estimated as a combination of both propagated measurement uncertainty and the assumption of linearity during the chosen period. This rate is the average over the initial growth period that is identifiable as growth only of particles less than 10 nm. As observed in Figure 5.6, the use of other or smaller averaging periods change this formation rate considerably, with resulting J_3 values ranging between $0.2 - 1.1 \pm 0.1 \ cm^{-3}s^{-1}$. These values compare well with others measured in both the Antarctic region (Davison et al., 1996; Koponen et al., 2003; Asmi et al., 2010; Järvinen et al., 2013) and in various continental mid-latitude locations which range from 0.001-10 $cm^3.s^1$ but can reach into the tens of thousands (see review by Kulmala et al. (2004)).

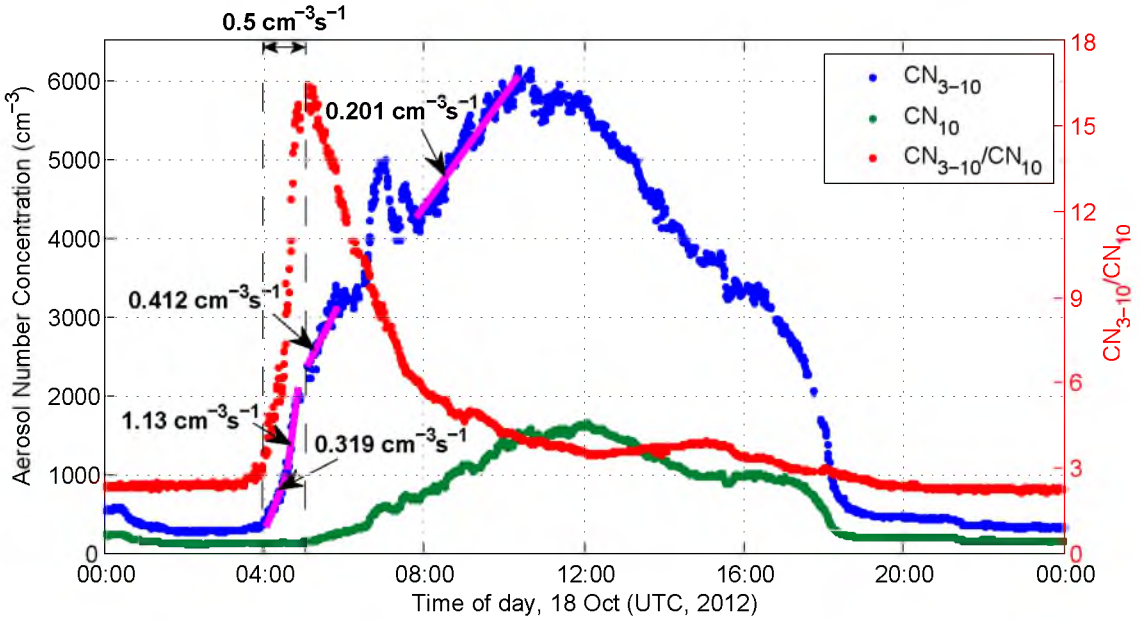

Figure 5.6: Formation rate of aerosols of 3 nm diameter, J_3, calculated for periods where the gradient of CN_{3-10} was approximately constant. An average of 0.5 ± 0.1 $cm^{-3}s^{-1}$ was calculated for the full period of increase in ratio CN_{3-10}/CN_{10}, however the shorter periods calculated here show formation rates of more than double the average.

5.3.3 Particle Growth Rate

Aerosol growth is clearly observed in the data-set as a delay in increasing number concentrations between the two measured size bins. Quantifying this growth with the available data is difficult and requires careful selection of the data, and an assumption that during the period chosen, increases in number concentrations are caused by the nucleation event, and not fluctuations in the background aerosol. The choice of the 1.25 hour period shown in Figure 5.7 was determined by the constant increase in the CN_{3-10}/CN_{10} ratio, and is identified as the clearest period from which growth can be determined to be linear between 3 nm and 10 nm. This period is essentially the same as was used for determination of the nucleation rate in the previous section, however there is no requirement for linearity in the gradient of the data, but is rather determined by the changes in the sign of the gradient (i.e. increasing to decreasing) since this reflects growth into and out-of the 3-10 nm size range. The growth rate can then be calculated as the width of the ratio size range, 7 nm, divided by the time it takes to transit that size range (1.25 hours). The resulting growth rate of 5.6 ± 0.9 $nm.hr^{-1}$ is similar in magnitude to recent results of new particle formation from continental biogenic precursors (Kyrö et al., 2013), is 2-6 times larger than those observed at other Antarctic locations (Gras, 1993; Koponen et al., 2003; Park et al., 2004; Asmi et al., 2010; Belosi et al., 2012; Järvinen et al., 2013) and is comparable to observations at other mid-latitude coastal locations

(O'Dowd et al., 1998; O'Dowd et al., 1999; O'Dowd et al., 2002a; Kulmala et al., 2004).

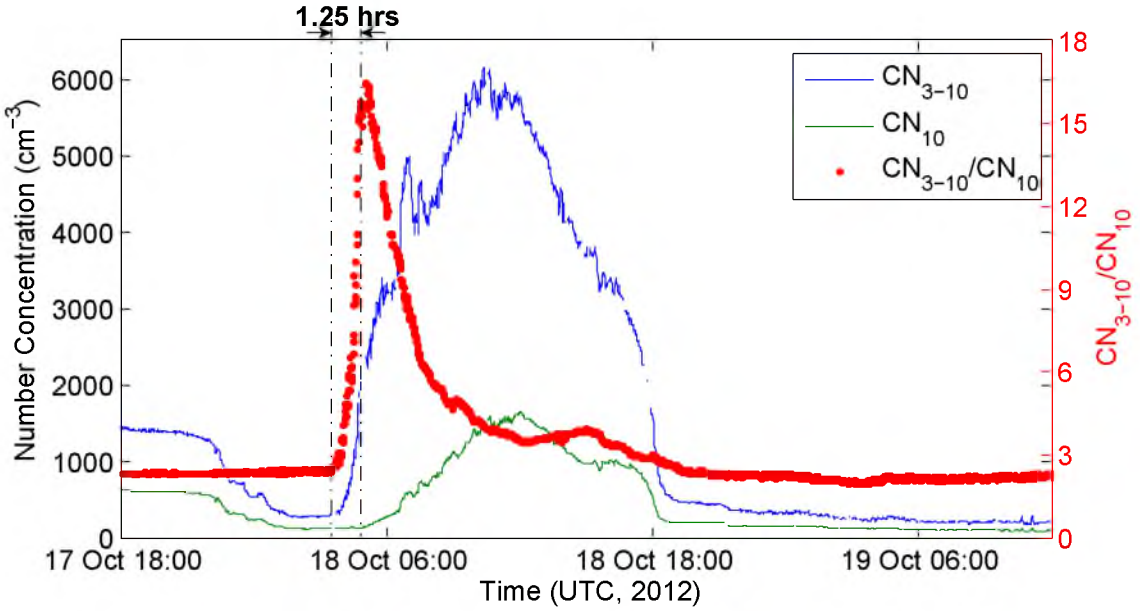

Figure 5.7: The ratio CN_{3-10}/CN_{10} shows a clear period of particle formation and growth to 10 nm that occurs within approximately 1.25 hours. This timeframe gives the best estimate of growth rate possible with the available data and results in a rate of 5.6 ± 0.9 $nm.hr^{-1}$.

5.3.4 Loss Processes

The decline of CN to background at the end of the event is worth detailed consideration for a full understanding of the event. Although trajectories and ancillary data show that the final decline of CN to background (**VII** of Figure 5.2) is a result of an air-mass change, the gradual decline preceding this (period **VI**) is likely to be driven by other loss mechanisms. Following the discussion by Davison et al. (1996), other than dilution, loss mechanisms that influence this gradual decline period include horizontal dispersion and/or advection; vertical mixing; and coagulation.

Dispersion and advection describe the horizontal transport of a component of the atmosphere from its origin to a region downwind, sometimes diluting in the process. Although trajectories suggest horizontal mixing is an important factor in the decrease of number concentrations, the influence was further analysed using the technique outlined in Davison et al. (1996). The horizontal dispersion, s, can be described in terms of the time, t, and the eddy diffusivity, D, such that $s = \sqrt{2Dt}$. Even if a large eddy diffusivity of 15 $m^2.s^{-1}$ is assumed, a maximum value of horizontal dispersion over the seven hour period of CN decline is less than 1 km. Taking the average wind speed of 3.3 $m.s^{-1}$, a CN decline timescale of seven hours

of our event corresponds to a horizontal dispersion of over 80 km. This suggests a negligible effect of horizontal dispersion.

Horizontal advection assumes that the measurement point lies on the edge of the formation region, and that the decline in CN is a result of moving out of the formation air-mass. Under this assumption, calculating the expected time for decline to background is simply a case of considering the distance the elevated concentrations are spread across (i.e. the horizontal dispersion), and how fast this air-mass is travelling past a fixed point. Taking the average wind speed (3.3 $m.s^{-1}$) and a calculated horizontal dispersion of less than 1 km, the expected time for elevated CN to decline to background would be a maximum of 300 seconds. Since the decline via advection is too rapid to explain the observed seven hour decline, we discount this as a major loss mechanism.

The influence of vertical mixing and coagulation can be modelled assuming a well-mixed boundary layer capped with an inversion where particle free air is being entrained from the free troposphere. This can be quantified by the following equation (Davison et al., 1996) which describes the time rate of change of CN concentration:

$$\frac{dn}{dt} = -n\left(\frac{kn}{2} + \frac{v_d}{H}\right) \tag{5.8}$$

where n is the total CN concentration, t is time, k is the coagulation coefficient, v_d is the entrainment velocity and H is the boundary layer mixing height. Integration yields a function dependent only on k, v_d, H and n_0, the initial concentration, such that

$$n = \frac{ace^{-bt}}{1 - ce^{-bt}} \tag{5.9}$$

where $b = v_d/H$, $a = 2b/k$ and $c = n_0/(a + n_0)$. Taking an entrainment velocity (v_d) of 0.34 $cm.s^{-1}$ (from calculations performed with Weddell Sea measurements by Davison et al. (1996)), a calculated boundary layer height (H) of 200 m (based on trajectories calculated with the UK Met Office's Numerical Atmospheric-dispersion Modelling Environment (Schofield, Harris, and Connors, 2014)) and an initial CN concentration of 7500 cm^{-3}, a coagulation coefficient (k) of $(8 \pm 2) \times 10^{-9}$ $cm^{-3}.s^{-1}$ results in the best fit to period **VI** of the data, shown in Figure 5.8. The two variables H and v_d, are assumed from the literature and need an assessment of sensitivity. Calculation of k is insensitive to boundary layer height, but highly sensitive to entrainment velocity. Reducing the entrainment velocity by a factor of 10 increases k by only a factor of two and results in a similarly good fit. However, an increase in the entrainment velocity by an order of magnitude results in the inability to find a value of k that fits the measurements, a fact consistent with the unrealistic nature of this change. Although the uncertainty around the entrainment velocity

parameter is high, it is still possible to conclude that coagulation and vertical mixing are sufficient to explain the loss.

The reduction of CN concentrations during the event is therefore likely to be explained by three periods. The first, period **V** (Figure 5.2), involves very slow loss during which photochemistry is still possible before sunset. During this period, coagulation has already started but CN concentrations are being maintained by continued production. At sunset, production ceases and coagulation dominates the changing concentrations of period **VI**. CN losses increase drastically during period **VII**, coinciding with the air-mass change described previously and shown in Figure 5.4C.

Comparison of this coagulation coefficient ($(8 \pm 2) \times 10^{-9}\ cm^{-3}.s^{-1}$), derived during period **VI**, to those of coefficients calculated using Fuchs formula at -11°C (Seinfeld and Pandis, 2006) yields information about the likely sizes of coagulating aerosols. Fuchs formula calculates the coagulation coefficient by considering the coagulation of two particles with wet diameters D_1 and D_2. Resulting calculations yield coagulation coefficients of $(8 \pm 0.1) \times 10^{-9}\ cm^{-3}.s^{-1}$, only when a D_1/D_2 ratio of 5.1 ± 0.3 exists. Particles with the appropriate diameter ratio, for example 3 and 17 nm, or 4 and 21 nm, are therefore the most likely to be present and responsible for the observed coagulation rate.

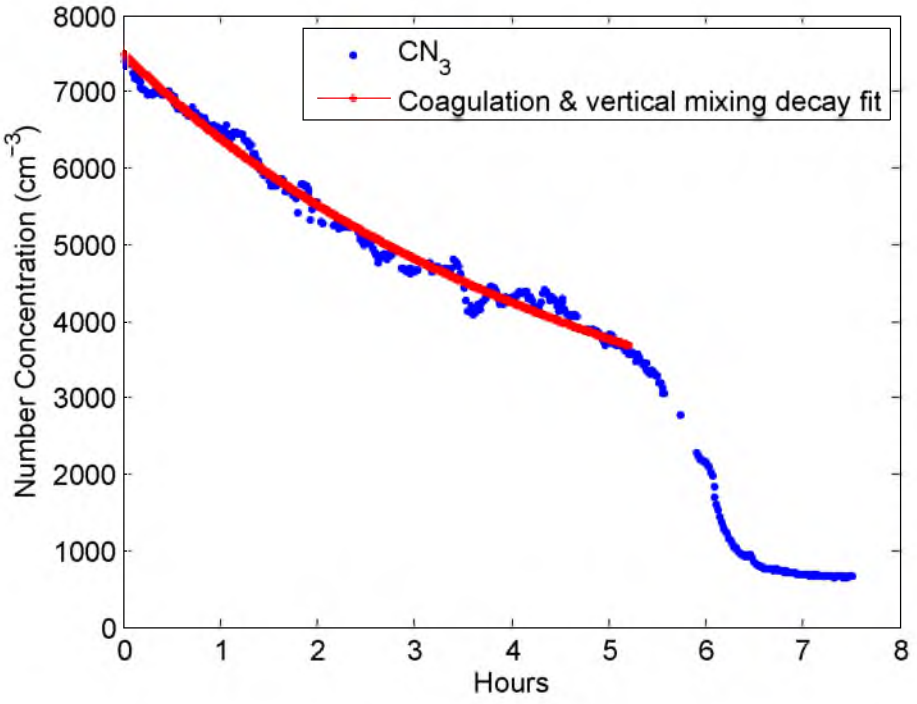

Figure 5.8: CN_3 data with the coagulation and vertical mixing decay fit that is found to fit for the first five hours of decay, before an air-mass change results in rapid decay to background at around 5.5 hours. Zero hours corresponds to midday (UTC).

5.3.5 Aerosol Surface Area

If existing aerosol concentrations provide sufficient surface area, precursors are more likely to condense onto these surfaces rather than nucleate to form new nuclei. Although aerosol surface area cannot be calculated accurately from the available data, approximate values can be inferred using Antarctic aerosol size distributions from the literature, along with size information revealed from theoretical calculations (above). Assuming a mean background aerosol population diameter of 100 nm, consistent with measurements by Koponen et al. (2002), the air-mass change prior to the event resulted in a transition in pre-existing aerosol surface area from 19 to 4 $\mu m^2.cm^{-3}$. During nucleation, the aerosol population changes drastically, increasing in number, but decreasing in mode size. Using the number concentrations and size information derived from coagulation calculations, aerosol surface area remains below 5 $\mu m^2.cm^{-3}$, until nucleated particles grow to sizes exceeding ~30 nm in diameter. Previous studies have suggested that NPF is possible in the MBL only when pre-existing aerosol surface area is below 5-25 $\mu m^2.cm^{-3}$ (Covert et al., 1992; Raes, 1995; Clarke et al., 1998), suggesting that conditions before and during this event are suitable for precursor nucleation rather than scavenging.

5.3.6 Characterising Photochemistry: Solar Radiation and Clouds

This event was characterised by an abnormally high incoming solar radiation (global irradiance) which was a result of exceptionally clear cloud conditions that were uncommon during the cruise, as shown in Figure 5.9. Sustained periods of solar radiation reached above 700 $W.m^{-2}$ at midday, at least 100 $W.m^{-2}$ higher than any other day during the 32 day measurement period. Ship based web-camera data, shown in Figure 5.10, shows that between thick periods of stratocumulus surrounding the event, light cumulus clouds dominated. Figure 5.11 gives a closer look at the solar radiation on the 18th October, along with its various with respect to aerosol and TGM concentrations (discussed in detail later), showing short-term (~10 minute) decreases from the clear-sky radiation due to various periods of cloud, as well as short-term increases resulting from cloud-edge effects.

Thick stratocumulus cloud began to clear at approximately 0120 (UTC) and full cloud-free conditions lasted for around 4.5 hours, encompassing solar noon. The start of the NPF event, as evidenced by increasing CN_{3-10}, was found to occur approximately two hours after the clouds cleared. If the nucleation event was photochemically initiated, this two hour period gives an estimate of the time-frame required for precursor oxidation, nucleation and subsequent growth up to 3 nm (where detection occurs).

Although the rate of increase of CN_{3-10} reduced when clouds returned towards the end of the day, concentrations continued to rise until around sunset (1200 UTC). A similar pattern was observed in the CN_{10} dataset, which together suggested photochemically driven nucleation. This relationship may be explained by one of two options: the high levels of solar radiation that may have been necessary for initiation, were no longer required for continued chemistry; or the high levels of radiation produced a reservoir of oxidised species that were slowly depleted throughout the day. Although interesting, determination of this level of detail of the nucleation mechanism is premature and would need additional measurements (e.g. photolysis rates, measurements of OH), unavailable during this campaign. A qualitative investigation of reacting species is the more important first step.

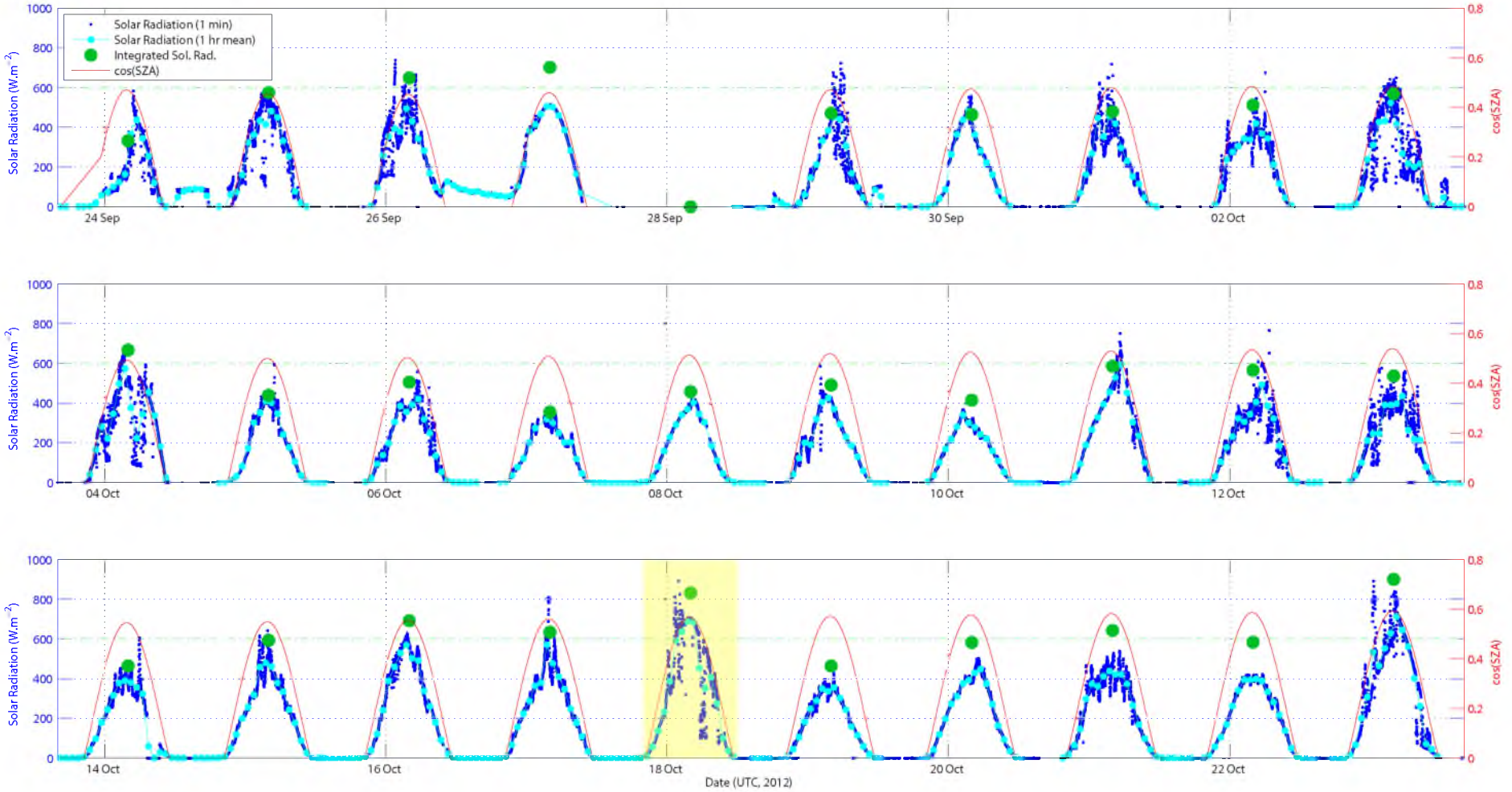

Figure 5.9: Incident solar radiation (both minute and hour averages) for the full period within the sea ice zone while aerosol measurements were being made. Also plotted is the integral of solar radiation for each day (normalised by a factor of 0.0027) and the cosine of the solar zenith angle (SZA). The highlighted new particle formation event day can be seen to be the first of the record to observe sustained radiation above the 600 $W.m^{-2}$ reference line (green). Smooth, clear sky periods are rare, with variability caused by varying cloud thickness. Single point spikes are real, and caused by cloud edge effects. One other day of sustained radiation above 600 $W.m^{-2}$ occurred on 23 October which coincided with a local pollution event from the ship resulting in data being unusable.

Time (UTC)	Cloud Event (type)	Ref.
Prior to 0118	Thick cloud cover (**stratocumulus**)	**A**
0118	Thick cloud clears	
0154	Partly cloudy conditions ensue (**cumulus**)	**B**
0240	Clouds clear completely	**C**
0548	Light cloud (**cumulus**)	**D**
0758	Light cloud clears	
0842	Thick cloud arrives and stays (**stratocumulus**)	**E**

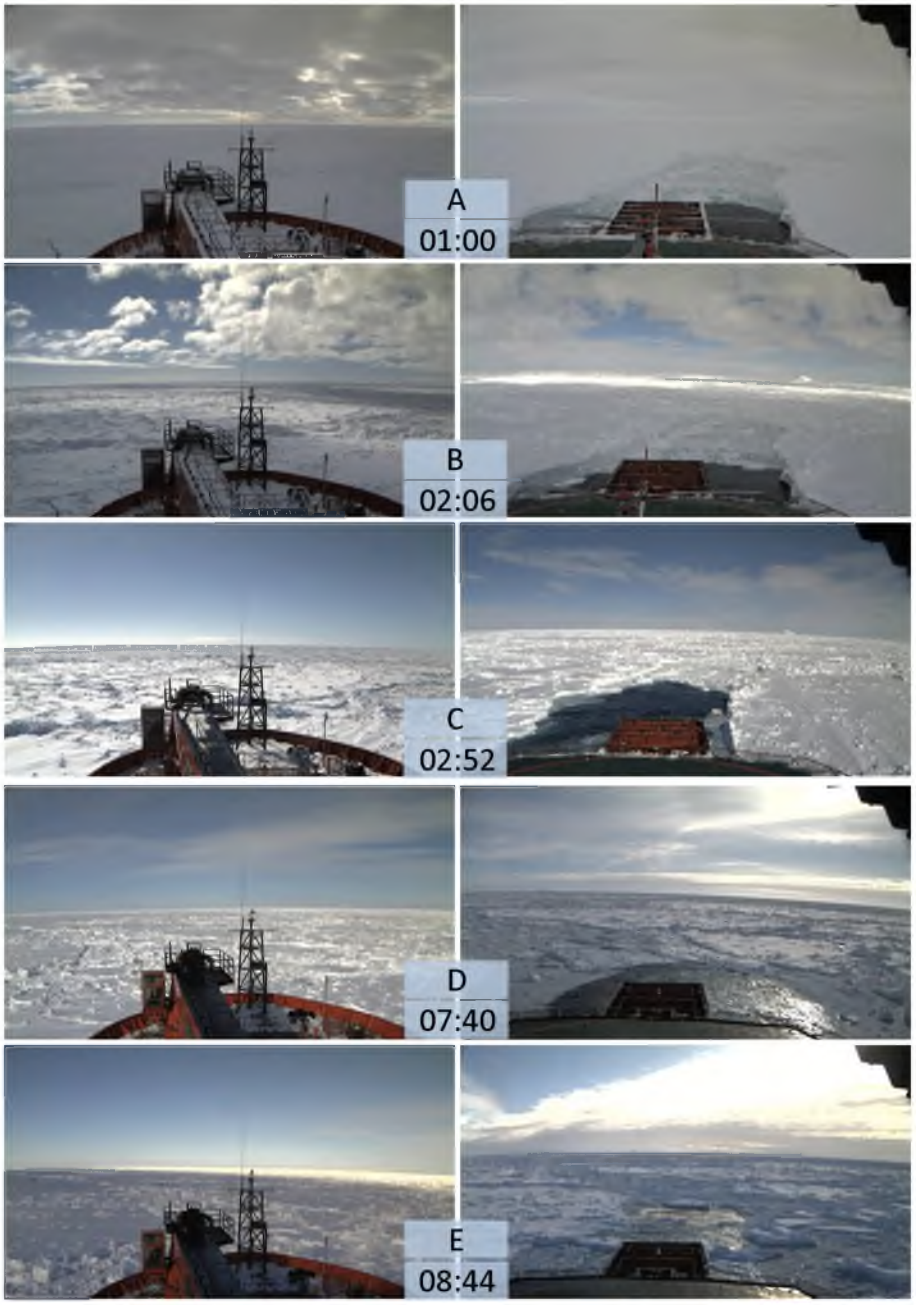

Figure 5.10: Cloud conditions during the 18th October (with timestamp in UTC) along with a table outlining the timeline of events. Photos from Aurora Australis' aft and fore cameras - courtesy of AAD. More photos during the day are given in Appendix C.2.

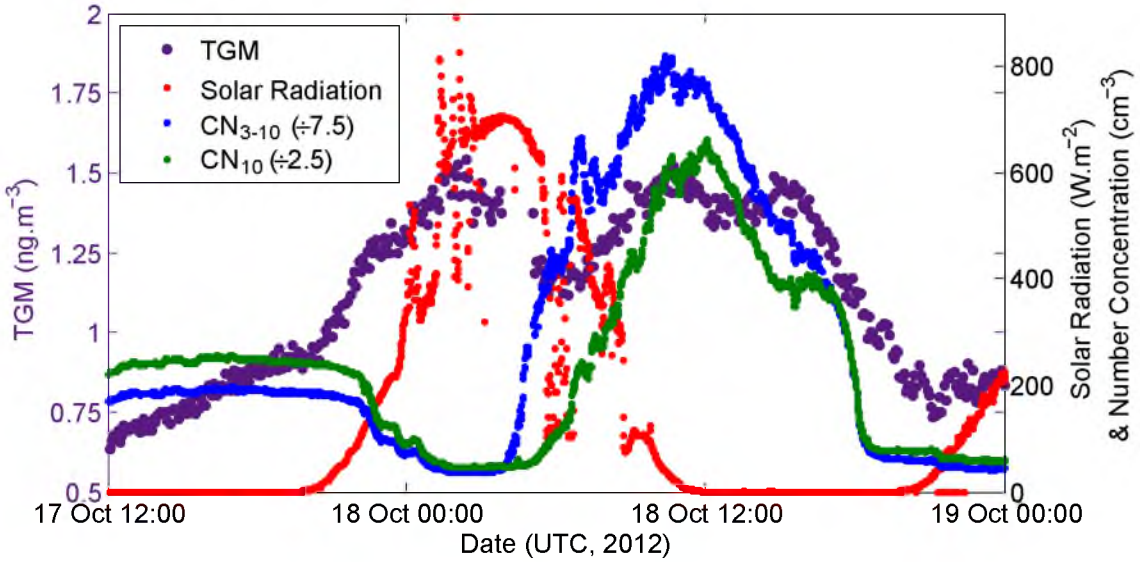

Figure 5.11: Time series of TGM and incident solar radiation, with particle number concentrations as a reference. TGM is found to decrease considerably simultaneously with the sun coming out after a period of thick stratocumulus cloud. The decrease in TGM continues until thick cloud returns.

5.3.7 Nucleating Species and Mechanism

To understand the nucleation chemistry occurring during the day, an assessment of the various known mechanisms is performed to determine the likelihood of each. Where possible, measurements of possible precursors are utilised, and in their absence, modelling studies are employed.

5.3.7.1 Volatile Organic Chemistry

Pre-existing aerosol concentrations in the air-mass were sufficient ($CN_3 = 280\ cm^{-3}$) to seed aerosol growth via condensation of volatile organic compounds (VOCs) (Hoffmann et al., 1997), or extremely low volatility organic compounds (ELVOCs; which are able to condense with even lower aerosol concentrations). For this heterogeneous growth to occur, VOC concentrations must be sufficiently high to condense onto pre-existing surfaces. In the MBL, VOC concentrations necessary to form Secondary Organic Aerosol (SOA) are generally only observed during heavy phytoplankton blooms (e.g. Meskhidze and Nenes, 2006). Although a full suite of VOC concentrations were not measured during SIPEXII, proxies for biological activity were. Atmospheric biogenic halogenated compounds, measured using GC-ECD (e.g. $CHBr_3$), showed no deviation from baseline in the days encompassing the event. Surface water fluorescence was measured during the voyage, and after conversion to chlorophyll concentration (a proxy for biological activity), can be compared to previous studies relating chlorophyll to SOA formation. Studies by Hu et al. (2013) showed that

chlorophyll concentrations necessary for organic concentrations sufficient for SOA formation are of the order of 10-60 $mg.m^{-3}$, which were the result of summer phytoplankton blooms in Prydz Bay, Antarctica. During SIPEXII, no such phytoplankton blooms were observed, and chlorophyll concentrations, shown in Figure 5.12, reached a maximum of 0.4 $mg.m^{-3}$ (median of 0.15 $mg.m^{-3}$) during the aerosol measurement period, with order of magnitude lower concentrations on the event day, averaging 0.06 ± 0.03 (2σ) $mg.m^{-3}$. Additionally, back-trajectories showed that recent air-mass history avoided common high chlorophyll areas such as Prydz Bay, ruling out transport from biologically active regions. Chlorophyll-a concentrations acquired from the NASA Oceancolor website (http://oceancolor.gsfc.nasa.gov) confirm *in-situ* data, with concentrations well below 0.3 $mg.m^{-3}$ in the hundreds of kilometers surrounding the measurement location. Despite this, nucleating species could be produced *in-situ*. However, measurements taken aboard SIPEXII strongly indicate that their concentrations, if present, are at a minimum during the event compared to other periods of the voyage, suggesting their involvement is unlikely.

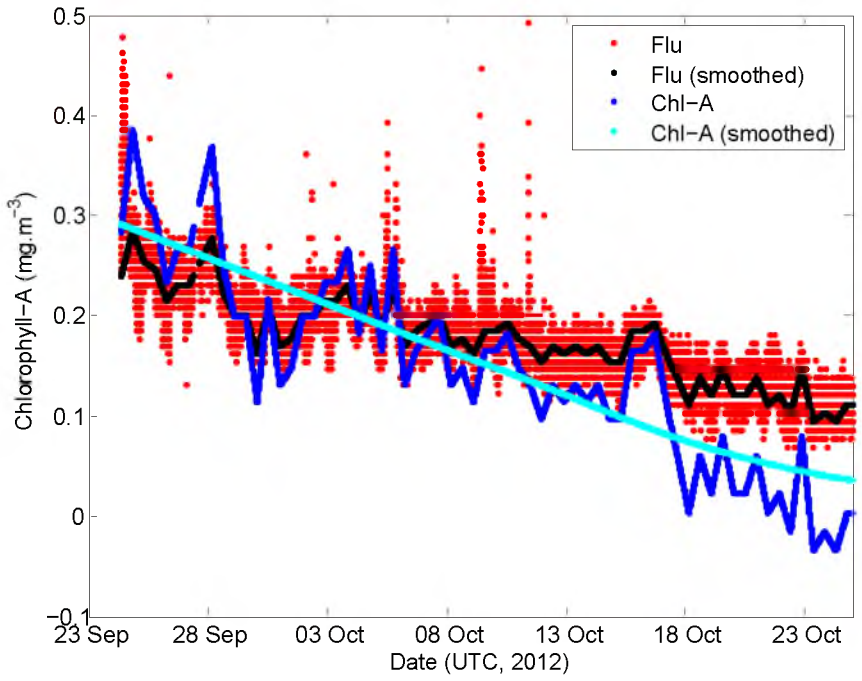

Figure 5.12: Time series of fluorescence data (Flu) and chlorophyll-A (Chl-A) data for the period coinciding with aerosol measurements. Chl-A data are obtained by calibrating Flu data to chlorophyll concentrations obtained from four water samples taken sporadically throughout the voyage and analysed with High Pressure Liquid Chromatography (HPLC). Negligible chlorophyll concentrations were observed during the voyage, consistent with the minimal biological activity experienced. On the 18th October, concentrations were lower than any previously observed during the voyage, suggesting biologically produced organic vapours are unlikely to be involved in nucleation mechanisms.

5.3.7.2 Halogen Chemistry

Active nucleation chemistry involving iodine oxidation has been demonstrated to occur rapidly on the local scale when coastal kelp-beds are exposed during low-tide periods (O'Dowd et al., 1998; O'Dowd et al., 1999; O'Dowd et al., 2002a). This chemistry is found to coincide with high levels of iodine monoxide (IO) of up to 6 pptv (Saiz-Lopez and Plane, 2004). *In-situ* (Frieß et al., 2001; Frieß et al., 2010; Saiz-Lopez et al., 2007a; Atkinson et al., 2012) and satellite (Saiz-Lopez et al., 2007b; Schönhardt et al., 2008; Schönhardt et al., 2012) measurements of IO (and I_2) reveal Antarctica as a global iodine hotspot, particularly in the West Antarctic during spring, where concentrations of 6 pptv are frequent, and midday values up to 20 pptv have been observed. Although these high concentrations suggest that nucleation from iodine chemistry could be prolific in the Antarctic region in general (as suggested in Chapter 3), measurements during this voyage found IO concentrations, shown in Figure 5.13, average below about 0.5 ppt, and during the nucleation event, concentrations were at the detection limit of approximately 0.1 ppt. The influence of a single regional air-mass, combined with the exceedingly low IO concentrations measured during the event, make it unlikely that iodine chemistry was responsible for this observed nucleation event.

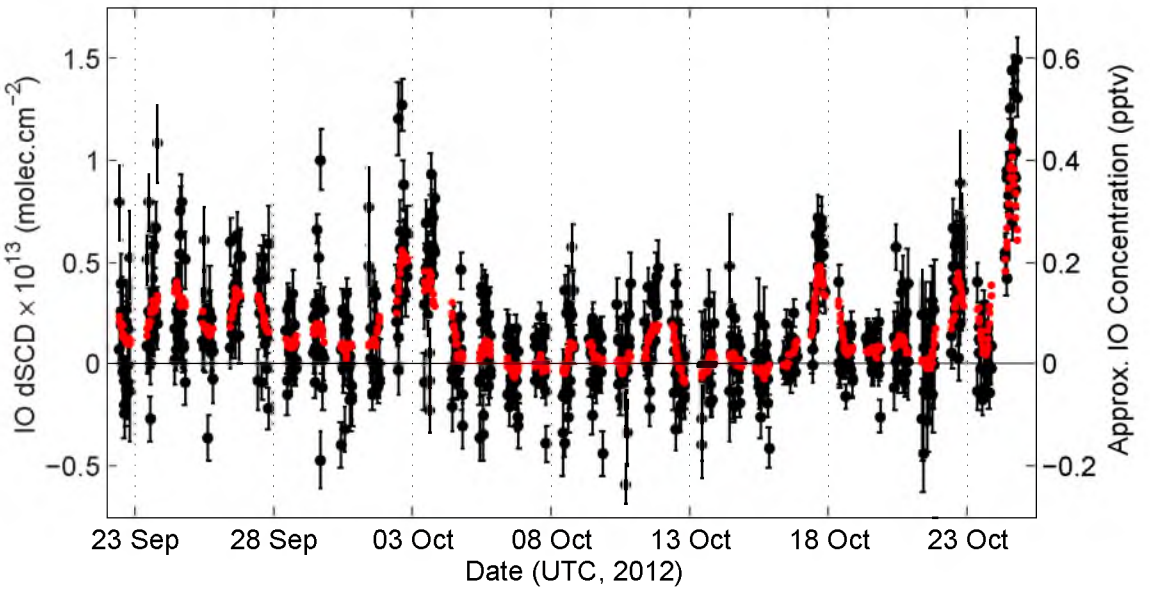

Figure 5.13: IO differential Slant Columns Densities (dSCD) in the sea ice zone, measured at 2° elevation using the MAX-DOAS, together with 19 point running means (red). The right-hand y-axis shows an approximate scale for when dSCDs are converted to mixing ratios assuming a 10 km effective column (Johnston, 2014). Concentrations are negligible throughout the cruise, and particularly so on the event day.

5.3.7.3 Sulfur Chemistry

Nucleation mechanisms involving sulfuric acid (e.g. binary nucleation of H_2SO_4 and H_2O) are the most common in the atmosphere. Because of this ubiquity, these mechanisms are often the only ones included in chemistry and climate models.

In this study, it was not possible to determine whether sulfur chemistry was involved in nucleation using the available measurements. Flask measurements of DMS began on the 18th October, however these measurements were made with an instrument that was designed for aqueous-phase DMS concentrations, and thus lacked the sensitivity to measure gas-phase DMS. These measurements are useful, however, to get a rough estimate of sulfur loading. On the 18th October, measurements using this method retrieved high DMS concentrations on the order of 400 pptv, suggesting DMS oxidation pathways could be responsible for this formation event.

To fill this gap in measurements, the TOMAS box model was employed to examine whether existing nucleation schemes involving sulfuric acid could explain the observed nucleation rates. The source of H_2SO_4 employed in this box model was the biggest natural sulfur source, DMS. Utilisation of a box model was suitable for this study primarily because of the single homogeneous air-mass influencing the measurement location during the event.

The purpose of the modelling study was to determine whether existing H_2SO_4-dependent nucleation schemes could account for observations under the measured conditions. If, even under the most favourable conditions for DMS driven nucleation and growth (high DMS and $OH^{\bullet}$ concentrations), the model cannot produce the observed number and rate of growth, it is likely that another species or alternate chemical mechanism is driving the nucleation chemistry. Because the study aims for a qualitative result, the (potentially high) uncertainty associated with the input variables was not quantified in detail.

The range of plausible input variables used for model simulations was outlined earlier in this chapter in Table 5.2. Analysis of results determined that no combination of input parameters utilising either nucleation mechanism included in the model (binary homogeneous nucleation or IMN) could simultaneously produce both the formation and growth rates necessary to explain the observed nucleation event.

Interestingly, when the background aerosol population was initialised with a single mode with a diameter of less than 3 nm (simulating seed aerosol), model simulations were able to reproduce the observed rates using a range of input variables. However, it was suspected that this result was a consequence of the removal of the accumulation mode background populations which would usually scavenge much of the condensible material, providing conditions where growth rates at these early stages were unrealistically high. To test realistic conditions, where both a seed pop-

ulation and an accumulation mode background population are present, the initial aerosol population was modified to have a dual mode distribution, with peaks in both the nucleation (1.5 nm) and accumulation (100, 150, and 300 nm) modes, as shown in Figure 5.14. Reintroduction of this background aerosol load, at a modest number concentration of 120 cm^{-3} (based on measurements), meant that even when seed populations were present, no set of input parameters could be found that could explain observations.

Inclusion of MSA chemistry into the model was performed using an oversimplified method that allowed qualitative testing of its involvement in nucleation and growth processes. MSA simulations increased growth rates significantly, however this modification still did not result in any simulations that were able to reproduce observations.

It could be concluded that known sulfur chemistry alone, with or without MSA, is insufficient to explain the growth rates observed during the new particle formation event. Since the most common precursors (i.e. organics, halogens and sulfuric acid) are unlikely to be able to explain the nucleation and growth alone, it is likely that an alternative species or mechanism must be participating in this process.

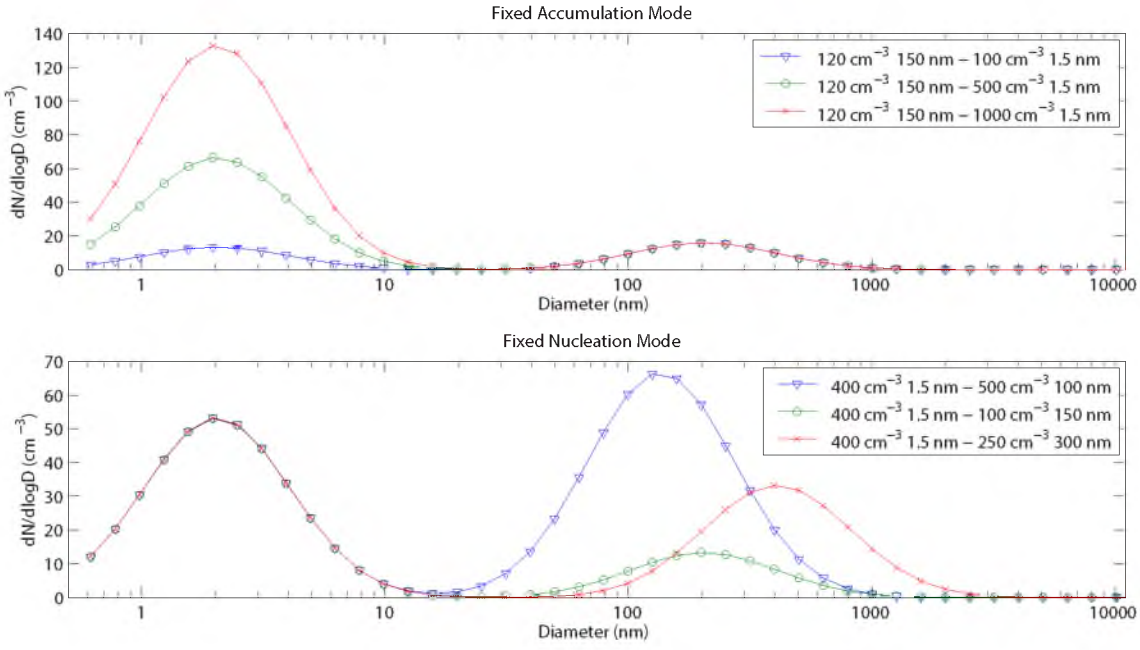

Figure 5.14: Examples of dual mode distributions which initialise the model. Top plot shows simulations where the accumulation mode has a fixed number concentration of 120 cm^{-3}, based on measurements, while lower plots show fixed nucleation mode number concentrations at 400 cm^{-3}. Note, the scale is such that the integral of accumulation mode distribution equals 120 cm^{-3} for the top plot with similar normalisation applied to the lower plot.

5.3.7.4 Mercury Chemistry (Total Gaseous Mercury, TGM)

From the investigation discussed above, known nucleation mechanisms involving sulfuric acid, iodine or organics were unable to explain the observed aerosol data, leaving previously unidentified chemistry the likely explanation. No correlations were found with other measured data except for, surprisingly, TGM.

During the particle formation event, TGM was found to exhibit the highest sustained concentration in this dataset, varying from sustained concentrations of around 1.5 $ng.m^{-3}$. The four hour cloud-free period, described in the Section 5.3.6, was found to correspond directly with the full duration of the first decline in TGM concentration (Figure 5.11). The beginning of this decline corresponded directly with the clearing of the major cloud bands which experienced significantly high peaks of cloud-edge effect radiation. The period of declining TGM ended simultaneously with the appearance of a temporary cloud period around 0600 (UTC), and did not begin to decline again when this cloud cleared and solar radiation had dropped below 600 $W.m^{-2}$ (Figure 5.11). This correlation suggests possible photochemically driven chemistry involving TGM that may require high incoming solar radiation levels - chemistry that is consistent with previous studies that have observed photochemically derived mercury oxidation products in the Arctic atmosphere (Lindberg et al., 2002).

This four hour period of declining TGM concentrations, from a baseline of 1.50 ± 0.05 $ng.m^{-3}$ down to 1.16 ± 0.05 $ng.m^{-3}$, represents an atmospheric TGM depletion of about 20%. The decline, along with the four hour recovery back to baseline, was most likely caused by *in-situ* chemistry, rather than an air-mass change which has been discounted for this period by previous arguments. As discussed by Lindberg et al. (2002), photochemical reactions producing halogen and $OH^{\bullet}$ radicals are able to react with Hg^0 to produce oxidised compounds such as HgO, $Hg(OH)_2$, HgX_2 or HgXY (where X and Y are halogens). Additionally, Hg(II) products are able to be photolytically released directly to the atmosphere from surfaces such as the snowpack (United Nations Environmental Programme, 2008). Oxidation products have properties that make them suitable for nucleation processes, such as being solid at equilibrium under atmospheric conditions making them unlikely to evaporate (Schroeder and Munthe, 1998). Production of these species can occur by direct emission, or *in-situ* chemistry. Ordinarily, Hg oxidation products, once produced, are readily scavenged by pre-existing aerosol populations. This interpretation could be largely driven by the location of most Hg studies being in regions of high pre-existing aerosol surface area. In more pristine conditions where pre-existing aerosol surface area is low, such as those observed in this Antarctic study, these oxidation products have the potential to nucleate rather than adhere to existing surfaces.

To further investigate the possibility of nucleation involving Hg, a lagged correlation was calculated between TGM and CN_{3-10}. Unfortunately, there was insufficient data ($n = 40$) for a full mathematical derivation of the lag period that produced the best correlation. The best fit was determined by calculating the linear model iteratively, incrementing the lag time by five minute steps (limited by TGM time resolution) and visual assessment. Figure 5.15 shows the resulting best fit that occurred at a time delay of around two hours and yielded a negative correlation with an R^2 value of 0.74. If Hg chemistry was involved in aerosol nucleation, the two hour time delay from these calculations puts a time-frame on the chemical mechanism from gas phase (either Hg^0 or Hg(II)) to 3 nm aerosol, consistent with the two hour estimates from solar radiation data.

The influence of a single air-mass throughout the period suggests that the recovery of TGM after nucleation was the result of a new source rather than an air-mass change. It is well established that Hg oxidation products can be photolytically reduced back to Hg^0 and in aqueous environments such as those found in cloud droplets (International Programme on Chemical Safety, 2001; United Nations Environmental Programme, 2008; Feddersen et al., 2012). Aerosol nucleation and growth processes almost invariably require water molecules to adhere to the other condensing species, thereby creating an environment potentially suitable for aqueous chemistry leading to Hg^0 emission. Heterogeneous surface chemistry is also possible in these environments, which may lead to similar emission of Hg^0 and recovery of TGM concentrations (Schroeder and Munthe, 1998). As such, the new source that

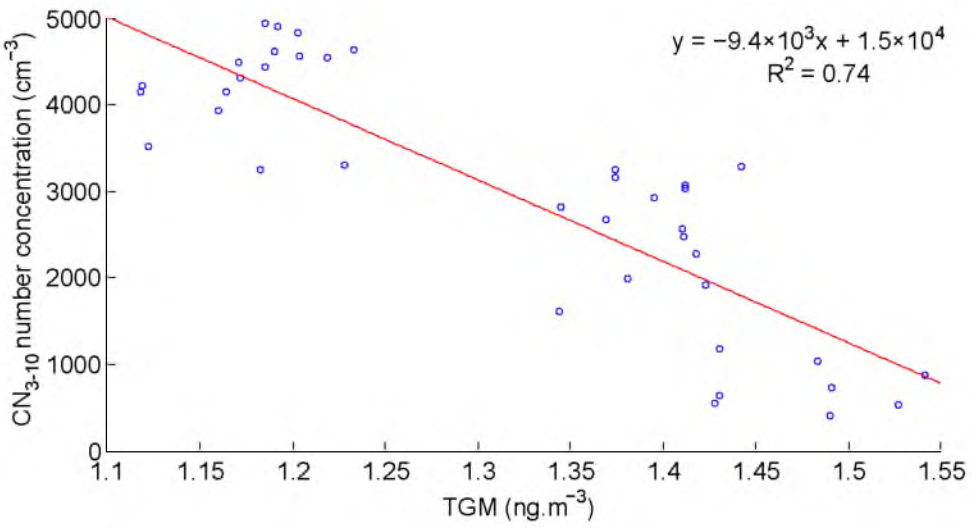

Figure 5.15: A negative linear correlation was found when CN_{3-10} was time lagged by two hours relative to Total Gaseous Mercury (TGM), suggesting involvement of Hg in the nucleation chemistry. The data gap surrounding a TGM concentration of 1.3 $ng.m^{-3}$ is a result of routine calibrations which coincided with the period of interest, and resulted in a 90 minute data gap.

may lead to TGM recovery is likely to be the nucleating aerosol itself. This idea is supported by positive linear correlations between TGM , and CN_{3-10} and CN_{10} (R^2 of 0.53 and 0.67, respectively) during the period between the beginning of TGM recovery and the end of the event, as shown in Figure 5.16. Re-emission of Hg^0 or Hg(II) after its involvement in nucleation means that Hg species may not be found in elemental analyses of grown particles that may be performed in the future.

Although correlation does not imply causation, these correlations suggest, rather surprisingly, the involvement of mercury in the initial nucleation stages onto which other unidentified species can condense and grow. Oxidised mercury products are formed regularly in the atmosphere, and are found frequently in atmospheric particulate matter (termed particulate mercury, Hg(p)). The processes leading to the formation of Hg(p) generally involve the oxidation of Hg^0 to reactive gaseous mercury compounds (Hg(II)) which are of sufficiently low vapour pressure that they readily bind to pre-existing aerosol surfaces. This process of oxidation to deposition occurs on the timescale of hours to days (United Nations Environmental Programme, 2008). In the case where pre-existing aerosol concentrations are low, such as those observed in the event being described, it is reasonable to suggest that reactive gaseous mercury may nucleate by itself, or together with other species, to form new aerosol particles.

Figure 5.17 show a significant TGM depletion that was observed on the day preceding the new particle formation event. As shown in Appendix Figure C.4, this event corresponds to high BrO concentrations, suggesting bromine-driven depletion similar to those commonly observed in the Arctic spring-time (e.g. Schroeder et al., 1998; Lu et al., 2001; Ebinghaus et al., 2002; Boudries and Bottenheim, 2000; Lindberg et al., 2002) together with high snowfall (shown in Appendix Figure C.1). The chemistry involved in this mercury depletion results in oxidised mercury species being deposited onto the snowpack surface of the sea ice from which it can enter the hydrosphere and biosphere, or can be re-emitted back to the atmosphere photolytically. Given the high solar radiation that influenced the event, it is possible that reactive mercury compounds were photolytically re-emitted directly from the surface from the previous day's deposition event. These direct emissions of condensible material (which may or may not undergo further *in-situ* chemical reactions), could be sufficient to explain observations.

It is also possible that Hg^0, readily available from long-range transport, is oxidised *in-situ* to Hg(II) compounds which then condense to form the new nuclei. Hg^0 can be oxidised by numerous species including ozone (Snider, Raofie, and Ariya, 2008), $OH^{\bullet}$ and halogens (X), producing a range of Hg(II) compounds suitable for condensation (some listed above).

The identity of the oxidant in this event is worthwhile considering, and likely

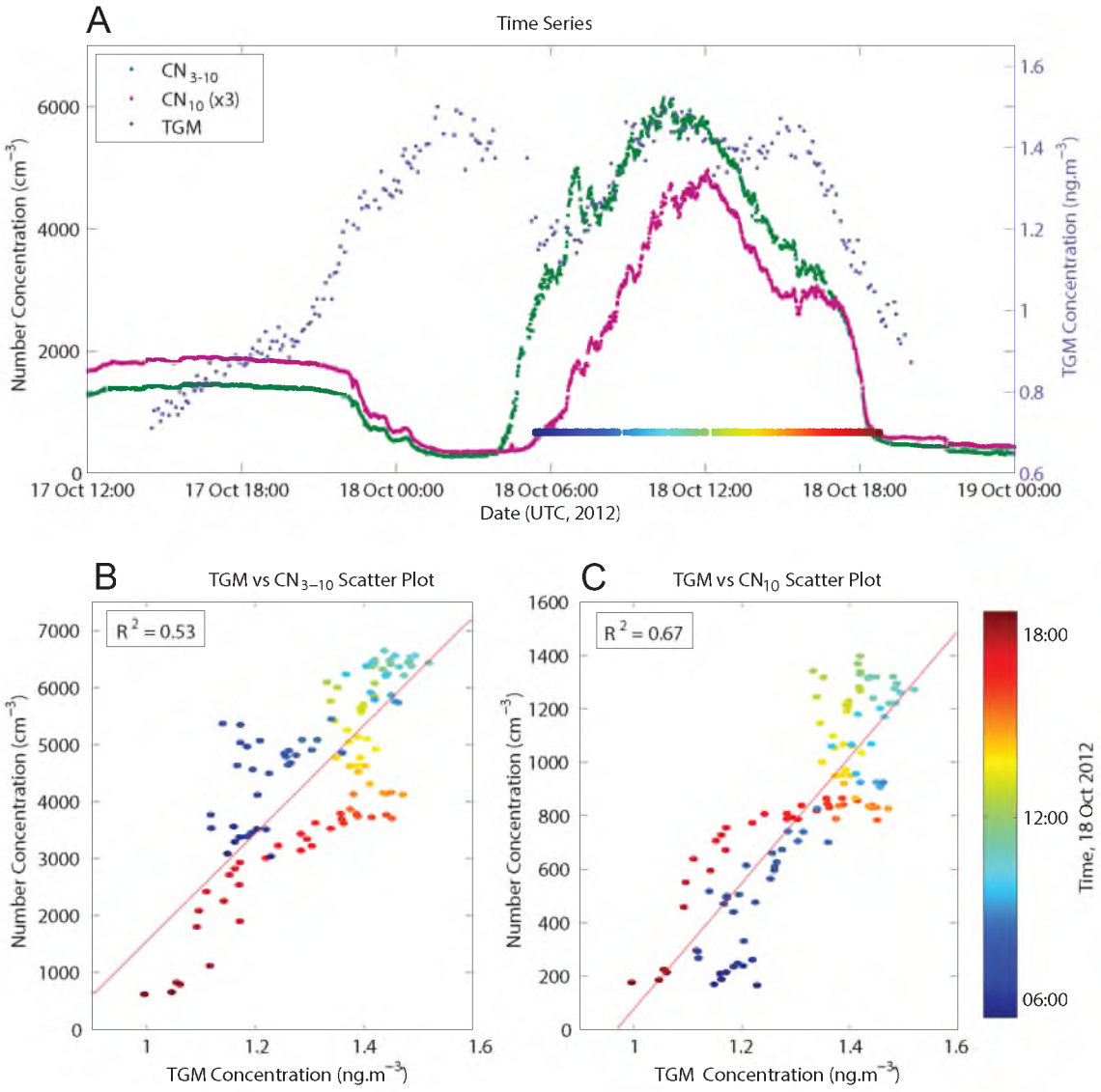

Figure 5.16: Total Gaseous Mercury (TGM) and number concentrations of aerosols in the two measured size bins during the 18th Oct particle formation event. **A**: Time series showing variations in concentrations of both CN_{3-10} and TGM. **B** and **C** present correlation plots relating TGM with number concentrations of CN_{3-10} and CN_{10}, respectively. Both correlation plots show positive relationships, with deviations occurring primarily because of short term variations in aerosol concentrations. The correlation plots are coloured according to time of day, which is referenced directly to the time-series plot (**A**), and include robust linear regression lines with corresponding R^2 values. Removal of the 'wings' of plot **B**, a result of short term variations in background aerosol concentrations (as evidenced by the lack of variation in ratio data), increases the R^2 value to 0.85 (not shown).

candidates are summarised in Table 5.3. Steady concentrations of O_3 at around 27.5 ppb throughout the period, together with a slow reaction rate (gas phase rate constant of $(3\pm2)\times10^{-20}\ cm^3.molec^{-1}.s^{-1}$ (Hall, 1995)) suggest it was not involved, although the magnitude of concentrations means that a deviation in O_3 signal may not be observed (at 1 atm and $0°C$, 27.5 ppb $\approx 7.5\times10^{11}\ molec.cm^{-3}$ while 1.5

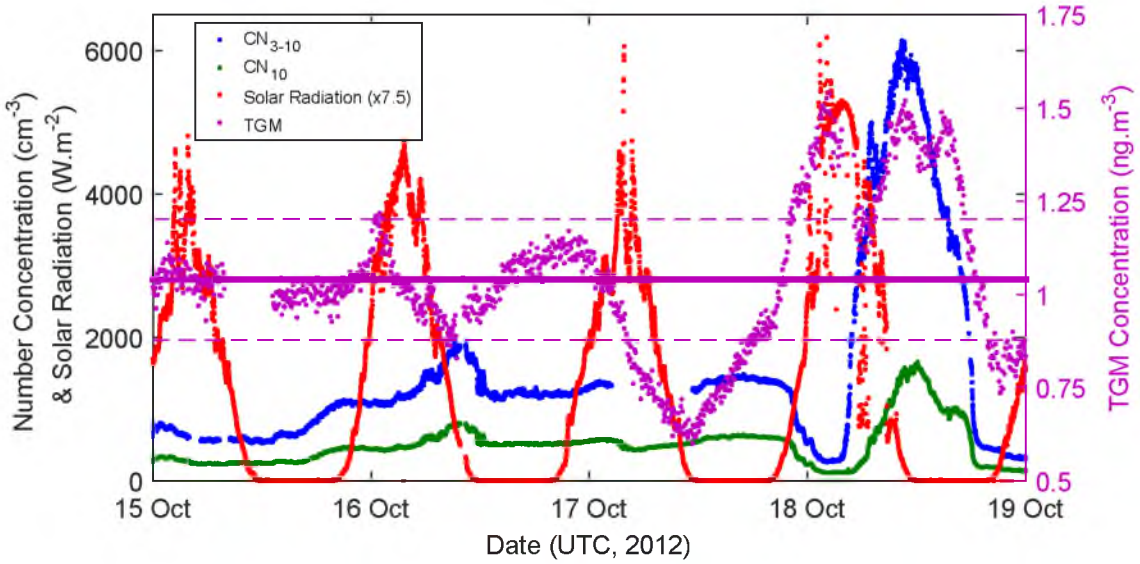

Figure 5.17: Four days of Total Gaseous Mercury (TGM) data together with aerosol data and solar radiation for reference. Horizontal lines depict median (bold) and median absolute deviation values (dashed) for the full TGM dataset. The data clearly depict a TGM depletion event on October 17 followed by the high concentrations of October 18 discussed previously.

$ng.m^{-3}$ of Hg is $\approx 4.5 \times 10^6$ $molec.cm^{-3}$). $OH^{\bullet}$ concentrations on the 18th October were calculated to be high, likely due to a combination of enhanced solar radiation levels and high surface albedo, at 3.4×10^6 $molec.cm^{-3}$, and together with a relatively fast rate constant of $(10.1 \pm 1.3) \times 10^{-14}$ $cm^3.molec^{-1}.s^{-1}$ (at event temperature of 266 K) (Pal and Ariya, 2004), suggest possible $OH^{\bullet}$ involvement. Discussed in detail in Appendix C.3, an assessment of measurements and the literature suggests that although the reaction rates of Hg with iodine and chlorine radicals are high (rate constant for $Cl^{\bullet}$ is $(1.0 \pm 0.2) \times 10^{-11}$ $cm^3.molec^{-1}.s^{-1}$ (Ariya, Khalizov, and Gidas, 2002; Stephens et al., 2012)), their concentrations are too low to be likely oxidants in this event. Bromine, however, although observed in low concentrations relative to other periods, could be present in sufficient concentrations such that when combined with its fast rate constant ($(3.2 \pm 0.3) \times 10^{-12}$ $cm^3.molec^{-1}.s^{-1}$ for $Br^{\bullet}$ radicals (Ariya, Khalizov, and Gidas, 2002; Stephens et al., 2012)) could be a prime candidate for the oxidant of this event, however evidence is still limited to make a firm conclusion here.

Whatever the mechanism of production or identity of the oxidant, oxidised mercury species have the potential to condense, either homogeneously or on pre-existing sub-critical nuclei, to form critical nuclei from which rapid growth can occur via condensation of other species (or other oxidised Hg compounds). A back-of-the-envelope calculation, based on observed loss rates of TGM (with a reasonable assumption that it is primarily Hg^0 (Slemr, Schuster, and Seiler, 1985; Schroeder and Jackson, 1987)) and a 1:1 stoichiometry, puts the production rate of oxidised mercury compounds

Table 5.3: Rate constants for a variety of possible oxidants. Unless otherwise stated, concentrations are estimated from measurements.

Oxidant	Approx concentration ($molec.cm^{-3}$)	Rate Constants, k ($cm^3.molec^{-1}.s^{-1}$)	k[oxidant] (s^{-1})
O_3	7.5×10^{11}	3.0×10^{-20}	2×10^{-8}
$OH^{\bullet}$	3.4×10^{6}	9.0×10^{-14}	3×10^{-7}
$Cl^{\bullet}$ [a]	6×10^{4}	1.0×10^{-11}	6×10^{-7}
$Br^{\bullet}$	1×10^{7}	3.2×10^{-12}	3×10^{-5}

[a] Concentration estimated from Stephens et al. (2012).

at $(2.1 \pm 0.2) \times 10^{14}$ $molec.cm^{-3}.hr^{-1}$. It is possible then, that Hg was a catalyst for aerosol nucleation in this event where background aerosol surface area was sufficiently low. A possible nucleation pathway, catalysed by Hg, is outlined in Figure 5.18. Importantly, the oxidized Hg resulting from this reaction mechanism may be recycled back to TGM, (given the trends and relationship presented in Figure 5.16) resulting in no net effect on the mercury budget. Although this mechanism is theoretically possible, Hg catalysed aerosol nucleation has not been previously described, and correlations in experimental data could be coincidental, rather than reflective of a causal relationship.

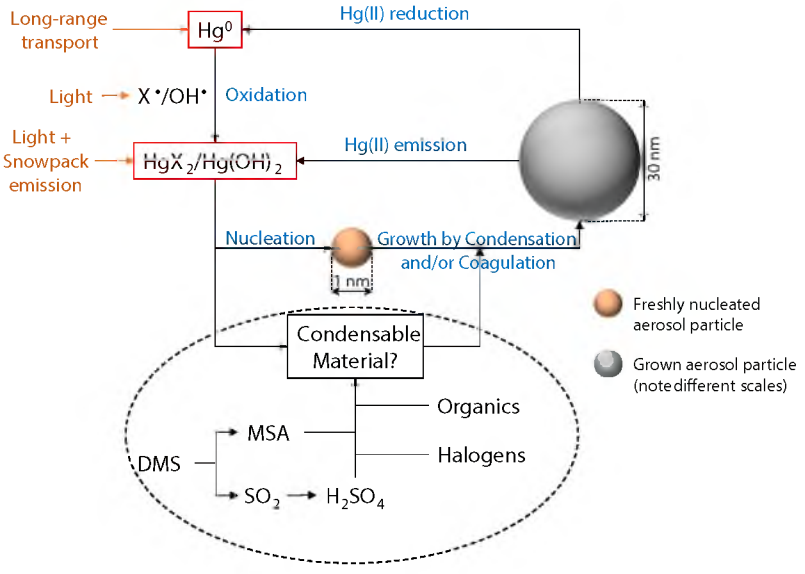

Figure 5.18: A suggested nucleation and growth mechanism catalysed by atmospheric mercury present from long-range transport. This chemistry is likely only to occur under conditions of low background aerosol surface area, otherwise these reaction products are more likely to adhere to pre-existing aerosol surfaces. Species highlighted in red constitute what is measured as TGM. Evidence suggests that no single species, DMS, organics, or halogens, can explain growth rates, however they may combine into a single reservoir of condensable material that may contribute to the process.

5.4 Summary and Discussion

Aerosol concentrations at two size thresholds, together with ancillary atmospheric composition data, were used to investigate the only *in-situ* particle formation event that occurred during the 32 days of measurements during a marine science voyage in the pack ice off the East Antarctic coast. The significant particle formation event occurred within a single, homogeneous air-mass and resulted in CN_3 particle concentrations reaching almost 7700 cm^{-3} within a few hours after being at background values under 400 cm^{-3}. Formation rates of 3 nm particles ranged from $0.2-1.1\pm0.1$ $cm^{-3}s^{-1}$, higher than most events observed in the Antarctic region, and similar to a recently described rare continentally derived event (Kyrö et al., 2013). Estimated growth rates were higher than those previously observed in the region, being 5.6 ± 0.9 $nm.hr^{-1}$ during growth from 3 to 10 nm diameters. An assessment of the reduction in particle numbers found that loss processes were dominated by coagulation, with calculations yielding a coagulation coefficient of $(8 \pm 2) \times 10^{-9}$ $cm^{-3}s^{-1}$, consistent with coagulation of particles with diameters, D_1 and D_2, and a D_1/D_2 ratio of 5.1 ± 0.3 (e.g. 3 nm and 17 nm particles), corresponding to the likely sizes present.

The event was characterised by pre-existing aerosol surface areas below 5 $\mu m^2.cm^{-3}$, along with abnormally clear cloud conditions that resulted in incoming solar radiation fluxes higher than observed on any other day during the voyage, reaching over 600 $W.m^{-2}$ for numerous hours (up to 700 $W.m^{-2}$ at midday).

An evaluation of the mechanism responsible for nucleation found that it was unlikely that known chemistry could explain observed nucleation and growth rates. Statistically significant correlations were found to exist between CN_3 and TGM concentrations, as well as incoming solar radiation. A mercury catalysed nucleation mechanism is suggested as responsible for the observed nucleation.

Instead of oxidised Hg(II) products nucleating homogeneously to form seeds, it is plausible that the Hg products combine with other low-volatility species such as H_2SO_4, forming the critical clusters that are available for growth via condensation. With further measurements using instruments such as an Atmospheric Pressure Ionization Time of Flight Mass Spectrometer (API-ToF-MS), cluster Chemical Ionisation Mass Spectrometer (CIMS), or sub-nanometre instruments such as the neutral cluster and air ion spectrometer (NAIS), it may be possible to determine whether this chemistry is occurring.

The mercury processing involved in the precursor and nucleation chemistry described here is much more complex than represented in the model employed in this study. For example, the simple box model employed here did not model mercury chemistry explicitly, nor account for cloud cycling. Mercury and its oxidation products undergo numerous reactions in the atmosphere, including oxidation and reduc-

tion, as well as within cloud droplets, where ion exchange and reduction reactions can occur (e.g. Selin et al., 2007). Additionally, the changes in chemical and physical properties of cloud cycling on aerosols, although not a major factor in this study because of the minimal influence of cloud during the measurement period, could be important in other environments. Further modelling work is required in future studies to enable better parameterisation of mercury chemistry and partitioning as well as the inclusion of interactions with clouds and the ice surface.

Although only one particle formation event was observed during our campaign, it is possible that these events are occurring frequently in the Southern Ocean and Antarctic regions. This event required, most importantly, high TGM concentrations ($\geq$1.5 $ng.m^{-3}$) and high incident solar radiation, both of which only occurred simultaneously once during the measurement period. Although sustained periods of high TGM concentration were only observed once during this campaign, Hg^0 concentrations in the lower latitudes are often found to be higher than those found during this voyage (Baker et al., 2002). Since transport of air-masses from lower latitudes is relatively frequent (shown previously), high TGM concentrations in the Antarctic region may be frequent.

The incident solar radiation was increasing consistently throughout the voyage. As summer approaches, the increasing solar radiation will provide ample photolytic conditions required for nucleation. Climatological data of mean daily sunshine hours from other stations in the Antarctic continent and Southern Ocean (Macquarie Island, Casey, Mawson and Davis stations were compared; http://www.bom.gov.au/) show that between 20-40% of daylight hours have direct sunshine (as measured by Campbell-Stokes recorder) between September and April, dependent primarily on location. Although this fraction is significantly higher than what was observed during this campaign, it suggests that many areas of the region provide sufficient photolytic conditions to allow this nucleation mechanism to occur frequently in the Antarctic boundary layer.

The photolytic release of oxidised mercury species from the snowpack, and subsequent nucleation, could be occurring in many other regions around the globe. Mercury depletion events were first reported from measurements in the Arctic springtime (Schroeder et al., 1998). It is possible that re-emission of deposited mercury compounds is occurring in both polar regions, resulting in sufficient atmospheric concentrations under suitable photolytic conditions for aerosol nucleation to occur. Additionally, other surface emissions of reactive gaseous mercury, which are substantial around the globe (United Nations Environmental Programme, 2008), could lead to nucleation when pre-existing aerosol surface areas are low enough.

The prerequisites for nucleation via the *in-situ* oxidation mechanism proposed from this study are unlikely to be confined to the polar boundary layer. Condi-

tions of low pre-existing aerosol surface area are common above clouds in the free-troposphere and stratosphere. Coincidentally, these locations also experience high levels of solar radiation. In the northern hemisphere in particular, TGM concentrations are also likely to be sufficient at these altitude levels given the significantly higher boundary layer concentrations (Schroeder and Munthe, 1998; Slemr et al., 2003). This suggests that this nucleation mechanism could be occurring throughout the atmosphere.

Other high mercury, low particle environments may also host this type of nucleation. Coal-fired power plants are the largest single source of mercury in most countries, with an estimated 25% of global anthropogenic emissions to the atmosphere (United Nations Environmental Programme, 2008). Power plant exhaust plumes can have TGM concentrations enhanced up to 6.4 $ng.m^{-3}$ above ambient concentrations (Deeds et al., 2013) that are commonly much higher than those observed here (e.g. ambient concentrations at Alert Station in the Canadian Arctic are 2 $ng.m^{-3}$ and over 5 $ng.m^{-3}$ in Asia (United Nations Environmental Programme, 2008)). Filtering of primary particulate emissions from power plant exhaust is mandatory in many countries around the world. Within these plumes, it is possible that the ratio between Hg^0 concentrations and pre-existing aerosol surface area is high enough that secondary particle formation catalysed by mercury is possible. If this were the case, this chemistry could lead to an additional aerosol burden in industrial environments which should be quantified.

The correlations between nucleation mode aerosol and mercury observations, and thus the proposal of this nucleation mechanism, has not been suggested before, most likely because coincident measurements of particle formation events and mercury are rare. These two measurements only occurred in this study serendipitously. Additionally, high aerosol concentrations in commonly sampled areas results in reactive, low-volatility mercury products being scavenged by pre-existing particles, removing them from the atmosphere and preventing their nucleation.

Results described here represent only a basic measurement suite. More detailed measurements of aerosols, including full size distributions and chemical and elemental composition (e.g. fractions of organic matter, sea salt, sulfate, or other species such as mercury), along with detailed mercury and sulfur speciation, are necessary for full experimental characterisation of this chemistry. Further aerosol focussed studies are necessary in this environment to more completely characterise the aerosol loading as well as the frequency and impact of new particle formation. Ideally, these measurements would be both campaign based and long-term (e.g. the O-buoy system (Knepp et al., 2010)), although the latter presents significant logistical challenges in the dynamic sea ice zone. Laboratory (in particular chambers) and modelling based studies would help to determine, both qualitatively and quantita-

tively, whether this chemistry has any atmospheric significance. If true, the newly described nucleation mechanism could be important in regions where pre-existing aerosol populations, and resulting scavenging rates of oxidised mercury products, are low.

Chapter 6

Summary, Conclusions and Future Directions

This thesis describes the results of a sub-micron aerosol study of the sea ice region off the coast of East Antarctica. The work is based primarily on experimental data obtained during an intensive field campaign aboard the ice-breaker *Aurora Australis*, within the East Antarctic pack ice region (approx. 65°S, 120°E) during the spring (September to November) of 2012. Having never been sampled previously, the primary aim of this aerosol campaign was to characterise the aerosol loading in the region, and to understand the chemistry of any new particle formation that occurred.

The study represents one of only a handful of aerosol measurements in the Antarctic sea ice region, and the only one undertaken in the East Antarctic (0-180°E) sector. The rarity of measurements in this region makes this a valuable dataset, particularly so because aerosol loading in the Antarctic and Southern Ocean regions is currently underestimated in many state-of-the-art global models.

The aerosol data was found to exhibit two main features that framed this thesis. First, it was found that background aerosol concentrations were the highest ever observed in the Antarctic region, with CN_3 number concentrations averaging 1130 cm^{-3}. This surprisingly high aerosol loading was found only in the Polar cell sector of the voyage, with an order of magnitude lower concentrations observed in the latitudes of the Ferrel Cell, closer to the Southern Ocean. The second major feature that occurred was a significant particle formation and growth event that saw CN_3 concentrations reach over 7700 cm^{-3} within the space of a few hours, from background concentrations of just a few hundred.

The background aerosol populations were found to show no signs of growth at the smallest size ranges, and had a fairly consistent size ratio, with around 70% of the measured population having a diameter below 10 nm. This recently nucleated aerosol population was found, through trajectory analyses, to have come recently

(average of 36 hours) from the free troposphere above the Antarctic continent via a well-defined downward flow that atmospherically isolated the sea ice region from the continent to the south and the Southern Ocean to the north.

This well-defined atmospheric flow was found to be a crucial feature leading to the surprisingly high measured aerosol concentrations for two reasons: it limited dilution over larger areas and also prevented observation in coastal regions such as those undertaken in the past at the nearby Casey station. Importantly, spatial analyses found that this well-defined downward flow was present at all longitudes surrounding the continent, with particular strength in the East Antarctic, and weakest around the Antarctic Peninsula. Temporal studies also determined that this circulation was persistent year-round, with a weakening in the summer months. The absence of a description of this circulation in the literature is likely a consequence of most sea ice campaigns occurring in the West Antarctic during summer, where the flow is at its weakest. This highlights how atmospherically distinct the sea ice region is, and the need for further measurements, particularly outside of summer months (i.e. between April and November).

Further trajectory analyses found that air-masses measured in the sea ice region would travel north into the Southern Ocean region above the marine boundary layer. Since the measured aerosol population is likely to have a high albedo, transport away from the similarly high albedo surface of the snow covered sea ice, and into the Southern Ocean region where surface albedo is low, could have potentially significant impacts on the radiative balance of the region. The potential of these aerosols to grow to CCN is also an important aspect necessary for consideration of radiative impacts.

Global modelling studies undertaken as part of this study revealed that the composition of these spring-time aerosols cannot be explained by DMS - the most commonly identified aerosol precursor in the Antarctic region. Simulations using two different global chemistry and transport models, that use distinctly different nucleation mechanisms, significantly underestimate the aerosol loading in the region. Additionally, both show much lower concentrations in the sea ice region compared to the continent - a pattern contrary to measurements.

Although providing an important contribution to the scientific understanding of aerosols in the Antarctic and Southern Ocean region, this study has also highlighted a number of areas requiring further study. The identification of the sea ice region as being atmospherically distinct from the more frequently studied adjacent regions of the continent and Southern Ocean, particularly in non-summer months, highlights the need for significantly more measurements aimed simply at characterising the sea ice atmosphere - both in terms of aerosols, but also of gaseous chemistry and composition that are also likely to differ from previous measurements in adjacent

terrestrial and marine atmospheres.

The flows that result in this atmospheric isolation are currently not well represented in global chemistry and transport models, resulting in incorrect spatial distributions of aerosol populations in the Antarctic region. More work is required to improve this situation. This improvement is likely to require work from both measurement and modelling perspectives. Measurements will improve the characterisation of Antarctic atmospheric dynamics, and may include a range of experimental techniques such as satellite-based sensors, tethered and untethered sondes, wind lidars, or an ensemble of neutral buoyancy, GPS equipped balloons that are released at altitude (by flights or other balloons), for example. Other parameters that may affect dynamics could also be measured, such as aerosol reflectivity and albedo. Modelling work may require changes in model resolution in the region that may not currently be sufficient to capture the important features, as well as improving input meteorological datasets, which again ultimately rely on better measurements.

The question of aerosol composition, and consequently of the chemistry of nucleation in this region remains to be answered. Both measurement and modelling studies are necessary to answer these questions. It is desirable that future experimental studies would employ continuous online measurement techniques, such as size distribution (e.g. Scanning Mobility Particle Sizer Spectrometer, SMPS), CCN and CN concentration (CCN Counter and Condensation Particle Counter, respectively), as well as sampling of the sub-micron aerosol population for later analyses of chemical and elemental composition.

Model studies undertaken to determine the chemistry of nucleation would require the use of global chemical and transport models, and the inclusion of new chemical mechanisms driven by measurements as described above. Current state-of-the-art global models primarily only include DMS emissions and sulfur chemistry for aerosol nucleation, however simulations in this study indicate that this chemistry, in its present parameterisation, is insufficient to explain observations. Further developments may include the inclusion of ternary heterogeneous nucleation mechanisms and emissions of ammonium compounds, or iodine oxide mechanisms that have been shown recently to have potential importance in this region. Additionally, nucleation involving organic compounds, in this region emitted from ocean biota, may be another aspect of future development. One important aspect worth considering in prioritising which mechanism to include first, is the seasonality of the precursors in comparison to that of the aerosol measurements, which shows an important spring peak prior to the summer maximum (the latter of which is driven by DMS and is thus reflected in current model simulations).

The significant underestimation of aerosol loading in the Antarctic and Southern Ocean region in global climate models suggests that the regional radiative impact

may be severely underestimated. As such, it was initially planned to perform radiative impact modelling as part of this project. However, because of the poor representations of both aerosol spatial distributions and magnitude, both of which were deemed a prerequisite for these simulations, this modelling was not sensible at this stage. Once the magnitude of aerosol concentrations and their distributions in the region are better represented in global models through the work described above, an assessment of the radiative impact of this high aerosol loading may be possible and is an important aspect of future work.

The single new particle formation event identified as part of this study was found to coincide with one of only two, almost cloud-free days within the measurement period. During this event, number concentrations rose quickly, from background CN_3 values of 390 cm^{-3}, to over 7700 cm^{-3} within just six hours. An increase in CN_{10} occurred shortly after, from background concentrations of 120 cm^{-3} up to 1600 cm^{-3}, the delay a result of growth at a calculated rate of 5.6 $nm.hr^{-1}$.

Many of the fluctuations in the dataset that occurred during the event were found to correspond with changes in solar irradiance. For example, nucleation and growth rates changed relative to cloud activity, while any signs of nucleation ended completely at sunset.

The nucleation event, which occurred within a single air-mass that extended over several hundred kilometers, exhibited formation rates of 3 nm particles (J_3) that ranged between $0.2 - 1.13 \pm 0.1$ $cm^{-3}.s^{-1}$, rates consistent with those measured at other Antarctic and mid-latitude locations. Coagulation was calculated to be sufficient to explain the decreasing particle concentrations that occurred after sunset, provided diameters, D_1 and D_2, of coagulating particles included in calculations had a D_1/D_2 ratio of 5.1 ± 0.3. Examples of particle diameters corresponding to this ratio include 3 and 17 nm, or 4 and 21 nm, likely scenarios given the recent nucleation.

An assessment of the chemistry of nucleation determined that no known nucleation chemistry was able to explain observations. With some surprising correlations observed between coincident measurements of TGM and aerosol number concentrations, a mercury catalysed nucleation mechanism was proposed that may explain the observations. This mechanism involves the condensation of oxidised mercury species (present from light initiated re-emissions from the surface or oxidation of gaseous elemental mercury), followed by growth via condensation of mercury compounds or other species such as sulfuric acid.

This newly suggested nucleation chemistry requires most importantly, low pre-existing aerosol surface area, high solar radiation, and reasonably high concentrations of TGM (or RGM) to occur. There are numerous locations and circumstances throughout the global atmosphere where these conditions are satisfied, for example, in some particle filtered coal powered power plant plumes. Consequently, this

mechanism could be important outside the Antarctic region.

It is important to note that the mechanism described here is only a preliminary suggestion based on the available observations. Thorough laboratory and modelling based studies are necessary to determine whether this chemistry actually occurs under atmospheric conditions. Future modelling work could first be performed using a simple box model to determine initial parameterisations of the chemistry occurring. If the mechanism proves to be atmospherically important, incorporation into a regional or global model would be the logical next step that would allow qualitative and quantitative assessment of its impact.

In addition to laboratory and modelling based studies, further, more thorough experimental field measurements are necessary to better assess whether this chemistry is actually occurring. Measurements with a more thorough suite of gaseous and aerosol instrumentation are required to further characterise the particle formation events occurring in the East Antarctic sea ice region and determine whether known mechanisms, this newly proposed mechanism, or currently unknown mechanisms are important here. Additionally, given the statistically significant correlations discovered between the aerosol and mercury data, as well as the possibility of this chemistry occurring in other regions around the globe, it is suggested that future field measurements of aerosol nucleation be conducted with measurements of full mercury speciation alongside the traditional instrument suite. Ideally, these experimental field measurements would occur in the sea ice off the Antarctic coast while simultaneously measurements were conducted at nearby permanent coastal stations.

Overall, this work has revealed some novel features of aerosol loading and chemistry that are occurring both in the Antarctic and Southern Ocean regions, and potentially in other parts of the global atmosphere. As highlighted above, many questions remain in relation to these findings which require significant work. In particular, the fact that only a handful of measurements exist for the Antarctic sea ice region as a whole means that significantly more field measurements are required to fully understand this atmospherically distinct region. These measurements can occur in two forms. Intensive campaign based measurements, such as those undertaken as part of this thesis, are important to provide a better understanding of the chemistry and transport that is occurring because of the concentrated time, effort and in particular, instrumentation that is involved. It is particularly desirable however, to set up long-term measurement platforms in the sea ice region to quantify and characterise this unique atmosphere and understand its seasonality. These measurements could occur via two platforms: permanent instruments on ice breakers servicing the continent; and sea ice buoys permanently attached to ice floes (e.g. O-Buoys, http://www.o-buoy.org/). Instruments on ice breakers are relatively easier to undertake, however they only provide limited time and spatial resolution,

and are generally limited to spring and summer months when access to the continent is logistically feasible. Sea ice buoys are logistically much more difficult, and would require significant engineering considerations to accomplish, being both power and space limited, and require instrumentation that does not need regular maintenance. Despite this, measurements like this have the potential to occur year-round, and the ability to be expanded into a spatially expansive network. Depending on the design, these buoys could be deployed throughout the different conditions of the sea ice region, from the multi-year sea ice closer to the continent, out to the Marginal Ice Zone.

This work represents some significant advances in our understanding of both fundamental aerosol processes and the atmospheric processes that affect the large Antarctic and Southern Ocean region. The results described in this thesis have the potential to impact a variety of scientific fields, including simulations of future climate, aerosol and heterogeneous atmospheric chemistry, transport processes, as well as our understanding of clouds and the global radiative balance.

Bibliography

Abbatt, J P D et al. (2012). "Halogen activation via interactions with environmental ice and snow in the polar lower troposphere and other regions". In: *Atmos. Chem. Phys.* 12.14, pp. 6237–6271.

Adams, Peter J. and John H Seinfeld (2002). "Predicting global aerosol size distributions in general circulation models". In: *Journal of Geophysical Research* 107.D19, p. 4370. ISSN: 0148-0227.

Almeida, João Joao et al. (2013). "Molecular understanding of sulphuric acid-amine particle nucleation in the atmosphere." en. In: *Nature* 502.7471, pp. 359–63. ISSN: 1476-4687.

Arimoto, R et al. (2004). "Major ions and radionuclides in aerosol particles from the South Pole during ISCAT-2000". In: *Atmospheric Environment* 38.32, pp. 5473–5484. ISSN: 13522310.

Ariya, P. A. et al. (1998). "Measurements of C 2 -C 7 hydrocarbons during the Polar Sunrise Experiment 1994: Further evidence for halogen chemistry in the troposphere". In: *Journal of Geophysical Research* 103.D11, p. 13169. ISSN: 0148-0227.

Ariya, Parisa A., Alexei Khalizov, and Alexios Gidas (2002). "Reactions of Gaseous Mercury with Atomic and Molecular Halogens: Kinetics, Product Studies, and Atmospheric Implications". In: *The Journal of Physical Chemistry A* 106.32, pp. 7310–7320. ISSN: 1089-5639.

Ariya, Parisa A. et al. (2004). "The Arctic: a sink for mercury". en. In: *Tellus B* 56.5. ISSN: 1600-0889.

Asmi, A. et al. (2013). "Aerosol decadal trends Part 2: In-situ aerosol particle number concentrations at GAW and ACTRIS stations". English. In: *Atmospheric Chemistry and Physics* 13.2, pp. 895–916. ISSN: 1680-7324.

Asmi, E. et al. (2010). "Hygroscopicity and chemical composition of Antarctic submicrometre aerosol particles and observations of new particle formation". English. In: *Atmospheric Chemistry and Physics* 10.9, pp. 4253–4271. ISSN: 1680-7324.

Atkinson, H M et al. (2012). "Iodine emissions from the sea ice of the Weddell Sea". In: *Atmospheric Chemistry and Physics* 12.22, pp. 11229–11244.

Atkinson, R. et al. (1989). "Evaluated kinetic and photochemical data for atmospheric chemistry: Supplement III". In: *International Journal of Chemical Kinetics* 21.2, pp. 115–150. ISSN: 0538-8066.

Australian Antarctic Division (2010). *Aurora Australis*.

Ayers, G. P. and J. L. Gras (1980). "Ammonia gas concentrations over the Southern Ocean". In: *Nature* 284.10, pp. 539–540.

Ayers, G. P., J. P. Ivey, and R. W. Gillett (1991). "Coherence between seasonal cycles of dimethyl sulphide, methanesulphonate and sulphate in marine air". In: *Nature* 349.6308, pp. 404–406. ISSN: 0028-0836.

Ayers, G. P. et al. (1997). "Sulfur dioxide and dimethyl sulphide in marine air at Cape Grim, Tasmania". en. In: *Tellus B* 49.3. ISSN: 1600-0889.

Baker, P.G.L. et al. (2002). "Atmospheric mercury measurements at Cape Point, South Africa". In: *Atmospheric Environment* 36.14, pp. 2459–2465. ISSN: 13522310.

Barkay, Tamar and Alexandre J Poulain (2007). "Mercury (micro)biogeochemistry in polar environments." In: *FEMS microbiology ecology* 59.2, pp. 232–41. ISSN: 0168-6496.

Bates, T S et al. (1992). "Sulfur emissions to the atmosphere from natural sources". English. In: *Journal of Atmospheric Chemistry* 14.1-4, pp. 315–337.

Bates, Timothy S. et al. (1998). "International Global Atmospheric Chemistry (IGAC) Project's First Aerosol Characterization Experiment (ACE 1): Overview". In: *Journal of Geophysical Research* 103.D13, p. 16297. ISSN: 0148-0227.

Behera, Sailesh N and Mukesh Sharma (2011). "Degradation of SO2, NO2 and NH3 leading to formation of secondary inorganic aerosols: An environmental chamber study". In: *Atmospheric Environment* 45, pp. 4015–4024. ISSN: 1352-2310.

Bellouin, N. et al. (2013). "Impact of the modal aerosol scheme GLOMAP-mode on aerosol forcing in the Hadley Centre Global Environmental Model". English. In: *Atmospheric Chemistry and Physics* 13.6, pp. 3027–3044. ISSN: 1680-7324.

Belosi, F et al. (2012). "Aerosol size distribution at Nansen Ice Sheet Antarctica". In: *Atmospheric Research* 107, pp. 42–50.

Bergin, M. H. et al. (1998). "Relationship between continuous aerosol measurements and firn core chemistry over a 10-year period at the South Pole". In: *Geophysical Research Letters* 25.8, pp. 1189–1192. ISSN: 00948276.

Berresheim, H et al. (1998). "Measurements of dimethyl sulfide , dimethyl sulfoxide , dimethyl sulfone , and aerosol ions at Palmer Station , Antarctica ' l based on seawater DMS and wind speed". In: *Journal of Geophysical Research* 103, pp. 1629–1637.

Biester, Harald et al. (2007). "Modeling the Past Atmospheric Deposition of Mercury Using Natural Archives". In: *Environmental Science & Technology* 41.14, pp. 4851–4860. ISSN: 0013-936X.

Bigg, E K, J L Gras, and C Evans (1983). "Origin of aitken particles in remote regions of the Southern Hemisphere". In: *Journal of Atmospheric Chemistry* 1.2, pp. 203–214.

Bintanja, R. et al. (2013). "Important role for ocean warming and increased ice-shelf melt in Antarctic sea-ice expansion". In: *Nature Geoscience* 6.5, pp. 376–379. ISSN: 1752-0894.

Bitz, C. M. and L. M. Polvani (2012). "Antarctic climate response to stratospheric ozone depletion in a fine resolution ocean climate model". In: *Geophysical Research Letters* 39.20, n/a–n/a. ISSN: 00948276.

Bloss, W. J. et al. (2007). "Observations of OH and HO¡sub¿2¡/sub¿ radicals in coastal Antarctica". English. In: *Atmospheric Chemistry and Physics* 7.16, pp. 4171–4185. ISSN: 1680-7324.

Bonsang, Bernard, Claude Polle, and Gérard Lambert (1992). "Evidence for marine production of isoprene". In: *Geophysical Research Letters* 19.11, pp. 1129–1132. ISSN: 00948276.

Bork, N. et al. (2014). "Methane sulfonic acid-enhanced formation of molecular clusters of sulfuric acid and dimethyl amine". English. In: *Atmospheric Chemistry and Physics* 14.22, pp. 12023–12030. ISSN: 1680-7324.

Borrmann, S H, K L Davidson, and M E Miller (1987). "Aerosol size distributions in the marginal ice zone during the 1983 Marginal Ice Zone Experiment". In: *Journal of Geophysical Research: Oceans* 92.C7, pp. 6971–6976.

Bottenheim, Jan W. et al. (1990). "Depletion of lower tropospheric ozone during Arctic spring: The Polar Sunrise Experiment 1988". In: *Journal of Geophysical Research* 95.D11, p. 18555. ISSN: 0148-0227.

Boudries, Hacene and Jan W. Bottenheim (2000). "Cl and Br atom concentrations during a surface boundary layer ozone depletion event in the Canadian High Arctic". In: *Geophysical Research Letters* 27.4, pp. 517–520. ISSN: 00948276.

Bracegirdle, Thomas J. and Gareth J. Marshall (2012). "The Reliability of Antarctic Tropospheric Pressure and Temperature in the Latest Global Reanalyses". EN. In: *Journal of Climate* 25.20, pp. 7138–7146. ISSN: 0894-8755.

Brechtel, Fred J, Sonia M Kreidenweis, and Hilton B Swan (1998). "Air mass characteristics, aerosol particle number concentrations, and number size distributions at Macquarie Island during the First Aerosol Characterization Experiment (ACE 1)". In: *Journal of Geophysical Research: Atmospheres* 103.D13, pp. 16351–16367.

Breider, T J et al. (2010). "Impact of BrO on dimethylsulfide in the remote marine boundary layer". In: *Geophysical Research Letters* 37.2, p. L02807.

Broadgate, Wendy J., Peter S. Liss, and Stuart A. Penkett (1997). "Seasonal emissions of isoprene and other reactive hydrocarbon gases from the ocean". In: *Geophysical Research Letters* 24.21, pp. 2675–2678. ISSN: 00948276.

Brock, C A et al. (2011). "Characteristics, sources, and transport of aerosols measured in spring 2008 during the aerosol, radiation, and cloud processes affecting Arctic Climate (ARCPAC) Project". In: *Atmos. Chem. Phys.* 11.6, pp. 2423–2453.

Bzdek, Bryan R., Douglas P. Ridge, and Murray V. Johnston (2011). "Reactivity of methanesulfonic acid salt clusters relevant to marine air". In: *Journal of Geophysical Research* 116.D3, p. D03301. ISSN: 0148-0227.

Cameron-Smith, Philip et al. (2011). "Changes in dimethyl sulfide oceanic distribution due to climate change". In: *Geophysical Research Letters* 38.7, n/a–n/a. ISSN: 00948276.

Carslaw, K S et al. (2013). "Large contribution of natural aerosols to uncertainty in indirect forcing". In: *Nature* 503.7474, pp. 67–71.

Chang, Rachel Y.-W. et al. (2011). "Relating atmospheric and oceanic DMS levels to particle nucleation events in the Canadian Arctic". In: *Journal of Geophysical Research* 116, D00S03. ISSN: 0148-0227.

Che, Dung L et al. (2009). "Quantifying the reactive uptake of OH by organic aerosols in a continuous flow stirred tank reactor." In: *Physical chemistry chemical physics : PCCP* 11.36, pp. 7885–95. ISSN: 1463-9076.

Chen, G. et al. (2005). "An investigation of the chemistry of ship emission plumes during ITCT 2002". In: *Journal of Geophysical Research* 110.D10, D10S90. ISSN: 0148-0227.

Chen, Liqi et al. (2012). "Latitudinal distributions of atmospheric MSA and MSA/nss-SO 4 2- ratios in summer over the high latitude regions of the Southern and Northern Hemispheres". In: *Journal of Geophysical Research* 117.D10, p. D10306. ISSN: 0148-0227.

Chin, Mian et al. (1996). "A global three-dimensional model of tropospheric sulfate". In: *Journal of Geophysical Research* 101.D13, p. 18667. ISSN: 0148-0227.

Choi, Jung et al. (2014). "Further observational evidence of Hadley cell widening in the Southern Hemisphere". In: *Geophysical Research Letters* 41.7, pp. 2590–2597. ISSN: 00948276.

Clarke, A D et al. (1998). "Particle production in the remote marine atmosphere: Cloud outflow and subsidence during ACE 1". In: *Journal of Geophysical Research: Atmospheres* 103.D13, pp. 16397–16409.

Coffman, Derek J. and Dean. A. Hegg (1995). "A Preliminary study of the effect of ammonia on particle nucleation in the marine boundary layer". In: *Journal of Geophysical Research* 100.D4, pp. 7147–7160. ISSN: 0148-0227.

Collaud Coen, M. et al. (2013). "Aerosol decadal trends Part 1: In-situ optical measurements at GAW and IMPROVE stations". English. In: *Atmospheric Chemistry and Physics* 13.2, pp. 869–894. ISSN: 1680-7324.

Covert, D S et al. (1996). "Aerosol number size distributions from 3 to 500 nm diameter in the arctic marine boundary layer during summer and autumn". In: *Tellus, Series B: Chemical and Physical Meteorology* 48.2, pp. 197–212.

Covert, David S. et al. (1992). "New particle formation in the marine boundary layer". In: *Journal of Geophysical Research* 97.D18, p. 20581. ISSN: 0148-0227.

Creasey, D. J. et al. (2003). "Measurements of OH and HO2 concentrations in the Southern Ocean marine boundary layer". In: *Journal of Geophysical Research* 108.D15, p. 4475. ISSN: 0148-0227.

Curran, Mark A. J. and Graham B. Jones (2000). "Dimethyl sulfide in the Southern Ocean: Seasonality and flux". In: *Journal of Geophysical Research* 105, p. 20451. ISSN: 0148-0227.

Dall'Osto, Manuel et al. (2012). "Nitrogenated and aliphatic organic vapors as possible drivers for marine secondary organic aerosol growth". In: *Journal of Geophysical Research: Atmospheres* 117.D12311. ISSN: 01480227.

Davis, D. et al. (1998). "DMS oxidation in the Antarctic marine boundary layer: Comparison of model simulations and held observations of DMS, DMSO, DMSO2, H2SO4(g), MSA(g), and MSA(p)". In: *Journal of Geophysical Research* 103.D1, p. 1657. ISSN: 0148-0227.

Davis, D D et al. (2004). "An overview of ISCAT 2000". In: *Atmospheric Environment* 38.32, pp. 5363–5373.

Davis, Sean M. and Karen H. Rosenlof (2012). "A Multidiagnostic Intercomparison of Tropical-Width Time Series Using Reanalyses and Satellite Observations". EN. In: *Journal of Climate* 25.4, pp. 1061–1078. ISSN: 0894-8755.

Davison, Brian et al. (1996). "Dimethyl sulfide, methane sulfonic acid and physicochemical aerosol properties in Atlantic air from the United Kingdom to Halley Bay". In: *Journal of Geophysical Research* 101.D17, pp. 22855–22867.

Dawson, Matthew L et al. (2012). "Simplified mechanism for new particle formation from methanesulfonic acid, amines, and water via experiments and ab initio calculations." In: *Proceedings of the National Academy of Sciences of the United States of America* 109.46, pp. 18719–24. ISSN: 1091-6490.

Dee, D. P. et al. (2011). "The ERA-Interim reanalysis: configuration and performance of the data assimilation system". In: *Quarterly Journal of the Royal Meteorological Society* 137.656, pp. 553–597. ISSN: 00359009.

Deeds, Daniel A. et al. (2013). "Mercury speciation in a coal-fired power plant plume: An aircraft-based study of emissions from the 3640 MW Nanticoke Generating

Station, Ontario, Canada". In: *Journal of Geophysical Research: Atmospheres* 118.10, pp. 4919–4935. ISSN: 2169897X.

Deshpande, C. G. and a. K. Kamra (2004). "Physical properties of aerosols at Maitri, Antarctica". In: *Journal of Earth System Science* 113.1, pp. 1–25. ISSN: 0253-4126.

Dommergue, A. et al. (2010). "Overview of mercury measurements in the Antarctic troposphere". English. In: *Atmospheric Chemistry and Physics* 10.7, pp. 3309–3319. ISSN: 1680-7324.

Doney, Scott C et al. (2009). "Ocean acidification: the other CO2 problem." en. In: *Annual review of marine science* 1, pp. 169–92. ISSN: 1941-1405.

Donohoue, Deanna L, Dieter Bauer, and Anthony J Hynes (2005). "Temperature and pressure dependent rate coefficients for the reaction of Hg with Cl and the reaction of Cl with Cl: a pulsed laser photolysis-pulsed laser induced fluorescence study." en. In: *The journal of physical chemistry. A* 109.34, pp. 7732–41. ISSN: 1089-5639.

Douglas, T. A. (2005). "Elevated mercury measured in snow and frost flowers near Arctic sea ice leads". In: *Geophysical Research Letters* 32.4, p. L04502. ISSN: 0094-8276.

Doyle, George J. (1961). "Self-Nucleation in the Sulfuric Acid-Water System". In: *The Journal of Chemical Physics* 35.3, p. 795. ISSN: 00219606.

Draxler, R R and G D Hess (1998). "An Overview of the HYSPLIT_4 Modelling System for Trajectories, Dispersion, and Deposition". In: *Australian Meteorological Magazine* 47, pp. 295–308.

Ebinghaus, Ralf et al. (2002). "Antarctic Springtime Depletion of Atmospheric Mercury". In: *Environmental Science & Technology* 36.6, pp. 1238–1244.

Eguchi, K. et al. (2009). "Trans-pacific dust transport: Integrated analysis of NASA/-CALIPSO and a global aerosol transport model". In: *Atmospheric Chemistry and Physics* 9.9, pp. 3137–3145. ISSN: 16807316.

Enghoff, M. B. and H. Svensmark (2008). "The role of atmospheric ions in aerosol nucleation a review". English. In: *Atmospheric Chemistry and Physics* 8.16, pp. 4911–4923. ISSN: 1680-7324.

Ervens, B., B. J. Turpin, and R. J. Weber (2011). "Secondary organic aerosol formation in cloud droplets and aqueous particles (aqSOA): a review of laboratory, field and model studies". English. In: *Atmospheric Chemistry and Physics* 11.21, pp. 11069–11102. ISSN: 1680-7324.

Ervens, Barbara (2015). "Modeling the Processing of Aerosol and Trace Gases in Clouds and Fogs." In: *Chemical reviews* 115.10, pp. 4157–4198. ISSN: 1520-6890.

Feddersen, D. M. et al. (2012). "Size distribution of particulate mercury in marine and coastal atmospheres". In: *Atmospheric Chemistry and Physics* 12.22, pp. 10899–10909. ISSN: 1680-7324.

Finlayson-Pitts, Barbara J (2009). "Reactions at surfaces in the atmosphere: integration of experiments and theory as necessary (but not necessarily sufficient) for predicting the physical chemistry of aerosols". In: *Physical Chemistry Chemical Physics* 11, pp. 7760–7779. ISSN: 1463-9076.

Flanner, Mark G. (2013). "Arctic climate sensitivity to local black carbon". In: *Journal of Geophysical Research: Atmospheres* 118.4, pp. 1840–1851. ISSN: 2169897X.

Foster, K L et al. (2001). "The role of Br2 and BrCl in surface ozone destruction at polar sunrise." In: *Science (New York, N.Y.)* 291.5503, pp. 471–4. ISSN: 0036-8075.

Friedl, Randall R. and Stanley P. Sander (1989). "Kinetics and product studies of the reaction chlorine monoxide + bromine monoxide using discharge-flow mass spectrometry". EN. In: *The Journal of Physical Chemistry* 93.12, pp. 4756–4764. ISSN: 0022-3654.

Frieß, U et al. (2001). "Spectroscopic measurements of tropospheric iodine oxide at Neumayer Station, Antarctica". In: *Geophysical Research Letters* 28.10, pp. 1941–1944.

Frieß, U et al. (2010). "Iodine monoxide in the Antarctic snowpack". In: *Atmospheric Chemistry and Physics* 10.5, pp. 2439–2456.

Gaman, Anca I et al. (2004). "Binary homogeneous nucleation in water-succinic acid and water-glutaric acid systems." In: *The Journal of chemical physics* 120.1, pp. 282–91. ISSN: 0021-9606.

Gantt, B. et al. (2012). "Global distribution and climate forcing of marine organic aerosol Part 2: Effects on cloud properties and radiative forcing". English. In: *Atmospheric Chemistry and Physics* 12.14, pp. 6555–6563. ISSN: 1680-7324.

Gattuso, Jean-Pierre and Lina Hansson, eds. (2011). *Ocean Acidification*. Oxford University Press, p. 352.

Ghan, Steven J. et al. (2013). "A simple model of global aerosol indirect effects". In: *Journal of Geophysical Research: Atmospheres* 118.12, pp. 6688–6707. ISSN: 2169897X.

Glasow, R. von and P. J. Crutzen (2004). "Model study of multiphase DMS oxidation with a focus on halogens". English. In: *Atmospheric Chemistry and Physics* 4.3, pp. 589–608. ISSN: 1680-7324.

Goldenson, N et al. (2012). "Arctic climate response to forcing from light-absorbing particles in snow and sea ice in CESM". In: *Atmospheric Chemistry and Physics* 12.17, pp. 7903–7920.

Gómez Martín, Juan C. et al. (2013). "Iodine chemistry in the eastern Pacific marine boundary layer". In: *Journal of Geophysical Research: Atmospheres* 118.2, pp. 887–904. ISSN: 2169897X.

Gostlow, B et al. (2010). "μDirac: an autonomous instrument for halocarbon measurements". In: *Atmos. Meas. Tech.* 3.2, pp. 507–521.

Gras, J. L. (1983). "Ammonia and ammonium concentrations in the Antarctic atmosphere". In: *Atmospheric Environment* 17.4, pp. 815–818.

Gras, J L (1993). "Condensation nucleus size distribution at Mawson, Antarctica: seasonal cycle". In: *Atmospheric Environment. Part A. General Topics* 27.9, pp. 1417–1425.

Guenther, A. B. et al. (2012). "The Model of Emissions of Gases and Aerosols from Nature version 2.1 (MEGAN2.1): an extended and updated framework for modeling biogenic emissions". English. In: *Geoscientific Model Development* 5.6, pp. 1471–1492. ISSN: 1991-9603.

Guo, H. et al. (2012). "Observation of aerosol size distribution and new particle formation at a mountain site in subtropical Hong Kong". English. In: *Atmospheric Chemistry and Physics* 12.20, pp. 9923–9939. ISSN: 1680-7324.

Hall, B. (1995). "The gas phase oxidation of elemental mercury by ozone". In: *Water, Air, & Soil Pollution* 80.1-4, pp. 301–315. ISSN: 0049-6979.

Hallar, A Gannet et al. (2011). "Persistent daily new particle formation at a mountain-top location". In: *Atmospheric Environment* 45, pp. 4111–4115. ISSN: 1352-2310.

Hallquist, M. et al. (2009). "The formation, properties and impact of secondary organic aerosol: current and emerging issues". English. In: *Atmospheric Chemistry and Physics* 9.14, pp. 5155–5236. ISSN: 1680-7324.

Hansen, Anthony D.A. et al. (2001). "Black Carbon Aerosol at McMurdo Station, Antarctica". en. In: *Journal of the Air & Waste Management Association* 51.4, pp. 593–600. ISSN: 1096-2247.

Hansen, Georg et al. (2009). "Atmospheric monitoring at the Norwegian Antarctic station Troll: measurement programme and first results". en. In: *Polar Research* 28.3, pp. 353–363. ISSN: 0800-0395.

Hara, K et al. (2011). "Seasonal variations and vertical features of aerosol particles in the Antarctic troposphere". In: *Atmospheric Chemistry and Physics* 11.11, pp. 5471–5484.

Hara, Keiichiro (2004). "Chemistry of sea-salt particles and inorganic halogen species in Antarctic regions: Compositional differences between coastal and inland stations". In: *Journal of Geophysical Research* 109.D20, p. D20208. ISSN: 0148-0227.

Heintzenberg, Jost et al. (2004). "Structure, variability and persistence of the submicrometre marine aerosol". en. In: *Tellus B* 56.4. ISSN: 1600-0889.

Herrmann, Hartmut et al. (2015). "Tropospheric Aqueous-Phase Chemistry: Kinetics, Mechanisms, and Its Coupling to a Changing Gas Phase." In: *Chemical reviews* 115.10, pp. 4259–4334. ISSN: 1520-6890.

Hoffmann, Thorsten, Colin D. O'Dowd, and John H. Seinfeld (2001). "Iodine oxide homogeneous nucleation: An explanation for coastal new particle production". In: *Geophysical Research Letters* 28.10, pp. 1949–1952. ISSN: 00948276.

Hoffmann, Thorsten et al. (1997). "Formation of Organic Aerosols from the Oxidation of Biogenic Hydrocarbons". en. In: *Journal of Atmospheric Chemistry* 26.2, pp. 189–222. ISSN: 1573-0662.

Holland, Paul R. and Ron Kwok (2012). "Wind-driven trends in Antarctic sea-ice drift". In: *Nature Geoscience* 5.12, pp. 872–875. ISSN: 1752-0894.

Holmes, C. D. et al. (2010). "Global atmospheric model for mercury including oxidation by bromine atoms". English. In: *Atmospheric Chemistry and Physics* 10.24, pp. 12037–12057. ISSN: 1680-7324.

Hu, Qi-Hou et al. (2013). "Secondary organic aerosols over oceans via oxidation of isoprene and monoterpenes from Arctic to Antarctic." en. In: *Sci. Rep.* 3, p. 2280. ISSN: 2045-2322.

Hudson, James G, Yonghong Xie, and Seong Soo Yum (1998). "Vertical distributions of cloud condensation nuclei spectra over the summertime Southern Ocean". In: *Journal of Geophysical Research: Atmospheres* 103.D13, pp. 16609–16624.

Humphries, Ruhi et al. (2014). *In-situ total aerosol number using condensation particle counters as observed during the SIPEX II voyage of the Aurora Australis, 2012.*

Impey, G. A. et al. (1997). "Measurements of photolyzable chlorine and bromine during the Polar Sunrise Experiment 1995". In: *Journal of Geophysical Research* 102.D13, p. 16005. ISSN: 0148-0227.

Inoue, J and T Toyota (2005). "Characteristics of aerosol number concentrations over the ice-covered Okhotsk Sea". In: *Journal of The Meteorological Society of Japan* 83.4, p. 8.

International Programme on Chemical Safety, IPSC (2001). *INCHEM Mercuric Oxide.*

IPCC (2001). *Climate Change 2001: The Scientific Basis.* Ed. by J. T. Houghton et al. Cambridge, United Kingdom and New York, NY, USA: Cambridge University Press.

— (2007). *Climate Change 2007 - The Physical Science Basis: Working Group I Contribution to the Fourth Assessment Report of the Intergovernmental Panel on Climate Change.* Ed. by S Solomon et al. Cambridge, UK and New York, NY, USA: Cambridge University Press. ISBN: 0521880092.

IPCC (2013). *Climate Change 2013: The Physical Science Basis. Contribution of Working Group I to the Fifth Assessment Report of the Intergovernmental Panel on Climate Change*. Ed. by T.F. Stocker et al. Cambridge, United Kingdom and New York, NY, USA: Cambridge University Press, p. 1535. ISBN: ISBN 978-1-107-66182-0.

Ito, T. (1985). "Study of background aerosols in the Antarctic troposphere". In: *Journal of Atmospheric Chemistry* 3.1, pp. 69–91. ISSN: 0167-7764.

— (1989). "Antarctic Submicron Aerosols and Long-Range Transport of Pollutants". In: *Ambio* 18.1, pp. 34–41.

Ito, T (1993). "Size distribution of Antarctic submicron aerosols". In: *Tellus, Series B* 45 B.2, pp. 145–159.

Ito, T. (1995). "Nature and Origin of Antarctic Submicron Aerosols". In: *Ice Core Studies of Global Biogeochemical Cycles* 30, pp. 23–38.

Järvinen, E. et al. (2013). "Seasonal cycle and modal structure of particle number size distribution at Dome C, Antarctica". English. In: *Atmospheric Chemistry and Physics* 13.15, pp. 7473–7487. ISSN: 1680-7324.

Jefferson, A. et al. (1998). "OH photochemistry and methane sulfonic acid formation in the coastal Antarctic boundary layer". In: *Journal of Geophysical Research* 103.D1, p. 1647. ISSN: 0148-0227.

Jiang, Jingkun et al. (2011a). "Electrical Mobility Spectrometer Using a Diethylene Glycol Condensation Particle Counter for Measurement of Aerosol Size Distributions Down to 1 nm". In: *Aerosol Science and Technology* 45.4, pp. 510–521. ISSN: 0278-6826.

Jiang, Jingkun et al. (2011b). "First Measurements of Neutral Atmospheric Cluster and 1 2 nm Particle Number Size Distributions During Nucleation Events". In: *Aerosol Science and Technology* 45.4, pp. ii–v.

Jimenez, Jose L. et al. (2003). "New particle formation from photooxidation of diiodomethane (CH2I2)". In: *Journal of Geophysical Research* 108.D10, p. 4318. ISSN: 0148-0227.

Jobson, B. T. et al. (1994). "Measurements of C 2 -C 6 hydrocarbons during the Polar Sunrise1992 Experiment: Evidence for Cl atom and Br atom chemistry". In: *Journal of Geophysical Research* 99.D12, p. 25355. ISSN: 0148-0227.

Johnston, Paul (2014). *Personal Communication*.

Jones, Andy et al. (2001). "Indirect sulphate aerosol forcing in a climate model with an interactive sulphur cycle". In: *Journal of Geophysical Research* 106.D17, p. 20293. ISSN: 0148-0227.

Jourdain, Bruno (2002). "Year-round records of bulk and size-segregated aerosol composition and HCl and HNO 3 levels in the Dumont d'Urville (coastal Antarc-

tica) atmosphere: Implications for sea-salt aerosol fractionation in the winter and summer". In: *Journal of Geophysical Research* 107.D22, p. 4645. ISSN: 0148-0227.

Jung, J., Y. Miyazaki, and K. Kawamura (2013). "Different characteristics of new particle formation between urban and deciduous forest sites in Northern Japan during the summers of 20102011". English. In: *Atmospheric Chemistry and Physics* 13.1, pp. 51–68. ISSN: 1680-7324.

Kaleschke, L. (2004). "Frost flowers on sea ice as a source of sea salt and their influence on tropospheric halogen chemistry". In: *Geophysical Research Letters* 31.16, p. L16114. ISSN: 0094-8276.

Kanakidou, M. et al. (2005). "Organic aerosol and global climate modelling: a review". English. In: *Atmospheric Chemistry and Physics* 5.4, pp. 1053–1123. ISSN: 1680-7324.

Kanamitsu, Masao (1989). "Description of the NMC Global Data Assimilation and Forecast System". EN. In: *Weather and Forecasting* 4.3, pp. 335–342. ISSN: 0882-8156.

Karl, M. et al. (2007). "Intercomparison of dimethylsulfide oxidation mechanisms for the marine boundary layer: Gaseous and particulate sulfur constituents". In: *Journal of Geophysical Research* 112.D15, p. D15304. ISSN: 0148-0227.

Kavouras, Ilias G and Euripides G Stephanou (2002). "Direct evidence of atmospheric secondary organic aerosol formation in forest atmosphere through heteromolecular nucleation." In: *Environmental science & technology* 36.23, pp. 5083–91. ISSN: 0013-936X.

Keil, Adam D. and Paul B. Shepson (2006). "Chlorine and bromine atom ratios in the springtime Arctic troposphere as determined from measurements of halogenated volatile organic compounds". In: *Journal of Geophysical Research* 111.D17, p. D17303. ISSN: 0148-0227.

Kettle, A J et al. (1999). "A global database of sea surface dimethylsulfide (DMS) measurements and a procedure to predict sea surface DMS as a function of latitude, longitude, and month". In: *Global Biogeochemical Cycles* 13.2, pp. 399–444.

Kipling, Z. et al. (2013). "Constraints on aerosol processes in climate models from vertically-resolved aircraft observations of black carbon". English. In: *Atmospheric Chemistry and Physics* 13.12, pp. 5969–5986. ISSN: 1680-7324.

Kirkby, Jasper et al. (2011). "Role of sulphuric acid, ammonia and galactic cosmic rays in atmospheric aerosol nucleation". In: *Nature* 476.7361, pp. 429–433. ISSN: 0028-0836.

Kistler, R. et al. (2001). "The NCEPNCAR 50Year Reanalysis: Monthly Means CDROM and Documentation." In: *Bulletin of the American Meteorological Society* 82, pp. 247–267.

Knepp, T. N. et al. (2010). "Development of an autonomous sea ice tethered buoy for the study of ocean-atmosphere-sea ice-snow pack interactions: the O-buoy". English. In: *Atmospheric Measurement Techniques* 3.1, pp. 249–261. ISSN: 1867-8548.

Kohout, A L et al. (2014). "Storm-induced sea-ice breakup and the implications for ice extent." In: *Nature* 509.7502, pp. 604–7. ISSN: 1476-4687.

Koponen, Ismo K. et al. (2002). "Number size distributions and concentrations of marine aerosols: Observations during a cruise between the English Channel and the coast of Antarctica". In: *Journal of Geophysical Research* 107.D24, p. 4753. ISSN: 0148-0227.

Koponen, Ismo K et al. (2003). "Number size distributions and concentrations of the continental summer aerosols in Queen Maud Land, Antarctica". In: *Journal of Geophysical Research: Atmospheres* 108.D18, p. 4587.

Kopp, Greg and Judith L. Lean (2011). "A new, lower value of total solar irradiance: Evidence and climate significance". In: *Geophysical Research Letters* 38.1, n/a–n/a. ISSN: 00948276.

Koren, Ilan et al. (2012). "Aerosol-induced intensification of rain from the tropics to the mid-latitudes". In: *Nature Geosci* 5, pp. 118–122. ISSN: 1752-0894.

Korhonen, Hannele et al. (2008). "Influence of oceanic dimethyl sulfide emissions on cloud condensation nuclei concentrations and seasonality over the remote Southern Hemisphere oceans: A global model study". In: *Journal of Geophysical Research* 113.D15, p. D15204. ISSN: 0148-0227.

Korhonen, P. et al. (1999). "Ternary nucleation of H 2 SO 4 , NH 3 , and H 2 O in the atmosphere". In: *Journal of Geophysical Research* 104.D21, p. 26349. ISSN: 0148-0227.

Kukui, A. et al. (2014). "Measurements of OH and RO2 radicals at Dome C, East Antarctica". English. In: *Atmospheric Chemistry and Physics* 14.22, pp. 12373–12392. ISSN: 1680-7324.

Kulmala, M (2003). "How Particles Nucleate and Grow". In: *Science* 302.5647, pp. 1000–1001.

Kulmala, M., K. E. J. Lehtinen, and A. Laaksonen (2006). "Cluster activation theory as an explanation of the linear dependence between formation rate of 3nm particles and sulphuric acid concentration". English. In: *Atmospheric Chemistry and Physics* 6.3, pp. 787–793. ISSN: 1680-7324.

Kulmala, M et al. (2004). "Formation and growth rates of ultrafine atmospheric particles: a review of observations". In: *Journal of Aerosol Science* 35.2, pp. 143–176.

Kulmala, Markka, Ari Laaksonen, and Liisa Pirjola (1998). "Parameterizations for sulfuric acid/water nucleation rates". In: *Journal of Geophysical Research* 103.D7, p. 8301. ISSN: 0148-0227.

Kulmala, Markku and Ari Laaksonen (1990). "Binary nucleation of watersulfuric acid system: Comparison of classical theories with different H2SO4 saturation vapor pressures". In: *The Journal of Chemical Physics* 93.1, p. 696. ISSN: 00219606.

Kulmala, Markku, Liisa Pirjola, and Jyrki M Makela (2000). "Stable sulphate clusters as a source of new atmospheric particles". In: *Nature* 404.6773, pp. 66–69.

Kulmala, Markku et al. (2012). "Measurement of the nucleation of atmospheric aerosol particles." In: *Nature protocols* 7.9, pp. 1651–67. ISSN: 1750-2799.

Kyrö, E M et al. (2013). "Antarctic new particle formation from continental biogenic precursors". In: *Atmos. Chem. Phys.* 13.7, pp. 3527–3546.

Lai, S C, T Hoffman, and Z Q Xie (2008). "Iodine speciation in marine aerosols along a 30,000 km round-trip cruise path from Shanghai, China to Prydz Bay, Antarctica". In: *Geophysical Research Letters* 35.21.

Lana, A et al. (2011). "An updated climatology of surface dimethlysulfide concentrations and emission fluxes in the global ocean". In: *Global Biogeochemical Cycles* 25.1, GB1004.

Lee, L. A. et al. (2013). "The magnitude and causes of uncertainty in global model simulations of cloud condensation nuclei". English. In: *Atmospheric Chemistry and Physics* 13.17, pp. 8879–8914. ISSN: 1680-7324.

Lee, S.-H. et al. (2003). "Particle Formation by Ion Nucleation in the Upper Troposphere and Lower Stratosphere". In: *Science* 301.5641, pp. 1886–1889.

Legrand, Michel et al. (1998). "Ammonium in coastal Antarctic aerosol and snow: Role of polar ocean and penguin emissions". In: *Journal of Geophysical Research* 103.D9, p. 11043. ISSN: 0148-0227.

Legrand, Michel et al. (2001). "Subdaily variations of atmospheric dimethylsulfide, dimethylsulfoxide, methanesulfonate, and non-sea-salt sulfate aerosols in the atmospheric boundary layer at Dumont d'Urville (coastal Antarctica) during summer". In: *Journal of Geophysical Research* 106.2000, p. 14409. ISSN: 0148-0227.

Levasseur, M., M. Gosselin, and S. Michaud (1994). "A new source of dimethylsulfide (DMS) for the arctic atmosphere: ice diatoms". In: *Marine Biology* 121.2, pp. 381–387. ISSN: 0025-3162.

Levasseur, Maurice (2011). "Ocean science: If Gaia could talk". In: *Nature Geosci* 4.6, pp. 351–352.

Li, Zhanqing et al. (2011). "Long-term impacts of aerosols on the vertical development of clouds and precipitation". In: *Nature Geosci* 4, pp. 888–894. ISSN: 1752-0894.

Liao, J. et al. (2012). "Observations of inorganic bromine (HOBr, BrO, and Br 2) speciation at Barrow, Alaska, in spring 2009". In: *Journal of Geophysical Research* 117, D00R16. ISSN: 0148-0227.

Liao, Jin et al. (2014). "High levels of molecular chlorine in the Arctic atmosphere". In: *Nature Geosci* 7.2, pp. 91–94.

Lindberg, Steve E et al. (2002). "Dynamic Oxidation of Gaseous Mercury in the Arctic Troposphere at Polar Sunrise". In: *Environmental Science & Technology* 36.6, pp. 1245–1256.

Liss, P S and L. Merlivat (1986). "Air-sea gas exchange rates: introduction and synthesis." In: *The Role of Air-Sea Exchange in Geochemical Cycling*. Ed. by D Reidel, pp. 113–127.

Loose, B. et al. (2011). "Gas diffusion through columnar laboratory sea ice: implications for mixed-layer ventilation of CO2 in the seasonal ice zone". In: *Tellus B* 63.1, pp. 23–39. ISSN: 02806509.

Loukhovitskaya, Ekaterina et al. (2009). "Laboratory study of the interaction of HO2 radicals with the NaCl, NaBr, MgCl(2).6H2O and sea salt surfaces." In: *Physical chemistry chemical physics : PCCP* 11.36, pp. 7896–905. ISSN: 1463-9076.

Lu, Julia Y. et al. (2001). "Magnification of atmospheric mercury deposition to polar regions in springtime: The link to tropospheric ozone depletion chemistry". In: *Geophysical Research Letters* 28.17, pp. 3219–3222. ISSN: 00948276.

Lucas, Christopher, Bertrand Timbal, and Hanh Nguyen (2014). "The expanding tropics: a critical assessment of the observational and modeling studies". In: *Wiley Interdisciplinary Reviews: Climate Change* 5.1, pp. 89–112. ISSN: 17577780.

Mann, G. W. et al. (2010). "Description and evaluation of GLOMAP-mode: a modal global aerosol microphysics model for the UKCA composition-climate model". English. In: *Geoscientific Model Development* 3.2, pp. 519–551. ISSN: 1991-9603.

Mann, G. W. et al. (2012). "Intercomparison of modal and sectional aerosol microphysics representations within the same 3-D global chemical transport model." In: *Atmospheric Chemistry and Physics* 12, pp. 4449–4476.

Mann, G. W. et al. (2014). "Intercomparison and evaluation of global aerosol microphysical properties among AeroCom models of a range of complexity". English. In: *Atmospheric Chemistry and Physics* 14.9, pp. 4679–4713. ISSN: 1680-7324.

Marchand, R et al. (2014). "Clouds , Aerosols , Radiation and Air-Sea Interface of the Southern Ocean: Establishing Directions for Future Research". In: March 2014. University of Washington , Seattle.

Marti, James J. et al. (1997). "New particle formation at a remote continental site: Assessing the contributions of SO 2 and organic precursors". In: *Journal of Geophysical Research* 102.D5, pp. 6331–6339. ISSN: 0148-0227.

Mauldin, R. L. et al. (2001). "Measurements of OH, H 2 SO 4 , and MSA at the South Pole during ISCAT". In: *Geophysical Research Letters* 28.19, pp. 3629–3632. ISSN: 00948276.

McGraw, Robert and Renyi Zhang (2008). "Multivariate analysis of homogeneous nucleation rate measurements. Nucleation in the p-toluic acid/sulfuric acid/water system." In: *The Journal of chemical physics* 128.6, p. 064508. ISSN: 0021-9606.

Menke, R and G Wallis (1980). "Detection of mercury in air in the presence of chlorine and water vapor." In: *American Industrial Hygiene Association journal* 41.2, pp. 120–4. ISSN: 0002-8894.

Menon, S et al. (2002). "GCM simulations of the aerosol indirect effect: Sensitivity to cloud parameterization and aerosol Burden". In: *Journal of the Atmospheric Sciences* 59.3 PT 2, pp. 692–713.

Merikanto, J. et al. (2009). "Impact of nucleation on global CCN". English. In: *Atmos. Chem. Phys.* 9.21, pp. 8601–8616. ISSN: 1680-7324.

Meskhidze, Nicholas and Athanasios Nenes (2006). "Phytoplankton and cloudiness in the Southern Ocean." In: *Science (New York, N.Y.)* 314.5804, pp. 1419–23. ISSN: 1095-9203.

Metzger, Axel et al. (2010). "Evidence for the role of organics in aerosol particle formation under atmospheric conditions." In: *Proceedings of the National Academy of Sciences of the United States of America* 107.15, pp. 6646–51. ISSN: 1091-6490.

Middlebrook, Ann M., Daniel M. Murphy, and David S. Thomson (1998). "Observations of organic material in individual marine particles at Cape Grim during the First Aerosol Characterization Experiment (ACE 1)". In: *Journal of Geophysical Research* 103.D13, p. 16475. ISSN: 0148-0227.

Middleton, Paulette and C.S. Kiang (1978). "A kinetic aerosol model for the formation and growth of secondary sulfuric acid particles". In: *Journal of Aerosol Science* 9.4, pp. 359–385. ISSN: 00218502.

Miller, Lisa A. et al. (2011). "Carbon dynamics in sea ice: A winter flux time series". In: *Journal of Geophysical Research* 116.C2, p. C02028. ISSN: 0148-0227.

Milne, Peter J. et al. (1995). "Measurement of vertical distribution of isoprene in surface seawater, its chemical fate, and its emission from several phytoplankton monocultures". In: *Marine Chemistry* 48.3-4, pp. 237–244. ISSN: 03044203.

Minikin, Andreas et al. (1998). "Sulfur-containing species (sulfate and methanesulfonate) in coastal Antarctic aerosol and precipitation". In: *Journal of Geophysical Research* 103.D9, p. 10975. ISSN: 0148-0227.

Mock, Thomas and Nikolai Hoch (2005). "Long-term temperature acclimation of photosynthesis in steady-state cultures of the polar diatom Fragilariopsis cylindrus." In: *Photosynthesis research* 85.3, pp. 307–17. ISSN: 0166-8595.

Moore, J Keith and Mark R Abbott (2000). "Phytoplankton chlorophyll distributions and primary production in the Southern Ocean". In: *Journal of Geophysical Research: Oceans* 105.C12, pp. 28709–28722.

Moore, R. M., D. E. Oram, and S. A. Penkett (1994). "Production of isoprene by marine phytoplankton cultures". In: *Geophysical Research Letters* 21.23, pp. 2507–2510. ISSN: 00948276.

Muthuramu, K. et al. (1994). "Relationships between organic nitrates and surface ozone destruction during Polar Sunrise Experiment 1992". In: *Journal of Geophysical Research* 99.D12, p. 25369. ISSN: 0148-0227.

National Research Council (2005). *Radiative Forcing of Climate Change: Expanding the Concept and Addressing Uncertainties*. Tech. rep., p. 244.

Nilsson, E D et al. (2001). "Effects of continental boundary layer evolution, convection, turbulence and entrainment, on aerosol formation". In: *Tellus B* 53.4, pp. 441–461.

Nomura, Daiki, Hisayuki Yoshikawa-Inque, and Takenobu Toyata (2006). "The effect of sea-ice growth on air-sea CO 2 flux in a tank experiment". In: *Tellus B* 58.5, pp. 418–426. ISSN: 0280-6509.

Nomura, Daiki et al. (2010). "Effects of snow, snowmelting and refreezing processes on airsea-ice CO¡SUB¿2¡/SUB¿ flux". In: *Journal of Glaciology* 56.196, pp. 262–270. ISSN: 00221430.

Nomura, Daiki et al. (2012). "Direct measurements of DMS flux from Antarctic fast sea ice to the atmosphere by a chamber technique". In: *Journal of Geophysical Research* 117.

O'Dowd, Colin et al. (1999). "On the photochemical production of new particles in the coastal boundary layer". In: *Geophysical Research Letters* 26.12, pp. 1707–1710. ISSN: 00948276.

O'Dowd, Colin D. et al. (1997). "Biogenic sulphur emissions and inferred non-sea-salt-sulphate cloud condensation nuclei in and around Antarctica". In: *Journal of Geophysical Research: Atmospheres* 102.D11, pp. 12839–12854. ISSN: 0148-0227.

O'Dowd, Colin D. et al. (1998). "New particle formation: Nucleation rates and spatial scales in the clean marine coastal environment". In: *Geophysical Research Letters* 25.10, pp. 1661–1664. ISSN: 00948276.

O'Dowd, Colin D. et al. (2002a). "A dedicated study of New Particle Formation and Fate in the Coastal Environment (PARFORCE): Overview of objectives

and achievements". In: *Journal of Geophysical Research* 107.D19, p. 8108. ISSN: 0148-0227.

O'Dowd, Colin D et al. (2002b). "Aerosol formation: atmospheric particles from organic vapours." en. In: *Nature* 416.6880, pp. 497–8. ISSN: 0028-0836.

O'Dowd, Colin D et al. (2002c). "Marine aerosol formation from biogenic iodine emissions". In: *Nature* 417.6889, pp. 632–636.

O'Dowd, Colin D et al. (2004). "Biogenically driven organic contribution to marine aerosol." en. In: *Nature* 431.7009, pp. 676–80. ISSN: 1476-4687.

Oum, K. W., M. J. Lakin, and B. J. Finlayson-Pitts (1998). "Bromine activation in the troposphere by the dark reaction of O 3 with seawater ice". In: *Geophysical Research Letters* 25.21, pp. 3923–3926. ISSN: 00948276.

Pal, Biswajit and Parisa A. Ariya (2004). "Gas-Phase HO -Initiated Reactions of Elemental Mercury: Kinetics, Product Studies, and Atmospheric Implications". In: *Environmental Science & Technology* 38.21, pp. 5555–5566. ISSN: 0013-936X.

Pant, Vimlesh, Devendraa Siingh, and A K Kamra (2011). "Size distribution of atmospheric aerosols at Maitri, Antarctica". In: *Atmospheric Environment* 45.29, pp. 5138–5149.

Papakyriakou, Tim and Lisa Miller (2011). "Springtime CO2 exchange over seasonal sea ice in the Canadian Arctic Archipelago". In: *Annals of Glaciology* 52.57, pp. 215–224.

Park, J et al. (2004). "Aerosol size distributions measured at the South Pole during ISCAT". In: *Atmospheric Environment* 38.32, pp. 5493–5500.

Parkinson, C. L. and D. J. Cavalieri (2012). "Antarctic sea ice variability and trends, 19792010". English. In: *The Cryosphere* 6.4, pp. 871–880. ISSN: 1994-0424.

Pfaffhuber, K. A. et al. (2012). "Atmospheric mercury observations from Antarctica: seasonal variation and source and sink region calculations". English. In: *Atmospheric Chemistry and Physics* 12.7, pp. 3241–3251. ISSN: 1680-7324.

Pham, M. et al. (1995). "A three-dimensional study of the tropospheric sulfur cycle". In: *Journal of Geophysical Research* 100.D12, p. 26061. ISSN: 0148-0227.

Pierce, J. R. and P. J. Adams (2009a). "A Computationally Efficient Aerosol Nucleation/ Condensation Method: Pseudo-Steady-State Sulfuric Acid". In: *Aerosol Science and Technology* 43.3, pp. 216–226. ISSN: 0278-6826.

— (2009b). "Uncertainty in global CCN concentrations from uncertain aerosol nucleation and primary emission rates". English. In: *Atmospheric Chemistry and Physics* 9.4, pp. 1339–1356. ISSN: 1680-7324.

Pierce, Jeffrey R. and Peter J. Adams (2006). "Global evaluation of CCN formation by direct emission of sea salt and growth of ultrafine sea salt". In: *Journal of Geophysical Research* 111.D6, p. D06203. ISSN: 0148-0227.

Pirjola, Liisa (1999). "Effects of the increased UV radiation and biogenic VOC emissions on ultrafine sulphate aerosol formation". In: *Journal of Aerosol Science* 30.3, pp. 355–367.

Platt, U., W. Allan, and D. Lowe (2004). "Hemispheric average Cl atom concentration from ¡sup¿13¡/sup¿C/¡sup¿12¡/sup¿C ratios in atmospheric methane". English. In: *Atmospheric Chemistry and Physics* 4.9/10, pp. 2393–2399. ISSN: 1680-7324.

Pöhler, Denis et al. (2010). "Observation of halogen species in the Amundsen Gulf, Arctic, by active long-path differential optical absorption spectroscopy." In: *Proceedings of the National Academy of Sciences of the United States of America* 107.15, pp. 6582–7. ISSN: 1091-6490.

Pöhlker, Christopher et al. (2012). "Biogenic potassium salt particles as seeds for secondary organic aerosol in the Amazon." In: *Science (New York, N.Y.)* 337.6098, pp. 1075–8. ISSN: 1095-9203.

Pöschl, Ulrich (2005). "Atmospheric aerosols: composition, transformation, climate and health effects." In: *Angewandte Chemie (International ed. in English)* 44.46, pp. 7520–40. ISSN: 1433-7851.

Prados-Roman, C. et al. (2015). "Iodine oxide in the global marine boundary layer". English. In: *Atmospheric Chemistry and Physics* 15.2, pp. 583–593. ISSN: 1680-7324.

Prinn, R et al. (1987). "Atmospheric trends in methylchloroform and the global average for the hydroxyl radical." In: *Science (New York, N.Y.)* 238.4829, pp. 945–950. ISSN: 0036-8075.

Prinn, R G et al. (1995). "Atmospheric Trends and Lifetime of CH3CCI3 and Global OH Concentrations." In: *Science (New York, N.Y.)* 269.5221, pp. 187–192. ISSN: 0036-8075.

Quinn, P. K. et al. (1998). "Aerosol optical properties in the marine boundary layer during the First Aerosol Characterization Experiment (ACE 1) and the underlying chemical and physical aerosol properties". In: *Journal of Geophysical Research* 103.D13, p. 16547. ISSN: 0148-0227.

Quinn, P. K. et al. (2000). "A comparison of aerosol chemical and optical properties from the 1st and 2nd Aerosol Characterization Experiments". en. In: *Tellus B* 52.2. ISSN: 1600-0889.

Radke, Lawrence F. (1982). "Sulphur and sulphate from Mt Erebus". In: *Nature* 299.5885, pp. 710–712. ISSN: 0028-0836.

Raes, Frank (1995). "Entrainment of free tropospheric aerosols as a regulating mechanism for cloud condensation nuclei in the remote marine boundary layer". In: *Journal of Geophysical Research* 100.D2, p. 2893. ISSN: 0148-0227.

Raes, Frank, Andrea Saltelli, and Rita Van Dingenen (1992). "Modelling formation and growth of H2SO4-H2O aerosols: Uncertainty analysis and experimental evaluation". In: *Journal of Aerosol Science* 23.7, pp. 759–771. ISSN: 00218502.

Ramacher, B., J. Rudolph, and R. Koppmann (1999). "Hydrocarbon measurements during tropospheric ozone depletion events: Evidence for halogen atom chemistry". In: *Journal of Geophysical Research* 104.D3, p. 3633. ISSN: 0148-0227.

Ramanathan, V et al. (2001). "Atmosphere: Aerosols, climate, and the hydrological cycle". In: *Science* 294.5549, pp. 2119–2124.

Rankin, Andrew M. and Eric W. Wolff (2003). "A year-long record of size-segregated aerosol composition at Halley, Antarctica". In: *Journal of Geophysical Research: Atmospheres* 108.D24, n/a–n/a. ISSN: 01480227.

Rankin, Andrew M., Eric W. Wolff, and Seelye Martin (2002). "Frost flowers: Implications for tropospheric chemistry and ice core interpretation". In: *Journal of Geophysical Research* 107.D23, p. 4683. ISSN: 0148-0227.

Ravishankara, A. R. and P. H. Wine (1980). "A laser flash photolysis-resonance fluorescence kinetics study of the reaction Cl(2P) + CH4CH3 + HCl". In: *The Journal of Chemical Physics* 72.1, p. 25. ISSN: 00219606.

Read, K. A. et al. (2008). "DMS and MSA measurements in the Antarctic Boundary Layer: impact of BrO on MSA production". English. In: *Atmospheric Chemistry and Physics* 8.11, pp. 2985–2997. ISSN: 1680-7324.

Reeve, Jono (2013). "Aurora Australis Voyage VMS 2012/13 Track and Underway Data (SIPEX II)". In: *Australian Antarctic Data Centre*.

Reifenhäuser, Werner and Klaus G Heumann (1992). "Determinations of methyl iodide in the Antarctic atmosphere and the south polar sea". In: *Atmospheric Environment. Part A. General Topics* 26.16, pp. 2905–2912.

Richter, A. et al. (2002). "Gome measurements of stratospheric and tropospheric BrO". In: *Advances in Space Research* 29.11, pp. 1667–1672. ISSN: 02731177.

Robinson, A. D. et al. (2014). "Long term halocarbon observations from a coastal and an inland site in Sabah, Malaysian Borneo". English. In: *Atmospheric Chemistry and Physics Discussions* 14.2, pp. 1919–1969. ISSN: 1680-7375.

Rohrer, Franz and Harald Berresheim (2006). "Strong correlation between levels of tropospheric hydroxyl radicals and solar ultraviolet radiation." In: *Nature* 442.7099, pp. 184–7. ISSN: 1476-4687.

Rosenfeld, D et al. (2008). "Flood or drought: How do aerosols affect precipitation?" In: *Science* 321, pp. 1309–1313. ISSN: 00368075 (ISSN).

Rosenfeld, Daniel, Hailong Wang, and Philip J. Rasch (2012). "The roles of cloud drop effective radius and LWP in determining rain properties in marine stratocumulus". In: *Geophysical Research Letters* 39.13, n/a–n/a. ISSN: 00948276.

Rudolph, Jochen et al. (1999). "Halogen atom concentrations in the Arctic Troposphere derived from hydrocarbon measurements: Impact on the budget of formaldehyde". In: *Geophysical Research Letters* 26.19, pp. 2941–2944. ISSN: 00948276.

Russell, L M et al. (2013). "Southern Ocean Aerosols: Particle Composition and the Mass and Number Budget (Invited)". In: *Abstract A32C-04 presented at 2013 Fall Meeting*. San Francisco, Calif., 9-13 Dec.

Saiz-Lopez, A. et al. (2006). "Modelling molecular iodine emissions in a coastal marine environment: the link to new particle formation". English. In: *Atmospheric Chemistry and Physics* 6.4, pp. 883–895. ISSN: 1680-7324.

Saiz-Lopez, Alfonso. (2014). *Iodine chemistry in the marine troposphere*.

Saiz-Lopez, Alfonso and Roland von Glasow (2012). "Reactive halogen chemistry in the troposphere". In: *Chemical Society Reviews* 41.19, pp. 6448–6472.

Saiz-Lopez, Alfonso and John M. C. Plane (2004). "Novel iodine chemistry in the marine boundary layer". In: *Geophysical Research Letters* 31.4, p. L04112. ISSN: 0094-8276.

Saiz-Lopez, Alfonso. et al. (2007a). "Boundary layer halogens in coastal Antarctica". In: *Science* 317.5836, pp. 348–351.

Saiz-Lopez, Alfonso et al. (2007b). "First observations of iodine oxide from space". In: *Geophysical Research Letters* 34.12, p. L12812.

Saiz-Lopez, Alfonso et al. (2011). "Atmospheric Chemistry of Iodine". In: *Chemical Reviews* 112.3, pp. 1773–1804.

Samson, J A et al. (1990). "On the systematic variation in surface aerosol concentration at the South Pole". In: *Atmospheric Research* 25.5, pp. 385–396.

Sander, S P et al. (2011). *Chemical Kinetics and Photochemical Data for Use in Atmospheric Studies, Evaluation Number 17, JPL Publication 10-6*. Tech. rep. Pasedena, California: Jet Propulsion Laboratory, California Institute of Technology.

Saunders, Russell W. and John M. C. Plane (2005). "Formation Pathways and Composition of Iodine Oxide Ultra-Fine Particles". en. In: *Environmental Chemistry* 2.4, p. 299. ISSN: 1448-2517.

Savoie, D. L. et al. (1992). "Nitrogen and sulfur species in acrosols at Mawson, Antarctica, and their relationship to natural radionuclides". English. In: *Journal of Atmospheric Chemistry* 14.1-4, pp. 181–204. ISSN: 0167-7764.

Scarchilli, Claudio, Massimo Frezzotti, and Paolo Michele Ruti (2010). "Snow precipitation at four ice core sites in East Antarctica: provenance, seasonality and blocking factors". In: *Climate Dynamics* 37.9-10, pp. 2107–2125. ISSN: 0930-7575.

Schofield, R., N. R. P. Harris, and S. Connors (2014). *Numerical Atmospheric dispersion Modeling Environment - an operational particle dispersion model using the Met Office Unified Model and ECMWF Numerical Weather Prediction meteorology data - raw, gridded SIPEX II data.*

Schofield, R and A Klekociuk (2014). *Hysplit atmospheric back-trajectories at 10m, 500m, 1000m, 1500m, 2000m, 2500m, 3000m, 3500m, 4000m collected during the SIPEX II voyage of the Aurora Australis, 2012.*

Schofield, R et al. (2014a). *Gaseous elemental mercury measurements of boundary layer air made by a Tekran 2537 during the SIPEX II voyage of the Aurora Australis, 2012.*

Schofield, R et al. (2014b). *In-situ Halocarbon trace-gas concentrations measured by the Dirac GC-ECD during the SIPEX II voyage of the Aurora Australis, 2012.*

Schofield, R et al. (2014c). *Trace-gas profiles of the boundary layer from Multi-Axis Differential Optical Spectroscopy MAX-DOAS collected during the SIPEX II voyage of the Aurora Australis, 2012.*

Schofield, Robyn and Jenny Fisher (2014). "Personal communication: Modelling elemental mercury in the boundary layer of the Southern Ocean and Antarctic sea-ice during SIPEX II."

Schofield, Robyn et al. (2014d). *In-situ atmospheric ozone measurements observed during the SIPEX II voyage of the Aurora Australis, 2012.*

Schönhardt, A et al. (2008). "Observations of iodine monoxide columns from satellite". In: *Atmos. Chem. Phys.* 8.3, pp. 637–653.

Schönhardt, A et al. (2012). "Simultaneous satellite observations of IO and BrO over Antarctica". In: *Atmos. Chem. Phys.* 12.14, pp. 6565–6580.

Schroeder, W H et al. (1998). "Arctic springtime depletion of mercury". In: *Nature* 394.6691, pp. 331–332.

Schroeder, William H. and R.A. Jackson (1987). "Environmental measurements with an atmospheric mercury monitor having speciation capabilities". In: *Chemosphere* 16.1, pp. 183–199. ISSN: 00456535.

Schroeder, William H. and John Munthe (1998). "Atmospheric mercuryAn overview". In: *Atmospheric Environment* 32.5, pp. 809–822. ISSN: 13522310.

Seidel, Dian J. et al. (2008). "Widening of the tropical belt in a changing climate". In: 1.1, pp. 21–24. ISSN: 1548-7091.

Seinfeld, John H and Spyros N Pandis (2006). *Atmospheric Chemistry and Physics - From Air Pollution to Climate Change (2nd Edition).* John Wiley & Sons. ISBN: 978-0-471-72018-8.

Selin, Noelle E. et al. (2007). "Chemical cycling and deposition of atmospheric mercury: Global constraints from observations". In: *Journal of Geophysical Research: Atmospheres* 112.2, pp. 1–14. ISSN: 01480227.

Semiletov, Igor et al. (2004). "Atmospheric CO 2 balance: The role of Arctic sea ice". In: *Geophysical Research Letters* 31.5, n/a–n/a. ISSN: 00948276.

Sharon, T M et al. (2006). "Aerosol and cloud microphysical characteristics of rifts and gradients in maritime stratocumulus clouds". In: *Journal of the Atmospheric Sciences* 63, pp. 983–997. ISSN: 00224928 (ISSN).

Shaw, Glenn E (1982). "Atmospheric Turbidity in the Polar Regions". In: *Journal of Applied Meteorology* 21.8, pp. 1080–1088.

— (1988). "Antarctic aerosols: A review". In: *Reviews of Geophysics* 26.1, pp. 89–112.

Shaw, Stephanie L., Sallie W. Chisholm, and Ronald G. Prinn (2003). "Isoprene production by Prochlorococcus, a marine cyanobacterium, and other phytoplankton". In: *Marine Chemistry* 80.4, pp. 227–245. ISSN: 03044203.

Shindell, D T et al. (2013). "Radiative forcing in the ACCMIP historical and future climate simulations". In: *Atmos. Chem. Phys.* 13.6, pp. 2939–2974.

Sigmond, Michael and John C. Fyfe (2014). "The Antarctic Sea Ice Response to the Ozone Hole in Climate Models". EN. In:

Sihto, S.-L. et al. (2006). "Atmospheric sulphuric acid and aerosol formation: implications from atmospheric measurements for nucleation and early growth mechanisms". English. In: *Atmospheric Chemistry and Physics* 6.12, pp. 4079–4091. ISSN: 1680-7324.

Simpson, W. R. et al. (2007). "First-year sea-ice contact predicts bromine monoxide (BrO) levels at Barrow, Alaska better than potential frost flower contact". English. In: *Atmospheric Chemistry and Physics* 7.3, pp. 621–627. ISSN: 1680-7324.

Sipilä, Mikko et al. (2010). "The Role of Sulfuric Acid in Atmospheric Nucleation". In: *Science* 327, pp. 1243–1246.

Six, Katharina D et al. (2013). "Global warming amplified by reduced sulphur fluxes as a result of ocean acidification". In: *Nature Clim. Change* 3.11, pp. 975–978. ISSN: 1758-678X.

Sjostedt, S.J. et al. (2007). "Observations of hydroxyl and the sum of peroxy radicals at Summit, Greenland during summer 2003". In: *Atmospheric Environment* 41.24, pp. 5122–5137. ISSN: 13522310.

Slemr, F., G. Schuster, and W. Seiler (1985). "Distribution, speciation, and budget of atmospheric mercury". In: *Journal of Atmospheric Chemistry* 3.4, pp. 407–434. ISSN: 0167-7764.

Slemr, F. et al. (2011). "Worldwide trend of atmospheric mercury since 1995". English. In: *Atmospheric Chemistry and Physics* 11.10, pp. 4779–4787. ISSN: 1680-7324.

Slemr, F. et al. (2015). "Comparison of mercury concentrations measured at several sites in the Southern Hemisphere". English. In: *Atmospheric Chemistry and Physics* 15.6, pp. 3125–3133. ISSN: 1680-7324.

Slemr, Franz et al. (2003). "Worldwide trend of atmospheric mercury since 1977". In: *Geophysical Research Letters* 30.10. ISSN: 00948276.

Smith, Robin S., Clotilde Dubois, and Jochem Marotzke (2010). "Global Climate and Ocean Circulation on an Aquaplanet OceanAtmosphere General Circulation Model". EN. In:

Snider, Graydon, Farhad Raofie, and Parisa A Ariya (2008). "Effects of relative humidity and CO(g) on the O3-initiated oxidation reaction of Hg0(g): kinetic & product studies". In: *Physical Chemistry Chemical Physics* 10.36, pp. 5616–5623.

Stefels, Jacqueline et al. (2007). "Environmental constraints on the production and removal of the climatically active gas dimethylsulphide (DMS) and implications for ecosystem modelling". In: *Biogeochemistry* 83.1-3, pp. 245–275. ISSN: 0168-2563.

Stephens, Chelsea R et al. (2012). "The relative importance of chlorine and bromine radicals in the oxidation of atmospheric mercury at Barrow, Alaska". In: *Journal of Geophysical Research: Atmospheres* 117.D14, D00R11.

Stieb, D M, S Judek, and R T Burnett (2002). "Meta-analysis of time-series studies of air pollution and mortality: Effects of gases and particles and the influence of cause of death, age, and season". In: *Journal of the Air and Waste Management Association* 52.4, pp. 470–484.

Stohl, A and H Sodemann (2010). "Characteristics of atmospheric transport into the Antarctic troposphere". In: *Journal of Geophysical Research:* 115.D2, p. D02305.

Stohl, A. et al. (2013). "Black carbon in the Arctic: the underestimated role of gas flaring and residential combustion emissions". English. In: *Atmospheric Chemistry and Physics* 13.17, pp. 8833–8855. ISSN: 1680-7324.

Subir, Mahamud, Parisa A. Ariya, and Ashu P. Dastoor (2012). "A review of the sources of uncertainties in atmospheric mercury modeling II. Mercury surface and heterogeneous chemistry A missing link". In: *Atmospheric Environment* 46, pp. 1–10. ISSN: 13522310.

Tao, W K et al. (2007). "Role of atmospheric aerosol concentration on deep convective precipitation: Cloud-resolving model simulations". In: *Journal of Geophysical Research D: Atmospheres* 112. ISSN: 01480227 (ISSN).

Tao, Wei-Kuo et al. (2012). "Impact of aerosols on convective clouds and precipitation". In: *Rev. Geophys.* 50, RG2001. ISSN: 8755-1209.

Taraborrelli, D. et al. (2012). "Hydroxyl radical buffered by isoprene oxidation over tropical forests". In: *Nature Geoscience* 5.3, pp. 190–193. ISSN: 1752-0894.

Temme, Christian et al. (2003a). "Measurements of Atmospheric Mercury Species at a Coastal Site in the Antarctic and over the South Atlantic Ocean during Polar Summer". In: *Environmental Science & Technology* 37.1, pp. 22–31. ISSN: 0013-936X.

Temme, Christian et al. (2003b). "Response to Comment on Measurements of Atmospheric Mercury Species at a Coastal Site in the Antarctic and over the South Atlantic Ocean during Polar Summer". In: *Environmental Science & Technology* 37.14, pp. 3241–3242. ISSN: 0013-936X.

Thompson, David W J et al. (2011). "Signatures of the Antarctic ozone hole in Southern Hemisphere surface climate change". In: *Nature Geosci* 4.11, pp. 741–749.

Tison, J.-L. et al. (2010). "High-resolution dimethyl sulfide and dimethylsulfoniopropionate time series profiles in decaying summer first-year sea ice at Ice Station Polarstern, western Weddell Sea, Antarctica". In: *Journal of Geophysical Research* 115.G4, G04044. ISSN: 0148-0227.

Topping, D O and G McFiggans (2012). "Tight coupling of particle size, number and composition in atmospheric cloud droplet activation". In: *Atmos. Chem. Phys.* 12, pp. 3253–3260. ISSN: 1680-7324.

Tortell, Philippe et al. (2012). "Spatial distribution of pCO2, ΔO2/Ar and dimethylsulfide (DMS) in polynya waters and the sea ice zone of the Amundsen Sea, Antarctica". In: *Deep Sea Research Part II: Topical Studies in Oceanography* 71-76.

Trevena, Anne and Graham Jones (2012). "DMS flux over the Antarctic sea ice zone". In: *Marine Chemistry* 134-135.

TSI (2002). *Model 3025A Ultrafine Condensation Particle Counter - Instruction Manual*, p. 121.

Tsigaridis, K. et al. (2006). "Change in global aerosol composition since preindustrial times". English. In: *Atmospheric Chemistry and Physics* 6.12, pp. 5143–5162. ISSN: 1680-7324.

Turco, Richard P., Jing-Xia Zhao, and Fangqun Yu (1998). "A new source of tropospheric aerosols: Ion-ion recombination". In: *Geophysical Research Letters* 25.5, pp. 635–638. ISSN: 00948276.

Twomey, S (1974). "Pollution and the planetary albedo". In: *Atmospheric Environment (1967)* 8.12, pp. 1251–1256.

Udisti, R et al. (2012). "Sea spray aerosol in central Antarctica. Present atmospheric behaviour and implications for paleoclimatic reconstructions". In: *Atmospheric Environment* 52.0, pp. 109–120.

Udisti, Roberto et al. (2004). "Atmospheresnow interaction by a comparison between aerosol and uppermost snow-layers composition at Dome C, East Antarctica". In: *Annals of Glaciology* 39.1, pp. 53–61. ISSN: 02603055.

United Nations Environmental Programme (2008). *The Global Atmospheric Mercury Assessment: Sources, Emissions and Transport.* Tech. rep. United National Environment Programme.

Vanhanen, J. et al. (2011). "Particle Size Magnifier for Nano-CN Detection". In: *Aerosol Science and Technology* 45.4, pp. 533–542. ISSN: 0278-6826.

Virkkula, Aki et al. (2006). "Chemical size distributions of boundary layer aerosol over the Atlantic Ocean and at an Antarctic site". In: *Journal of Geophysical Research* 111.D5, p. D05306. ISSN: 0148-0227.

Virkkula, Aki et al. (2007). "Charged particle size distributions and analysis of particle formation events at the Finnish Antarctic research station Aboa". 1239-6095. In: *Boreal Environment Research* 12.3, pp. 397–408.

Virkkula, Aki et al. (2009). "Review of Aerosol Research at the Finnish Antarctic Research Station Aboa and its Surroundings in Queen Maud Land , Antarctica". In: *Geophysica* 45, pp. 163–181.

Vlasenko, A et al. (2009). "Kinetics of the heterogeneous reaction of nitric acid with mineral dust particles: an aerosol flowtube study." en. In: *Physical chemistry chemical physics : PCCP* 11.36, pp. 7921–30. ISSN: 1463-9076.

Wagenbach, D. et al. (1998). "Sea-salt aerosol in coastal Antarctic regions". In: *Journal of Geophysical Research* 103.D9, p. 10961. ISSN: 0148-0227.

Wang, Zhien et al. (2008). "Association of Antarctic polar stratospheric cloud formation on tropospheric cloud systems". In: *Geophysical Research Letters* 35.13, p. L13806. ISSN: 0094-8276.

Warren, Dale R and John H Seinfeld (1985). "Prediction of aerosol concentrations resulting from a burst of nucleation". In: *Journal of Colloid and Interface Science* 105.1, pp. 136–142. ISSN: 00219797.

Warren, Stephen G. (2002). "Snowball Earth: Ice thickness on the tropical ocean". In: *Journal of Geophysical Research* 107.C10, p. 3167. ISSN: 0148-0227.

Weber, R. J. et al. (1999). "Intercomparison of airborne and surface-based measurements of condensation nuclei in the remote marine troposphere during ACE 1". In: *Journal of Geophysical Research: Atmospheres* 104.D17, pp. 21673–21683. ISSN: 0148-0227.

Weber, R J et al. (2001). "Measurements of enhanced H2SO4 and 34 nm particles near a frontal cloud during the First Aerosol Characterization Experiment (ACE 1)". In: *Journal of Geophysical Research: Atmospheres* 106.D20, pp. 24107–24117.

Weber, Rodney J et al. (1998). "A study of new particle formation and growth involving biogenic and trace gas species measured during ACE 1". In: *Journal of Geophysical Research: Atmospheres* 103.D13, pp. 16385–16396.

Weiden, S.-L. von der, F. Drewnick, and S. Borrmann (2009). "Particle Loss Calculator a new software tool for the assessment of the performance of aerosol inlet systems". English. In: *Atmospheric Measurement Techniques* 2.2, pp. 479–494. ISSN: 1867-8548.

Weller, R et al. (2011). "Characterization of the inter-annual, seasonal, and diurnal variations of condensation particle concentrations at Neumayer, Antarctica". In: *Atmos. Chem. Phys.* 11.24, pp. 13243–13257.

West, R. E. L. et al. (2014). "The importance of vertical velocity variability for estimates of the indirect aerosol effects". English. In: *Atmospheric Chemistry and Physics* 14.12, pp. 6369–6393. ISSN: 1680-7324.

Whitehead, J D et al. (2012). "Particle fluxes and condensational uptake over sea ice during COBRA". In: *Journal of Geophysical Research: Atmospheres* 117.D15, p. D15202.

Wichmann, H.-Erich and Annette Peters (2000). "Epidemiological evidence of the effects of ultrafine particle exposure". In: *Philosophical Transactions of the Royal Society of London. Series A: Mathematical, Physical and Engineering Sciences* 358.1775, pp. 2751–2769.

Wiedensohler, A et al. (1996). "Occurrence of an ultrafine particle mode less than 20 nm in diameter in the marine boundary layer during Arctic summer and autumn". In: *Tellus, Series B: Chemical and Physical Meteorology* 48.2, pp. 213–222.

Wiedensohlet, A et al. (1997). "Intercomparison Study of the Size-Dependent Counting Efficiency of 26 Condensation Particle Counters". In: *Aerosol Science and Technology* 27.2, pp. 224–242.

Williams, G. et al. (2014). "Thick and deformed Antarctic sea ice mapped with autonomous underwater vehicles". In: *Nature Geoscience* 8.1, pp. 61–67. ISSN: 1752-0894.

Wilson, S. R. (2014). "Characterisation of ¡i¿J¡/i¿(O¡sup¿1¡/sup¿D) at Cape Grim 20002005". English. In: *Atmospheric Chemistry and Physics Discussions* 14.12, pp. 18389–18419. ISSN: 1680-7375.

Wofsy, S C (2011). "HIAPER Pole-to-Pole Observations (HIPPO): fine-grained, global-scale measurements of climatically important atmospheric gases and aerosols." In: *Philosophical transactions. Series A, Mathematical, physical, and engineering sciences* 369.1943, pp. 2073–86. ISSN: 1364-503X.

Wolff, Eric W. and Hélène Cachier (1998). "Concentrations and seasonal cycle of black carbon in aerosol at a coastal Antarctic station". In: *Journal of Geophysical Research* 103.D9, p. 11033. ISSN: 0148-0227.

World Meteorological Organization et al. (2008). *Future Climate Change Research and Observations: GCOS, WCRP and IGBP learning from the IPCC Fourth Assessment Report*. Tech. rep. Sydney, p. 68.

Wright, Simon W. et al. (2010). "Phytoplankton community structure and stocks in the Southern Ocean (3080E) determined by CHEMTAX analysis of HPLC pigment signatures". In: *Deep Sea Research Part II: Topical Studies in Oceanography* 57.9-10, pp. 758–778. ISSN: 09670645.

Xia, Chonghuan, Zhouqing Xie, and Liguang Sun (2010). "Atmospheric mercury in the marine boundary layer along a cruise path from Shanghai, China to Prydz Bay, Antarctica". In: *Atmospheric Environment* 44.14, pp. 1815–1821. ISSN: 13522310.

Yang, Xin, John A. Pyle, and Richard A. Cox (2008). "Sea salt aerosol production and bromine release: Role of snow on sea ice". In: *Geophysical Research Letters* 35.16, p. L16815. ISSN: 0094-8276.

Yokouchi, Yoko et al. (1999). "Isoprene in the marine boundary layer (southeast Asian Sea, eastern Indian Ocean, and Southern Ocean): Comparison with dimethyl sulfide and bromoform". In: *Journal of Geophysical Research* 104.D7, p. 8067. ISSN: 0148-0227.

Yokouchi, Yoko et al. (2011). "Diurnal and seasonal variations of iodocarbons (CH2ClI, CH2I2, CH3I, and C2H5I) in the marine atmosphere". In: *Journal of Geophysical Research: Atmospheres* 116.D6, p. D06301.

Yu, F. (2006). "From molecular clusters to nanoparticles: second-generation ion-mediated nucleation model". English. In: *Atmospheric Chemistry and Physics* 6.12, pp. 5193–5211. ISSN: 1680-7324.

Yu, Fangqun (2010). "Ion-mediated nucleation in the atmosphere: Key controlling parameters, implications, and look-up table". In: *Journal of Geophysical Research* 115.D3, p. D03206. ISSN: 0148-0227.

Yu, Fangqun and Gan Luo (2010). "Oceanic Dimethyl Sulfide Emission and New Particle Formation around the Coast of Antarctica: A Modeling Study of Seasonal Variations and Comparison with Measurements". In: *Atmosphere* 1.1, pp. 34–50.

Yu, Fangqun and Richard P. Turco (2000). "Ultrafine aerosol formation via ion-mediated nucleation". In: *Geophysical Research Letters* 27.6, pp. 883–886. ISSN: 00948276.

Yu, Fangqun et al. (2010). "Spatial distributions of particle number concentrations in the global troposphere: Simulations, observations, and implications for nu-

cleation mechanisms". In: *Journal of Geophysical Research* 115.D17, p. D17205. ISSN: 0148-0227.

Yu, S, V K Saxena, and Z Zhao (2001). "A comparison of signals of regional aerosol-induced forcing in eastern China and the southeastern United States". In: *Geophysical Research Letters* 28.4, pp. 713–716.

Zemmelink, H J et al. (2005). "Emission of dimethylsulfide from Weddell Sea leads". In: *Geophysical Research Letters* 32.

Zemmelink, H. J. et al. (2006). "CO 2 deposition over the multi-year ice of the western Weddell Sea". In: *Geophysical Research Letters* 33.13, p. L13606. ISSN: 0094-8276.

Zemmelink, H J et al. (2008). "Dimethylsulfide emissions over the multi-year ice of the western Weddell Sea". In: *Geophysical Research Letters* 35.

Zhang, Renyi (2010). "Getting to the Critical Nucleus of Aerosol Formation". In: *Science* 328, pp. 1366–1367.

Zhang, Renyi et al. (2004). "Atmospheric New Particle Formation Enhanced by Organic Acids". In: *Science* 304, pp. 1487–1490.

Zhang, Renyi et al. (2012). "Nucleation and growth of nanoparticles in the atmosphere." In: *Chemical reviews* 112.3, pp. 1957–2011. ISSN: 1520-6890.

Appendix A

Background Polar Cell Aerosols

A.1 Latitudinal Aerosol

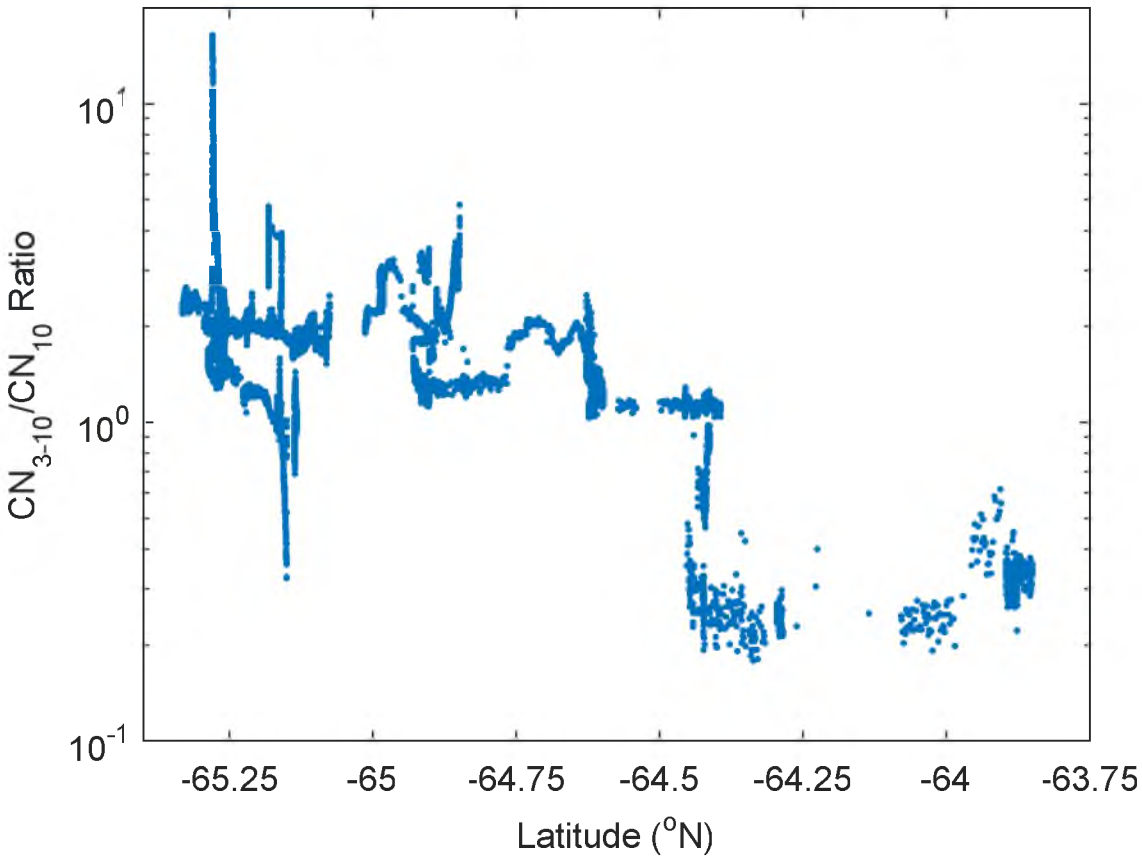

Figure A.1: The aerosol size ratio shows a similar latitudinal step change as the raw aerosol data from which it is calculated, changing magnitude at the proposed Polar Front latitude.

A.2 Comparison of Antarctic Aerosol Concentrations

Table A.1: Summary of surface aerosol number concentrations reported in the literature in the Antarctic and Southern Ocean regions. Data reported includes those able to be extracted from relevant literature, and includes mean and median values, as well as ranges in parentheses. Where relevant, the air-mass is identified as either continental (CntAM) or coastal (CstAM).

Location	Coordinates	CN_3	CN_{10}	Source
Sea Ice Measurements				
East Antarctic Sea Ice, SIPEXII	~120°E, ~65°S	720_{med} 1012_{mean} (97-7699)	250_{med} 334_{mean} (59-1655)	This study
Ship in Weddell Sea & Halley Bay	~45°W, south of 58°S	910_{mean} (150 - 4325) $(400\text{-}600)_{bkgd}$	-	Davison et al., 1996; O'Dowd et al., 1997
Nansen Ice Sheet Glacier	163°27'E, 74°30'S	-	630 (169 - 1385)	Belosi et al., 2012
Continental and Coastal Measurements				
Neumayer Station	8.25° W, 70.64° S	258_{med} 343_{mean} (~30 - ~1100)	-	Weller et al., 2011
South Pole	0°E, 90°S	(100 - 300)	-	Park et al., 2004
Aboa	13°25'W, 73°03'S	-	$\sim 200_{median}$	Kyrö et al., 2013
Aboa	13°25'W, 73°03'S	580_{mean} $(200\text{-}500)_{CntAM}$ $(300\text{-}2000)_{CstAM}$	-	Koponen et al., 2003
Aboa	13°25'W, 73°03'S	289_{med} 374_{mean} (50-3000)	-	Asmi et al., 2010

Continued on next page

Table A.1 – *Continued from previous page*

Location	**Coordinates**	**CN_3**	**CN_{10}**	**Source**
Dome C	123.35°E, 75.10°S	-	109_{med} (15 - 260)	Järvinen et al., 2013
Maitri	11.73°E, 70.76°S	$\sim 500_{mean}$	-	Pant, Siingh, and Kamra, 2011
Maitri	11.73°E, 70.76°S	(800-1000)	-	Deshpande and Kamra, 2004
Mawson	62.87°E, 67.60°S	(400-500)	-	Gras, 1993
Troll	2.53°E, 72.00°S	-	204_{med} 348_{mean} (19 - 3768)	Hansen et al., 2009
Syowa	39.58°E, 69.00°S	-	403_{mean} 273_{median} (18-5766)	Hara et al., 2011
Syowa	39°30'E, 69°S	(210-370)	-	Ito, 1985
Southern Ocean Measurements				
ACE1 Campaign	137-160°E, 41-54°S	-	$\sim 400_{median}$	Hudson, Xie, and Yum, 1998
Macquarie Island	158.95°E, 54.5°S	675_{mean} (100-1800)	-	Brechtel, Kreidenweis, and Swan, 1998
ACE1 flights	140-147°E, 40.5-43.5°S	-	<1000	Clarke et al., 1998

A.3 Calculating the lifetime of aerosol in the Antarctic Free Troposphere

The lifetime of aerosols in the Antarctic troposphere was calculated using formula outlined in section 13.3 of Seinfeld and Pandis (2006). Results are presented in Figure A.2. It was determined that under the reasonable assumption of a starting number concentration of 10000 cm^{-3}, aerosol populations coagulated at a rate that resulted in number concentrations similar to those observed at the surface. The resulting number concentrations after a particular time period depended on the assumption of aerosol size distributions and starting concentrations.

These results suggest that the lifetimes of particles in the Antarctic free troposphere, where number concentrations are likely to be within the range modelled here, and whose size distribution is likely to be at the lower end of those modelled here, are long enough to be able to be transported the long distances that trajectories suggest are possible (up to 10 days).

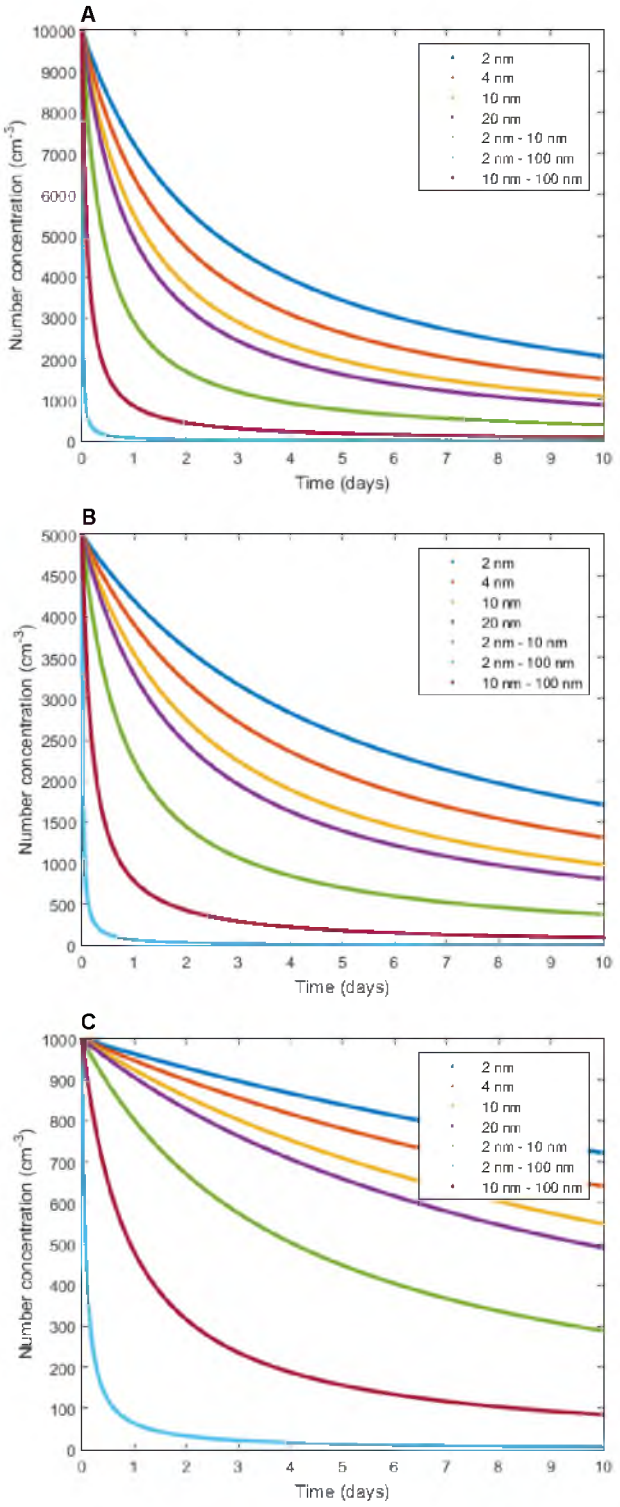

Figure A.2: Decreases in number concentrations modelled utilising only coagulational loss mechanisms. Aerosol populations modelled represent either mono-modal (one number represented in legend), or bi-modal (for example, 2 nm and 10 nm particles are coagulating). **A)** represents initial number concentration of 10000 cm^{-3}, **B)** 5000 cm^{-3} and **C)** 1000 cm^{-3}, all within the range of those possible in this region.

A.4 9th October

There are two periods in the aerosol record that showed short-term (~hours) increases in number concentrations that at first glance, are indicative of local new particle formation events. The largest of these, occurring on October 18, did prove to be a local event and this is described in detail in Chapter 5. The second period, occurring on October 9, is worth a more thorough analysis here.

This event was characterised by a sharp increase in number concentrations in both size bins, and a simultaneous (albeit modest relative to the 18 October event) increase in the ratio value. Despite this significant increase in number concentrations, time delays between increases in the size bins were not existent, suggesting no growth occurred and making local formation unlikely.

Backward trajectories were calculated to assess whether air-mass history was different during the event compared to the remaining background period. As discussed in Chapter 3, background aerosol populations were found to be transported within air-masses that had recently come from the Antarctic Free Troposphere (AFT). It is possible that after formation in the AFT, condensational growth halted, while coagulation processes continued slowly, at a rate that is not measurable with the current instrumentation. This process would slowly reduce the ratio value. In this circumstance, the more time that has elapsed since formation in the AFT, the lower the ratio value, assuming no addition of condensing species (reasonable considering the air-mass is lofted from the surface). Consequently, it is possible that a temporary increase in the ratio value that occurs without any other growth indicators, such as that observed on 9 October, could be caused by an aerosol populations that has been more recently formed compared to the remaining background measurements.

Figure A.3 shows 36 hour backward trajectories calculated using NOAA's HYSPLIT model. Trajectories released before the event (08:00 and 10:00) were found to be representative of the majority of the Polar Cell trajectories, travelling from the east along the sea ice surface for around 36 hours after having descended from the AFT. The following three trajectories, chosen to end during the period of increase aerosol concentration, were found to have come from the south, and have been in the AFT less than 24 hours before measurement. The beginning of the declining number concentrations coincided with air-masses that had had at least 36 hours within the surface layer (below 500 m) prior to measurement. This supports the suggestion that the enhanced aerosol population during this period was a result of more recent influence from the AFT where nucleation was likely to be occurring.

This significant drop in temperature is indicative of the temperatures one would observe in air that has recently been in the AFT at a latitude further south than measured. Figure A.4 shows the inverse relationship between air temperature and

aerosol number concentrations during this event, with temperatures plummeting from around -9°C before and after the event, down to below -15°C during the period when aerosol numbers are highest and when trajectories suggest air-masses have more recently been in the AFT.

Both trajectory calculations and *in-situ* air temperature data support the conclusion suggested from aerosol data that this significant increase in aerosol number concentrations is not the result of local new particle formation. Instead, the increased concentrations result from air-masses that have more recently come from the AFT, providing less time for number concentrations to reduce from coagulational processes, and therefore leaving a higher portion of the population in the sub-10 nm size range compared to the remaining background populations.

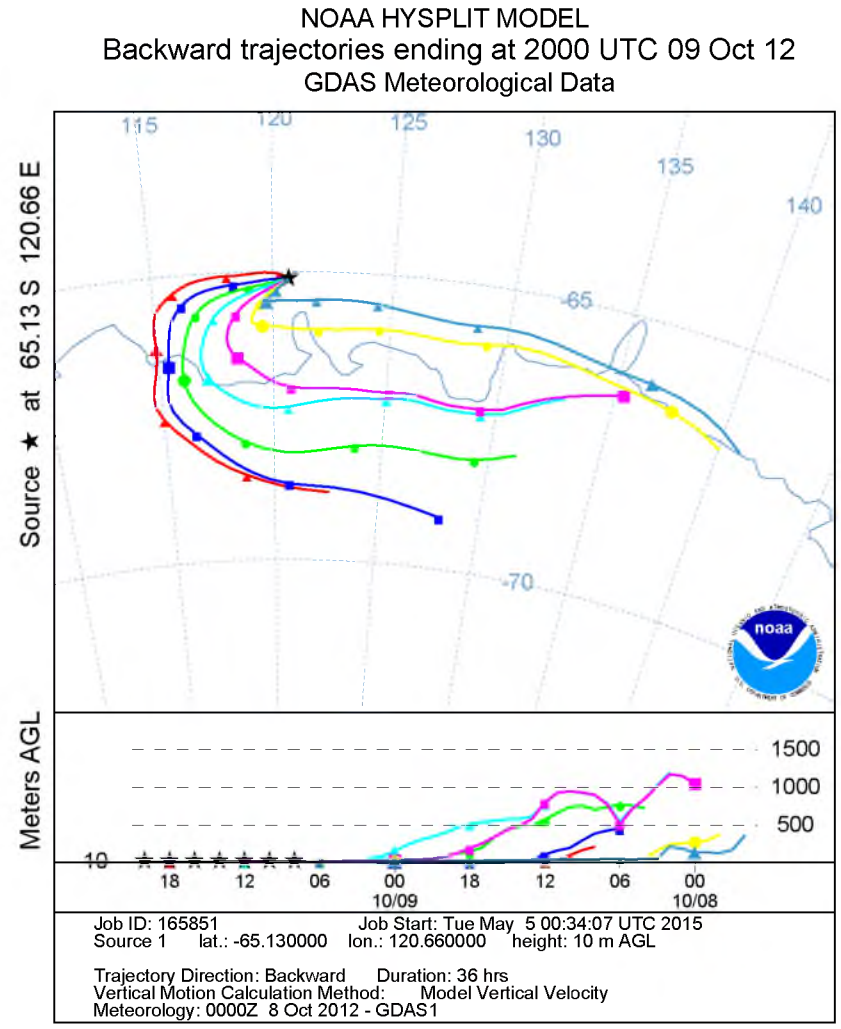

Figure A.3: 36 hour backward trajectories released every two hours from the measurement location (10 m above sea level) and spanning the 9 October enhanced aerosol event.

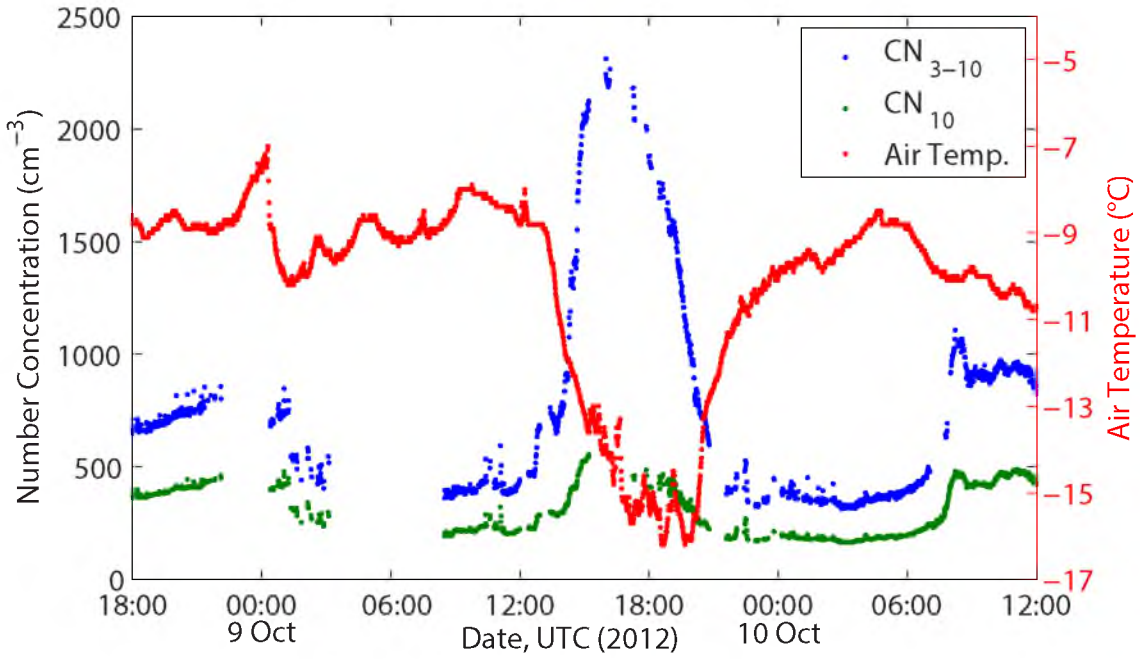

Figure A.4: Air temperature and aerosol number concentrations in the two size ranges during the enhanced aerosol event of the 9 October.

A.5 Back Trajectories

A multitude of trajectory calculations and plotting methods were used to discern and confirm the characteristics of the circulation described in Chapter 3. Some of the additional plots that contribute to, or provide support for, the circulation features are included below. Also included are examples of the meridional mass stream function that was calculated for each day throughout the voyage.

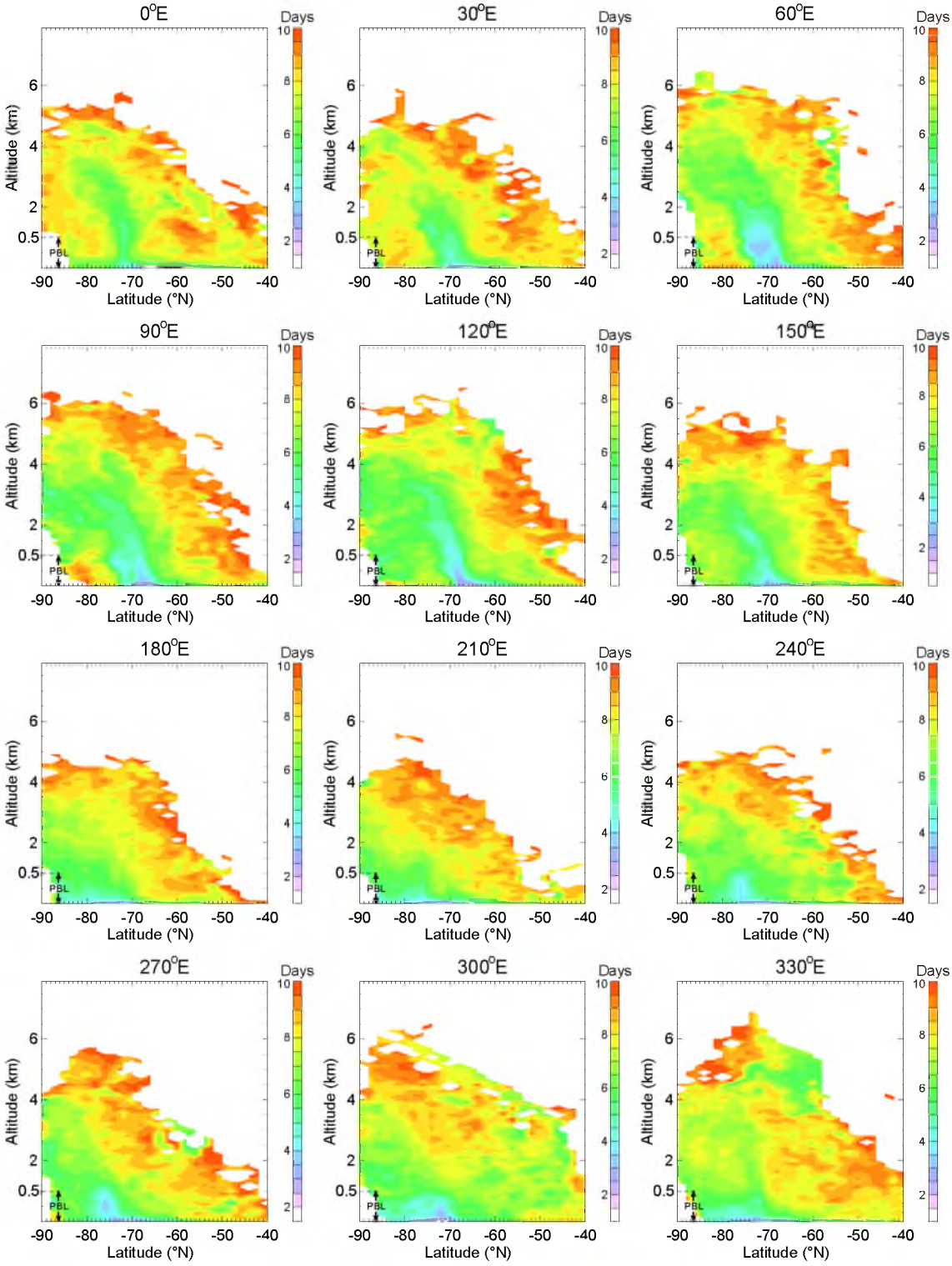

Figure A.5: Longitudinal dependence of circulation features, based on longitudinally averaged cross-sections (altitude above sea level) showing the mean age climatology from 3 years of trajectories released from ice stations around the continent for the month of October 2012. The weaker downward flow strength in West Antarctica (bottom 6 plots) compared to the stronger East Antarctic locations (top 6) is apparent.

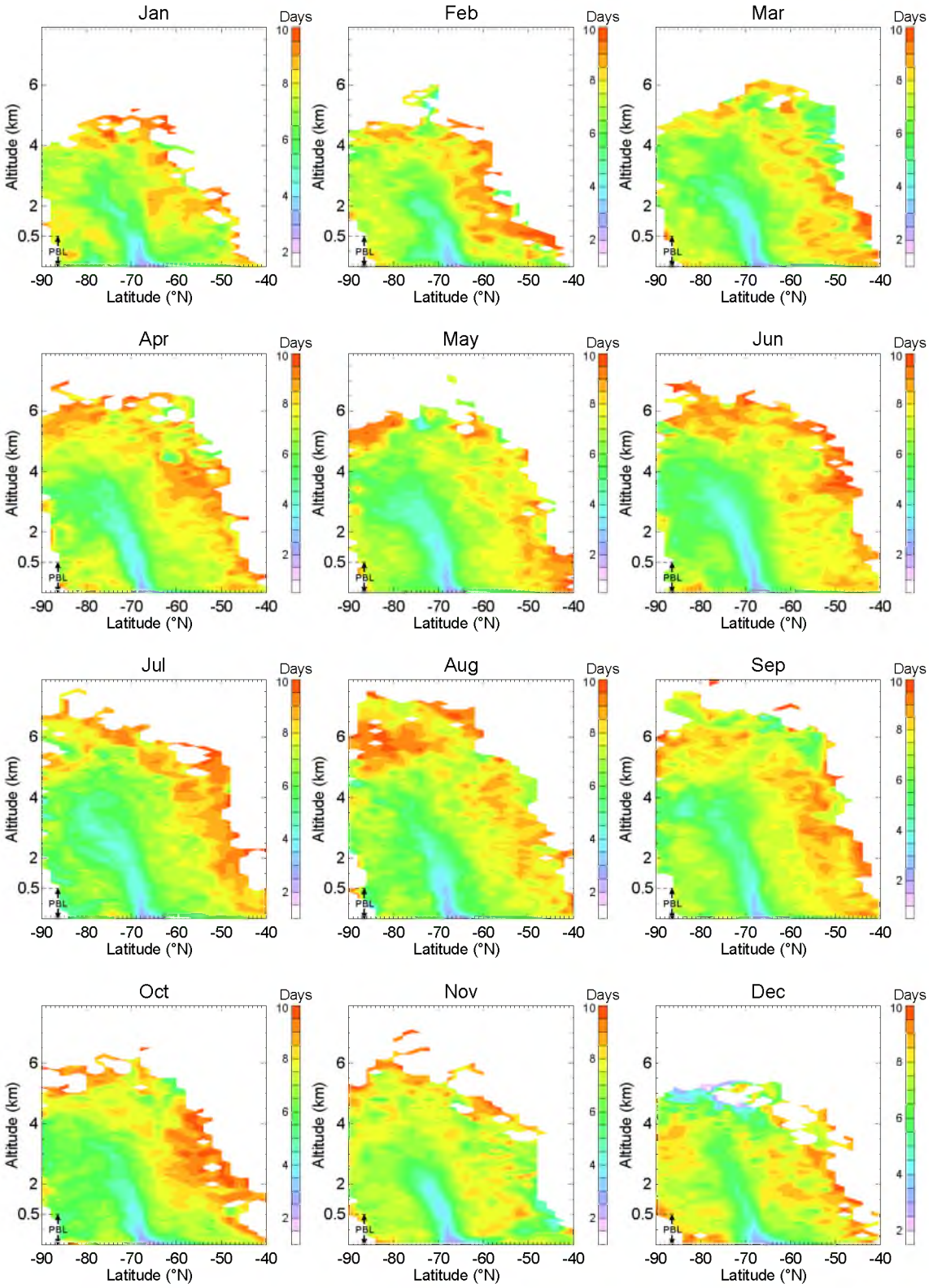

Figure A.6: Longitudinally averaged cross sections (altitude above sea level) showing the monthly mean age of trajectories from 3 years of back trajectories from (65°S, 120°E) virtual ice station. The seasonal cycle of the downward flow is observed to be present year round, with a minimum in Southern Hemisphere summer. Note the white space in the bottom left corner of each plot, which indicates no data due to the presence of the continent, is smeared due to longitudinal averaging.

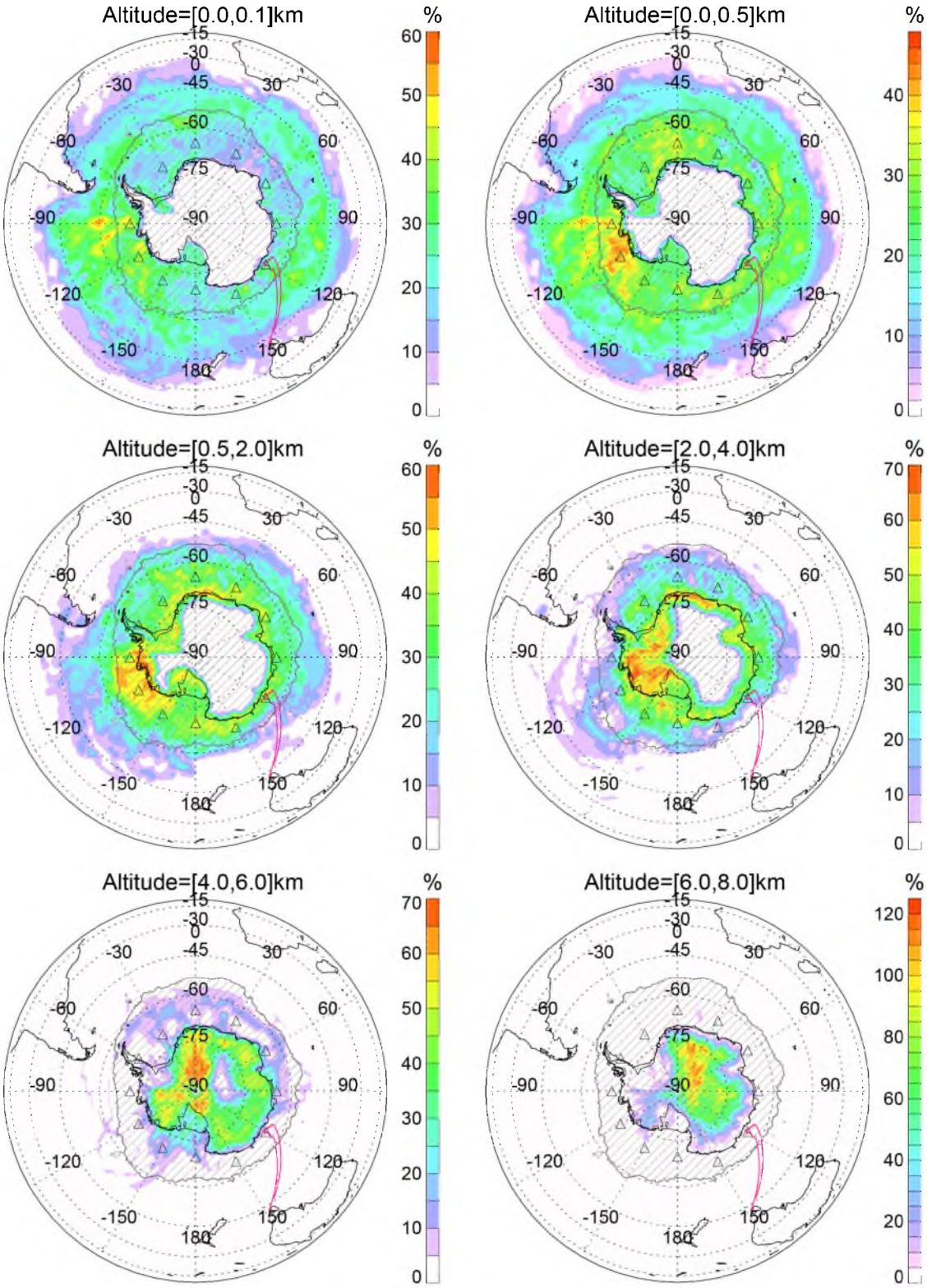

Figure A.7: As in Figure 3.16, but using back-trajectories instead of forward. The two different influences on the sea ice region are observed to be the surface layer of the southern Ocean, and the Antarctic free-troposphere.

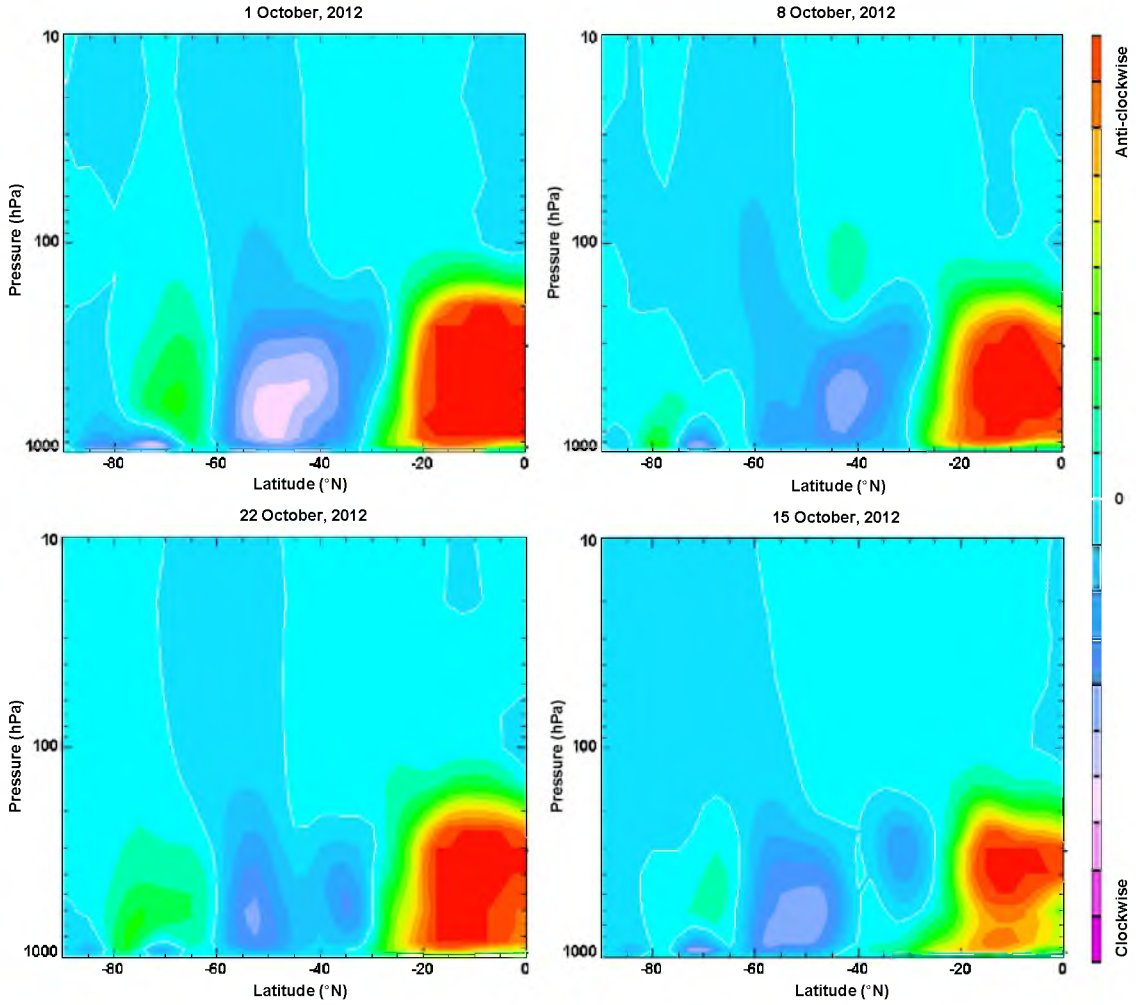

Figure A.8: A sample of daily average meridional mass stream function results across the aerosol measurement time period shows the major circulation features obtained from back-trajectories. Clearly visible circulation cells (from right to left) are: Hadley cell, Ferrel Cell, Polar Front, Polar Cell and underlying surface circulation, depicted more clearly in Figure 3.17

A.6 Background Aerosol and Relation to Cyclone Activity

Background aerosol number concentrations varied considerably throughout the voyage, particularly within the Polar Cell. As observed in Figure 3.6, background number concentrations varied by over 1000 cm^{-3} on an hourly-daily timescale. These variations were investigated by comparison with meteorological, *in-situ* gas composition, and trajectory data. No visible relationship between variations in aerosol number concentrations were found with respect to gas composition (e.g. O_3, total gaseous mercury or halogenated volatile organic compounds) or relative humidity, however some dependencies were found to exist with atmospheric pressure, suggesting the influence of the passage of cyclones.

The measurement period was characterised by eight major pressure systems as identified by *in-situ* meteorological data. Table A.2 summarises the *in-situ* meteorological conditions present during these periods, together with coincident aerosol number concentrations. These periods were confirmed as either high or low pressure systems by meteorological models run as part of the voyage. In general, low pressure systems were associated with the highest aerosol concentrations, CN_3 generally reaching over 2000 cm^{-3}, while high pressure systems coincided with low concentrations, well below 1000 cm^{-3}. This relationship between pressure and aerosol number concentration is shown more clearly in Figure A.9, where a significant negative correlation is observed, with an R^2 value of 0.41. A positive correlation is also apparent with potential temperature (not shown), a trend that seems to be driven primarily by measured pressure.

To assess this idea further, back-trajectories were compared between periods which experienced high and low pressure (and consequently aerosol number concentration). In this analysis, five day trajectories were calculated with endpoints at the measurement location throughout the voyage, but for two distinct pressure regimes: those when the air pressure at the trajectory endpoint was in the lowest 20th percentile (coinciding to pressures below 969.8 hPa); and those in the highest 20th percentile (pressures above 989.8 hPa). Results from this analysis are shown in Figure A.10. The spatial frequency component of the trajectories, shown in panels A and B, show distinctly different influence between the two scenarios. During low pressure periods, air-mass influence from the upper troposphere increases substantially compared to the high pressure case. During the high pressure periods, dominant influence remains below around 3 km altitude. Interestingly, the well defined downward flow is apparent in both scenarios, however the depth of its penetration into the upper troposphere differs significantly. This is confirmed by an analysis of the exposure of trajectories to different levels in the atmosphere (panels

Table A.2: Summary of meteorological parameters and corresponding CN_3 number concentrations. Low aerosol concentrations (top four rows) correspond to calm conditions while high aerosol conditions (lower four rows) correspond to parameters that suggest cyclone activity.

Date	Atm. Pressure (hPa)	Wind Speed ($m.s^{-1}$)	CN_3 (cm^{-3})
4-6 Oct	~975, steady	< 10	< 1000
11-14 Oct	~980, slowly increasing	< 10	< 1000
15 Oct	<990, ridge	<15	<1000
19-21 Oct	1000 - 980, decreasing	< 15	<900 [a]
7-8 Oct	<960, trough	> 20	1400-2100
10 Oct	<962, trough	> 20	1200-2000
16-17 Oct	<968, trough	>15	1500-2700
22-23 Oct	<970, trough	> 20	900-1900

C and D). The high pressure scenarios show peak influence (above the surface layer) in the 1-2 km altitude layer, with a rapid drop at higher levels. On the other hand, the low pressure scenario shows significant influence all the way up to 6 km.

This inverse relationship between pressure and aerosol number concentration suggests an association with the passage of cyclones, a pattern consistent with previous studies (e.g. Ito, 1989; Hara, 2004; Hara et al., 2011). Given that the previously presented back-trajectory analysis suggested an AFT source region for the aerosol, it is reasonable to suggest that cyclones provide an accelerated pathway for air-mass subsidence from the AFT to the surface where measurement occurs. The positive latitudinal correlation observed in the Polar Cell in CN_{3-10} data (Figure 3.2), as well as ratio data (Appendix Figure A.11), also support this idea, reflecting the higher concentrations of smaller particles at locations closer to the continent where air-masses first reach the surface. This relationship, between aerosol number concentration and transit time, could be the result of coagulational growth mechanisms that lead to increasing aerosol size, but decreasing number concentration. The longer the period of time since nucleation, the greater time for coagulation to occur, and therefore, the lower the number of aerosols in the airmass.

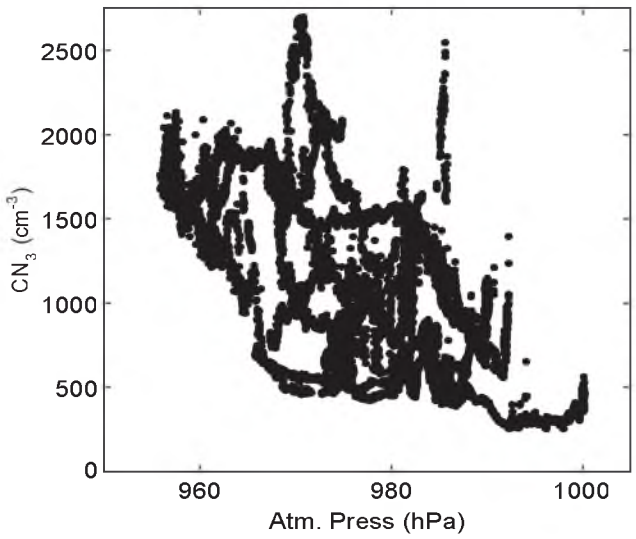

Figure A.9: Measured atmospheric surface pressure (hPa) vs CN_3 (cm^{-3}) for the period of 4-25 October (prior to this period, influence came primarily from the north-west marine boundary layer). Short-term enhancement events on the 9th and 18th October are removed.

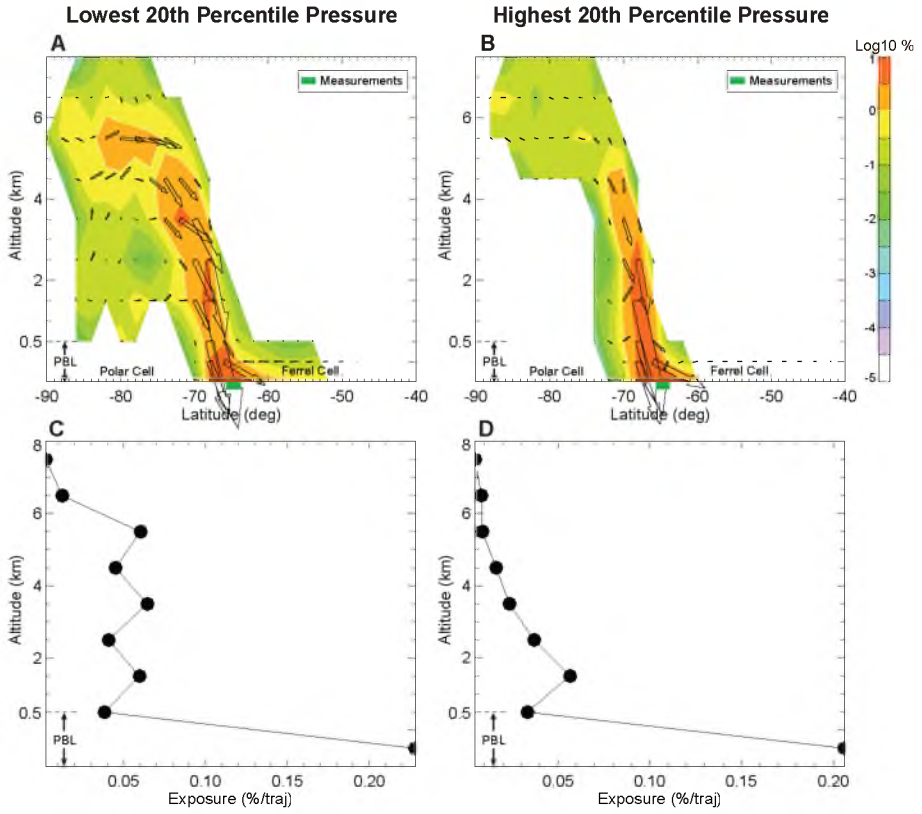

Figure A.10: Analysis of five-day back-trajectories released at 10 m height from the marked (green) measurement location every hour of sea ice voyage for the two different pressure scenarios: the lowest 20th percentile of pressures (**A** and **C**) and the highest 20th percentile of pressures (**B** and **D**). Panels **A** and **B** are similar to Figure 3.7, but show the frequency (i.e. number of times a trajectory passes through a given grid box) component, colours plotted in log scale. **C** and **D** show the exposure of the trajectories to each altitude interval. This is defined as the mean percentage of time trajectories spent in each 1 km layer of the atmosphere up to 8 km. Note again the expansion of the PBL in all plots.

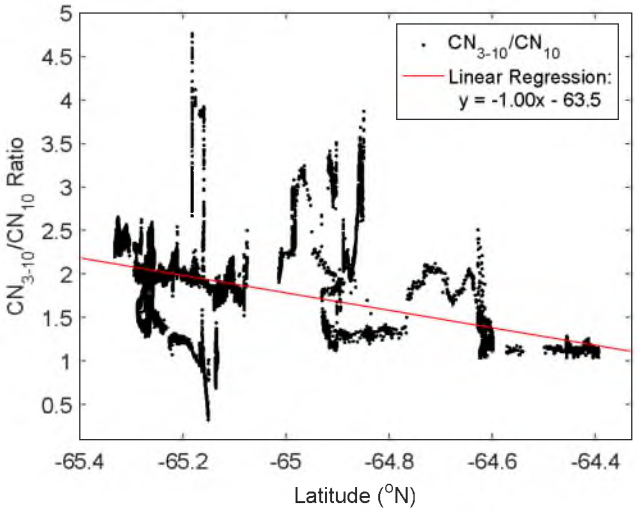

Figure A.11: The ratio CN_{3-10}/CN_{10} is shown only for Polar Cell latitudes. The new particle formation event on the 18th October (Chapter 5) was removed to result in a background dataset. The linear regression shows a substantial increase with latitude.

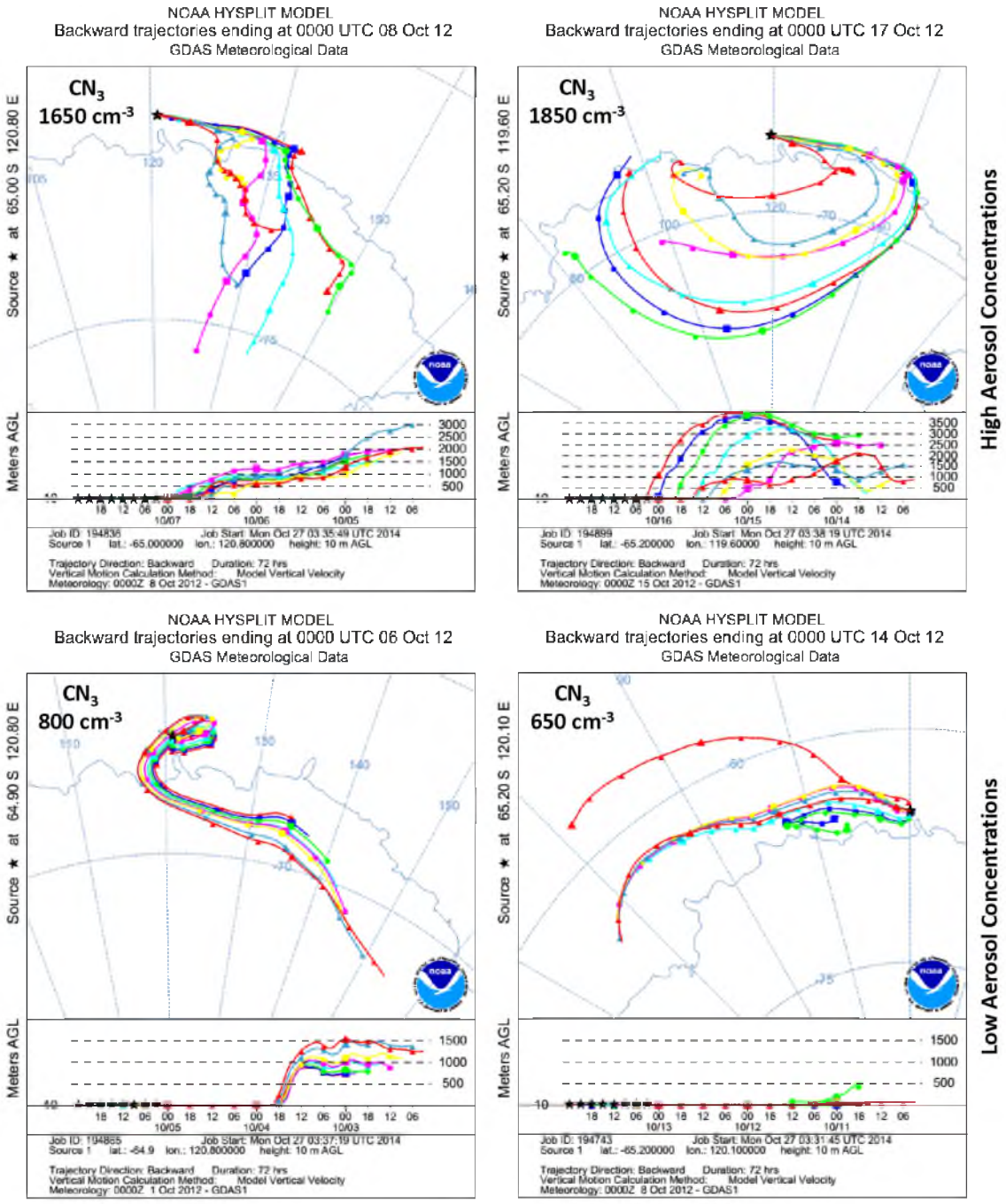

Figure A.12: A sample of the HYSPLIT trajectories calculated for periods of high aerosol concentrations (top row) and low aerosol concentrations (bottom row). Actual concentrations are shown in top right of each trajectory. High aerosol concentrations are found to occur when trajectories place air-masses in the free-troposphere immediately prior to measurement. Lower concentrations are observed when air-masses have spent at least 30 hours in the boundary layer.

A.7 Precursors

The iodine nucleation mechanism has been shown to exist only in the last decade, however it has been previously limited to local nucleation events at coastal locations. Given the globally high concentrations of iodine compounds observed in the Antarctic region though, the mechanism, show here in Appendix Figure A.13, could be active over a regional scale and impact a wide spatial area.

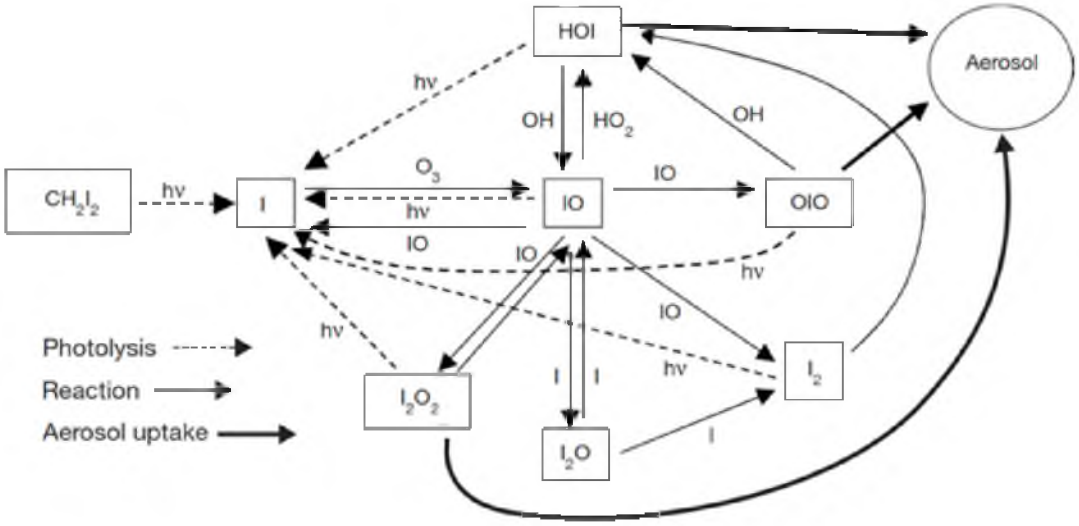

Figure A.13: Chemistry scheme of aerosol production from biogenic organoiodine. Figure taken from O'Dowd et al. (2002c).

Appendix B

Modelling Background Polar Cell Aerosols

```
1  REAL :: dms_em_combined(row_length,rows)   ! Combined DMS emissns
2  REAL :: land_fract(row_length, rows)       ! Fraction of land in grid
       cell
3  REAL :: dms_em_ancil(row_length,rows)      ! Ancillary DMS emiss (surf)
       - land
4  REAL :: dms_em_inter(aero_dim1,aero_dim2) ! Interactive DMS emissns -
       ocean
5  REAL :: ice_fract (row_length, rows)       ! Fraction of sea ice in grid
        cell
6  REAL :: dms_conc(row_length,rows)          ! Seawater DMS conc (nM)
7
8  dms_em_combined(i, j)
9      = (land_fract(i, j) * dms_em_ancil(i, j))                ! land
           source
10     + ( ((1.0 - land_fract(i, j)) * dms_em_inter(i, j))          ! ocean
            source
11     * (1.0 - ice_fract(i, j)) )
```

Algorithm B.1: Snippet of the standard DMS emission routine in GLOMAP, with relevant definitions included.

```
1  REAL :: dms_em_combined(row_length,rows)   ! Combined DMS emissns
2  REAL :: land_fract(row_length, rows)
3  REAL :: dms_em_ancil(row_length,rows)      ! Ancillary DMS emiss (surf)
4  REAL :: dms_em_inter(aero_dim1,aero_dim2) ! Interactive DMS emissns
5  REAL :: ice_fract (row_length, rows)
6  REAL :: dms_conc(row_length,rows)          ! Seawater DMS conc (nM)
7  REAL :: ice_dms_scalar                     ! Seaice DMS emiss scalar
8
9  !              ------------------------------------------------
10 !              ------------------------------------------------
```

```
11
12 ! DMS emission from sea-ice is proportional to underlying ocean DMS
       concentration.
13 ! Emission factor is 1.6 umol.m-2.d-1 for every 1 nM concentration.
14 ! (based on a few different independent measurements in pack ice,
15 ! this is consistent with estimates from Trevena et al 2012, and Lana
       et al, 2011)
16 ! 1.6 umol.m-2.d-1 to kg.m-2.s-1 :
17 ! * 1e-6 (umol to mol)
18 ! * 0.06213 (mol to kg(DMS))
19 ! * 32./62. (kg(DMS) to kg(S))
20 ! / 86400. (d-1 to s-1)
21 ! = 5.938e-13 kg.m-2.s-1
22
23 dms_em_combined(i, j)
24     = (land_fract(i, j) * dms_em_ancil(i, j))
25     + ( ((1.0 - land_fract(i, j)) * dms_em_inter(i, j))
26     * (1.0 - ice_fract(i, j)) )
27     + (ice_fract(i,j) * dms_conc(i,j) * 5.938e-13 * ice_dms_scalar)
```

Algorithm B.2: Snippet of modified DMS emission routine in GLOMAP, with relevant definitions included above. Line 27 of the code (highlighted red) was the modification made for this study, with the 'ice_dms_scalar' variable used for scaling the DMS emission in various scenarios (equal to 1 for default run of 1.6 $\mu mol.m^{-2}.d^{-1}$).

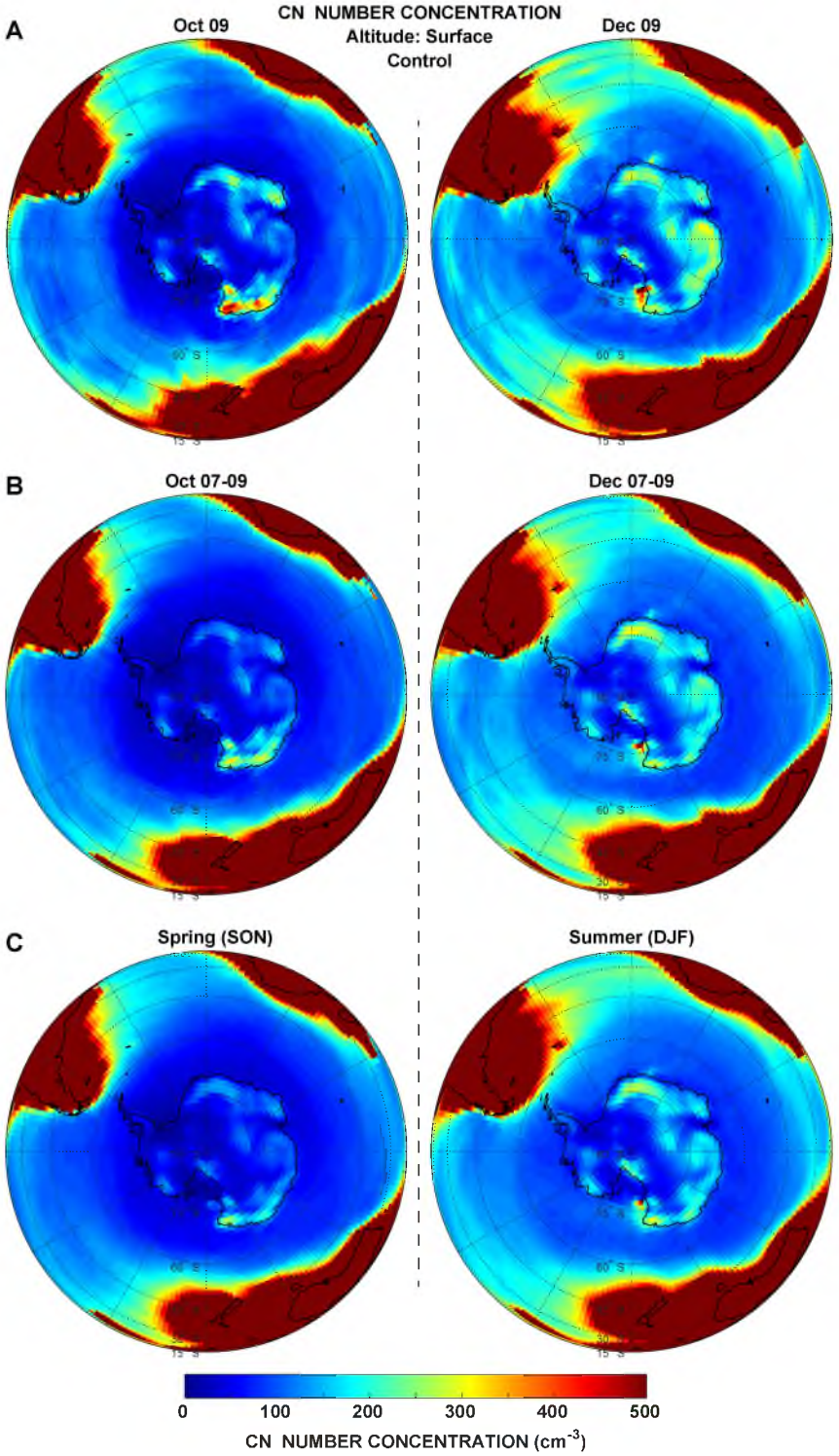

Figure B.1: Comparison of surface condensation nuclei number concentrations (cm^{-3}) output from the control simulation of the model for three different scenarios: (**A**) the October and December 2009 examples used as case studies throughout Chapter 4; (**B**) the October and December averages from all three simulated years (2007-2009); (**C**) and the two seasonal means corresponding to the periods of interest calculated from all three simulated years, spring including September, October and November (SON) and summer includes December, January and February (DJF). Spatial distributions are consistent between all results, and magnitudes only differ in the spring case, with the October 2009 example, used in the thesis, representing the upper limit in the variation.

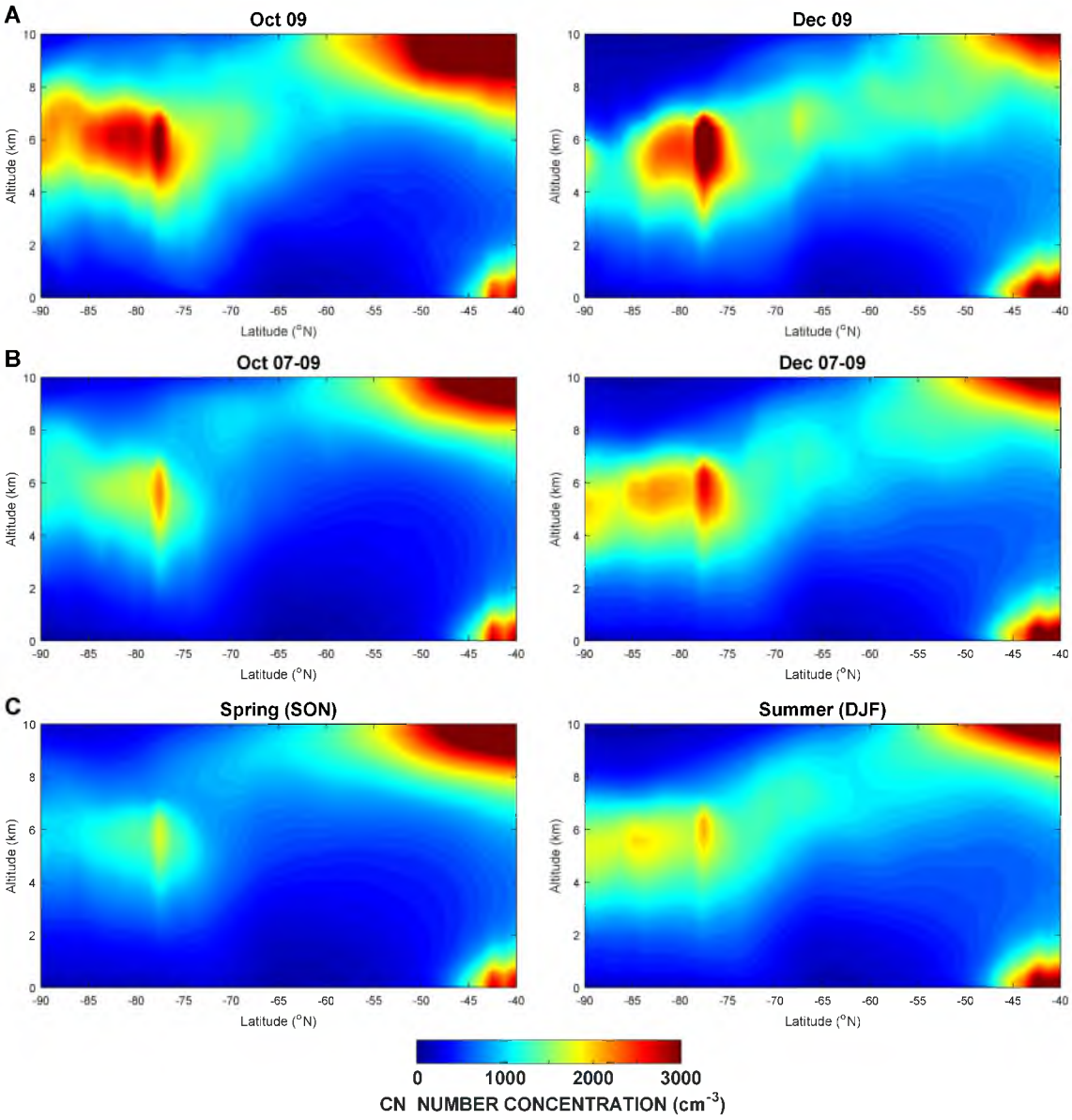

Figure B.2: As in Figure B.1 but showing latitudinal cross-sections with altitude using data from East Antarctica only. Again, patterns are consistent across all results, while the case studies chosen for study represent the upper limit in the inter-annual variability.

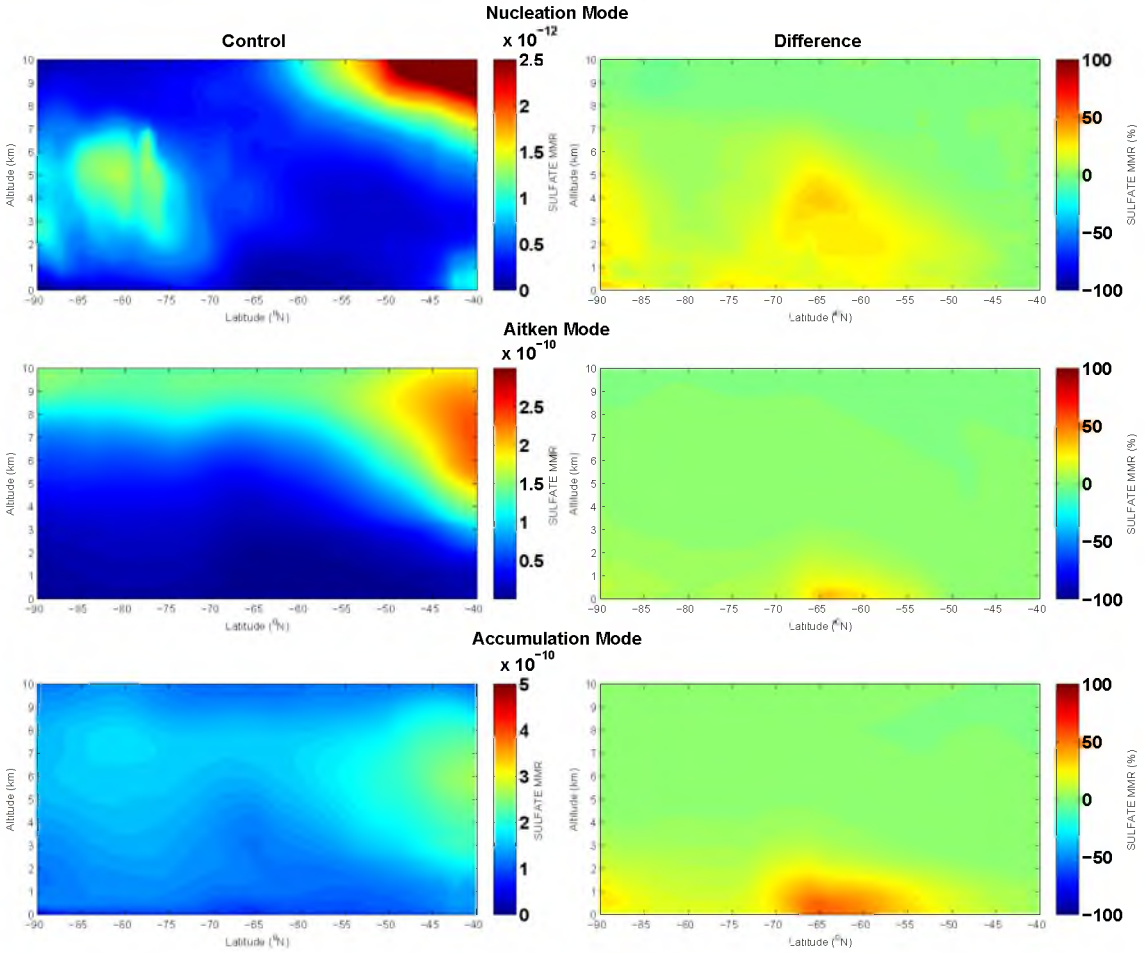

Figure B.3: A breakdown of the changes in mass mixing ratio of sulfate in the soluble mode of each of the three modes that would be affected by the increased DMS flux. In the left column is the mass mixing ratio ($kg.kg^{-1}$) of the control run, while the right column contains the percentage change compared to the control simulation. Data shown are for East Antarctica only and are from October 2009. Note the difference in scales in the left hand column. This change in scaling between plots was necessary because of the change in magnitude between the modes, which, when the difference plots are taken into account, shows that the majority of the mass added in the perturbation simulations moves into the accumulation mode.

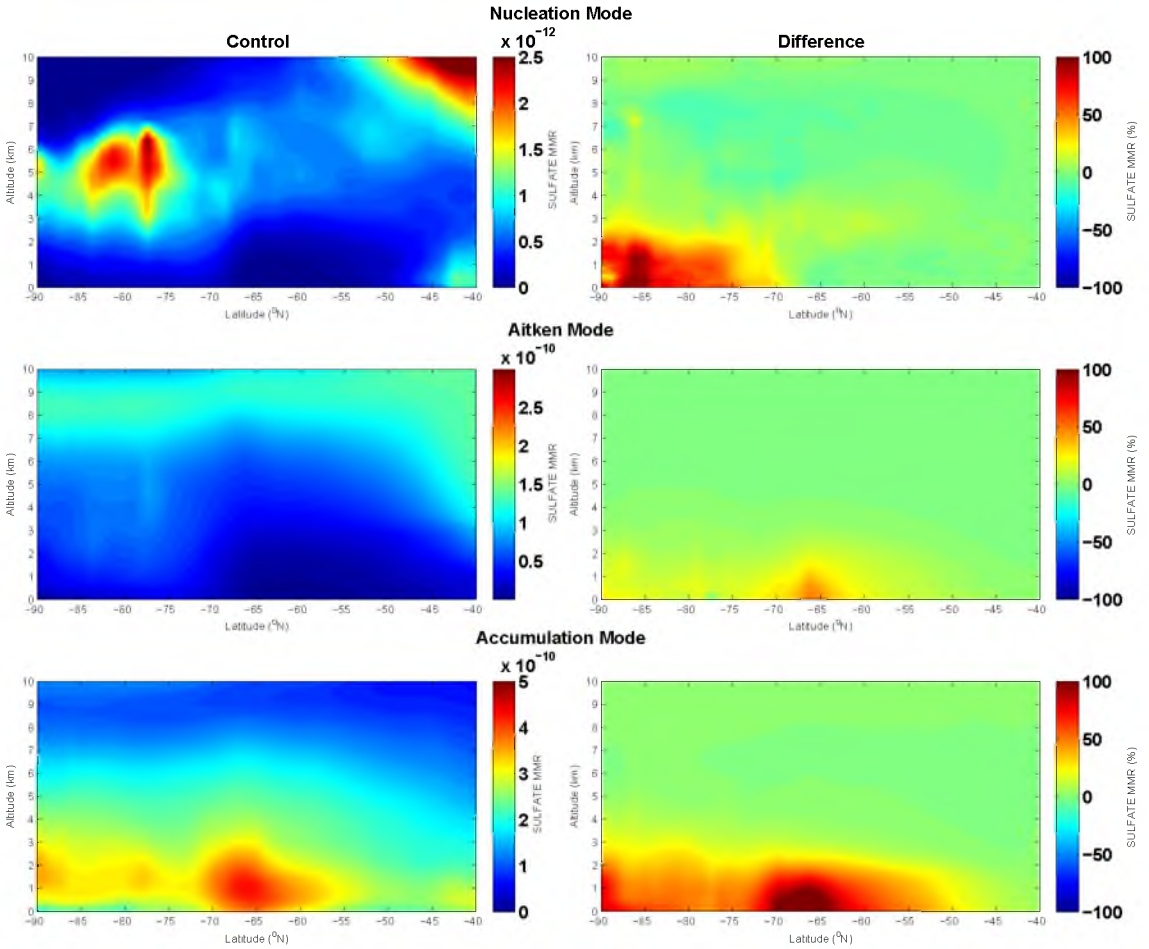

Figure B.4: As in Figure B.3 but for December 2009 data.

Appendix C

Nucleation Events over Antarctic Sea-Ice

C.1 Additional Meteorological Parameters

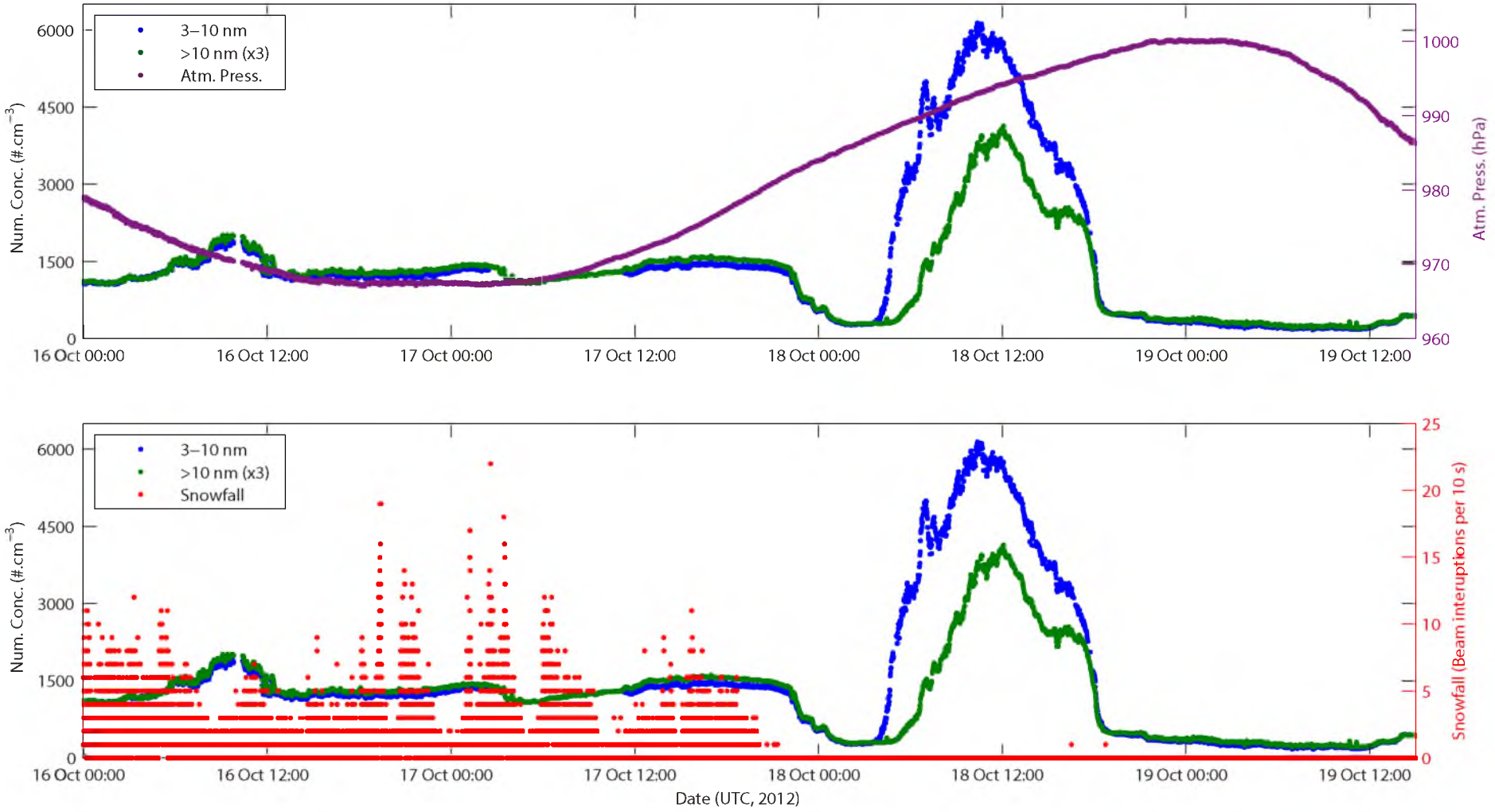

Figure C.1: Meteorological parameters measured during the cruise which, together with Figure 5.3, show the blizzard conditions prior in the days leading up to the fine weather of the formation event. **Top**: atmospheric surface pressure; **Bottom**: Snowfall. Note: the units of snowfall are instrumentally defined as the number of times a beam of light is interrupted as objects, nominally snowflakes, pass through it.


0100
0140
0206
0252
0500

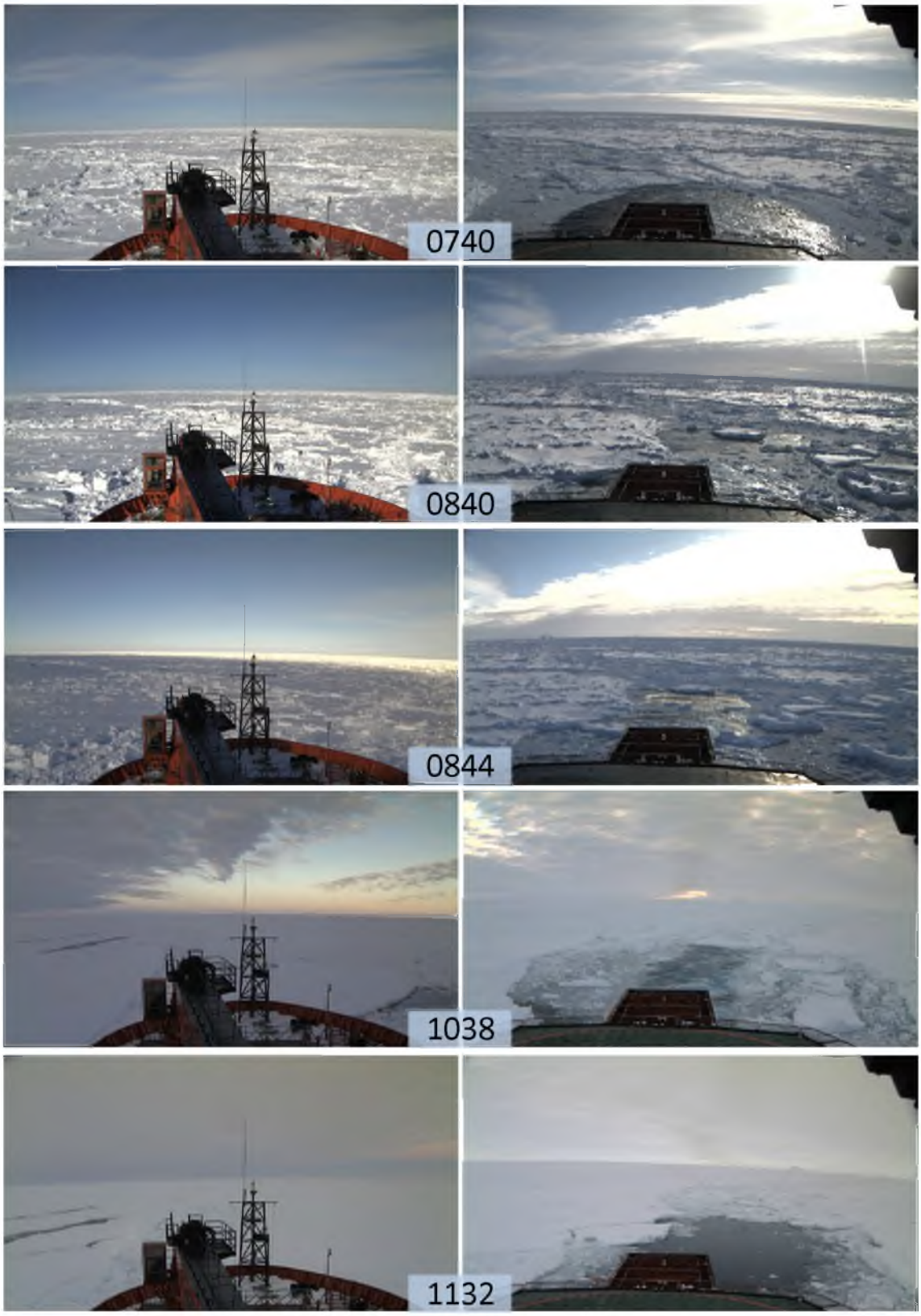

Figure C.2: Selected views (times in UTC) of changing cloud conditions as observed from the bow (left) and stern (right) mounted cameras of the Aurora Australis. Thick stratocumulus clouds prevailed at the beginning and end of the days, with periods of patchy clouds between. A relatively cloud-free period in the middle of the day lasted almost 7 hours.

C.2 Further Trajectory Results

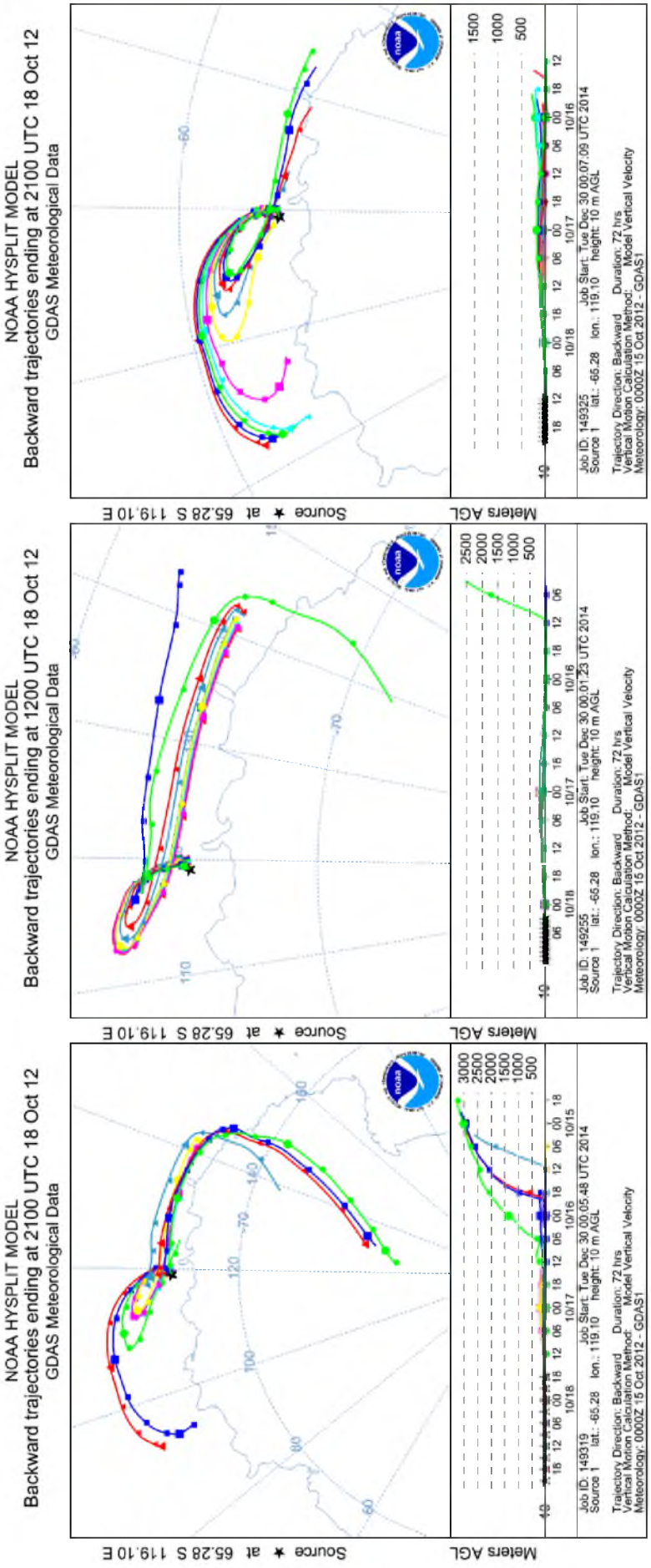
NOAA HYSPLIT MODEL
Backward trajectories ending at 2100 UTC 18 Oct 12
GDAS Meteorological Data
Source ★ at 65.28 S 119.10 E
Meters AGL
NOAA HYSPLIT MODEL
Backward trajectories ending at 1200 UTC 18 Oct 12
GDAS Meteorological Data
Source ★ at 65.28 S 119.10 E
Meters AGL
NOAA HYSPLIT MODEL
Backward trajectories ending at 2100 UTC 18 Oct 12
GDAS Meteorological Data
Source ★ at 65.28 S 119.10 E
Meters AGL

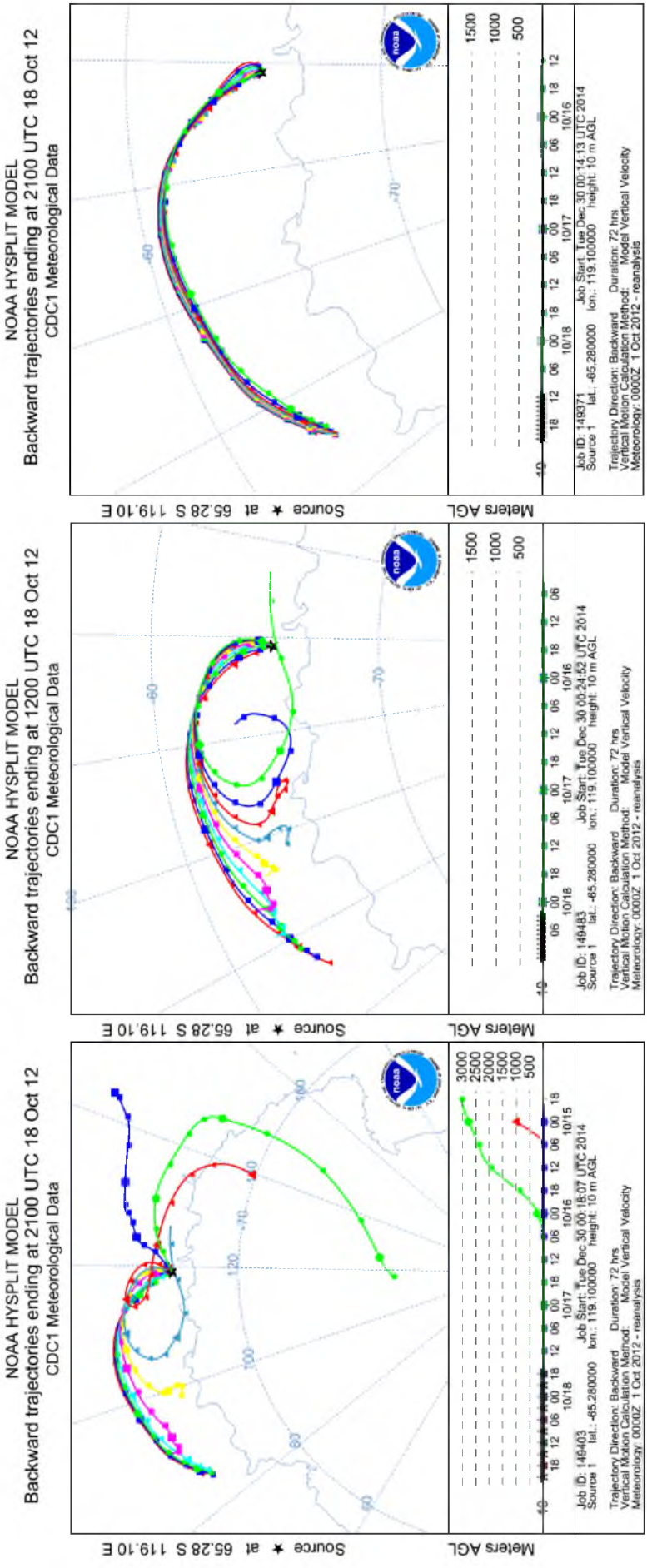
NOAA HYSPLIT MODEL
Backward trajectories ending at 2100 UTC 18 Oct 12
CDC1 Meteorological Data
Source ★ at 65.28 S 119.10 E
Meters AGL
NOAA HYSPLIT MODEL
Backward trajectories ending at 1200 UTC 18 Oct 12
CDC1 Meteorological Data
Source ★ at 65.28 S 119.10 E
Meters AGL
NOAA HYSPLIT MODEL
Backward trajectories ending at 2100 UTC 18 Oct 12
CDC1 Meteorological Data
Source ★ at 65.28 S 119.10 E
Meters AGL

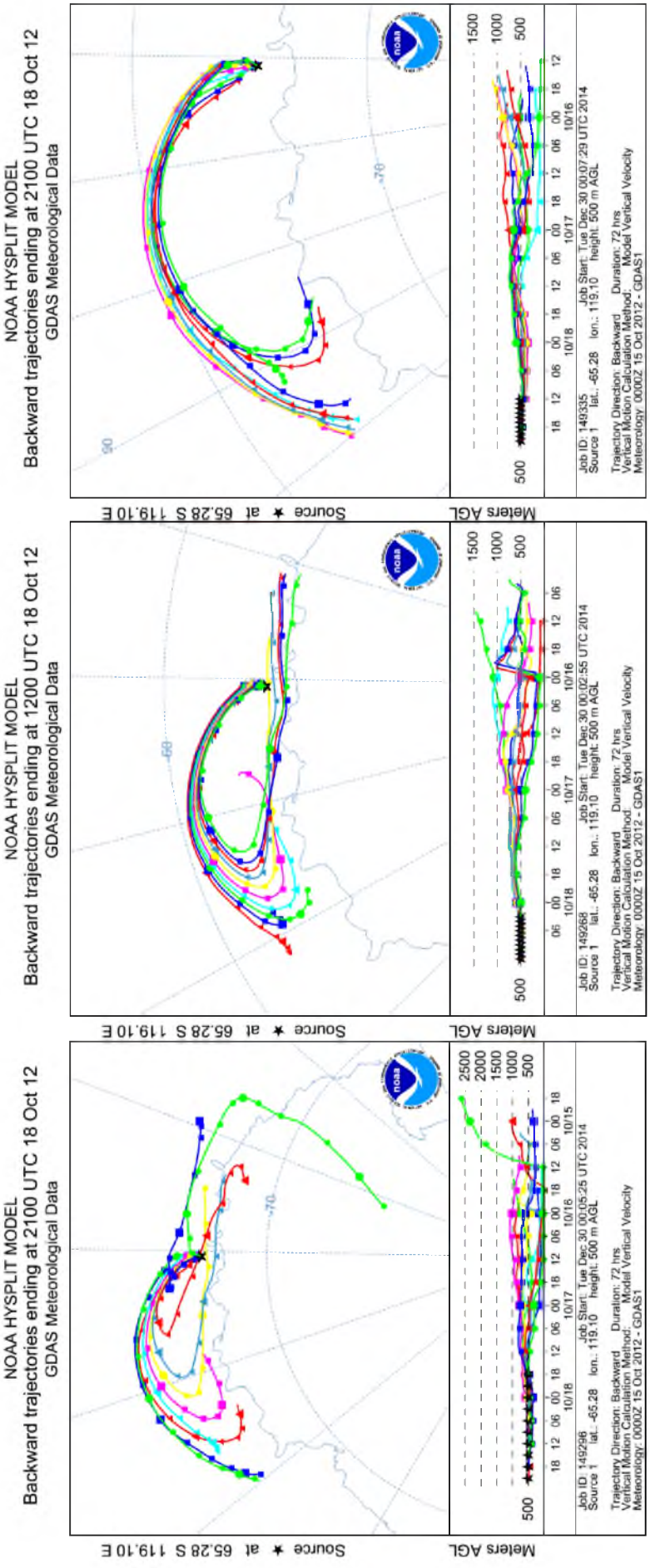
NOAA HYSPLIT MODEL
Backward trajectories ending at 2100 UTC 18 Oct 12
GDAS Meteorological Data
Source ★ at 65.28 S 119.10 E
Meters AGL
Job ID: 149296
Source 1 lat.: -65.28 lon.: 119.10 height: 500 m AGL
Job Start: Tue Dec 30 00:05:25 UTC 2014
Trajectory Direction: Backward Duration: 72 hrs
Vertical Motion Calculation Method: Model Vertical Velocity
Meteorology: 00002.15 Oct 2012 - GDAS1
NOAA HYSPLIT MODEL
Backward trajectories ending at 1200 UTC 18 Oct 12
GDAS Meteorological Data
Source ★ at 65.28 S 119.10 E
Meters AGL
Job ID: 149268
Source 1 lat.: -65.28 lon.: 119.10 height: 500 m AGL
Job Start: Tue Dec 30 00:02:55 UTC 2014
Trajectory Direction: Backward Duration: 72 hrs
Vertical Motion Calculation Method: Model Vertical Velocity
Meteorology: 00002.15 Oct 2012 - GDAS1
NOAA HYSPLIT MODEL
Backward trajectories ending at 2100 UTC 18 Oct 12
GDAS Meteorological Data
Source ★ at 65.28 S 119.10 E
Meters AGL
Job ID: 149335
Source 1 lat.: -65.28 lon.: 119.10 height: 500 m AGL
Job Start: Tue Dec 30 00:07:29 UTC 2014
Trajectory Direction: Backward Duration: 72 hrs
Vertical Motion Calculation Method: Model Vertical Velocity
Meteorology: 00002.15 Oct 2012 - GDAS1

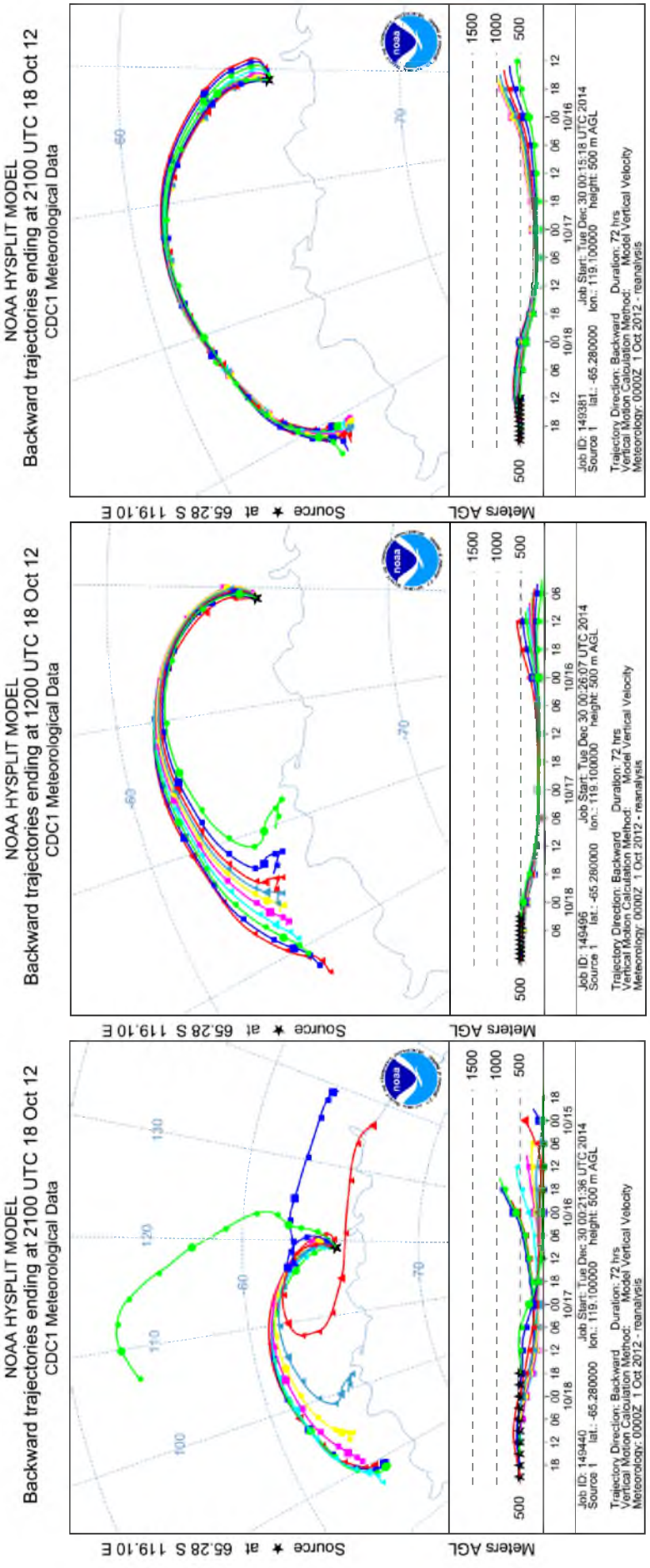
NOAA HYSPLIT MODEL
Backward trajectories ending at 2100 UTC 18 Oct 12
CDC1 Meteorological Data
Source ★ at 65.28 S 119.10 E
Meters AGL
NOAA HYSPLIT MODEL
Backward trajectories ending at 1200 UTC 18 Oct 12
CDC1 Meteorological Data
Source ★ at 65.28 S 119.10 E
Meters AGL
NOAA HYSPLIT MODEL
Backward trajectories ending at 2100 UTC 18 Oct 12
CDC1 Meteorological Data
Source ★ at 65.28 S 119.10 E
Meters AGL

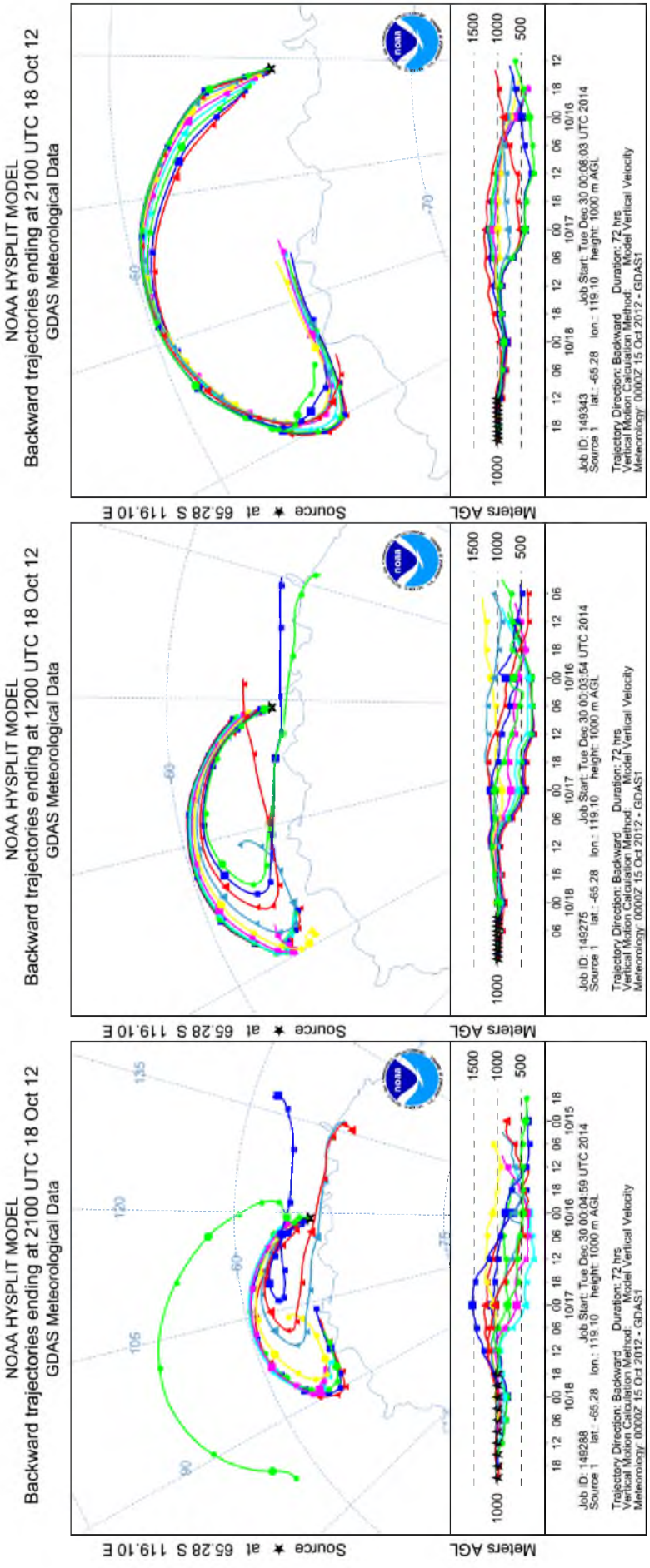
NOAA HYSPLIT MODEL
Backward trajectories ending at 2100 UTC 18 Oct 12
GDAS Meteorological Data
Source ★ at 65.28 S 119.10 E
Meters AGL
Job ID: 149288
Source 1 lat: -65.28 lon: 119.10 height: 1000 m AGL
Job Start: Tue Dec 30 00:04:59 UTC 2014
Trajectory Direction: Backward Duration: 72 hrs
Vertical Motion Calculation Method: Model Vertical Velocity
Meteorology: 00002 15 Oct 2012 - GDAS1
NOAA HYSPLIT MODEL
Backward trajectories ending at 1200 UTC 18 Oct 12
GDAS Meteorological Data
Source ★ at 65.28 S 119.10 E
Meters AGL
Job ID: 149275
Source 1 lat: -65.28 lon: 119.10 height: 1000 m AGL
Job Start: Tue Dec 30 00:03:54 UTC 2014
Trajectory Direction: Backward Duration: 72 hrs
Vertical Motion Calculation Method: Model Vertical Velocity
Meteorology: 00002 15 Oct 2012 - GDAS1
NOAA HYSPLIT MODEL
Backward trajectories ending at 2100 UTC 18 Oct 12
GDAS Meteorological Data
Source ★ at 65.28 S 119.10 E
Meters AGL
Job ID: 149343
Source 1 lat: -65.28 lon: 119.10 height: 1000 m AGL
Job Start: Tue Dec 30 00:06:03 UTC 2014
Trajectory Direction: Backward Duration: 72 hrs
Vertical Motion Calculation Method: Model Vertical Velocity
Meteorology: 00002 15 Oct 2012 - GDAS1

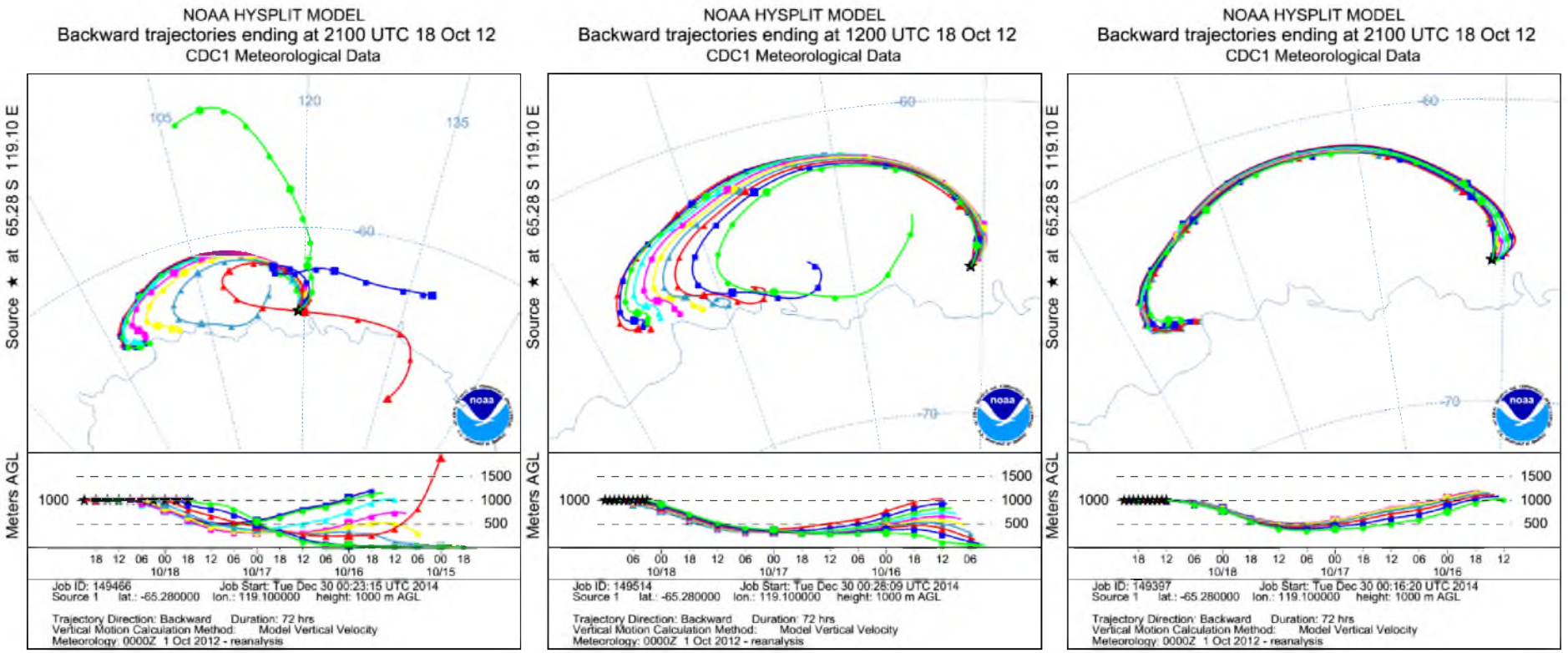

Figure C.3: Backward trajectories calculated using the HYSPLIT model's web interface using two different input meteorological datasets and three different starting heights. Generally speaking, trajectories show a similar story, with a small regional-scale northwest influence and a diluting air-mass towards the end of the event.

C.3 Possible oxidants of Hg in the Antarctic Atmosphere

Halogens are prominent in the polar regions. Halogen photochemistry is unique in the polar regions and is responsible for rapid GEM depletions (Lu et al., 2001; Schroeder and Munthe, 1998; Foster et al., 2001; Impey et al., 1997; Oum, Lakin, and Finlayson-Pitts, 1998). Unfortunately, halogen radicals cannot currently be measured directly. However measurement of oxidised species (e.g. IO and BrO) is possible using remote sensing technology and halocarbons can be measured *in-situ*. During SIPEXII, a number of halogen species were measured using both remote sensing and *in-situ* techniques.

Profiles of BrO and IO, close proxies for $I^{\bullet}$ and $Br^{\bullet}$ respectively, in the lowest 4 km of the atmosphere were measured on the voyage using MAX-DOAS. Both oxidised species are a single step away from their respective atomic radicals in their reaction chemistry, and as such, are a good proxy for their radical chemistry (see Appendix A.13 for an example schematic). Additionally, measurements of halocarbons (potential reservoir species and sources of reactive halogens (e.g. O'Dowd et al., 2002a), including all 3 likely halogen radicals $Cl^{\bullet}$, $Br^{\bullet}$ and $I^{\bullet}$), were made using GC-ECD and may give an indication of halogen loading.

C.3.1 Bromine

In Figure C.4, the integrated vertical BrO column is given along with the Hg^0 concentration for reference. Two features are important to note here. Firstly, BrO concentrations in the marine boundary layer north of the ice edge are close to the detection limit of the instrument, whereas in the pack ice region, concentrations fluctuate considerably. This confirms that the sea ice region is a prominent source of BrO and that northward transport within the boundary layer is minimal, owing to both circulation patterns and the short lifetime of BrO.

The second important feature is the BrO vertical column amount on the 18th October (highlighted) - our nucleation event. On this day, BrO levels are close to open ocean levels throughout the whole daylight period. If bromine were involved in the Hg chemistry, it is likely to go through BrO as an intermediate or by-product in the chemistry, and because the event happened around midday, the solar measurements of the MAXDOAS would have measured BrO at some time before or during the event.

Measurements of bromocarbons (CH_2Br_2 and $CHBr_3$) by GC-ECD during SIPEXII were also available. Although periods of enhanced concentrations were observed in the pack ice at various periods throughout the voyage, concentrations during and in

the days surrounding the event day saw no deviations from baseline concentrations.

Recent measurements by Liao et al. (2012) suggest that the lack of BrO on this day could suggest an abundance in Br_2 instead. Their data show that the concentration of Br_2 varies inversely with O_3, with high Br_2 levels observed only when ozone is depleted. The high concentration and lack of variation in O_3 during the nucleation event makes the presence of Br_2 unlikely, and thus reduces the likelihood of $Br^{\bullet}$ as the oxidant of this event. All this evidence together suggests that $Br^{\bullet}$ is unlikely to be implicated in the nucleation chemistry occurring on this day.

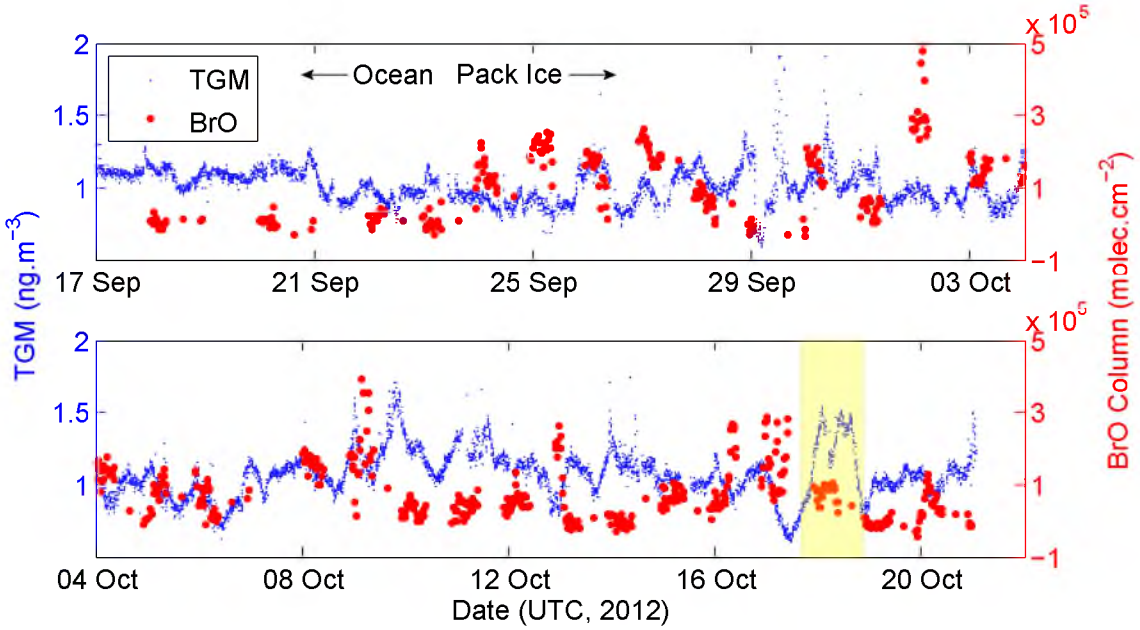

Figure C.4: BrO column densities (molecules.cm^{-3}) at the various viewing elevation angles, plotted with Total Gaseous Mercury (TGM) concentrations for reference. On the 18th October (highlighted), BrO column densities were close to zero, similar to concentrations outside of the sea ice source region which was entered on the 23 September. This data suggests that bromine species are unlikely to be involved in the chemistry leading to the observed new particle formation. The only other significant TGM concentrations, such as those observed around the 10th October, are associated with similarly low BrO concentrations, suggesting that BrO is a controlling species of TGM, as is expected from knowledge of Mercury Depletion Events. These other high mercury events though, did not result in particle formation, suggesting another trigger for formation.

C.3.2 Iodine

Figure 5.13 shows integrated vertical column densities of IO from the MAX-DOAS. IO was found not to be present at any time during the cruise at levels above ~0.15 ppt (1.5×10^{13} *molec.cm*$^{-2}$), however most measurements were well below this. During the event (day number 292), IO concentrations were close to zero (0.1×10^{13}

$molec.cm^{-2}$. GC-ECD measurements of CH_3I were, similarly to other halocarbons, markedly inactive during the period surrounding the event, showing no deviations from low baseline values. Although IO has been observed to be of globally significant concentrations in Antarctica, particularly in the sea ice region (Schönhardt et al., 2012; Schönhardt et al., 2008; Saiz-Lopez et al., 2007b), and investigations outline in Chapter 3 suggest it is responsible for background aerosol populations, measurements during SIPEXII found negligible concentrations, making it unlikely for this regional scale event.

C.3.3 Chlorine

Chlorine radicals, $Cl^{\bullet}$, are strong atmospheric oxidants (Jobson et al., 1994; Donohoue, Bauer, and Hynes, 2005; Ravishankara and Wine, 1980; Friedl and Sander, 1989) and have been identified to expedite the oxidation of Hg^0 to more toxic forms (Donohoue, Bauer, and Hynes, 2005), particularly in highly humid environments (Menke and Wallis, 1980) such as those observed in the sea ice region (see Figure 5.3). The presence of aggressive $Cl^{\bullet}$ chemistry in the Arctic marine boundary layer has been well recognised for some time (Ariya et al., 1998; Boudries and Bottenheim, 2000; Jobson et al., 1994; Keil and Shepson, 2006; Muthuramu et al., 1994; Ramacher, Rudolph, and Koppmann, 1999; Rudolph et al., 1999; Platt, Allan, and Lowe, 2004; Pöhler et al., 2010; Impey et al., 1997), and recent measurements found concentrations of molecular chlorine, Cl_2, in the Arctic at concentrations of up to 400 pptv - the highest concentration measured in any global location (Liao et al., 2014). Although direct reactions of Cl_2 are unlikely due to slower reaction kinetics compared to $Cl^{\bullet}$ (Stephens et al., 2012), the high Cl_2 concentrations serves as a significant reservoir of precursors of $Cl^{\bullet}$. The precursors, including for example Cl_2 and HOCl, have common sources with other halogen precursors, such as Br_2 and HOBr, which are currently believed to include hypersaline brine surfaces on young sea ice, frost flowers, surface hoar adjacent to refreezing leads, saline snowpacks and sea-salt aerosol (Stephens et al., 2012; Douglas, 2005; Kaleschke, 2004; Simpson et al., 2007; Foster et al., 2001; Saiz-Lopez and Glasow, 2012). Unsurprisingly, most of these studies have been conducted in the Arctic, however since environmental conditions are similar, source types are common, and other halogens which are often co-emitted with chlorine are found in high abundance, it is not unreasonably to conclude chlorine could be abundant in the Antarctic. The release of chlorine can also be triggered by photochemical processes (Saiz-Lopez and Glasow, 2012), which is coherent with the photochemical nature of the observed nucleation event.

No measurements of $Cl^{\bullet}$ were made during the voyage. However as stated above, chlorocarbons were measured by GC-ECD. None of the three measured chlorine

compounds (C_2Cl_4, CH_3CCl_3 and $CHCl_3$) showed any deviation from background in the days surrounding the event. Despite the literature suggesting that chlorine may be abundant in the Antarctic and could serve as an active oxidant in Hg chemistry, these measurements suggest, although not definitively, that $Cl^{\bullet}$ is an unlikely oxidant of this event. It is unclear, however, whether $Cl^{\bullet}$ occurs in significant concentrations when the concentrations of other halogen species are so low.